Advances in characterisation, preparation and application of polysaccharide-derived mesoporous carbons

Aleksandra Borisova

PhD

University of York
Chemistry
June 2015

Abstract

Starbons (Starbon®) are a group of mesoporous carbonaceous materials derived from renewable and readily available gelling polysaccharides — starch, alginic acid and pectin. They possess a high mesopore volume, a developed surface area, and a wide range of surface properties, ranging from oxygen-rich and hydrophilic to carbon-rich and hydrophobic, achieved by controlled pyrolysis of mesoporous polysaccharide aerogels in the 300–800 °C range.

The objective of the present work was to build on the existing knowledge and previous developments in characterisation and preparation of Starbons, and their application in adsorption of organic pollutants (phenolics, polycyclic aromatic hydrocarbons, dyes). The aim was to improve our understanding of the relationship between the material properties and application performance.

This thesis presents a systematic investigation of the change in chemical and textural properties of alginic acid and pectin-derived Starbons in the thermal range of 25–800 °C, using a wide range of complementary analytical techniques, such as N_2 adsorption/desorption porosimetry, IR spectroscopy, Raman spectroscopy, UV spectroscopy, TG-IR, elemental analysis, pH drift, SEM and TEM. Analysis of the data demonstrates the common features of the thermal degradation process between alginic acid and pectin aerogels, and a wide range of biomass, and provides a comprehensive understanding of the properties of carbonized materials at any given temperature.

An advancement in the preparation of highly-porous polysaccharide aerogels, using a novel freeze drying route, is reported. This development promises to lead to faster, lower cost and lower waste production of Starbons. The process is universally applicable to starch, alginic acid and pectin-derived materials.

Finally, this thesis reports a systematic in-depth investigation of adsorption of a range of phenols and naphthols on alginic acid-derived Starbons prepared at different temperatures and having different surface areas and pore volumes. The analysis of adsorption kinetics, isotherms, thermodynamics, and desorption provided a comprehensive understanding of the factors governing and influencing the adsorption processes. Starbons demonstrate quantitatively greater desorption than conventional activated carbons.

Contents

List of Figures

List of Tables

Acknowledgements

"Make good ~~art~~ [science]." *Neil Gaiman (scientific ed.)*

Now that I have come so far it does not really feel like it has been nearly four years since this journey began. It does, however, feel that I have grown as a scientist and a character, and this would not have been possible without contributions of knowledgeable, powerful, inspiring, enthusiastic, creative and wonderful human beings I worked with.

An enormous thank-you goes to Prof James Clark for giving me the opportunity to be where I am now, and for the support and freedom I was given to create and solve problems. An equally huge thank-you goes to Dr Vitaliy Budarin, without whom the world of academia would have been a dark and a lonely place, full of monsters and insurmountable hurdles. I am also grateful to Paul Matts, Simon Godfrey, Judith Kaumanns, and John Lankhol from P&G for their help throughout this project and financial support.

A huge thank-you to Paul Elliot for everyday science wisdom and knowledge nuggets that one would not find in textbooks and classrooms. Thanks to Dr Mario de Bruyn for making it hard for me; your challenges were greatly appreciated. Thanks to Dr Avtar Matharu for being a watchful eye over my progress throughout this journey. Thanks to everyone else who was helping here and there with advice and consultations: Andy, Helen, Rob, Jimbo, Jennie, Lorenzo, Tom F, Tom A, Mark. Thank you to Hannah and Charlotte.

Another huge thank you goes to the makers of my social life! The GCCE community is like no other, and you know it. I love you all!

Thank you to my best *fiends*, who did not experience Sasha with the PhD syndrome, and, therefore, who still love me — Arina, Nina, Grisha, Ira, Olia, Katia.

Finally, words cannot express how grateful I am to my family, old and new. I just wish all of you were still here.

Declaration

Some of the results presented in this thesis were obtained in collaboration with other individuals who are fully acknowledged in the text. All other results are the original work of the author and it has not been submitted for examination at this or any other institution for another award.

Part of the work presented in this thesis was published in the following publication:

A. Borisova, M. De Bruyn, V. L. Budarin, P. S. Shuttleworth, J. R. Dodson, M. L. Segatto and J. H. Clark, *Macromol. Rapid Commun.*, 2015, 36, 774—779.

Aleksandra Borisova

2015

Chapter 1

Introduction

1.1 Environmental impact of consumption

The tangible and beneficial impact of chemistry on our society is evident in all spheres of our lives. Industries such as pharmaceuticals, food, and cosmetics have undergone a dramatic transformation in just a century, significantly improving the quality of life. However, with the increasing range of affordable consumer products available, the volumes of disposable chemicals on the market are increasing rapidly. The environmental impacts associated with the different life cycle stages of these products, such as sourcing, manufacturing, and consumption, is becoming significant. Environmental assessment tools, such as Life Cycle Assessment (LCA), are gaining importance in identifying the major environmental impacts of these products, and are increasingly used to find solutions to the adverse effects.[1,2] There is a general drive towards a holistic approach to environmental impact assessment, acknowledging the intricate relationships between production, consumption, discarding of waste, and the environment.

Hair care is an example of a thriving and growing segment of the cosmetic market that consumes large volumes of chemicals. In 2010, 941 thousand tonnes of chemical ingredients were used in the hair care industry globally, generating $73.7 billion in value.[3,4] Hair dyes account for around 20 % of the hair care market. The first permanent hair dye formulation was patented in 1907 by Eugene Schueller, the founder of L'Oreal.[5] The patent reported oxidative coupling of colourless *p*-toluenediamine to yield a bulky coloured dye that would get trapped in the fibres of the hair strand, giving long lasting colour. In Figure 1.1, a generic oxidative coupling of hair dye precursors is shown. In this reaction, a *para*-substituted precursor (I, e.g. *p*-toluenediamine) is oxidized with hydrogen peroxide forming either benzoquinone diimine or benzoquinone monoimine (II), which is a very reactive intermediate. The intermediate II reacts with *meta*, *ortho* or *para* couplers (III, e.g. *p*-toluenediamine, resorcinol) to form a dimeric (IV) and/or trimeric (V) conjugated dyes. This oxidative coupling is a complex reaction, and despite over 100 years of commercial use its mechanism is not fully understood.[6]

This chemical reaction marked the beginning of the hair dye industry as we know it. Subsequently, more compounds were developed, to yield different colour palettes upon oxidative coupling. These compounds, referred to as precursors, included resorcinol, *m*-aminophenol, 1-naphthol, and 5-amino-*o*-cresol.

To date, the same chemistry is used in modern hair dye formulations, and it is not likely to change due to the high costs of development and high safety testing require-

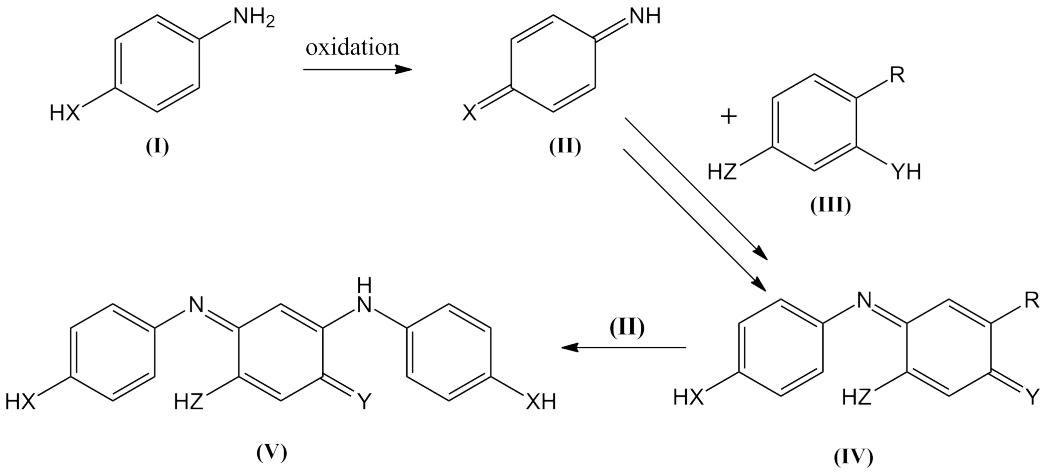

Figure 1.1: Oxidation reaction in hair colouring (X,Y, Z = O or NH)

ments.[7] In addition to the dye precursors, which make up 8 wt% of a formulation, hair dyes contain surfactants and preservatives. The majority of these chemicals are washed off after application of the hair dye. In a study on the levels of unconsumed and unreacted dye precursor, it was reported that up to 65 % of the original precursors end up in waste water, and the majority of these precursors are toxic.[8]

According to the personal care association of Europe, the LCA of products similar to hair dyes in composition and use pattern, e.g. shampoo, indicate that the part of the life cycle which contributes the most to the environmental impact of the product is usage by the consumer.[9] The outcomes of an LCA of a shampoo, shown in Figure 1.2, demonstrate that the global warming potential (GWP), water consumption and eutrophication resulting from the use of these product have the greatest environmental impacts.

Some of this environmental impact could be negated by trapping the waste chemicals at source, so they can be safely disposed of. The water could also potentially be reused, which is particularly applicable to the developing countries, where the personal hair care market is growing more rapidly than the water infrastructure.[11,12] Moreover, the recovery of chemicals for reuse is of particular interest to the emerging trend of closed-loop recycling and the circular economy.

However, the process of chemical recovery should itself be green and sustainable. The materials used for the recovery should be bio-derived, reusable, and easy to manufacture, and the recovery of the trapped chemicals should be straightforward. Ideally, the recovery process should be economically viable, and, on the whole, should reduce the amount of waste generated and energy consumed. These requirements constitute

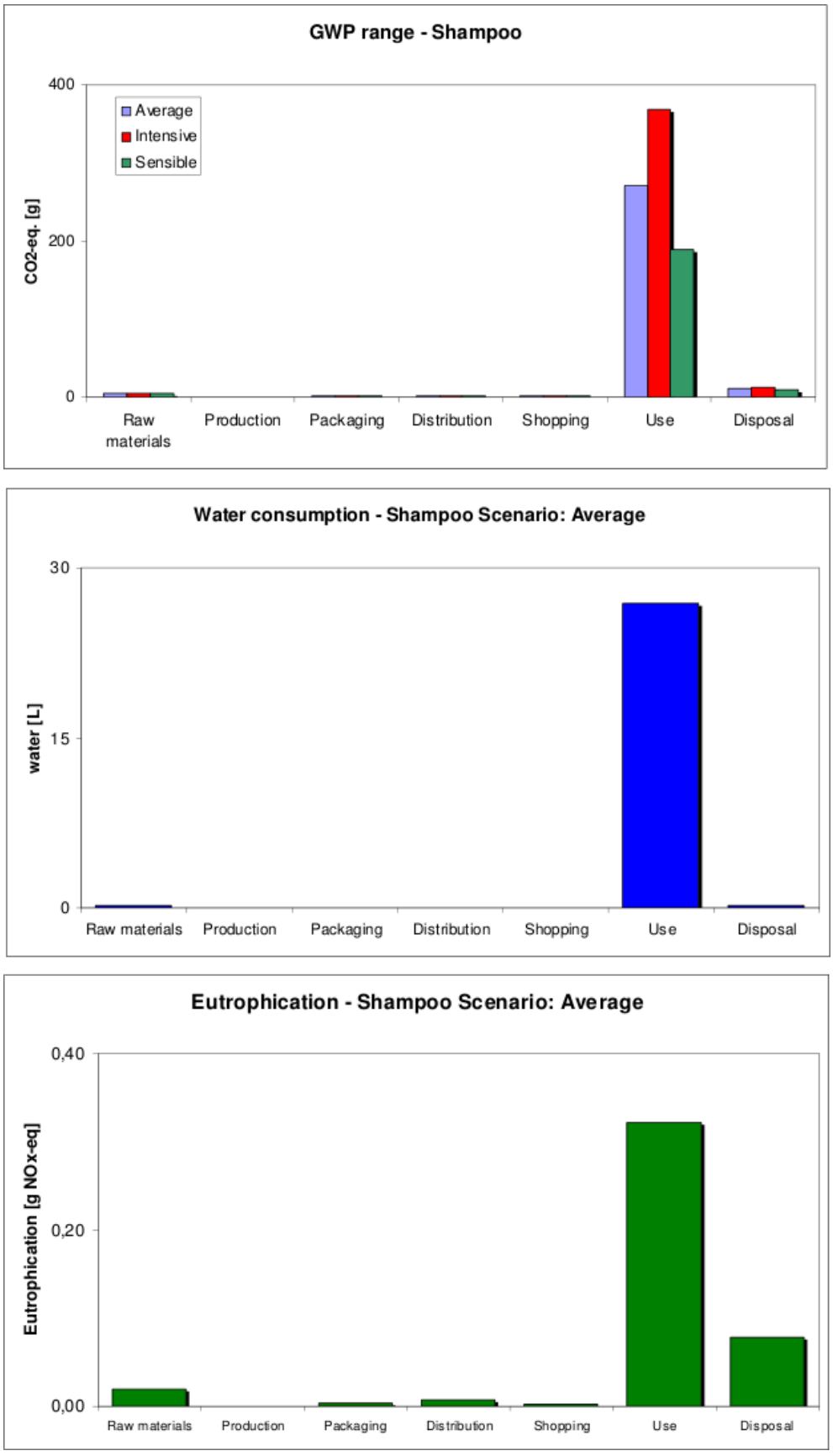

Figure 1.2: Findings from an LCA of shampoo (image taken from Henkel AG & Co. KGaA report)[10]

the holistic approach to the environmental problems: the environmental impacts associated with the proposed solutions should be taken into account, and compared to the anticipated environmental impact reduction.

One of the most common materials used for the removal of chemical contamination from waste water is activated carbon, a material with a high surface area (>500 $m^2\ g^{-1}$) and well developed microporosity ($\leq$2 nm pore diameter).[13] Activated carbons are produced by steam or acid activation of carbon-rich materials, such as coal, husks, nutshells, or wood. The underlying principle behind the effectiveness of activated carbon in the removal of contaminants is the strength of their adsorption on the high surface area of the material. Adsorption is a surface phenomenon, in which the chemicals adhere to the surface of an adsorbent through electrostatic interaction (ionic, π-π, hydrogen bonding, van der Waals forces) or chemical bonds (covalent bond formation). In small pores, such as micropores, a greater surface energy is exerted on the chemical contaminants, resulting in strong adhesion.[14]

Although activated carbons are effective adsorbents, they have a number of drawbacks, which limit their potential for chemical capture for desorption and reuse. The narrow pore diameter restricts the size of the adsorbates. The low pore volume limits the diffusion of the waste water through the porous network, and the desorption of the adsorbates is difficult to achieve due to the strong adsorption and low diffusion of the eluting phase into the pores. Therefore, an increase in the pore volume and the pore size could potentially yield a material better suited for adsorption and recovery of a wider range of chemical contaminants for their subsequent reuse. Therefore, the properties of mesoporous materials (2–50 nm pore diameter) could overcome the drawbacks of microporous carbons in chemicals capture for reuse.

1.2 Mesoporous materials

Mesoporous materials as a class are relatively new in the scientific community. This class encompasses various mesoporous materials, such as mesoporous silica, alumina, zirconia, zeolites etc., and mesoporous carbons. The distinctive characteristics of these materials are mesopores (2–50 nm), high pore volume (1–2 $cm^3\ g^{-1}$), and high surface area ($\approx$200 $m^2\ g^{-1}$).

1.2.1 Mesoporous silica

The earliest mesoporous material, reported in 1970s, was mesoporous silica.[15] The process involved hydrolysis of a silica precursor (tetramethyl orthosilicate, tetraethyl orthosilicate, sodium silicate) around sacrificial templates (surfactants) in the presence of ammonia. The template removal and improvement in the structural stability of the mesoporous network was achieved through high temperature calcination.[15] Initially, the material did not gain significant interest, until recently, when its potential in catalysis, separations, drug delivery, biomedical applications, CO_2 capture and energy storage was recognized.[16,17] The most prominent mesoporous silicas that put these materials under the scientific spotlight are MCM-41 and SB-15.

The MCM-41 (Mobil Composition of Matter No. 41) material, synthesized by Mobil, was characterized by the remarkable regularity of uniformly sized hexagonal mesopores.[18] In Figure 1.3 the production route of MCM-41 is schematically demonstrated. It follows similar method as the original process reported using different surfactant (e.g. cetyltrimethylammonium bromide). The SBA-15 (Santa Barbara Amorphous) is another well ordered mesoporous silica with hexagonal pores of a very narrow pore size distribution, synthesized in acidic media.[19]

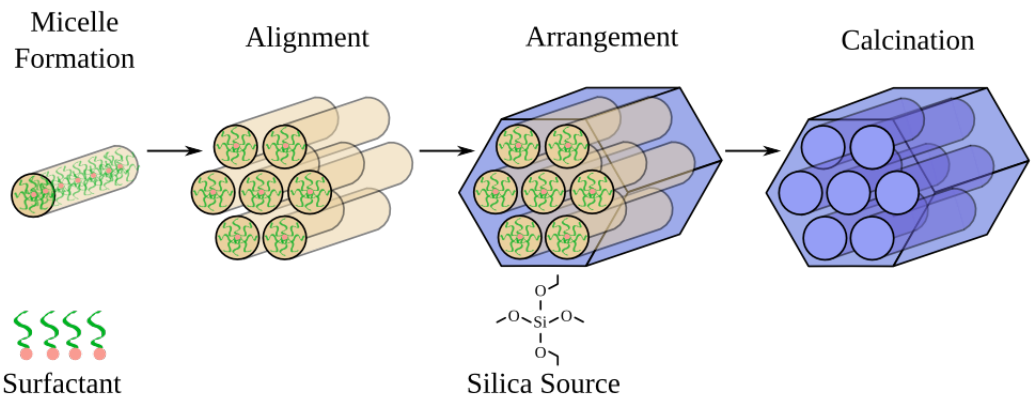

Figure 1.3: MCM-41 synthetic route

Mesoporous silica have demonstrated ability to adsorb and desorb a range of organic molecules; however, their effectiveness is limited by the hydrophilic surface functionality and complicated surface functionalisation.[20,21]

1.2.2 Mesoporous carbon

The preparation of mesoporous carbons was first reported in the early 1980s.[22] The most common carbon source for this material is phenolic or phenol-formaldehyde resins. The synthesis involves polymerisation of resin monomers around a sacrificial silica porogen of the shape and size of the desired pores. This method is referred to as hard-templation. The carbonisation of the resulting resin-silica hybrid, and dissolution of the silica template yield mesoporous carbon.[22] By controlling the parameters of the template, an array of mesoporous carbons with different pore size distributions, surface areas and regularity in the porous network can be created. However, there is limited control over surface functionality. Moreover, the process of mesoporous carbon fabrication is resource intensive, which negatively affects availability of the material, not to mention that it requires a petroleum-derived feedstock.

Due to the high process cost, the potential applications of mesoporous carbons tend to be advanced high end applications, for instance, in fuel cells, batteries, and specialized electronic applications.[23,24]

1.2.3 Polysaccharide-derived mesoporous carbon

A bio-derived alternative to conventional mesoporous carbons is a novel mesoporous carbonaceous material known as Starbon, developed at the Green Chemistry Centre of Excellence of the University of York.[25] Starbon precursors are mesoporous polysaccharide aerogels, formed due to the natural tendency of gelling polysaccharides to create extended 3D networks in water, i.e. gels. These gels, when dried appropriately, retain the porous structure of the 3D network, resulting in mesoporous polysaccharide aerogels with textural properties (surface area, pore volumes, pore size), dependent on the type of polysaccharide used. To date, preparation of Starbons from starch, alginic acid and pectin have been reported.[25–27]

1.2.4 Starbon production

The conventional production process of Starbons is shown in Figure 1.4, featuring gelatinisation, retrogradation, solvent exchange, drying and carbonisation steps.

Gelatinisation During thermal gelatinisation in water, the intermolecular bonds of a semi-crystalline polysaccharide are broken. The solvation of the polysaccharide

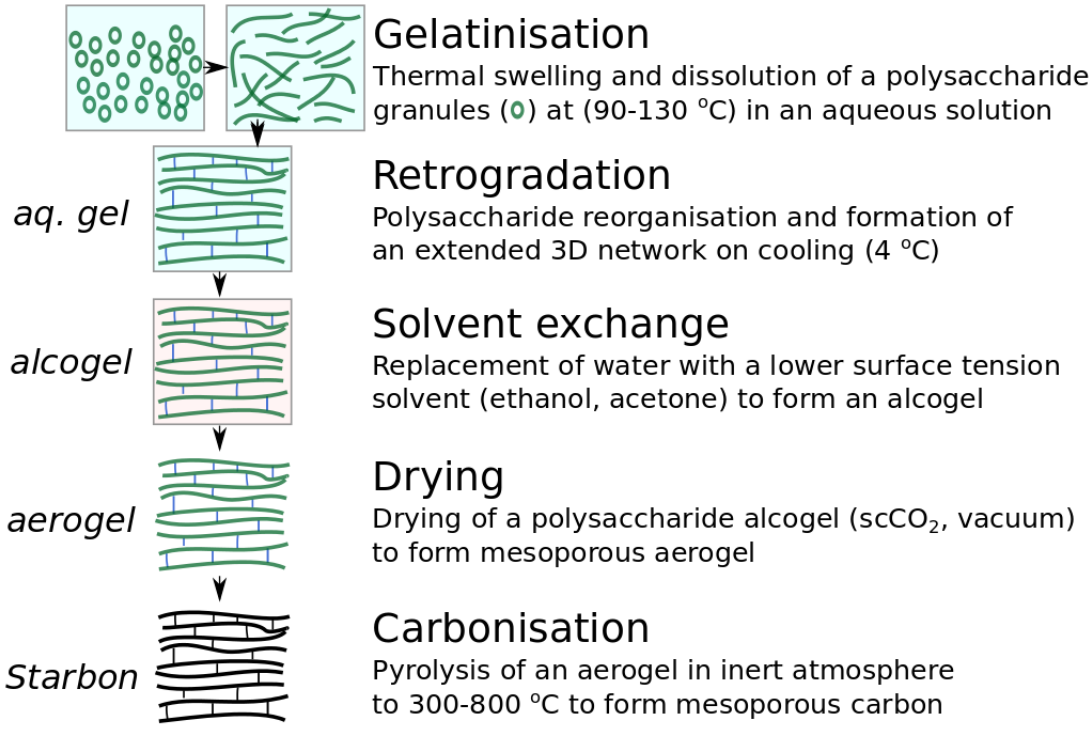

Figure 1.4: Conventional Starbon preparation process

chains increases through hydrogen bonding after the disruption of the crystallinity, leading to the distribution of the polysaccharide throughout the solution.[28]

Retrogradation Thickening of the gel occurs on cooling, due to the reformation of the intermolecular associations between the polysaccharide chains, and partial recrystallisation.[29]

Solvent Exchange Replacement of water in the polysaccharide gel with a lower surface tension solvent (ethanol, methanol, acetone) prevents the collapse of the porous network upon drying. The solvent exchange is repeated up to six times to ensure the maximum removal of water. The resulting material is refered to as an alcogel.

Drying Drying of the solvent produces a mesoporous aerogel. There are two common ways to drive off the solvent and obtain the aerogel — supercritical carbon dioxide ($scCO_2$) and vacuum drying. $scCO_2$ drying was demonstrated to yield the aerogels with the highest pore volume and surface area, whereas vacuum drying yields lower pore volume materials.[30]

Carbonisation Pyrolysis (300–800 °C) of the aerogel dehydrates and deoxygenates its

structure while stabilizing it. The material becomes more hydrophobic with temperature, which enables its application in aqueous environments and solvents. There is a relationship between the pyrolysis temperature and the surface chemistry, which allows the surface properties to be tuned for various applications.[25]

The existing Starbon production process has a range of technological and economical difficulties when applied to large scale production. The solvent exchange step generates considerable volumes of waste solvent, and is time consuming. The $scCO_2$ drying is technically difficult on a large scale, due to the limited availability of the technology, and high operational costs and maintenance requirements. However, there is scope for improvement and optimisation of the method, which was a part of this project.

1.2.5 Starch

Starch was the first reported substrate for Starbons.[25] It is an energy storage polysaccharide found in the most plants, and its common industrial sources are corn, potato, cassava, and wheat. According to the International Starch Institute, the estimated world production of starch in 2015 will reach 85 million tonnes.[31] Starch could also be produced from industrial food waste, e.g. potato peels.

The macromolecular structure of starch consists of linear amylose and branched amylopectin polymers. Both types of polymers are made up of α-D-glucose molecules linked by (1→4) glycosidic linkages, with (1→6) branching in amylopectin (Figure 1.5).

In a thermally treated aqueous solution, starch granules swell and amylose solubilises, leading to the viscosity increase. The swollen amylopectin granules form a network through hydrogen bonding and van der Waals interactions, surrounded by an amylose solution. On cooling and retrogradation, the amylose recrystallizes and the gel thickens.[29] This recrystallized starch takes up a greater volume, and contains water between the crystalline regions. Substitution of this water with low surface tension solvents, and subsequent drying, yields a low density mesoporous aerogel.[25] Acid-catalysed carbonization of expanded starch aerogels produces mesoporous Starbons. The typical textural properties of starch-derived aerogels and Starbons are presented in Table 1.1.

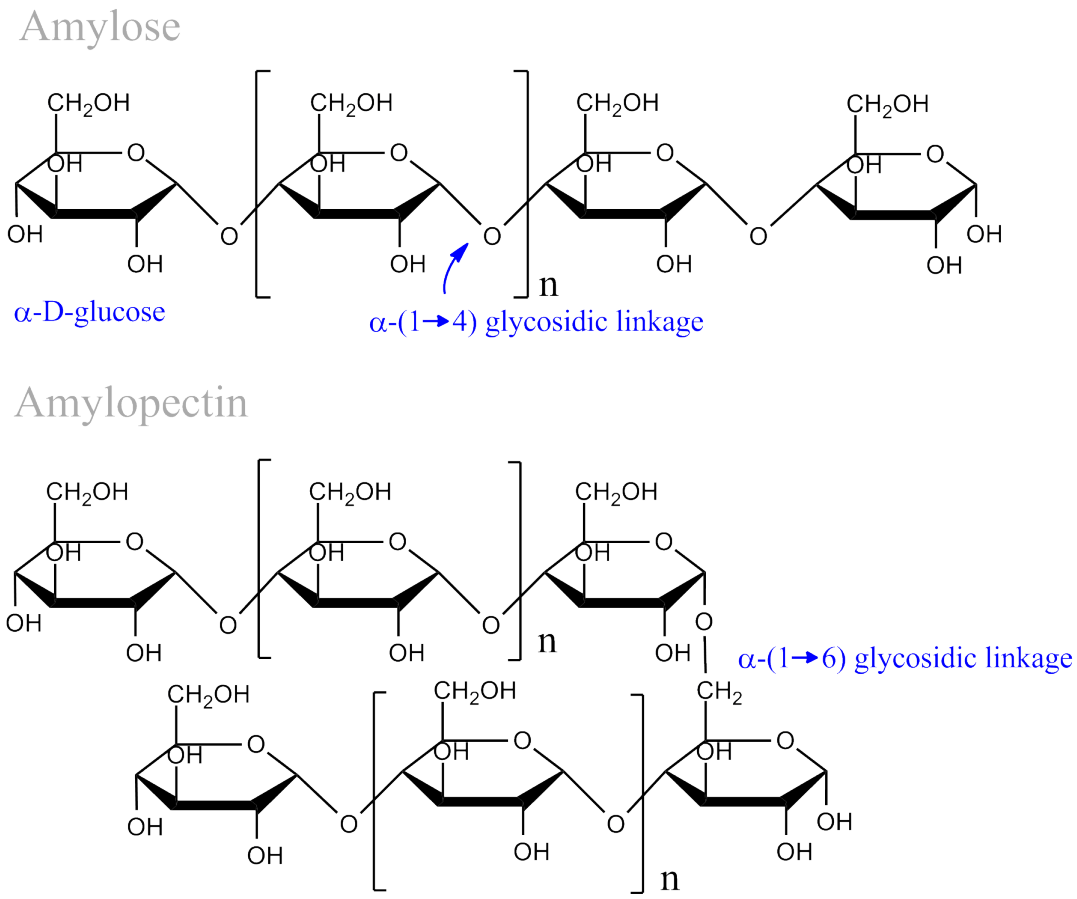

Figure 1.5: Structures of starch components — amylose and amylopectin

Table 1.1: Textural properties of starch-derived aerogel and Starbons (S), determined with nitrogen sorption porosimetry[25] (S300 prepared at 300 °C and S800 prepared at 800 °C)

	surface area [$m^2\ g^{-1}$]	pore volume [$cm^3\ g^{-1}$]	average pore diameter [nm]
aerogel	180	0.6	8
S300	300	0.55	16
S800	550	0.75	11

1.2.6 Alginic acid

Alginic acid is an anionic structural polysaccharide found in brown algae, which grows abundantly in various regions worldwide, and is harvested industrially in Norway, Scotland, USA, France, and China. In 2009, the world production of alginates reached 25.5 thousand tonnes.[32]

Alginic acid consists of two sugar monomers: β-D-mannuronate (M) and α-L-guluronate (G) (Figure 1.6). The monomers are linked through (1→4) glycosidic bonds in linear chains of homopolymeric blocks (MMM or GGG) or alternating blocks (MGMG), shown in Figure 1.6.

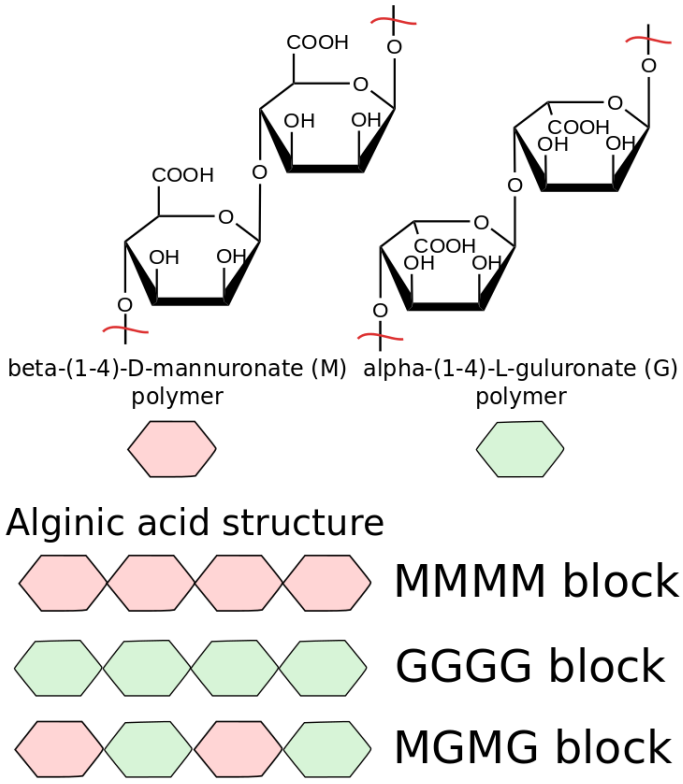

Figure 1.6: Structures of mannuronate (M) and guluronate (G), and their arrangements in alginic acid

In a thermally treated aqueous solution, alginic acid granules undergo similar transformations to starch. The intramolecular bonds break, and the polymers expand through solvation with water. Upon cooling, the molecular associations increase, leading to thickening and gel fomation.[33]The solvent exchange and drying procedures for alginic acid are the same as for the starch-derived aerogels. The typical textural properties of alginic acid-derived aerogels and Starbons are presented in Table 1.2. The difference in

the porosity characteristics (pore volume and diameter) between starch and alginic acid is attributed to the difference in the electrostatic interactions and intramolecular forces acting in neutral starch gel and anionic aliginic acid gel.[34]

Table 1.2: Textural properties of alginic acid-derived aerogel and Starbons, determined with nitrogen sorption porosimetry[34] (A300 prepared at 300 °C and A700 prepared at 700 °C)

	surface area [$m^2\ g^{-1}$]	pore volume [$cm^3\ g^{-1}$]	average pore diameter [nm]
aerogel	320	2.65	25
A300	216	0.9	18
A700	349	1	16

1.2.7 Pectin

Pectin is a structural anionic polysaccharide found in all terrestrial plants. It is a heteropolysaccharide, and is made up primarily of D-galacturonic acid linked by (1→4) glycosidic bonds. L-Rhamnose is the second most common pectin sugar, incorporated in the uronide backbone (Figure 1.7). D-Galacturonic acid exists in protonated, methoxylated and carboxylate forms. Polymer branching commonly occurs at L-rhamnose, and may contain arabinan, galactan, arabinogalactan, D-glucuronic acid, L-fucose, D-glucose, D-mannose and D-xylose.[35] Commercially, two types of pectin are distinguished, depending on their degree of esterification (DE): low-methoxyl (DE$\leq$50%) and high-methoxyl (DE>50%) pectin. Pectins are commercially extracted from apples and citrus peels. According to CP Kelco, the worlds largest pectin producer, world production of pectin in 2009 was 45 thousand tonnes.[36]

Due to its structural complexity, the gelation of pectin depends on the arrangement of its monomers and the DE of galacturonic acid. In an aqueous solution, high-methoxy pectin forms an extended 3D network, primarily through hydrogen bonding and hydrophobic interactions.[37] Low methoxy pectin requires divalent cations, e.g. Ca^{2+} for the polymers to form a cage structure. As a Starbon precursor, pectin is processed in

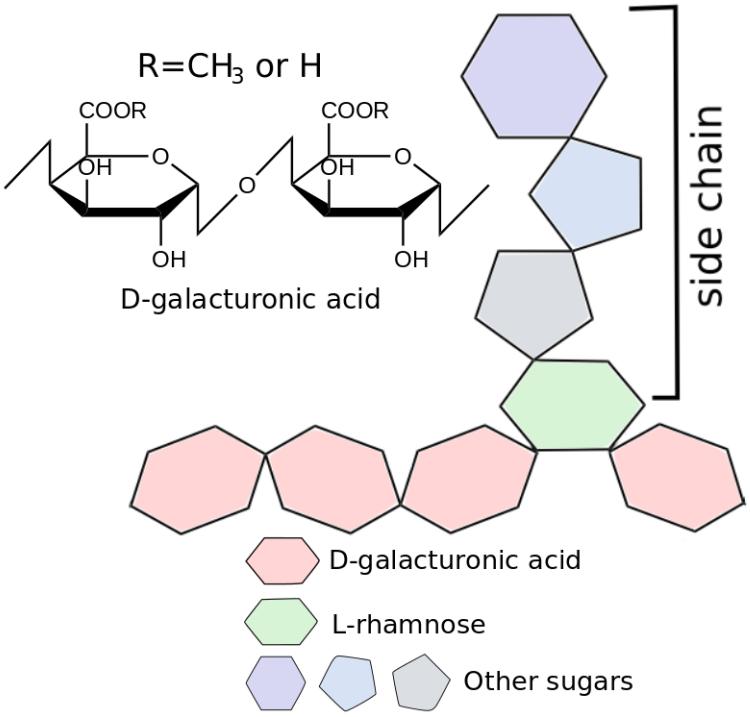

Figure 1.7: Structures of galacturonic acid and pectin

the same way as starch and alginic acid. In Table 1.3, the typical textural properties of alginic acid-derived aerogels and Starbons are presented.

Table 1.3: Textural properties of pectin-derived aerogel and Starbons, determined with nitrogen sorption porosimetry[27] (P400 prepared at 400 °C and P600 prepared at 600 °C)

	surface area $[m^2\ g^{-1}]$	pore volume $[cm^3\ g^{-1}]$	average pore diameter [nm]
aerogel	485	4.2	27
P400	274	0.78	11
P600	233	0.55	10

1.2.8 Starbons research

A number of reports on the preparation, characterisation and applications of Starbons are available. Starch-, alginic acid- and pectin-derived Starbons were characterised previously by Budarin et al., White et al., and Shuttleworth et al.[25–27,34,38] The most important common trend observed in the carbonisation of these polysaccharide aerogels is the transition of their surface chemistry from oxygen-rich and hydrophilic to carbon-rich and hydrophobic in character. It has also been established that the temperature of carbonisation provides control over the surface chemistry, which give access to a broad spectrum of materials for different application requirements.

The reported Starbon applications are catalysis, chromatographic separation, and adsorptions of organic compounds. Sulfonated Starbon acids were reported to be a good solid acid catalyst for esterification of different organic acids.[39] Microwave-assisted *N*-acylation of amines catalysed by sulfonated Starbons was also reported.[40] In alkylation and acetylation reactions Starbon showed good catalytic conversion.[41] Starbons have also been demonstrated to be an effective solid support for ruthenium, and Ru-Starbon materials were shown to catalyse hydrogenation of organic acids.[42] The successful use of alginic acid-derived Starbons as a stationary phase for chromatographic separation of polar neutral monosaccharides was reported.[34] The potential of Starbons for use in separation of different chemicals, and solid phase extractions, is being further developed.

The application of the most relevance to the present study is the use of starch and alginic acid-derived Starbons in adsorption. A range of phenols (phenol, *o*-cresol, 2-fluorophenol, 3-aminophenol, 4-methoxyphenol) and organic dyes (methylene blue, acid blue 92) were previously reported to adsorb well on Starbons from aqueous solutions. Good adsorption capacities for these molecules were demonstrated, with an indication that the adsorption performance depends on the nature of the molecule and the chemistry of the surface.[43,44] However, the application of pectin-derived Starbons has not been reported to date.

1.3 Scope of the present work

The objective of this project was to build on the existing knowledge of the preparation, characterisation and application of Starbons, in order to advance the understanding of these materials and to address some current challenges. The focus of this work was on

the less studied alginic acid- and pectin-derived Starbon materials.

In **Chapter 2**, a systematic investigation of changes in the chemical and textural properties of alginic acid aerogels with temperature is reported. A number of additional techniques, not used previously to characterise Starbons, such as Raman spectroscopy, pH drift, and van Krevelen diagram, were employed to investigate step-by-step thermal transitions.

In **Chapter 3**, a systematic investigation of the adsorption of three phenolic molecules (hair dye ingredients) on alginic acid-derived Starbons is reported. The main aim was to investigate the role of the surface chemistry and textural properties of the adsorbent on the adsorption, which has not been investigated to date. A conventional activated carbon was used as a benchmark material for comparison. Desorption of the phenolics with ethanol was also reported.

In **Chapter 4**, a similar experimental approach to that used with adsorption of phenolics was applied to the adsorption of a new type of chemical pollutant, 1-naphthol and 2-naphthol, on alginic acid-derived Starbons. The systematic approach to the investigation into adsorption of these two isomers yielded an interesting insight into the adsorption mechanism, drastically different to the adsorption of phenols. The addition of naphthols to the adsorption portfolio of the Starbon materials was important to expand the knowledge of their potential.

In **Chapter 5**, a novel approach to polysaccharide aerogel fabrication is reported. The conventional solvent exchange and $scCO_2$ drying steps were substituted with a freeze drying method. The mechanisms and effectiveness of the method were investigated in detail using pectin as the substrate. The method was then extended to starch and alginic acid, to demonstrate its versatility. Overall, the freeze drying route was shown to be more time and solvent efficient than the conventional route.

In **Chapter 6**, Starbons derived from pectin aerogel, prepared using the novel freeze drying route, are characterised. The systematic investigation of the changes in surface chemistry and textural properties with temperature were carried out, to demonstrate the suitability of freeze drying as a route to Starbons. The characterisation procedure used followed the procedure for alginic acid-derived Starbons, to enable future comparison between the materials. The application of pectin-derived Starbons for adsorption of methylene blue and acid blue dyes was also reported.

Chapter 2

Systematic investigation of the influence of temperature on chemical and textural properties of alginic acid-derived aerogel

Figure 2.3 appears in Shuttleworth et al., *Chem. Eur. J.*, 2013, 19, 9351–9557.[38]

Part of the work in this chapter was presented in a poster at the EcoBalt2013 conference in Vilnius (Lithuania, October 2013) and at the 5th IUPAC International Conference on Green Chemistry in Durban (South Africa, August 2014)

2.1 Introduction

Alginic acid-derived mesoporous carbonaceous materials, or algibons, are the second member of the Starbon family.[34] Their preparation and characterization were previously reported in a number of publications.[38,44] Algibons have been demonstrated to offer greater mesopore volume (1.3–2 $cm^3\ g^{-1}$) compared to starch-derived Starbons (0.4–0.8 $cm^3\ g^{-1}$).[25,26,34,44] This high mesoporosity gives algibons a range of advantages over starch-derived Starbons, in applications such as chromatographic separation and adsorption of large molecules. Parker et al. have previously reported that algibon adsorption capacity for organic dyes is greater than that of starch-derived Starbon and conventional activated carbon.[44] White et al. reported good chromatographic separation of neutral sugars with algibon as the stationary phase.[34]

It is known that the surface of expanded alginic acid undergoes a thermally-induced transition from an oxygen-rich hydrophilic state to carbon-rich hydrophobic with conjugated aromaticity.[38] This transition modifies the surface chemistry of the materials and, therefore, its functionality. For instance, the algibon preparation temperature was previously demonstrated to have an impact on the adsorption of dyes.[44] However, to date, a systematic investigation of this thermally-induced change has not been carried out. This information would improve our understanding of the relationship between material properties and their performance.

In this chapter, the investigation of the algibon surface chemistry at different temperatures was carried out with a range of complementary techniques. A systematic investigation of the algibons prepared in the temperature range of 50 to 800 °C with Fourier transform infra-red (FTIR) and Raman spectroscopies was carried out. These data were complemented with thermogravimetric analysis (TGA) and study of the elemental composition. The behaviour of algibons in the aqueous environment was investigated with respect to the surface charge and structural stability to leaching of the carbonisation products. The lack of comparison of algibons with other carbonaceous materials was also addressed.

Finally, consideration was given to the batch-to-batch variation of the key textural properties of algibon (surface area and pore volume). This is an important aspect for the design of algibon applications, since the performance in adsorption, separation and catalysis is anticipated to be linked to the textural properties.

2.2 Aims

A range of complementary analytical techniques were employed to systematically characterise the influence of temperature on the chemical and textural properties of algibons. This information was used to build a detailed understanding of the thermal decomposition process and its influence on the chemical, physical and textural properties of algibons. The ultimate goal was to systematize the information on the various properties of algibons prepared at any given temperature, up to 800 °C. More specifically, the experimental goals were:

- to investigate the thermal degradation profiles (or thermogravimetric curves) and to identify the degradation temperature of expanded and non-expanded alginic acid;
- to investigate the change in the elemental composition of expanded alginic acid with temperature and to plot these data on a van Krevelen diagram;
- to compare the van Krevelen coordinates of algibons to other classes of carbonaceous materials;
- to systematically investigate the change in the surface chemistry of algibons with temperature using IR-DRIFT and Raman spectroscopy;
- to compare the Raman spectra of A800 to alginic acid-derived char and a conventional activated carbon;
- to understand the algibon behaviour in the aqueous environment, such as surface charge and stability to leaching;
- to investigate the textural properties of algibons (surface area and pore volume) and their variation with temperature;
- to examine the batch-to-batch variability of the textural properties of algibons prepared in seven independent batches, and to discuss its influence on the algibon applications.

2.3 Results and Discussion

2.3.1 Thermogravimetric analysis (TGA)

The expanded (A0) and non-expanded (AA) alginic acid were subjected to TGA to investigate their thermal decomposition. The influence of the heating rate (0.5, 5 and 10 °C min^{-1}) on the decomposition of A0 was also investigated. In Figure 2.1.A, the obtained TGA profiles are presented. Their first derivatives are shown in Figure 2.1.B and Figure 2.1.C.

The TGA profiles of AA and A0 show two distinct mass losses. The first mass loss at 50–150 °C (8.5 % for AA and 10 % for A0, 0.5 K min^{-1}) is attributed to the physisorbed moisture. The thermal decomposition of A0 and AA occurs between 160 °C and 300 °C, evident from ≈50 % mass loss. This thermal decomposition is a combination of chemical reactions, including depolymerisation, dehydration, and decarboxylation of polymer chains with the formation of small molecular weight volatile compounds, e.g. H_2O, CO_2, CO, CH_4, low molecular weight organic acids, aldehydes, alcohols.[45]

The decomposition rates of the expanded A0 and the original AA have maxima at 211 °C (Figure 2.1.B), suggesting that the expansion process does not alter significantly the thermal stability of the polysaccharide. However, some differences in the dTG profiles are observed, e.g. AA dTG has a more pronounced shoulder at 190 °C, which are ascribed to the structural difference between the materials.

In the expanded A0, the decomposition temperature increases with the heating rate — 211, 233 and 237 °C for 0.5, 5 and 10 °C min^{-1}, respectively (Figure 2.1.C). This shift in the decomposition temperature of the biomass with the heating rate was previously observed and attributed to the combination of the heat transfer effect and the kinetics of the decomposition.[46,47]

Above 300 °C, the decomposition rate significantly decreases, plateauing just above 500 °C. At 500 °C, ≈75 % of the original mass is lost. Between 500 and 800 °C, a further 2–9 % of the original mass is lost, yielding ≈18–23 % of A800. The yield of A800, heated at 0.5 °C min^{-1}, is the lowest due to the high surface area of the material, and prolonged thermal treatment, which leads to oxidation with trace oxygen present in the N_2 supply.

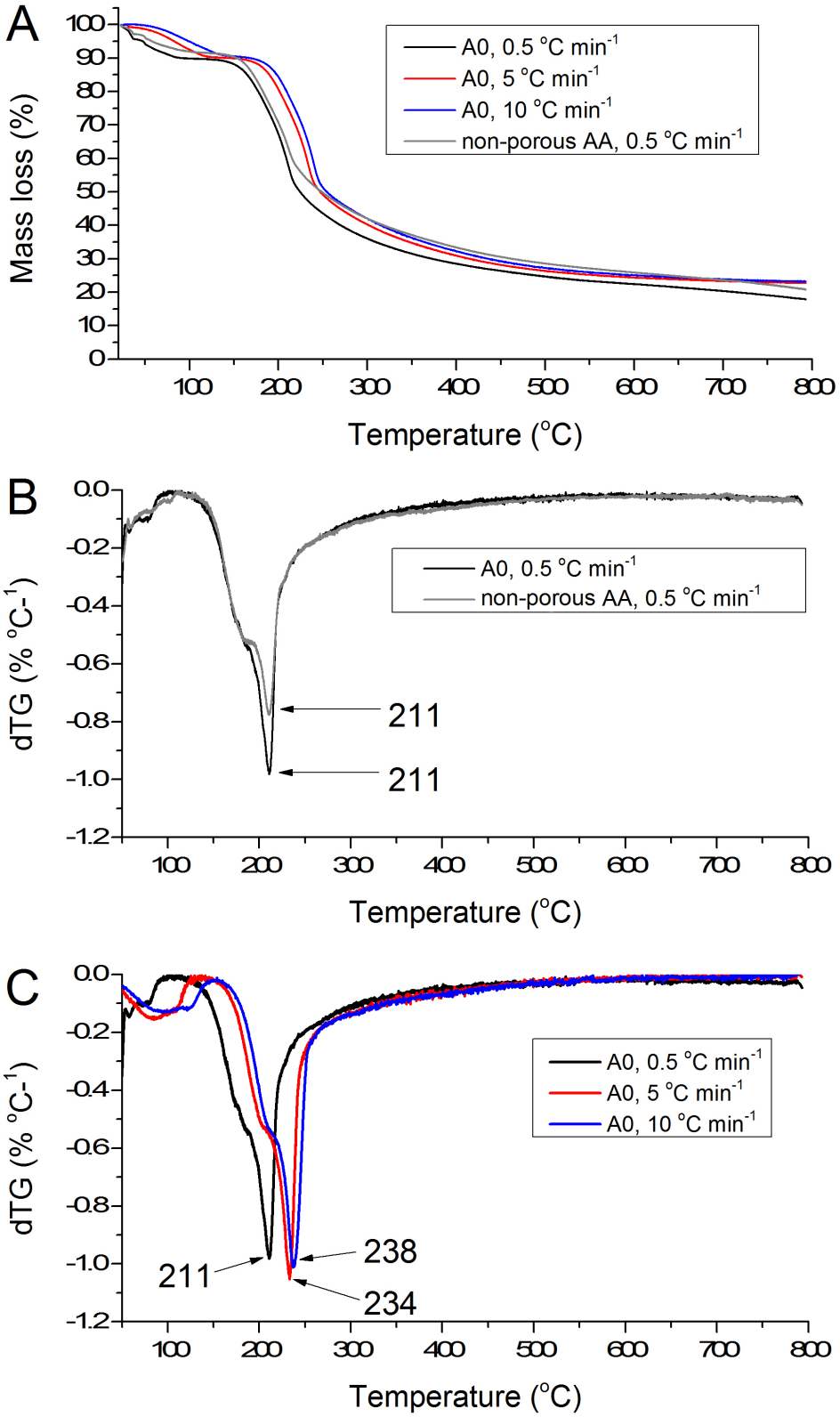

Figure 2.1: **A.** Thermogravimetric analysis of expanded alginic acid A0 carbonised at different rates and non-expanded alginic acid AA **B.** First derivatives of A0 and AA TG profiles (0.5 °C min^{-1}) **C.** First derivatives of A0 TG profiles at different carbonisation rates (0.5, 5, and 10 °C min^{-1})

2.3.2 Elemental analysis

A single batch of expanded A0 material was carbonised to different temperatures in the 300–800 °C range. The elemental compositions of the obtained algibons are presented in Table 2.1.

Table 2.1: Elemental composition of A0-A800 materials (where number is temperature, n=2); C, H and N determined with CHN analysis, ash determined with TG, oxygen determined by mass difference)

Material	C [%]	H [%]	O [%]	N [%]	Ash [%]
A0	36.35 ± 0.04	5.16 ± 0.08	56 ± 0.17	0.00	2.5 ± 0.15
A300	62.82 ± 0.21	3.56 ± 0.07	26 ± 0.37	0.00	7.3 ± 0.30
A400	70.93 ± 0.11	3.32 ± 0.03	16 ± 0.24	0.00	9.3 ± 0.21
A500	77.47 ± 0.03	3.02 ± 0.01	9 ± 0.41	0.17 ± 0.01	11 ± 0.41
A600	82.33 ± 0.24	2.30 ± 0.02	2 ± 0.27	0.00	13 ± 0.11
A700	84.37 ± 0.12	1.56 ± 0.01	0 ± 0.13	0.16 ± 0.01	14 ± 0.05
A800	84.85 ± 0.35	1.20 ± 0.07	0 ± 0.37	0.21 ± 0.04	14 ± 0.09

The oxygen (O) and hydrogen (H) content of A0 decrease with temperature, while the carbon (C) content increases. According to the H:O atomic ratio, dehydration is the main degradation pathway in the thermal range up to 300 °C. Between 300 and 400 °C, O is lost more rapidly than H, suggesting decarboxylaion with CO_2 loss. By 400 °C, 70% of the original O and 36 % of the original H have been lost. By 600 °C, no O remains according to the mass balance. From 500 to 700 °C, the loss of H is linear, indicating steady dehydrogenation/demethylation. Between 700 and 800 °C, the loss of H plateaus. The increase in wt% of ash in the carbonised material is proportional to the overall mass loss.

The change in CHO values was further analysed using a van Krevelen diagram, which is a graphical representation of CHO elemental content. The diagram is a plot of atomic O:C vs H:C values, and it was originally designed to classify different types

of biomass by its potential to form oil, coal or gas in geological processes.[48] To date, the van Krevelen coordinates of a wide range of carbonaceous materials have been reported.[49,50] Figure 2.2 shows the positions of algibons A0-A800 on the van Krevelen diagram along with the generalized positions of biomass, coal and highly conjugated carbon materials.[49]

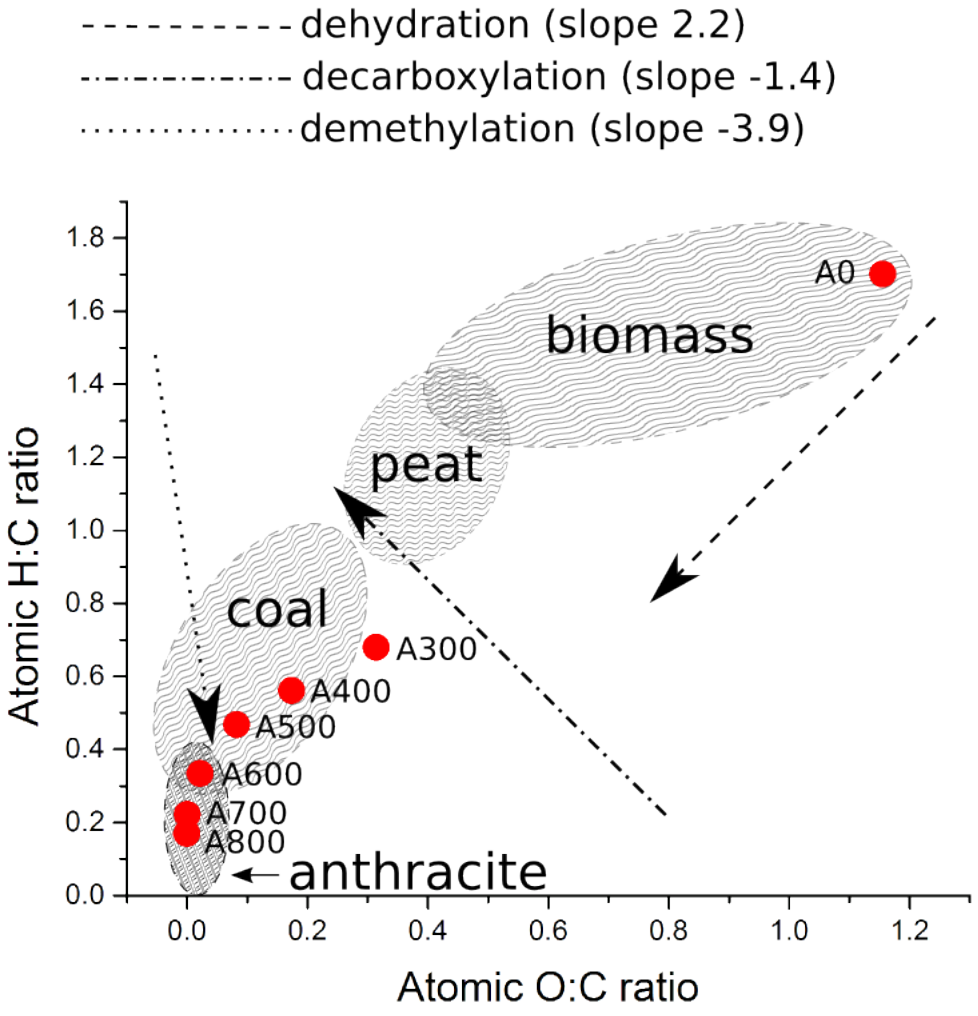

Figure 2.2: Van Krevelen diagram showing positions of A0-A800 algibons, general positions of biomass, coal and anthracite materials, and vectors of elemental composition change due to dehydration, decarboxylation and demethylation.[49] The slope values for each reaction are idealised and calculated based on only one type of reaction taking place

There is a clear separation in the position of A0 and A300 on the van Krevelen diagram. This shift has a slope of 1.2 which is closest to the expected slope of 2.2 for

dehydration. The deviation from the dehydration slope is due to the contribution of decarboxylation. Between 300 and 500 °C, there is a shallower linear decrease in H:C values, indicating a greater influence from the decarboxylation pathway. This is followed by a shift in the demethylation direction from 500 °C onwards.

The composition of A0 is consistent with biomass, whereas A300-A500 positions are similar to coal. Finally, A600-A800 algibons are oxygen- and hydrogen-poor, similar to carbonaceous materials with extended aromatic conjugation, e.g. anthracite.[49]

2.3.3 Systematic IR-DRIFT and Raman investigation of A0-A800

The underlying principle of IR spectroscopy is absorption of IR radiation (700 nm to 1 mm wavelength) by the chemical bonds, leading to change in bond vibrations. IR spectroscopy was previously used to investigate the surface chemistry of the carbonised expanded polysaccharides.[25,34] However, high temperature Starbons are electrically conductive and reflect the electromagnetic radiation.[51] As a result, their IR spectra become uninformative. In contrast to IR spectroscopy, Raman spectroscopy is based on the inelastic scattering, as opposed to absorption, of a monochromatic light in UV-Vis-IR region. Thus, it overcomes limitation of IR spectroscopy in investigation of carbonaceous materials, and provides useful information on carbon structure.[52,53]

Recent years have seen an increased interest in carbon-based materials, ranging from biochars to graphene. Raman spectroscopy has recommended itself as a simple, non-destructive analytical method to study carbon configuration (sp^2, sp^3) and macromolecular carbon structure (chains, rings).[52–54] The Raman data allow comparison across a wide range of materials and investigation of the structural change due to processing and thermal treatment (annealing).[53,55] However, to date, Starbons have not been systematically studied with Raman spectroscopy.

In the present work, a systematic investigation of the temperature-induced chemical change in expanded alginic acid was carried our with IR-DRIFT and Raman spectroscopy.

IR-DRIFT

The 2D IR contour spectrum of algibons is presented in Figure 2.3. The spectrum demonstrates that the original structure of expanded alginic acid is maintained until the decomposition temperature of around 210–225 °C, identified with TG. The polymer

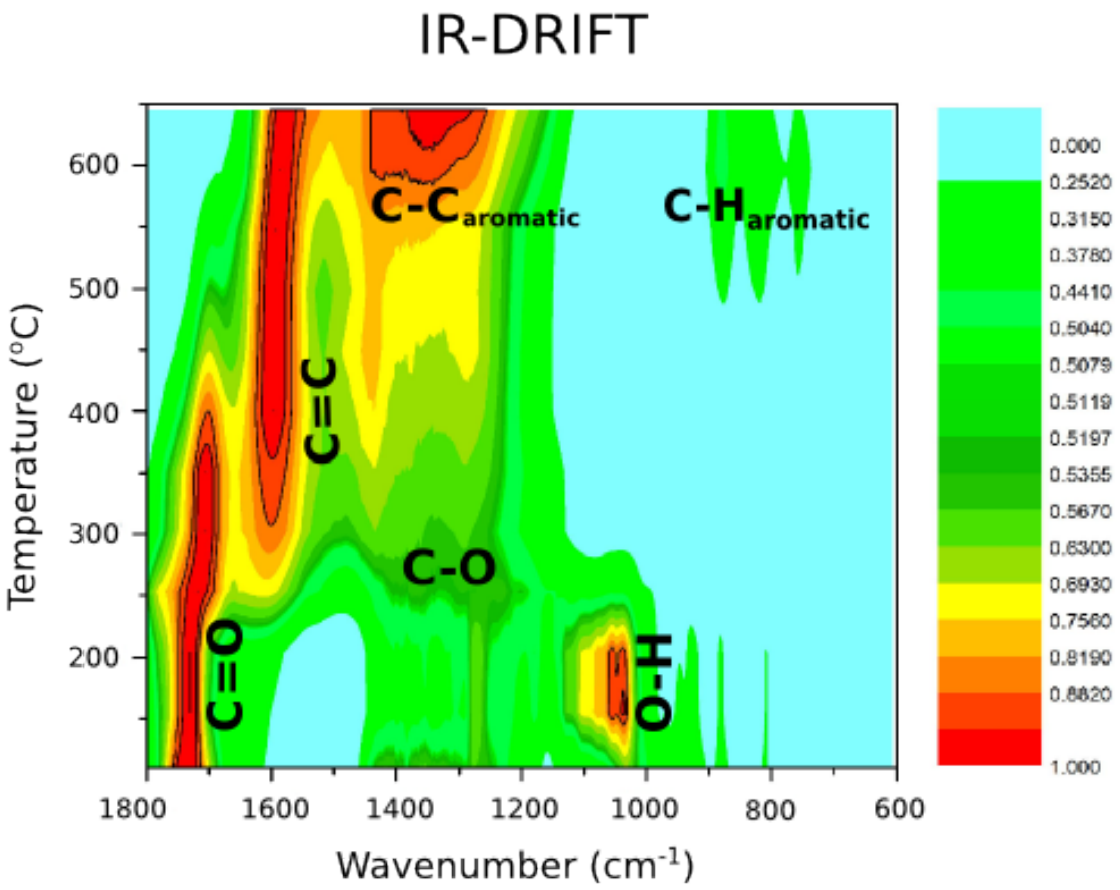

Figure 2.3: 2D IR-DRIFT contour spectrum of algibons A0-A800 °C, with key band assignments

backbone vibrations of pyranose rings at 1010–1120 cm^{-1}, arising from the combinations of C-OH, O-C-H, C-C, and O-H vibrational modes, rapidly disappear due to the thermal depolymerisation.[56] This depolymerisation occurs by a dehydration mechanism, as supported by the elemental analysis and the van Krevelen diagram (Figure 2.2). At 250 °C, the carbonyl vibration at 1720 cm^{-1} undergoes a transition to a lower frequency (≈1700 cm^{-1}) indicating onset of sp^2 conjugation, which is also evident in the development of the C=C band at 1600 cm^{-1}. The formation of a C-O band (around 1300 cm^{-1}) also follows depolymerisation. This band is likely to arise from ethers and lactones, which have been reported previously as a by-product of polysaccharide degradation.[45]

The carbonyl group gradually disappears between 400 and 500 °C, which coincides with the formation of aromatic conjugation. Development of aromatic character is observed in two key signals — out-of-plane C–H bending at 750–900 cm^{-1} and C–C aromatic stretching at 1300–1400 cm^{-1}. Above 650 °C, the IR spectra become uninformative due to the lack of characteristic bands. The higher wavenumber spectra (above 2000 $^{-1}$) were reported previously by Budarin et al. and it reflects all the changes observed in the 600–1800 cm^{-1} region.[25]

Raman

Raman spectroscopy was employed to complement IR data. Raman analysis allowed investigation of the thermal evolution of the carbon structure. The Raman spectra of A300-A800 are shown in Figure 2.4.

In general, first-order spectra (900–1900 cm^{-1}) of algibons feature bands at 1350 cm^{-1} and 1598 cm^{-1}. These bands are found in the spectra of a wide range of carbon materials and are referred to as D and G bands, respectively.[52] Both D and G bands arise due to sp^2 carbon.

The D band (1350 cm^{-1}), or defect band, is attributed to ring breathing modes of sp^2 C=C bonds in non-rigid carbon structures with various defects interrupting graphitic crystallinity, e.g. in amorphous and nanocrystalline carbons.[53] The D band is absent in Raman spectra of highly-ordered carbons, e.g. synthetic graphite.[52,54] It is also absent in spectra of conjugated carbons arranged in chains, eg. polymeric conjugated carbon.[53]

The narrow G band, or graphite band, arises due to in-plane stretching vibrations of sp^2 atoms in rings and chains. The first-order Raman spectrum of perfect graphite crystal features only a G band.[55]

The dominating bands in the Raman spectrum of uncarbonised alginic acid are 813,

890, 956, 1093, 1346, and 1409 cm^{-1}, as reported by Veij et al.[57] At 300 °C, the G band appears and dominates the spectrum, marking the presence of sp^2 bonds. In A300 and A400, two separate bands (1346 cm^{-1}, 1409 cm^{-1}) are observed in the D band region. The positions of these bands are similar to the bands of the original alginic acid, and they are likely to arise from scattering of C-H_x vibrations.

The second-order Raman spectra (2500-3300 cm^{-1}) of A500–A800 have a broad, low intensity band with a band at 2890 cm^{-1}, which is often attributed to the second-order scattering of the D band in disordered carbons.[52] However, Ferrari and Robertson attributed the band to C-H_x stretching modes, after hydrogen substitution with deuterium.[53] This assignment is plausible, since, according to CHN analysis (Table 2.1), there is a considerable amount of H present (1.20$\pm$0.07 wt%) in A800.

Overall, Raman data is consistent with the IR findings: at 300 °C presence of sp^2 carbon is detected and from 500 °C algibon starts to develop aromatic conjugation. The Raman spectra of algibons from A500 onwards are similar to a wide range of carbonaceous materials.

The onset and progress of ring formation was further investigated with the intensity ratio of G and D bands, (I(D)/I(G)), where intensity is the band height. This parameter is often used to determine the degree of graphitization.[53] In Figure 2.5, a plot of I(D)/I(G) vs. temperature is shown. Below 500 °C, the relative intensity of the D band is decreasing, supporting the conclusion that in A300 and A400 it is not a true D band. The increase in I(D)/I(G) ratio above 500 °C is attributed to an increase in aromatic conjugation and agglomeration of disordered graphitic "grains". This finding is in agreement with the IR data, showing the onset of aromaticity at 500 °C. The steep rise in conjugation between A600 and A700 is consistent with the increase in conductivity and IR invisibility of materials above A650.

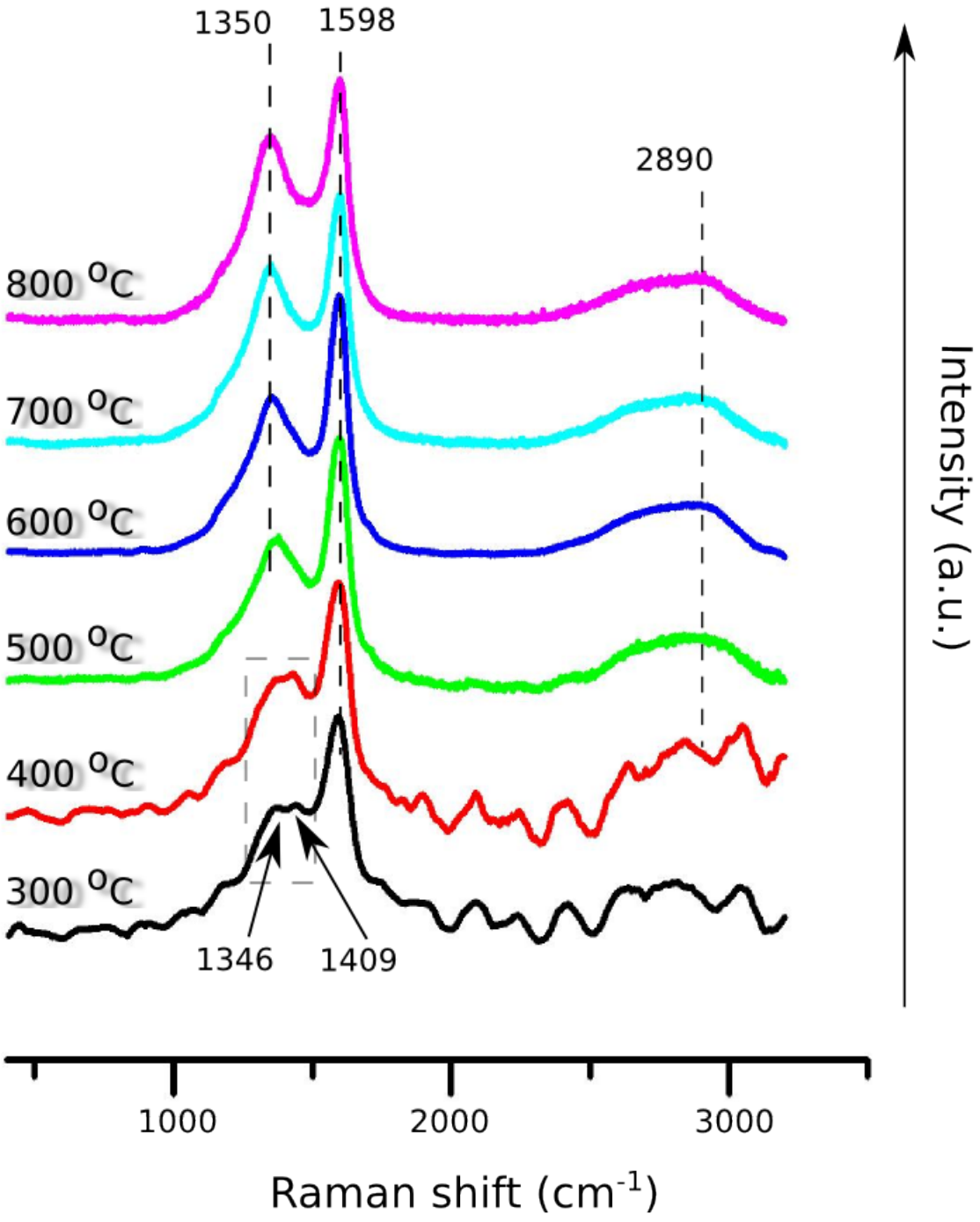

Figure 2.4: Raman spectra of A300-A800 (514 nm)

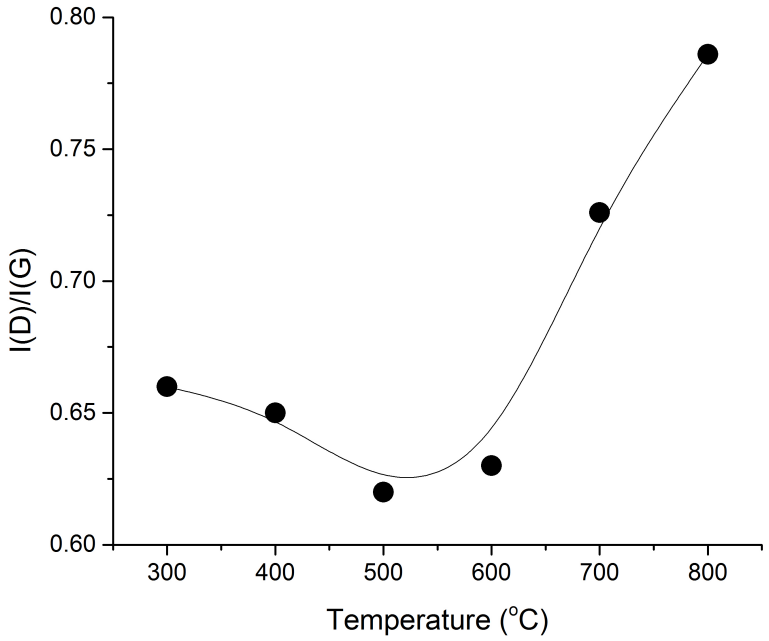

Figure 2.5: Change in the ratio of D to G band intensities, I(D)/I(G), with temperature

2.3.4 Raman spectra of A800, alginic acid char and activated carbon

Algibons prepared at 800 °C are the highest temperature materials of this type with reported applications, and there is a limited number of techniques to study their properties due to high conjugation. Therefore, the A800 Raman spectrum was further analysed and compared to the spectra of two other carbonaceous materials of practical interest: non-porous alginic acid char prepared under the same conditions as A800, and commercial powdered activated carbon (PAC). In Figure 2.6, the Raman spectra of A800, char and PAC are shown, demonstrating that all three materials have a profile characteristic of carbonaceous materials. The positions of the D and G bands are in the narrow range of 1350–1358 cm^{-1} and 1591–1598 cm^{-1}, respectively, which is consistent with the reported values.[52] The PAC spectrum has the greatest D and G band intensity and resolution, whereas the char has the most overlapping band profile.[52,53]

The second-order spectra of A800 and PAC have two broad overlapping bands at around 2680 and 2900 cm^{-1}. In ordered graphitic structures, such as synthetic and microcrystalline graphite, a sharp and intense band around 2650–2700 cm^{-1}, referred to as 2D, is well known and is linked to structural order.[52] The broadness and low intensity of this band in A800 and PAC indicate highly turbostratic graphitic structures. The presence of a band around 2900 cm^{-1} indicates highly disordered structure, and is attributed to C-H stretching modes and overtones of G and D bands.[53,58] In the char, the 2890 cm^{-1} band is more pronounced, hindering the 2D band, and indicating greater structural imperfections than in A800 and PAC.

Both of these second-order spectral features (2D and the band at 2900 cm^{-1}) are absent in highly disordered amorphous carbonaceous materials.

The presence of these bands in A800 and PAC indicates some degree of graphitic turbostratic arrangement, albeit with a significant impact from structural defects, such as non-hexagonal aromatic rings, heteroatoms, and amorphous regions.[52,59] The char, on the other hand, appears to be less ordered.

The presence of defects and impurities is also supported by the overlapping bands and shoulders around the D and G bands. A number of signal processing methods were reported to isolate the contributions of the individual bands.[52,58,60–63] The Raman spectra of alginic acid-derived materials closely resembles those of carbonaceous materials obtained by hydrothermal treatment of sugars.[61] Therefore, in the present study, the procedure for band separation developed for these materials was followed.

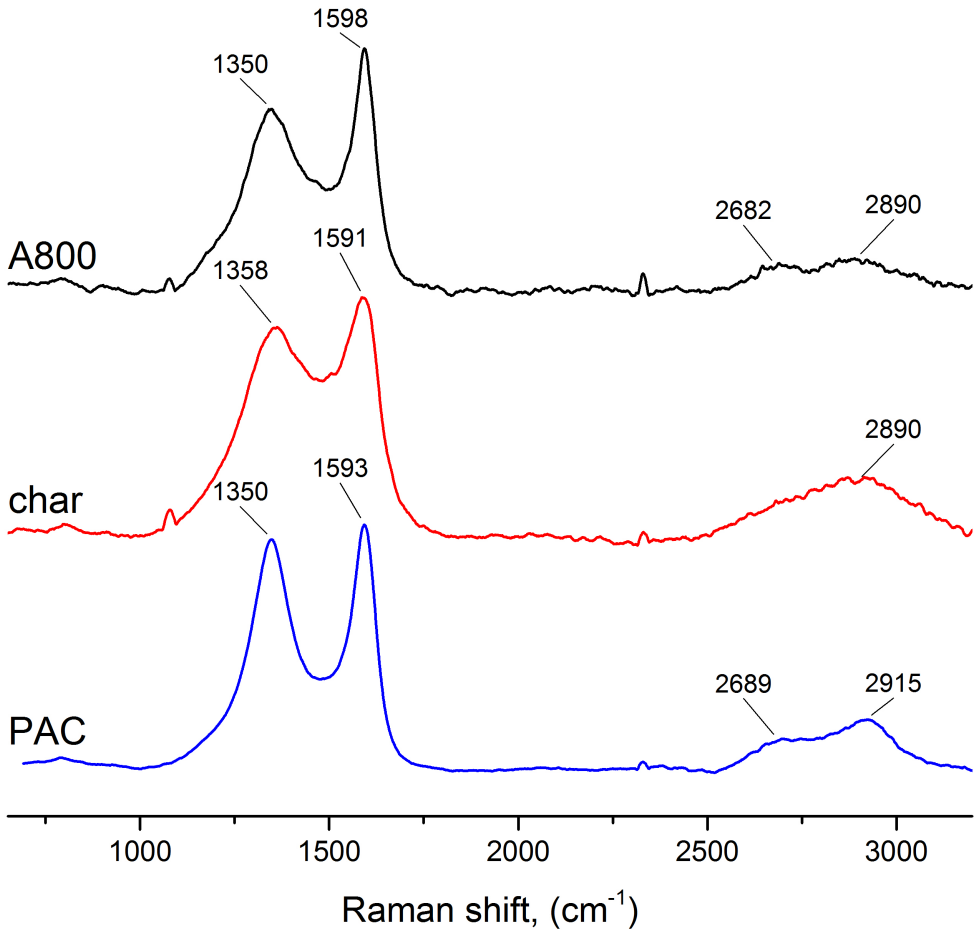

Figure 2.6: Raman spectra of A800, alginic acid-derived char and PAC (514 nm)

The baseline was corrected to a straight line, and the bands were fitted with 5 Gaussian peaks; the fitted spectra are shown in Figure 2.7.[61] Lorentzian and Voigt fitting, reported elsewhere, were also attempted; however, the Gaussian function yielded the greatest correlation coefficient.[52,58,62] Raman spectra of activated carbons have previously been fitted with four Gaussian peaks, which was also replicated in the present study.[58,60,62] For comparison, five peak fitting for the Raman spectrum of PAC is also shown. The key fitting parameters — position, height, full width at half maximum (FWHM) and integrated areas of the bands — are tabulated in Table 2.2.

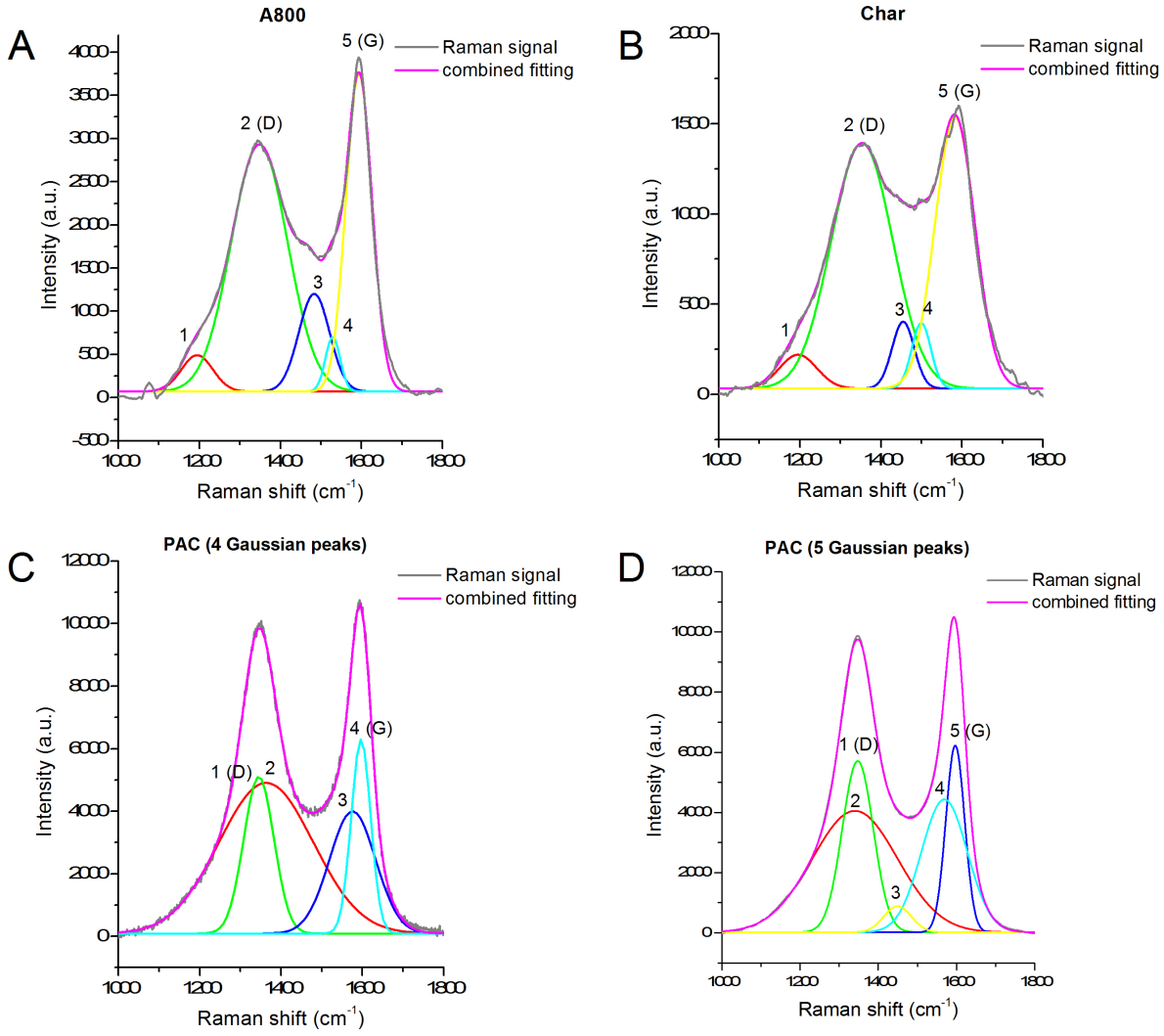

Figure 2.7: Raman spectra of A800 (**A**), alginic acid char (**B**) and powdered activated carbon fitted with four (**C**) and five (**D**) Gaussian peaks

Table 2.2: Fitting parameters of five Gaussian peaks in Raman spectra of A800, char and PAC, and four peaks in PAC only

A800 (R^2=0.993)	Peak 1	Peak 2	Peak 3	Peak 4	Peak 5
Position	1195	1348	1483	1528	1594
Height	421	2859	1131	628	3674
FWHM	78	139	76	37	65
Area	41068	497866	107642	28778	296979
char (R^2=0.990)	Peak 1	Peak 2	Peak 3	Peak 4	Peak 5
Position	1196	1353	1454	1500	1582
Height	187	1359	369	362	1504
FWHM	91	151	55	47	99
Area	21383	257296	25359	21449	185771
PAC 4 (R^2=0.999)	Peak 1	Peak 2	Peak 3	Peak 4	
Position	1363	1345	1576	1596	
Height	4819	5014	3906	6208	
FWHM	272	87	134	56	
Area	1399150	466467	556058	372021	
PAC 5 (R^2=0.999)	Peak 1	Peak 2	Peak 3	Peak 4	Peak 5
Position	1340	1347	1449	1569	1596
Height	4036	5690	864	4416	6207
FWHM	256	93	83	138	56
Area	1104030	565124	76426	649907	373026

Peak assignments

All fitted spectra feature D and G bands centred at 1342–1345 cm^{-1} and 1594–1596 cm^{-1}, respectively. The spectra of A800 and the char have similar profiles (peak intensities and positions) to hydrothermally treated sugars, reported earlier.[61] The fitted peaks in the PAC spectra closely resemble the spectra of a wide range of activated carbons.[58,60,62]

Although the debate on the nature of the additional peaks is ongoing, a variety of peak assignments has been proposed in recent years.[52] In graphene and graphite, similar fitted bands were previously attributed to crystal lattice anomalies and defects, such as heteroatoms, non-hexagonal rings and surface curvature.[52,55,62,64] However, in chars and bio-derived materials, these bands are often attributed to surface functionalities.[61]

The peak at 1200 cm^{-1} in A800 and char can be ascribed to sp^3 C-H_x vibrations present on the edges of conjugated aromatic clusters, and a similar peak was reported in lignin-derived char.[65] Seville et al. have attributed this peak to aryl-alkyl ethers; however, elemental analysis has not indicated the presence of oxygen in A800 and char.[61]

The peaks around 1460 cm^{-1}, seen in all materials, were previously attributed to semicircle ring stretching of aromatic non-hexagonal rings, such as fullerene rings, previously found in A800.[59,61] The peak around 1500 cm^{-1}, seen in A800 and the char and previously observed in pitch-derived carbon fibre, is attributed to amorphous carbon structures and heterocycles.[52]

The positions of the D and G bands in the PAC spectrum are within 3 cm^{-1} deviation from the corresponding bands in A800 and char. However, other PAC bands significantly differ in position and cannot be attributed to the same origin as in A800 and char. The four peak Gaussian fitting of the Raman spectrum of PAC is similar to the previously reported spectra for a range of activated carbons, where the additional bands were broadly assigned to defects in the graphitic structure.[58,60]

Spectra shapes and band separation

The relative band intensities and D/G band separations bear additional qualitative information. The char has the lowest intensity and band separation, followed by A800. The spectrum of PAC shows the greatest band separation and overall signal intensity.

Primo et al. have previously investigated the effect of thickness of chitosan-derived graphene on the intensity of the Raman signal.[64] The authors observed an increase in D and G band separation with progressive stacking of graphene layers. The spectrum

for a single layer of chitosan-derived graphene is similar to the char reported in this study. The Raman spectrum of A800 resembles the two-layer chitosan-derived graphene. The PAC spectrum is similar to the one arising from 4 layers of chitosan graphene.[64] Analogous findings were reported for pure graphene, where the intensity of the Raman spectra is also related to the number of graphene layers.[55]

The spectrum of A800 demonstrates greater stacking of graphitic layers than biomass pyrolysis char, in this study and as reported previously.[58,63,66] This could be attributed to the gelation process, which increases alignment and interactions in the polysaccharide matrix, leading to more ordered expanded material compared to its non-expanded counterpart. The biochars are commonly derived from complex mixtures of different natural polymers, resulting in greater disorder of the carbon structure.

The band separation and intensity of the PAC Raman spectrum appears to be greater than the other materials in this study. Although the method of preparation is unknown, the C:O ratio (Table 3.3) suggests that the temperature of carbonisation was similar to A800. Moreover, PAC preparation included activation with either acid or steam, and such an activation process has repeatedly been shown to increase separation and intensity of D and G bands.[60,66] This effect of activation is similar to annealing of non-graphitizing carbons, which improves the regularity of the graphitic structure, and, as a result, the resolution of Raman spectrum.[55]

Raman findings summary

Raman spectroscopy demonstrates that all materials under investigation have turbostratic graphitic character (Figure 2.8) with varying degrees of disorder, identified qualitatively. Comparison with numerous Raman spectra of carbonaceous materials available in the literature classes the materials as amorphous sp^2 carbons, unlike graphite and graphene. However, structural features are closer to nanocrystalline graphite as opposed to fully amorphous carbon. Other important findings are:

- the order of graphitic stacking is PAC>A800>char;
- PAC is more stacked and ordered due to activation treatment and greater density than A800;
- A800 structure has fewer stacked layers in graphitic crystallites than PAC, which is partially attributed to greater pore volume and partially due to structural disorder arising from ash and non-hexagonal ring impurities and defects;

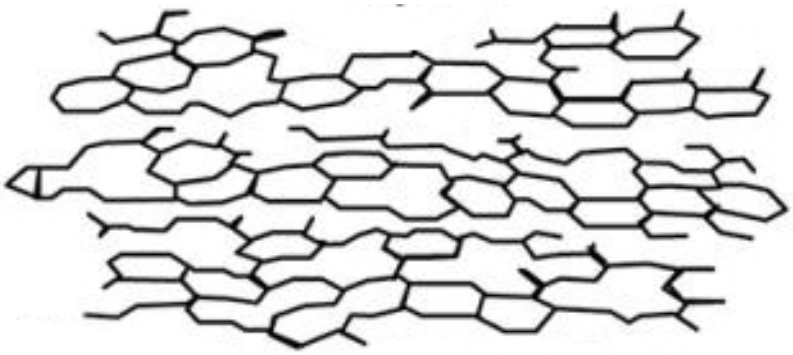

Figure 2.8: Turbostratic carbon structure

- the char is the most amorphous of the investigated materials, which is seen in the absence of 2D band in the second-order spectrum and poor band resolution, and this could be partially related to the amorphous nature of non-expanded alginic acid and presence of heteroatoms.

2.3.5 pH Drift

It is well known that the surface of any material exhibits behaviour different from the bulk, i.e. reactivity, charge distribution, functionality. The presence of surface charge, due to polar or ionic groups, inorganic impurities and unsatisfied bond valencies, plays an important role in the surface phenomena. The pH drift method is one of the simplest and most straightforward methods to investigate the impact of surface chemistry on material behaviour in the aqueous environment.

In the aqueous environment, the material's surface interacts with hydrogen (H^+) and hydroxyl ions (OH^-). This interaction affects the pH of the surrounding environment and the surface charge, which ultimately has an impact on material application, e.g. catalysis, adsorption and separation.[67–69] The underlying principle of the pH drift method is measuring the change in the pH of a solution induced by the material. The plot of the starting vs. final pH allows identification of the pH at which the surface of the materials has a net neutral surface charge, pH_{pzc}. Low pH_{pzc} indicates an acidic nature, whereas high pH_{pzc} indicates the basic nature of the material. In solutions with a pH above pH_{pzc} the net surface charge is negative, whereas below pH_{pzc} the net surface charge is positive.[67] Low pH_{pzc} is also linked to hydrophilicity, and high pH_{pzc} is linked to hydrophobicity.[69]

Algibons A300-A800 were immersed in a series of solutions with a pH ranging from

3 to 12. The drift in the pH induced by the materials was plotted against the original values, where the pH value of the intercept (or the plateau) is pH_{pzc} (Figure 2.9).

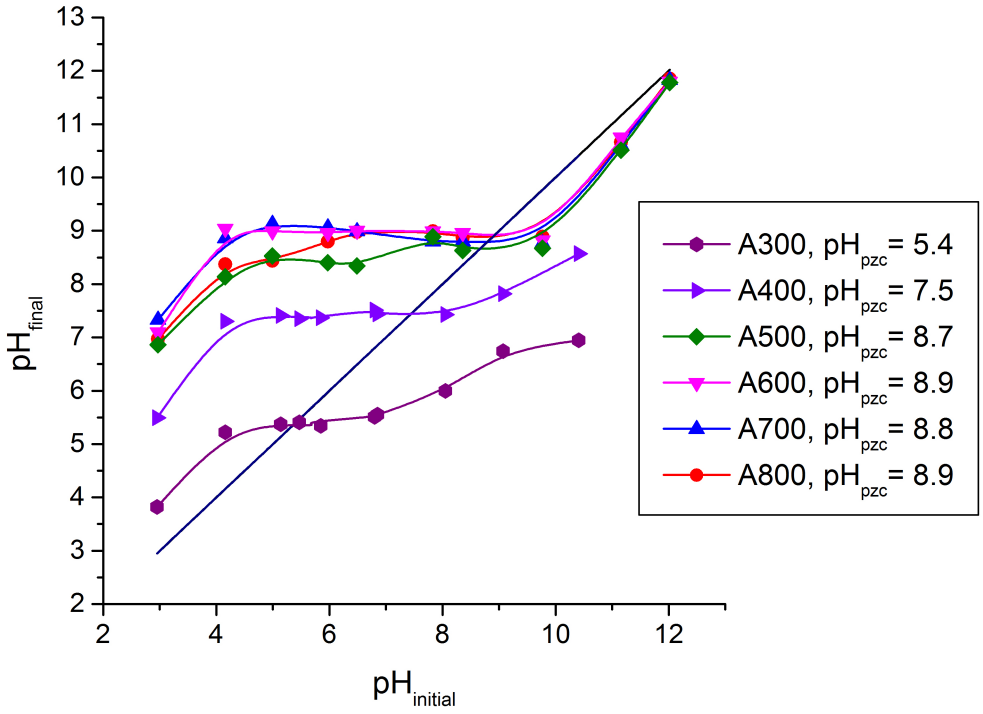

Figure 2.9: pH Drift plot for A300–A800 algibons, pH_{pzc} values are shown in the legend

According to the data, A300 is the most acidic of the materials (pH_{pzc}=5.4), followed by A400 (pH_{pzc}=7.5). From 500 °C onwards, all materials have a similar basic nature (pH_{pzc} of 8.7-8.9). The pH_{pzc} of expanded alginic acid A0 is ≈4 (not shown), and a dramatic thermally-induced change from acidic to basic character between A0 and A500 is evident. The shift from acidic to basic nature is attributed primarily to the loss of oxygen.

A correlation between oxygen content and surface acidity was previously demonstrated with a wide range of activated carbons of different origin.[70] The commonly identified acidic groups are carbonyl, carboxyl, hydroxyl and lactonic. The proposed origin of basicity in higher temperature materials (above 400 °C) is the presence of pyrone, chromene and quinone structures.[14]

2.3.6 Organic leaching

Another aspect of carbonaceous material behaviour in the aqueous environment is stability to leaching, which was investigated with UV spectroscopy. In Figure 2.10.A, UV

spectra of algibon filtrates obtained in deionized water are shown.

Algibons A300 and A400 show considerable leaching, detected in the 200–700 nm UV-Vis range. From A500, the UV intensity of the leached species declines, becoming negligible in A700 and A800. In order to characterise the leachate, it was extracted from A300 with deionized water, freeze dried and analysed with IR spectroscopy. The spectrum is shown in Figure 2.10.B.

The IR spectrum of the leachate is dominated by a small number of bands, and the bands were assigned as follows: hydroxyl group (3292 cm^{-1}), sp^3 C-H (2950 cm^{-1}), aromatic C-C (1580 and 1373 cm^{-1}), alcohol or ether C-O (1129 cm^{-1}), and out-of-plane C-H (778 cm^{-1}). Band assignments suggest that the leachate composition is predominantly of an aromatic nature with substitutions on the aromatic rings. Similar IR spectra were reported for humic acid of different origins, which suggests peat-like chemical structure of A300 and A400.[71,72]

2.3.7 Summary of carbonisation process

The sequence of temperature-dependent thermal events in A0 carbonisation is proposed by combining the findings from TG, elemental analysis, IR, Raman, pH drift, and the UV analysis of leachate. The temperature interval was broken down into three segments based on the basic chemical events: degradation (0–300 °C), de-oxygenation (300–400 °C), aromatization (500–800 °C).

Degradation (0–300 °C)

In the first thermal step, depolymerisation of alginic acid occurs with maximum degradation rate at 211 °C. The depolymerisation is evident in the loss of backbone vibrations in the IR spectrum with development of conjugated carbonyl and C-O functionalities. By 300 °C, 50 % of the original oxygen and 30 % of the hydrogen are lost, predominantly through the dehydration mechanism. This is supported by the positions of the materials on the van Krevelen diagram.

With the loss of C-O functionality in IR, at about 300 °C, the onset of sp^2 formation is seen, which is also confirmed by the formation of the G band in the Raman spectrum. The mass of the material continues to decline, indicating ongoing degradation reactions. The resulting A300 is acidic and hydrophilic with pH_{pzc}=5.4, and is structurally unstable, as indicated by leaching of decomposition products with structures similar to humic

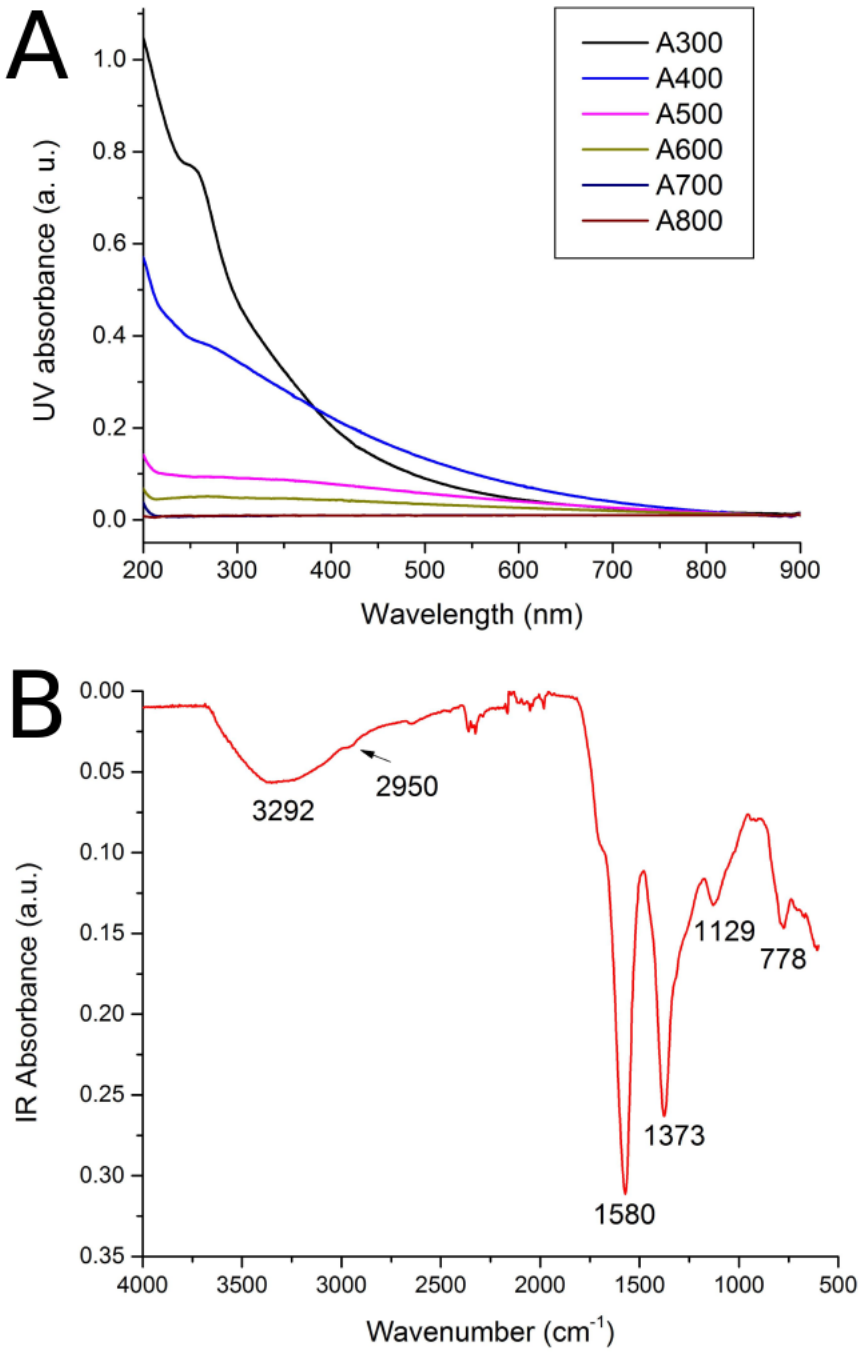

Figure 2.10: A. UV-Vis spectra of leaching from A300-A800 algibons B. FT-IR spectrum of leaching extracted from A300

acid.[71,72]

De-oxygenation (300–400 °C)

By 400 °C, mass loss reaches 70 % and its rate significantly decreases. Oxygen loss between 300 and 400 °C is the most dramatic compared to other elements, indicating that decarboxylation is the dominating degradation mechanism in this temperature interval. This is also supported by the IR data, which shows diminishing intensity of the C=O band. The pH drift demonstrates that the surface of algibon becomes more basic (pH_{pzc}=7.5). The C=C band remains the strongest in the IR spectra. A400 shows a decreased but still detectable level of leaching of humic acid, indicating a structure similar to A300.

Aromatization (500–800 °C)

From 500 °C, a change occurs in the degradation pathway from decarboxylation to demethylation, which is supported by elemental composition and the van Krevelen diagram. Demethylation leads to an increase in carbon content and sp^2 conjugation, evident in the Raman and IR data. The material's stability to leaching improves, due to increased carbon conjugation and hydrophobicity.

Progressive development of aromaticity, seen with IR, is complemented with increasing formation of conjugated ring structures, seen in the Raman data as an increase in I(D)/I(G) ratio. This, combined with negligible mass loss, suggests internal rearrangements as the primary mechanism for structural change, which is often referred to as secondary pyrolysis.[47] Despite continuous aromatization, the pH_{pzc} of A500-A800 remain in the narrow range of 8.7–8.9. The A800 material has a turbostratic graphitic structure, with a high degree of disorder due to low density, structural defects and high ash content; however, it is more ordered than alginic acid char.

2.3.8 N_2 Porosimetry

The mesoporous nature of A0-A800 algibons was confirmed with N_2 adsorption/desorption porosimetry. Representative adsorption isotherms of A0, A300 and A800 are shown in Figure 2.11, and calculated textural properties of algibons A0–A800 (Brunauer-Emmett-Teller (BET) surface area, Barrett-Joyner-Halenda model (BJH) total pore volume and average pore diameter) are tabulated in Table 2.3.

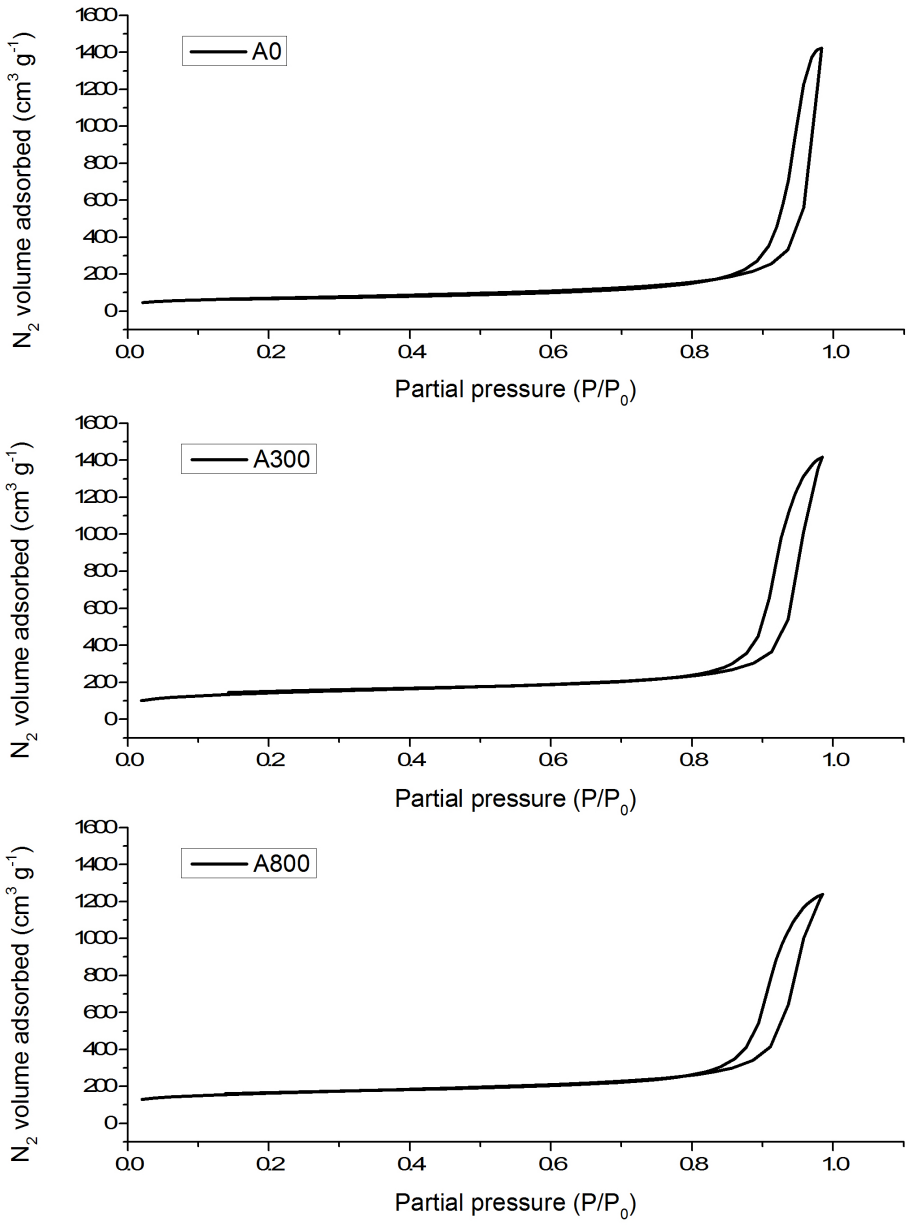

Figure 2.11: N_2 adsorption/desorption isotherms of A0, A300 and A800

Table 2.3: Textural properties of A0–A800 analysed with N_2 adsorption/desorption porosimetry (BET model for surface area, BJH model for desorption for total pore volume and average pore diameter

	SA_{BET}	SA_{mic}	PV_{total}	PV_{mic}	PD_{BJH}
	$[m^2\ g^{-1}]$	$[m^2\ g^{-1}]$	$[cm^3\ g^{-1}]$	$[cm^3\ g^{-1}]$	[nm]
A0	258	61	1.85	0.09	33
A300	297	78	1.94	0.10	26
A400	374	181	2.11	0.12	24
A500	523	310	2.07	0.15	23
A600	593	366	2.13	0.17	23
A700	564	350	1.95	0.16	21
A800	590	357	1.93	0.15	21

The A0 and algibon isotherms are type IV, according to the Brunauer-Deming-Deming-Teller (BDDT) classification, which is characteristic of mesoporous materials. The isotherms feature type H3/H1 hysteresis loops. The high surface area and mesoporosity of the materials is evident in Table 2.3. The increase in mesoporosity with temperature is seen in the increase in N_2 adsorption at low partial pressures between A0 and A800.

The BET surface area increases from 259 $m^2\ g^{-1}$ in A0 to 559 $m^2\ g^{-1}$ in in A800, which is attributed to an increase in microporosity and a decrease in average pore diameter. The total pore volume of meso- and micropores varied from 1.9 to 2.1 $cm^3\ g^{-1}$ without any trend. Overall, textural properties of algibons in this study are similar to those previously reported.[34]

2.3.9 Batch-to-batch variations

The batch-to-batch reproducibility of the textural properties of algibon has not been reported to date. In order to address this, the variation in the key quality control parameters, surface area and total pore volume, was investigated across seven batches. Each batch was subjected to porosimetry analysis, and carbonised to 300 °C and 800 °C. In Table 2.4, surface areas and pore volumes of A0, A300 and A800, obtained from each batch, are presented.

The data indicate that surface areas and pore volumes vary across batches. In A0, pore volume variation is two-fold (2.1–1.0 $cm^3\ g^{-1}$). This is also reflected in the variation in the pore volume of the carbonised materials — 1.9–0.7 $cm^3\ g^{-1}$ for A300 and 1.9–1.0 $cm^3\ g^{-1}$ for A800. There is a small variation in the surface area of A0 (237–287 $m^2\ g^{-1}$) and A300 (161–287 $m^2\ g^{-1}$); however, it increased with temperature to 235–605 $m^2\ g^{-1}$ in A800.

Overall, the observed batch-to-batch variations are significant, and could have a dramatic impact in applications where performance is directly related to pore volume and surface area. For instance, in adsorption, A800 with 605 $m^2\ g^{-1}$ would adsorb twice as much adsorbate than A800 with 235 $m^2\ g^{-1}$ if there is a direct relationship between adsorption capacity and surface area. However, to date, the relation between textural properties of Starbons and their performance has not been investigated.

Table 2.4: Batch-to-batch variations in BET surface area (SA) and pore volume (PV) of A0, A300 and A800 prepared in seven different batches

No	A0 SA_{BET} [$m^2\ g^{-1}$]	A0 PV_{total} [$cm^3\ g^{-1}$]	A300 SA_{BET} [$m^2\ g^{-1}$]	A300 PV_{total} [$cm^3\ cm^{-1}$]	A800 SA_{BET} [$m^2\ g^{-1}$]	A800 PV_{total} [$cm^3\ g^{-1}$]
1	287	2.1	287	1.9	590	1.9
2	276	2.0	246	1.2	566	1.7
3	247	2.1	161	0.8	605	1.7
4	273	1.6	182	0.7	235	1.5
5	237	1.0	250	1.1	253	1.1
6	245	1.5	239	1.0	412	1.0
7	243	1.1	204	1.1	237	1.0

2.4 Conclusions

In this chapter, the thermal evolution of the chemical properties of expanded alginic acid were systematically investigated, to provide information on the properties of algibon at any given preparation temperature. The key findings are as follows:

- the major thermal events in the decomposition of expanded alginic acid are degradation at 211 °C, sp^2 conjugation at 300 °C, and aromatization 500 °C;
- the CHO elemental compositions of the intermediate materials between A300 and A800 are close to peat (A300), coal (A400-A500) and anthracite. The change in elemental composition with temperature follows the same trend as a wide range of biochars.[50]
- A300 and A400 have relatively high oxygen content and undetectable aromatic conjugation; they are hydrophilic and unstable to leaching of water-soluble humic acid-like decomposition products;
- around 500 °C, a dramatic change in the carbon structure takes place, which has not been characterized to date. The change corresponds to a negligible mass loss with a significant decrease in oxygen content, as well as development of aromaticity, a change of degradation pathway to demethylation, and an increase in basicity of the surface and stability to leaching;
- from 500 °C, the increase in the size of the graphitic "grains" is evident from the upward trend in the I(D)/I(G) Raman band ratio;
- the A800 material is turbostratic with a high degree of disorder due to low density, high ash content, and structural defects, e.g. non-hexagonal aromatic rings.
- the turbostratic structure of A800 is more ordered than alginic acid derived char, which is attributed to the inherent structural ordering of the polysaccharide brought about by the gelation process;
- the porosimetry results of seven batches of algibon show batch-to-batch variation in surface area and pore volume, which could have an impact on application performance.

2.5 Future Work

A number of interesting findings were made that could be complemented by additional investigations, such as:

- the TG data obtained at different carbonisation rates could be used to calculate activation energy of carbonisation at different temperatures;
- the Raman study could be complemented with XRD to investigate the change in crystallinity with temperature, and to support the conclusion that A800 is more ordered than char, and PAC is more ordered than A800;
- multi-wavelength Raman could be used to further investigate the turbostratic structural features of algibons to confirm the origins of the Raman peaks, as described by Ferrari and Robertson;[53]
- inorganic leaching of ash and its contribution to the pH drift experiment needs to be identified;
- alternative methods to measure surface charge are required to eliminate the influence of organic and inorganic leaching;
- the influence of the textural properties on adsorption performance should be addressed.

The final suggestion is implemented in the subsequent chapters with application of algibons for adsorption of a range of aromatic compounds.

Chapter 3

Influence of chemical and textural properties of algibons on adsorption and desorption of phenols

3.1 Introduction

Phenols are common anthropogenic contaminants of natural waters. Their sources include petrochemical refineries, chemical manufacturing, and breakdown of waste, e.g. dyes, plastics, pesticides, etc.[14] One of the most widely employed remediation methods for phenols contamination is adsorption on activated carbons.[13,73] The key properties of activated carbons that make them good adsorbents are their high surface area (> 200 m^2 g^{-1}) and high microporosity ($\leq$ 2 nm pore diameter). However, the key disadvantages of activated carbons are the limited molecular size of adsorbates, limited diffusion in micropores and low desorption potential.[14]

Alginic acid-derived Starbons, or algibons, are mesoporous materials (2–50 nm pore diameter) with a high surface area.[25,34] Their greater pore size could potentially overcome some limitations of activated carbons.[14] Adsorption of phenols on algibon, prepared at 800 °C, was previously reported, demonstrating its effectiveness in uptake of phenols from aqueous solutions.[43] However, there are a number of unaddressed aspects of phenol adsorption on algibons, such as the influence of surface chemistry and textural properties of algibons and the chemical nature of phenols. To address these aspects, adsorption of three phenolic compounds commonly found in waste water from hair dyeing — resorcinol, 5-amino-*o*-cresol, *m*-aminophenol — was systematically investigated on a range of algibons, and a conventional microporous activated carbon and presented in this chapter.

3.2 Aims

The present work aims to understand adsorption of phenols on algibons by systematically investigating the effect of three variables: algibon preparation temperature, algibon textural properties, and the functionalisation of phenols. The experimental data from kinetic, equilibrium and desorption studies were used to establish relationships between adsorption performance and the properties of algibons. More specifically, the goals of the work were:

- to investigate the influence of the surface chemistry of algibons prepared at 500–800 °C on adsorption of phenols;
- to investigate the adsorption kinetics and isotherms of three phenols (resorcinol,

5-amino-*o*-cresol, *m*-aminophenol) on algibons with different textural properties and a microporous PAC;

- to carry out solvent desorption of phenols from algibons and PAC;
- to explore the correlations between the textural properties of adsorbents and the adsorption/desorption performance;
- to comment on the influence of the functionalisation of phenols on their adsorption and desorption;
- to propose a mechanism for adsorption of phenols on algibons.

3.3 Results and discussion

3.3.1 Algibon preparation temperature and adsorption

The influence of the surface chemistry of algibons A500–A800 on batch adsorption of three phenols (Figure 3.1) was investigated. Adsorption on the lower temperature algibons (below 500 °C) is not reported, as these materials leach UV-active humic acid, as reported in Section 2.3.6, which makes quantitation using UV spectroscopy unreliable.

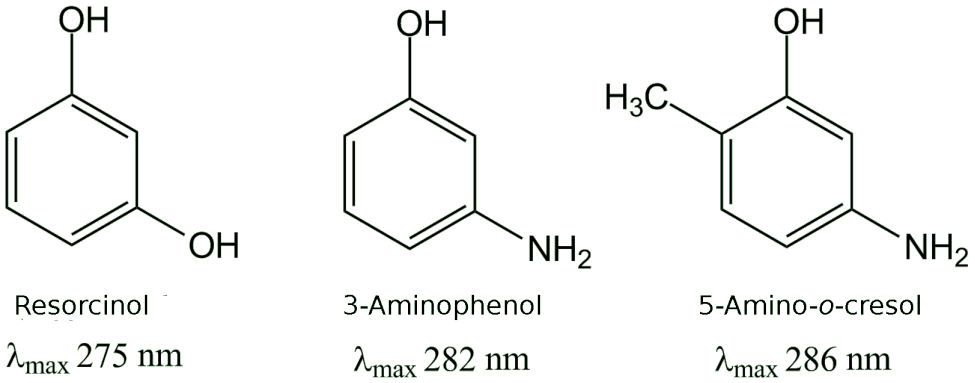

Figure 3.1: Chemical structure and UV maximum absorbance wavelength (λ_{max}) of resorcinol, 5-amino-*o*-cresol and *m*-aminophenol

The properties of A500–A800 algibons are discussed at length in Chapter 2, and the summary is given in Table 3.1. The surface chemistry of these materials displays decreasing oxygen content (9–0 wt%) and increasing levels of aromatic conjugation. The surfaces are basic, with pH_{pzc} in the range of 8.7–8.9. The BET surface area of the materials is in the narrow range of 523–590 $m^2\ g^{-1}$. Mesopore volume is in the range of 1.92–1.78 $cm^3\ g^{-1}$, and microporosity is negligible.

For batch adsorption on A500–A800, 10 mL of 200 mg L^{-1} solution of phenol was mixed with 20 mg of each adsorbent, in duplicate, and stirred until adsorption equilibrium was achieved. In Figure 3.2, the average percentage uptake of each adsorbate is shown. Algibon A500 shows the lowest adsorption of all phenols, with 40 to 45 % of the initial concentration adsorbed. The adsorption increases with preparation temperature. The A800 shows 100 % removal of resorcinol, 98 % of *m*-aminophenol, 60 % of 5-amino-*o*-cresol. PAC demonstrate 100 % adsorption of each phenol under the same experimental conditions (data not shown).

The observed trend of increasing adsorption with algibon preparation temperature

Table 3.1: Summary of chemical and textural properties of algibons A500–A800 (BET surface area (SA_{BET}), mesopore and micropore pore volumes (PV_{meso}, PV_{mic}) were determined with N_2 porosimetry, ratio of Raman D and G peaks were used as a proxy of aromaticity (Section 2.3.3), point-of-zero charge pH (pH_{pzc}) was determined with pH drift experiment (Section 2.3.5), oxygen content was determined with CHN and thermogravimetric analyses)

	A500	A600	A700	A800
SA_{BET} [$m^2\ g^{-1}$]	523	593	564	590
PV_{meso} [$cm^3\ g^{-1}$]	1.92	1.96	1.79	1.78
PV_{mic} [$cm^3\ g^{-1}$]	0.15	0.17	0.16	0.15
PD [nm]	23	23	21	21
Aromaticity [Raman I(D)/I(G)]	0.62	0.63	0.73	0.79
pH_{pzc}	8.7	8.9	8.8	8.9
Oxygen [wt%]	9±0.41	2±0.27	0	0

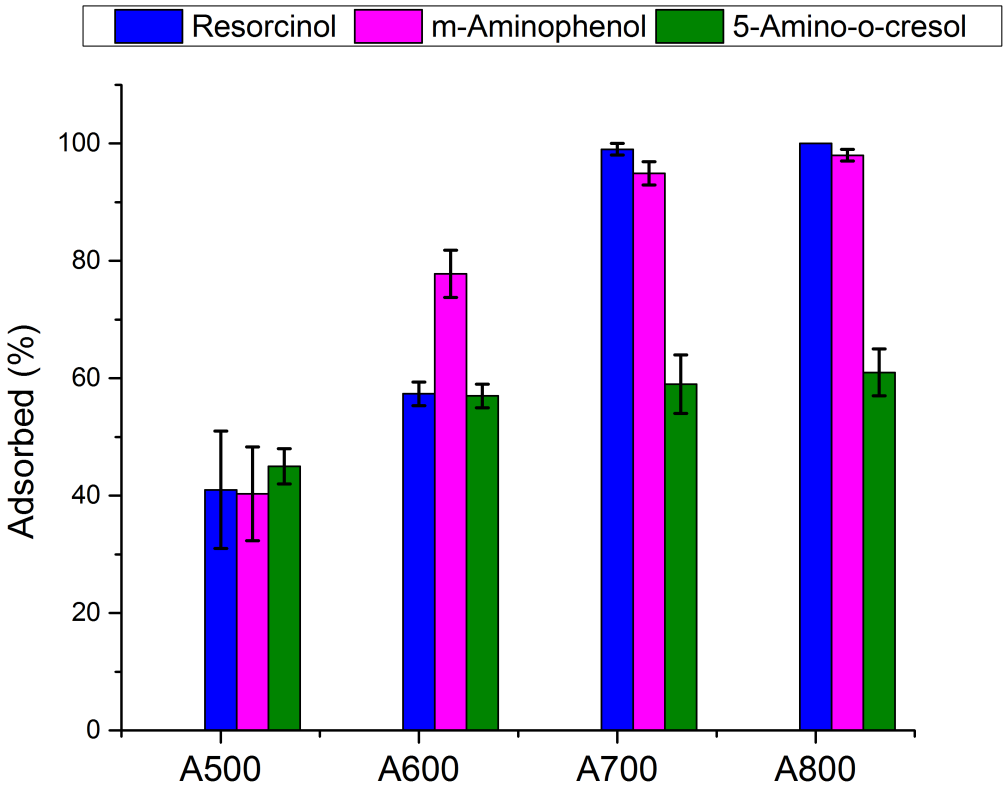

Figure 3.2: Adsorption of phenols by algibons A500–A800 from aqueous solution (n=2)

was rationalized by considering the chemical and textural properties of the materials. Variable importance analysis was carried out with the partial least squares regression tool in Origin Pro 9 software. The result of this analysis indicates that there are two algibon properties that significantly influence the adsorption: aromaticity and oxygen content.

The progressive thermal treatment of algibon renders the surface more aromatic with an increasing degree of aromatic conjugation, as was demonstrated with IR-DRIFT and Raman spectroscopy (Section 2.3.3), and expressed as a ratio of Raman D and G peaks (Table 3.1). The influence of aromaticity indicates that adsorption occurs through π-π interactions between algibons and phenols, and the more developed the aromatic system is, the greater the adsorption capacity. The increase in uptake of phenol with decreasing oxygen content suggests that surface oxygen is likely to electrostatically repel acidic phenols, negatively affecting their adsorption. This relationship between surface oxygen and phenol adsorption has previously been reported.[14]

The adsorption screening of algibons A500–A800 demonstrated that A800 has the greatest adsorption capacity for all three phenols, which was attributed to the high degree of aromatic conjugation and the oxygen-free surface. As a result, algibon A800 was selected for further adsorption investigations of the role of algibon textural properties in adsorption.

3.3.2 Textural properties of algibons A800 and PAC

The influence of textural properties (surface area, pore volume and mesoporosity) on the adsorption of phenols was further investigated with three A800 materials and the PAC. The textural properties of the materials, determined with nitrogen porosimetry, are presented in Table 3.2. The nitrogen adsorption/desorption isotherms are shown in Figure 3.3, and the pore diameter distributions are shown in Figure 3.4. The elemental compositions of the materials are shown in Table 3.3.

The greatest textural variation in the algibons under investigation was the pore volume (0.94–1.92 $cm^3\ g^{-1}$), which could be partially attributed to the small difference in the average pore diameter (14.6–21.0 nm). The surface area varies from 416 to 606 $m^2\ g^{-1}$. The nitrogen adsorption/desorption isotherms of the algibons feature a hysteresis loop (Figure 3.3), and are characteristic of mesoporous materials (type IV of the BDDT classification).

The PAC is a microporous material with a greater surface area (870 $m^2\ g^{-1}$) and

Table 3.2: Textural property of adsorbents under investigation identified with N_2 porosimetry (average of three measurements; BET model for surface area, BJH model applied to desorption for total pore volume and average pore diameter)

Material	BET SA_{total}	PV_{total}	PV_{meso}	PV_{micro}	PD_{BJH}
	[$m^2\ g^{-1}$]	[$cm^3\ g^{-1}$]	[$cm^3\ g^{-1}$]	[$cm^3\ g^{-1}$]	[nm]
A800_1	416 ± 7	0.94 ± 0.02	0.83 ± 0.03	0.11 ± 0.01	14.6 ± 0.7
A800_1.6	563 ± 8	1.61 ± 0.05	1.44 ± 0.05	0.17 ± 0.01	19.1 ± 0.1
A800_1.9	606 ± 33	1.92 ± 0.11	1.76 ± 0.10	0.16 ± 0.01	21.0 ± 0.0
PAC	870 ± 52	0.50 ± 0.02	0.13 ± 0.01	0.38 ± 0.03	4.5 ± 0.2

Table 3.3: Elemental composition of algibons and PAC (n=2), C, H and N were determined with CHN analysis, ash was determined with TGA, O was determined by difference

	C (%)	H (%)	N (%)	O (%)	Ash (%)
PAC	85.68 ± 0.51	1.21 ± 0.45	0.69 ± 0.28	1.62 ± 1.02	10.8 ± 0.71
A800_1	83.12 ± 0.12	1.64 ± 0.32	0.34 ± 0.51	1.8 ± 0.74	13.1 ± 0.41
A800_1.6	83.31 ± 0.56	1.02 ± 0.11	0.27 ± 0.14	0.9 ± 0.61	14.5 ± 0.15
A800_1.9	84.85 ± 0.35	1.20 ± 0.07	0 ± 0.37	0 ± 0.04	14 ± 0.09

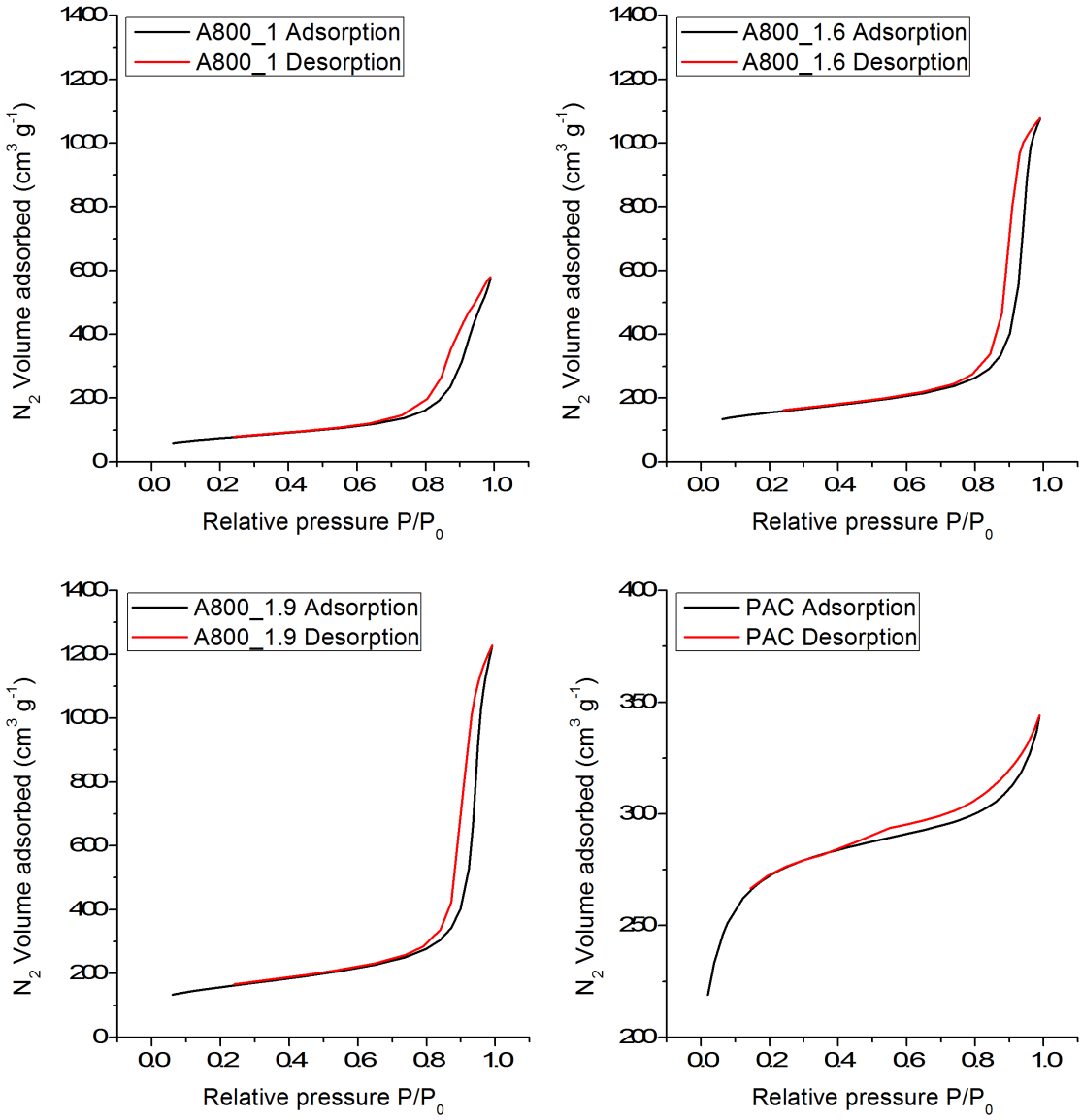

Figure 3.3: N_2 adsorption/desorption isotherms of algibons and PAC

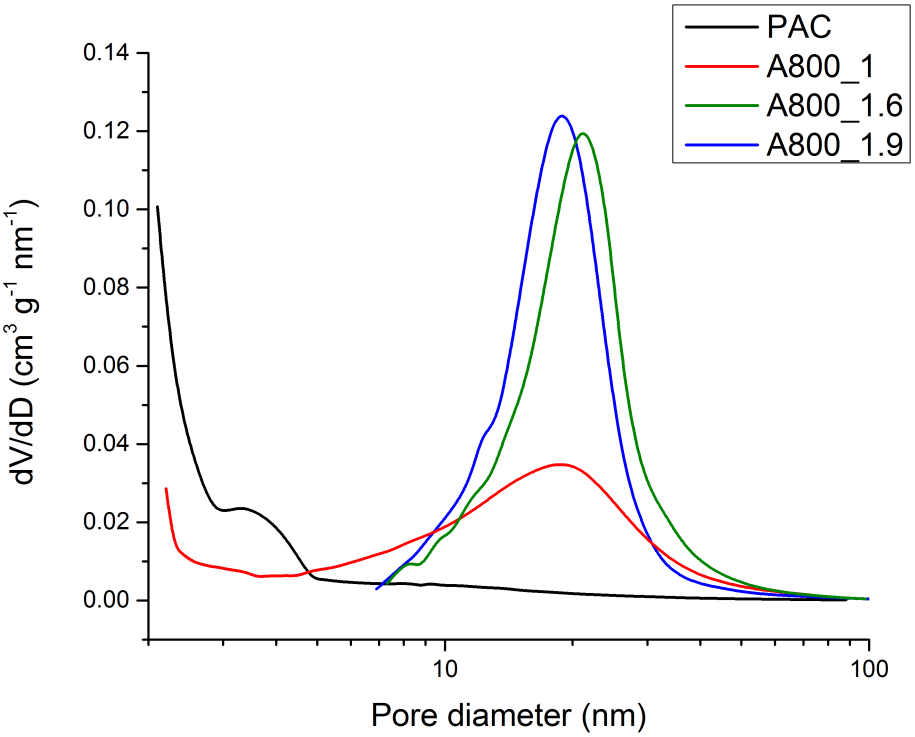

Figure 3.4: BJH pore diameter distributions in algibons and PAC calculated from N_2 desorption curves

lower pore volume (0.5 $cm^3\ g^{-1}$) than the algibons. The nitrogen adsorption/desorption isotherm, shown in Figure 3.3, is of type I of the BDDT classification, characteristic of microporous materials, although it shows some mesoporous character.

The algibons and the PAC have similar elemental compositions with respect to carbon, hydrogen and oxygen content. The algibons were sieved to match PAC particle size of $\leq$40 nm. The key assumption concerning the surface chemistry of the algibons, based on the findings of Chapter 2, is that all A800 materials have similar surface chemistry, with a graphitic-like character. Therefore, the difference in their adsorption performance is expected to arise solely from their textural properties.

3.3.3 Adsorption kinetics

The adsorption kinetics of resorcinol, *m*-aminophenol and 5-amino-*o*-cresol were investigated. In Figure 3.5, the change in adsorption capacity Q_t over time is shown, as determined with Equation 3.1. Initial data evaluation demonstrates that PAC has the greatest equilibrium capacity for all phenols. The equilibration times, under the experimental conditions, were 7 h for resorcinol, 75 h for *m*-aminophenol, and 90 h for 5-amino-*o*-cresol.

$$Q_t = \frac{C_0 - C_t}{m} V \tag{3.1}$$

Equation 3.1: Adsorption capacity formula, where Q_t is the amount adsorbed in mmol g^{-1} at time t, C_0 is initial concentration of a solution, C_t is concentration at time t in mmol L^{-1}, m is the amount of adsorbent in g, and V is the volume of solution in L.

The study of adsorption kinetics in porous materials is a complex subject. There are a number of events involved — diffusion, transport through the porous network, and desorption — each with individual kinetic parameters. The overall adsorption rate and the equilibrium constant depend on the combination of individual equilibrium constants and rates. A number of adsorption kinetic models are available, enabling approximation of the kinetic process and computation of the kinetic parameters. The most commonly used models are pseudo-first order,[74] pseudo-second order,[74,75] Elovich,[76] and intra-particle diffusion models.[74,77] Pseudo-first order, intra-particle diffusion and Elovich models yielded inadequate fitting of the experimental data, and are not discussed. The poor fit to the intraparticle diffusion model suggests that diffusion is not the rate limiting step, which could be linked to the small particle size.

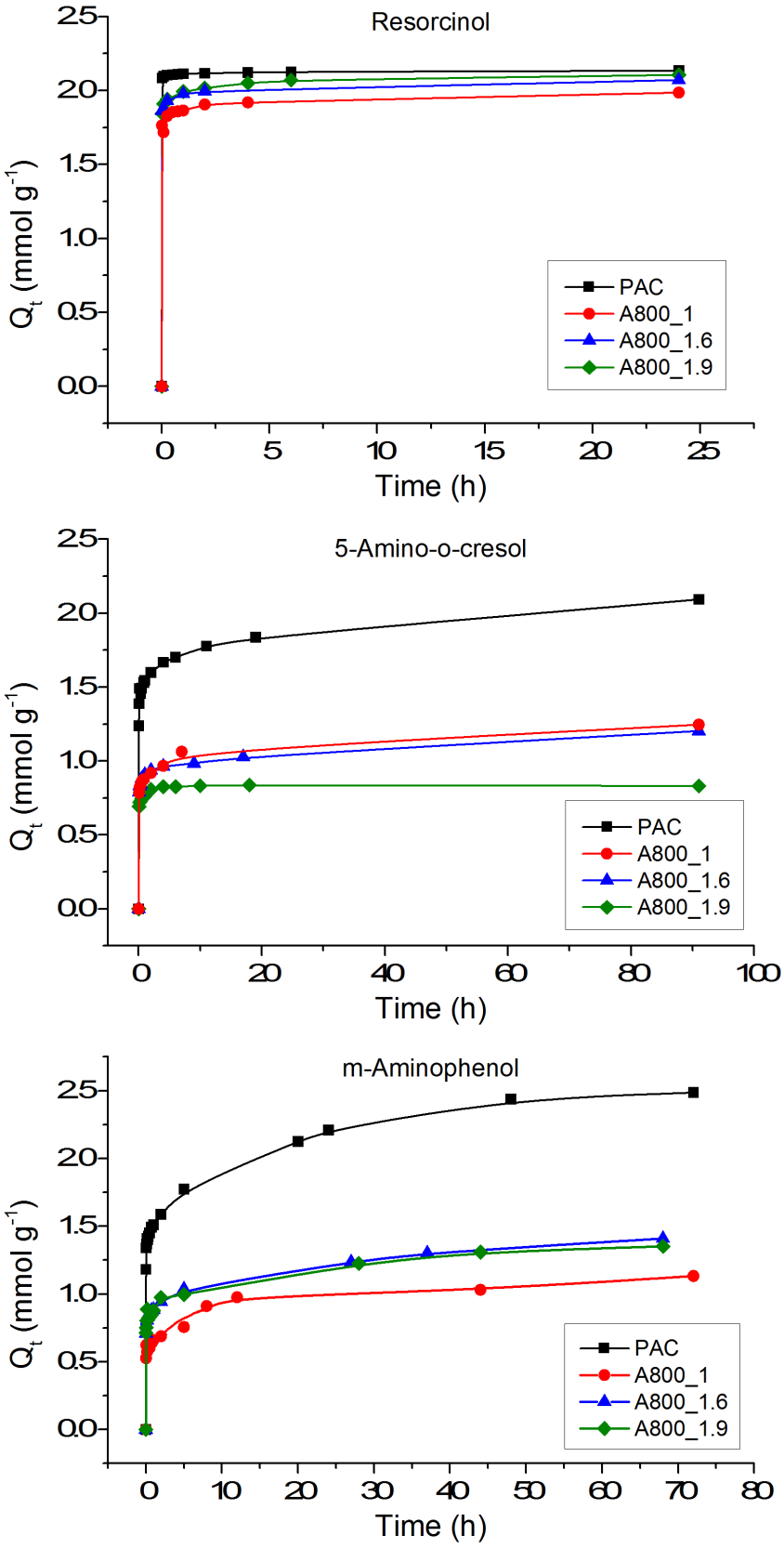

Figure 3.5: Change in the adsorption capacity of algibons and PAC over time for resorcinol (A), 5-amino-*o*-cresol (B), and *m*-aminophenol (C)

The experimental data were described well by the pseudo-second order adsorption model (Equation 3.2), which assumes that adsorption follows the Langmuir isotherm, formation of the adsorbate-adsorbent complex is the rate limiting step, and physisorption takes place.[75,78] In Figure 3.6, linear plots of the pseudo-second order kinetics are shown, and the pseudo-second order rate constants are tabulated in Table 3.4.

$$\frac{t}{Q_t} = \frac{1}{h} + \frac{1}{Qe}t \tag{3.2}$$

Equation 3.2: Linear pseudo-second adsorption kinetic model, where Q_e is equilibrium adsorption capacity in mmol g^{-1} (determined with Equation 3.1), Q_t is adsorption capacity at time t in mmol g^{-1} (calculated with Equation 3.1), t is time in min, and h is adsorption rate in mmol g^{-1} min^{-1}.

The data demonstrate that PAC has the greatest adsorption rates, followed by the similar rates of A800_1.9 and A800_1.6. Algibon A800_1 showed the lowest adsorption rates for all phenols. The values of the rate constants correlate with the BET surface area. Among phenols, the order of adsorption rates is resorcinol>*m*-aminophenol>5-amino-*o*-cresol. It appears that greater substitution on the aromatic ring leads to a slower adsorption rate and longer equilibration time. Overall, a number of trends were observed between the kinetic data, textural properties and the nature of phenols, which were further investigated with the adsorption isotherms.

3.3.4 Adsorption isotherms

The batch adsorptions of resorcinol, 5-amino-*o*-cresol, and *m*-aminophenol were investigated over a range of concentrations (100–700 mg L^{-1}). The isotherms were equilibrated for the time identified in the adsorption kinetics experiment. The equilibrium adsorption capacities were calculated with Equation 3.1, and the resulting adsorption isotherms are presented in Figure 3.7. The adsorption isotherms demonstrate that PAC has the greatest equilibrium adsorption capacities. The A800_1.9 and A800_1.6 demonstrate very similar isotherm curves, and A800_1 shows the lowest adsorption capacities.

The adsorption isotherms were analysed with two widely used adsorption isotherm models, Langmuir and Freundlich.[13,73] Each model has characteristics and limitations arising from the assumptions used to define the model. If adsorption data conforms to a model, it may be assumed that the physical assumptions of the model are satisfied — therefore, a good fit of experimental data to a model may give an insight into the

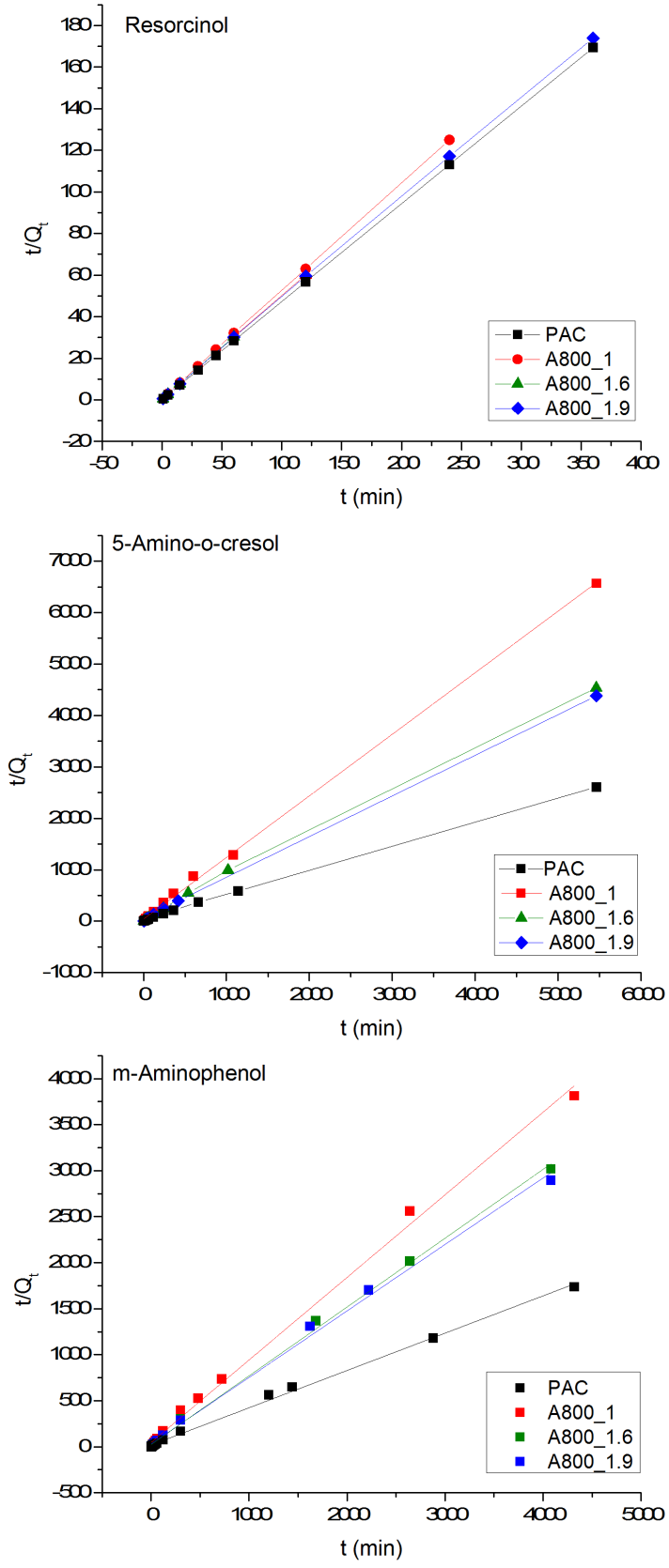

Figure 3.6: Pseudo-second order plots for adsorption of resorcinol (A), 5-amino-*o*-cresol (B), and *m*-aminophenol (C) on algibons and PAC

Table 3.4: Pseudo-second adsorption kinetic parameters for first hour of adsorption process

Resorcinol	h	R^2
	[g $mmol^{-1}$ min^{-1}]	
A800_1	6.6 ± 0.2	1.000
A800_1.6	8.5 ± 0.4	1.000
A800_1.9	8.4 ± 0.4	1.000
PAC	12.1 ± 0.5	1.000
5-Amino-*o*-cresol	h	R^2
	[g $mmol^{-1}$ min^{-1}]	
A800_1	0.1 ± 0.0	0.999
A800_1.6	0.7 ± 0.1	0.999
A800_1.9	1.0 ± 0.1	1.000
PAC	2.4 ± 0.3	1.000
m-Aminophenol	h	R^2
	[g $mmol^{-1}$ min^{-1}]	
A800_1	0.1 ± 0.0	0.995
A800_1.6	1.4 ± 0.1	0.999
A800_1.9	1.3 ± 0.1	0.999
PAC	2.4 ± 0.2	0.999

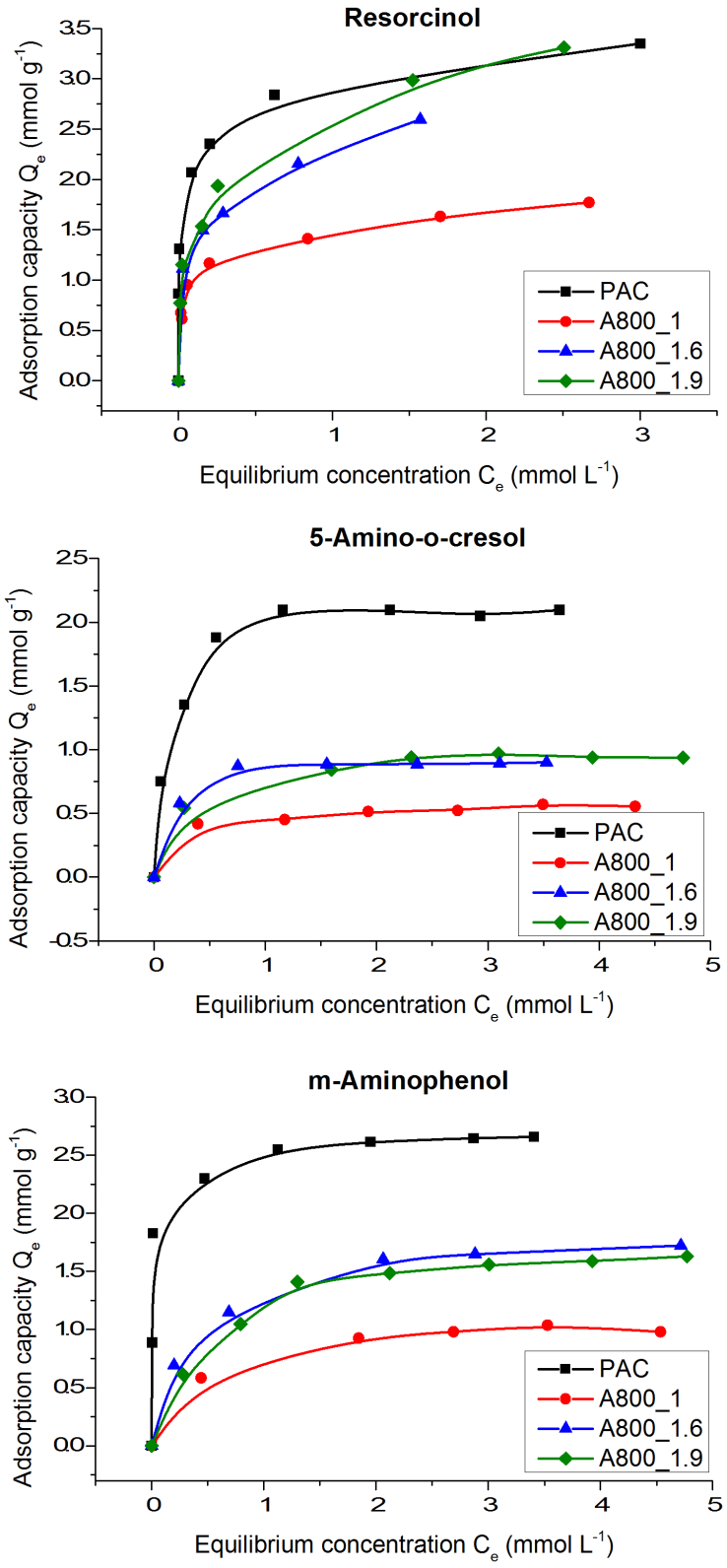

Figure 3.7: Adsorption isotherms for resorcinol (A), 5-amino-*o*-cresol (B) and *m*-aminophenol (C)

adsorption mechanism. The Langmuir adsorption isotherm, shown in Equation 3.3, is a theoretical model with the following assumptions:

- the surface is homogeneous, i.e. adsorption energy is constant for all adsorbent-adsorbate interactions;
- monolayer adsorption takes place, i.e. only one adsorbate molecule is accommodated on each adsorption site.[79]

$$Q_e = Q_{max}\frac{KC_e}{1+KC_e} \tag{3.3}$$

Equation 3.3: Langmuir adsorption isotherm model where C_e is equilibrium concentration in mmol L^{-1}, Q_e is equilibrium adsorption capacity in mmol g^{-1}, K is Langmuir adsorption constant in L $mmol^{-1}$, Q_{max} is maximum adsorption capacity of adsorbent in mmol g^{-1}.

The Freundlich adsorption isotherm, shown in Equation 3.4, is an empirical model, that assumes that the surface of the adsorbent is heterogeneous.

$$Q_e = KC_e^{\frac{1}{n}} \tag{3.4}$$

Equation 3.4: Freundlich adsorption isotherm model where Q_e is equilibrium adsorption capacity in mmol g^{-1}, K and n are empirical Freundlich constants that characterise the system at given conditions, where K is an indicator of adsorption capacity and n is an indicator of adsorption intensity, C_e is equilibrium concentration in mmol L^{-1}.

The Langmuir and Freundlich isotherm models were applied to the experimental data, and the results of the fitting are shown in Appendix A. Both models fitted the experimental data reasonably well (>0.89 R^2). The Freundlich model yielded a greater correlation coefficient for resorcinol adsorption (0.98–0.99 R^2). The 5-amino-*o*-cresol (0.98–0.99 R^2) and *m*-aminophenol (0.98–0.99 R^2) isotherms were described well by the Langmuir model. The Langmuir maximum adsorption capacities are in the order:

$$A800\_1 < A800\_1.6 < A800\_1.9 < PAC \tag{3.5}$$

This is the same trend reported above for pseudo-second order adsorption rate, and is likely to arise from the difference in the BET surface area of the materials. Overall, adsorption isotherms in this study are similar to the large number of phenolic adsorption isotherms reported in the literature for activated carbons.[14,80–82]

3.3.5 Relation between textural properties and adsorption parameters

The maximum adsorption capacities, identified from the adsorption isotherms, were correlated with the textural properties of the adsorbents (surface area and the pore volume). The BET surface area correlates well with the adsorption capacities (Figure 3.8). However, there is no correlation between the maximum adsorption capacity and the pore volumes. This is an interesting finding, which indicates that adsorption capacity of phenols is governed by the surface available, rather than the origin of this surface (e.g. micropore, mesopore). A similar finding was reported by Teng and Hsieh for phenol adsorption on microporous carbons with different BET surface areas.[83] However, no previous reports comparing phenol adsorption on highly mesoporous materials and highly microporous carbonaceous materials are available.

The surface occupied by each molecule, assuming face-to-face π-π interaction, was calculated with Equation 3.6 to identify the percentage of total surface occupied by the molecules. The data are tabulated in Table 3.5.

$$SA = Q_{max} \times N \times A_m \tag{3.6}$$

Equation 3.6: Determination of the surface area occupied by adsorbed molecule, where Q_{max} is maximum adsorption capacity determined with Langmuir model in mol g^{-1}, N is the Avogadro number, A_m is surface area of adsorbed molecule in m^2 determined with HyperChem software.[84]

Table 3.5: Percentage of the BET surface area of each adsorbent covered by resorcinol, 5-amino-*o*-cresol and *m*-aminophenol at maximum adsorption capacity determined with Langmuir model

	Resorcinol (%)	5-Amino-*o*-cresol (%)	*m*-Aminophenol (%)
A800_1	65	30	53
A800_1.6	71	37	65
A800_1.9	67	37	59
PAC	53	56	58

These data show that resorcinol has the greatest coverage density, followed by *m*-

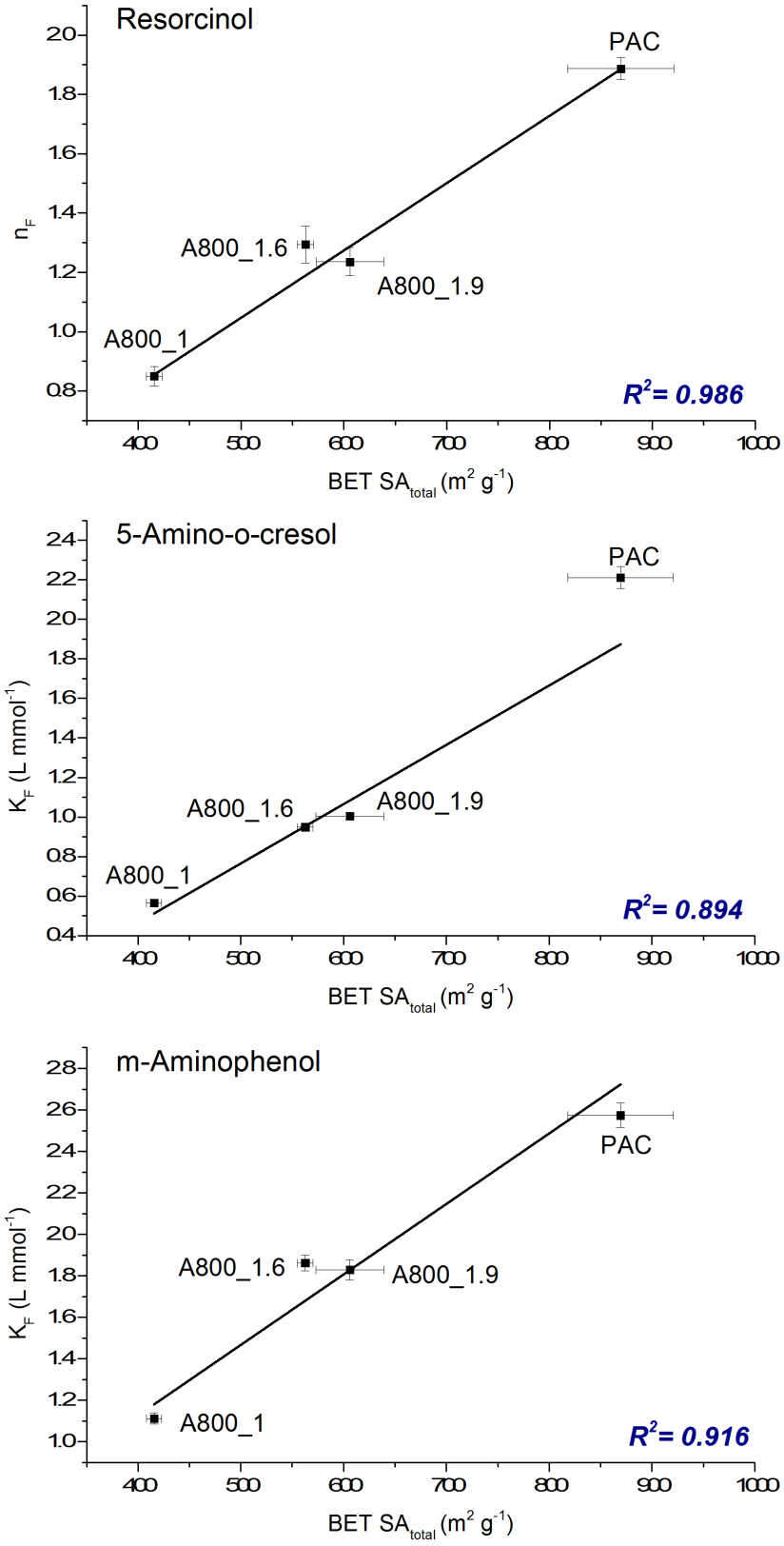

Figure 3.8: The relation between total BET surface area (BET SA_{total}) and maximum adsorption capacity determined with Freundlich model (n_F) for resorcinol (A), and Langmuir model (K_L) for 5-amino-*o*-cresol (B) and *m*-aminophenol (C) (error bars represent experimental errors of BET SA_{total} and n_F)

aminophenol and 5-amino-*o*-cresol. This trend could be linked to the restricted interaction between the adsorbate and the surface as the number and size of functional groups increases. Percentage surface coverage of algibons by resorcinol and *m*-aminophenol exceeds that of PAC. In the case of 5-amino-*o*-cresol, the surface coverage of PAC is greater, which could be attributed to the greater affinity of the 5-amino-*o*-cresol to the surface in micropores.

3.3.6 Desorptions of phenols

Desorption of phenols, following adsorption on a column, packed with each adsorbent, was performed in a flow system with ethanol. Three cycles of adsorption/desorption were carried out with consistent 100% adsorption rate. The desorption values for each phenol are shown in Figure 3.9.

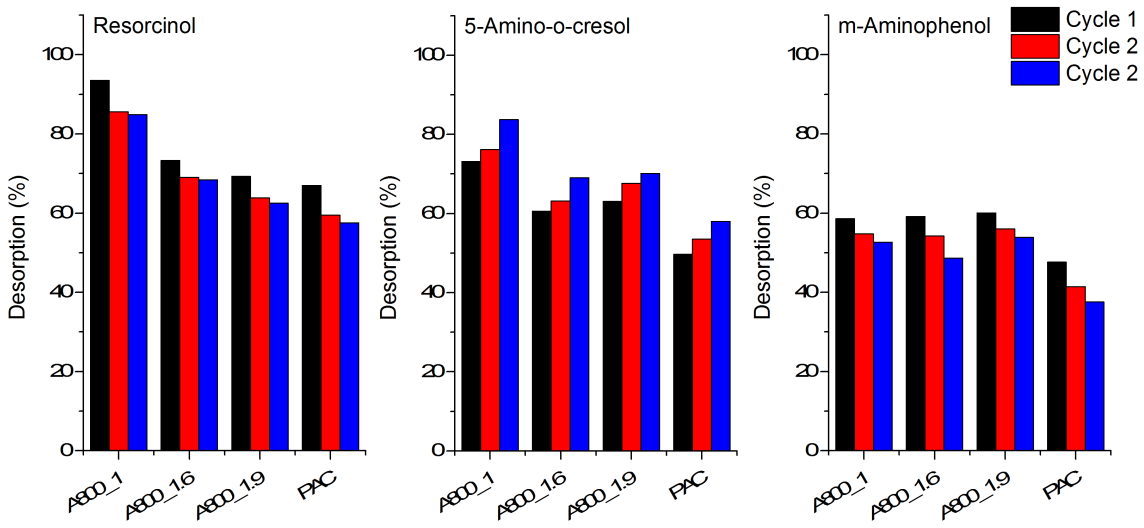

Figure 3.9: Desorption (%) of resorcinol, 5-amino-*o*-cresol and *m*-aminophenol at each adsorption/desorption cycle

The greatest desorption rates of resorcinol were achieved with A800_1 (95–73 %), followed by A800_1.6 (73–68 %), A800_1.9 (69–63 %), and PAC (67–57 %). Desorption of 5-amino-*o*-cresol showed a similar trend, with A800_1 desorbing the most (73–82 %), followed by A800_1.6 and A800_1.9 (60-70 %), and PAC (50–58 %). *m*-Aminophenol is the most difficult to desorb, with algibons achieving 60–49 % desorption, and PAC achieving 47–38 % desorption.

Overall, algibons demonstrate greater phenols recovery through desorption com-

pared to PAC. It is well accepted that mesoporous materials have an advantage over microporous materials in desorption, due to better diffusion of solvent into the porous network, and weaker adsorption, which is demonstrated in the present study.[85] However, the tendency of A800_1, the algibon with the lowest pore volume, to desorb the most phenols is not expected. It is plausible, that in A800_1, due to the lower mesopore volume, the distance the solvent has to travel within the porous network is shorter, which leads to faster diffusion in and out of the porous network and therefore higher desorption values. In PAC, however, transport of solvent through smaller pores is restricted, leading to lower desorption. It is likely that the mesoporosity in PAC plays an important role in the observed desorption.

The phenol desorption values achieved by ethanol elution in this study are greater than the previously reported maximum of 40 %, which was achieved at pH 13.[43] Generally, recovery of adsorbents and adsorbed molecules through desorption is an area that receives little attention. Thermal regeneration in inert atmosphere is the preferred recovery method of activated carbons, which leads to degradation of both the adsorbed molecules and the quality of the adsorbent.[13] Desorption rates achieved in the present study are among the highest reported for carbonaceous materials, which is a clear advantage of algibons over conventional activated carbons.[86,87]

3.4 Conclusion

In this chapter, adsorption of phenols (resorcinol, *m*-aminophenol and 5-amino-*o*-cresol) on algibons prepared at different temperatures and with different textural properties are discussed. A commercial powdered activated carbon, PAC, was used as a benchmark material. Three key factors affecting adsorption were investigated and discussed: the chemical nature of the adsorbing surface, the physical nature of the porous network, and the chemical structure of the adsorbate molecules.

The following findings were reported and discussed:

- the adsorption capacity of algibons for the investigated phenols increases with preparation temperature. This is attributed to the decrease in the surface oxygen and the increase in the aromaticity required for π-π interaction between phenols and the adsorbing surface;

- the maximum adsorption capacity for phenols and the pseudo-second order ad-

sorption rate in A800 algibons and PAC correlate with the BET surface area. No correlations between adsorption parameters and pore volumes were observed;

- the density of phenol surface coverage decreases with increasing substitution of the phenol ring (resorcinol>*m*-aminophenol>5-amino-*o*-cresol). Overall, the maximum adsorption capacity and adsorption rates were in the same order, suggesting that either bulky functional groups physically inhibit π-π interactions between phenols and the surface, or they polarize the molecule, affecting electron distribution;

- the non-destructive recovery of phenols from algibons can be achieved with ethanol elution, yielding up to 95 % recovery rates. The recovery values achieved with solvent elution are greater than previously reported. Desorption from PAC was the lowest (47–67 %), which was attributed to poorer diffusion in narrower pores and stronger interaction between phenols and the surface.

Overall, algibon adsorption capacities for phenols in this study are comparable to the previously reported capacities of microporous activated carbons and Starbons (Table 3.6). Although the apparent capacity values of algibons are lower than the capacities of PAC, when normalized to the surface area, comparable adsorption per unit of surface is achieved.

Moreover, efficient desorption of phenols from algibons provides a considerable advantage over activated carbon. The activated carbons adsorb more and faster; however, if desorption and recovery of chemicals is a priority, then algibon offers an advantage of greater solvent diffusion and, therefore, greater desorption rates. This is of particular advantage for solid-phase extractions, separation, and chromatography, and is consistent with the need for materials to support the circular economy.

3.5 Future work

Based on the findings of the present work, it would be interesting to investigate the adsorption/desorption performance of Starbons with a wider range of textural and surface properties, using more varied adsorbate chemicals, in order to build a greater understanding of the factors influencing the adsorption process. This would aid future optimization of Starbon materials for specific adsorption applications. For instance,

Table 3.6: Previously reported and present adsorption capacities of activated carbons and A800

Adsorbate	Material	Capacity [mg g^{-1}]	Reference
Resorcinol	A800	195-364	present work
	Powdered activated carbon	369	present work
	Granular activated carbon	143	Kumar et al.[82]
	Granular activated carbon	120–155	Suresh et al.[87]
	Granular activated carbon	0.9–3.6	Mohamed et al.[88]
m-Aminophenol	A800	83-123	present work
	Powdered activated carbon	263	present work
	A800	139	Parker et al.[43]
	S800	101	Parker et al.[43]
5-Amino-*o*-cresol	A800	56-92	present work
	Powdered activated carbon	219	present work
o-Cresol	A800	113	Parker et al.[43]
	S800	90	Parker et al.[43]

adsorption of larger aromatic molecules (e.g. polycyclics, complex dyes) should be evaluated in a similar manner to the method reported in this chapter.

Adsorption capacity could be enhanced, and selective adsorption could be explored, by considering the pH of the adsorption medium, pK_a values of adsorbates and pH_{pzc} of the algibon surface. An investigation into adsorption of charged species could also be undertaken.

The role of surface oxygen and aromaticity in phenol adsorption could be further investigated, by comparing normal and re-oxidized versions of higher temperature algibons (> 800 °C).

Chapter 4

Influence of chemical and textural properties of algibons on adsorption and desorption of 1-naphthol and 2-naphthol

4.1 Introduction

Naphthols belong to a group of common industrial pollutants — polycyclic aromatic hydrocarbons (PAHs). A number of PAHs are classed as toxins and carcinogens, such as benzo[a]pyrene, and are on national chemical watch-lists, e.g. the list of priority chemicals of USA Environmental Protection Agency.[89] Anthropogenic PAH contamination originates from the processing of crude oil, combustion of fossil fuels and carbon-rich waste, and post-consumer wastes. For example, 1-naphthol, used in hair dye formulations, is found in waste water streams.[8,90]

Adsorption on activated carbons is one of the preferred remediation methods for water contaminated with PAHs.[91] Although naphthols are non-toxic members of the PAH group, they represent a useful experimental model to screen adsorbents for PAH removal.[76] Therefore, investigation of naphthol adsorption on algibon would add a new class of environmental pollutants to its portfolio.

In this chapter, systematic investigation of adsorption of 1-naphthol and 2-naphthol on algibons is presented. The particular interests were the influence of algibon preparation temperature and its textural properties, e.g. surface area and pore volume, on adsorption. Adsorption kinetics, isotherms, thermodynamics and desorptions were evaluated, and performance of algibons was compared to a conventional activated carbon.

4.2 Aims

The aim of the present work is to systematically investigate adsorption of 1-naphthol and 2-naphthol on algibons to address the role of algibon preparation temperature and textural properties, as well as the chemical nature of naphthols, in adsorption performance. Adsorption kinetics, isotherms, thermodynamics and desorptions were investigated in order to:

- investigate the influence of preparation temperature on naphthol adsorption with A500–A800 algibons, extensively characterized in Chapter 2;
- identify the influence of textural properties (surface area, pore volume, mesoporosity) on adsorption of naphthols;
- compare adsorption performance to a conventional powdered activated carbon (PAC);

- propose adsorption mechanism of naphthols;
- compare algibon performance in the adsorption of naphthols to other carbonaceous materials.

4.3 Results and discussion

4.3.1 Algibon preparation temperature and adsorption

Algibons prepared at 500–800 °C were tested in a batch adsorption of 1-naphthol and 2-naphthol (Figure 4.1), to investigate the influence of the surface chemistry on naphthol uptake. The properties of A500–A800 algibons are discussed at length in Chapter 2, and summarised in Table 3.1. The surface chemistry of these materials displays decreasing oxygen content (9–0 wt%) and increasing levels of aromatic conjugation. The surfaces are basic, with pH_{pzc} in the range of 8.7–8.9. The BET surface area of the materials is in the narrow range of 523–590 $m^2\ g^{-1}$. Mesopore volume is in the range of 1.92–1.78 $cm^3\ g^{-1}$, and microporosity is negligible. Adsorption on the lower temperature algibons (below 500 °C) is not reported, as these materials leach UV-active humic acid, as reported in Section 2.3.6, which makes quantitation using UV spectroscopy unreliable.

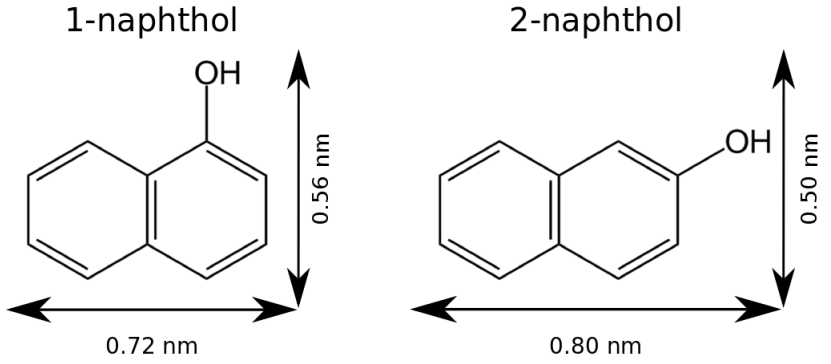

Figure 4.1: Chemical structure and molecular dimensions of 1-naphthol and 2-naphthol, determined with HyperChem software

In Figure 4.2, the average percentage removal of naphthols by algibons A500–A800 is shown. The data demonstrate that the uptake of naphthols increases with the preparation temperature of the algibons: 70–79 % removal was achieved with A500, 92–97 % with A600, 98–100 % with A700, and 100 % with A800. The same trend was reported in Chapter 3 for phenol adsorption, which was attributed to the increasing degree of aro-

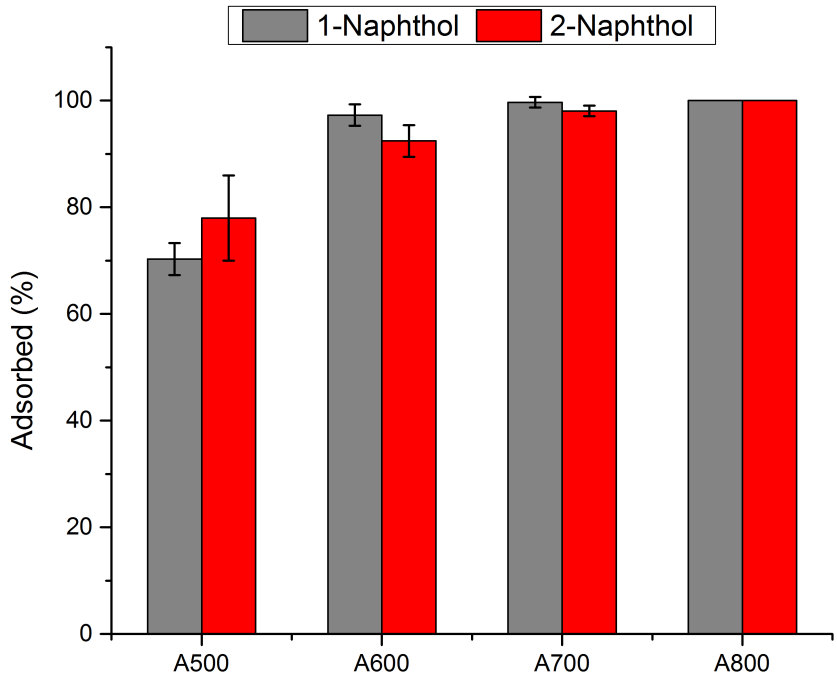

Figure 4.2: Influence of algibon preparation temperature on equilibrium adsorption (%) of 1-naphthol and 2-naphthol

maticity with temperature, i.e. π electron density, and decreasing levels of the surface oxygen.

Similar trend was previously observed by Chen and Chen for 1-naphthol adsorptions on orange peel biochars prepared at different temperatures.[92] The negative effect of the surface oxygen on the adsorption of naphthols was previously demonstrated with oxidized carbon nanotubes and graphene.[93,94]

4.3.2 Textural properties of adsorbents

The influence of algibon textural properties on adsorption of naphthols was investigated, using three A800 algibons possessing different textural properties. A commercial PAC was used as a benchmark adsorbent. The key textural properties of these materials are shown in Table 3.2. Nitrogen adsorption/desorption isotherms, elemental analysis and average pore volumes are presented in Section 3.3.2.

4.3.3 Influence of textural properties on adsorption kinetics

The rate of uptake of naphthols by A800_1, A800_1.6, A800_1.9 and PAC was investigated in a batch system. The change in adsorption capacity Q_t, calculated with Equation 4.1, is shown in Figure 4.3.

$$Q_t = \frac{C_0 - C_t}{m} V \tag{4.1}$$

Equation 4.1: Adsorption capacity formula, where Q_t is the amount adsorbed in mmol g^{-1} at time t, C_0 is initial concentration of a solution, C_t is concentration at time t in mmol L^{-1}, m is the amount of adsorbent in g, and V is the volume of solution in L.

The data demonstrate considerable differences in the adsorption profiles and capacities for 1-naphthol and 2-naphthol on the adsorbents. The order of the equilibrium adsorption capacity of the algibons for 1-naphthol and 2-naphthol is A800_1.9 > A800_1.6 > A800_1. The PAC, on the other hand, has the lowest capacity for 1-naphthol, and a similar capacity for 2-naphthol to A800_1.9 and A800_1.6, which is an unexpected behaviour for the highest surface area material, assuming adsorption based on face-to-face π-π interactions. 2-Naphthol appears to adsorb slower than 1-naphthol on all adsorbents. The onset of adsorption equilibrium is achieved faster with PAC for both naphthols, which could be attributed to the greater pore wall potential exerted on naphthols in small pores.

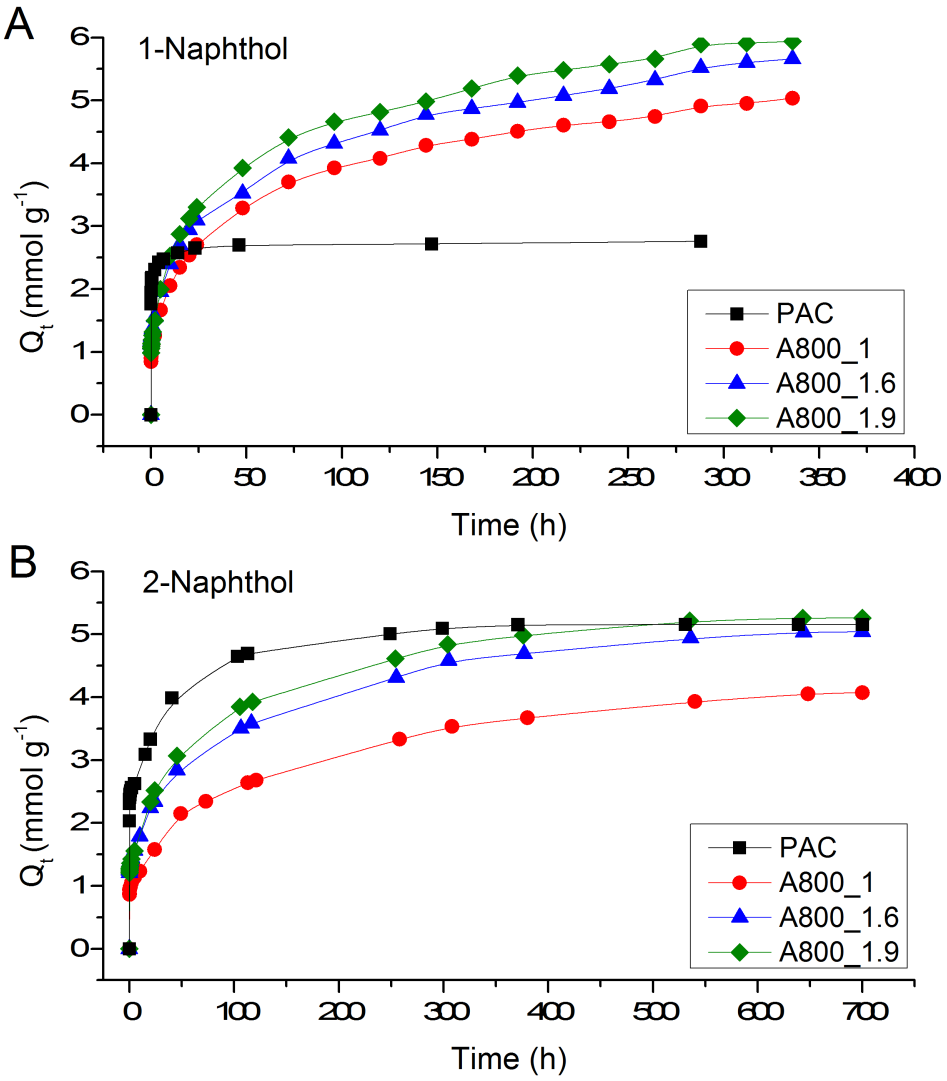

Figure 4.3: Change in adsorption capacity Q_t of 1-naphthol (A) and 2-naphthol (B) over time on algibons and PAC

These data suggest two interesting conclusions. Firstly, the mechanism of naphthol adsorption is different to phenols, which were found to adsorb more on PAC, the highest surface area material, with a linear correlation between the surface area and adsorption capacity (Section 3.3.5). Secondly, a small change in the molecular structure significantly affects the adsorption process, with PAC demonstrating the greatest sensitivity to the isomer effect.

The experimental results were analysed with common kinetic models: pseudo-first order, pseudo-second order and Elovich, which demonstrated a poor fit to the overall data. The resulting graphs are shown in Appendix B in Figure B.1. The pseudo-first and pseudo-second order kinetic models demonstrated unsatisfactory data approximation (R^2 0.38–0.90), whereas the Elovich model gave a better data fit (R^2 0.81–0.96).

Poor data fit with the kinetic models indicates the complexity of the adsorption process. It is plausible, considering the long equilibration times, that more than one adsorption mechanism is involved at different stages. Adsorption of 2-naphthol on activated carbon was previously found to follow pseudo-second order kinetics.[95] Adsorption of 1-naphthol on graphene nanosheets was demonstrated to follow the Elovich model.[76]

With the aid of linear forms of the pseudo-second order adsorption model (Equation 4.2), it was established that the initial adsorption follows pseudo-second order kinetics (Figure 4.4). The comparison of the initial pseudo-second order adsorption rates are shown in Figure 4.5.

$$\frac{t}{Q_t} = \frac{1}{h} + \frac{1}{Qe}t \tag{4.2}$$

Equation 4.2: Linear pseudo-second adsorption kinetic model, where Q_e is equilibrium adsorption capacity in mmol g^{-1} (calculated with Equation 4.1), Q_t is adsorption capacity at time t in mmol g^{-1} (calculated with Equation 4.1), t is time in min, and h is adsorption rate in mmol g^{-1} min^{-1}.

The initial rates of adsorption of 1-naphthol on algibons are slower than the initial rate of adsorption of 2-naphthol. The reverse trend is observed for PAC: adsorption of 1-naphthol is faster than adsorption of 2-naphthol, indicating that the spatial geometry of 2-naphthol restricts its interaction with the surface in the narrow pores of PAC. Based on the kinetic data, it is evident that the relation between the textural properties of adsorbents and the adsorption kinetics is not as straightforward as was reported for phenols in the previous chapter, and the adsorption mechanisms of 1-naphthol and

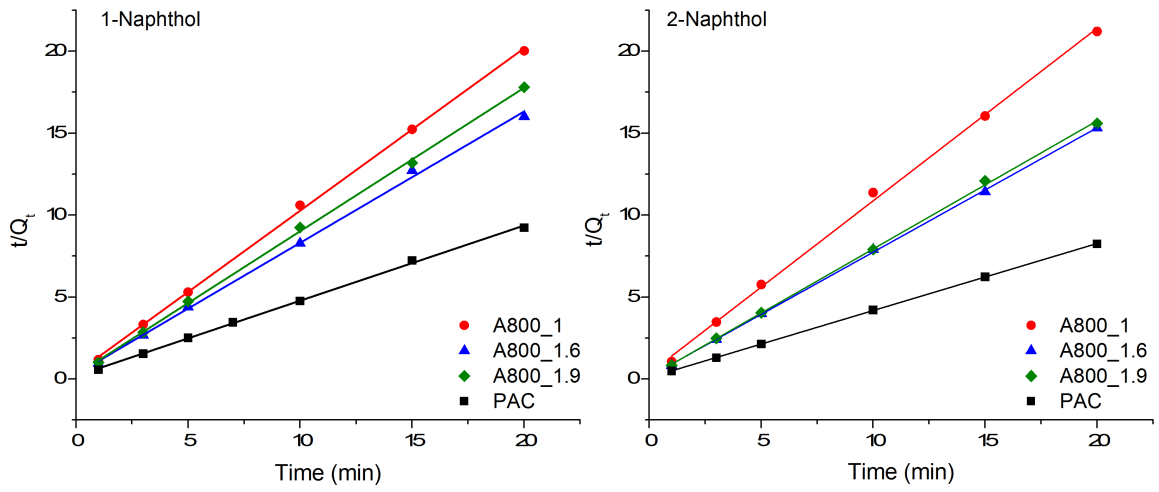

Figure 4.4: Linear pseudo-second adsorption kinetic plot of initial adsorption of 1-naphthol and 2-naphthol on algibons and PAC

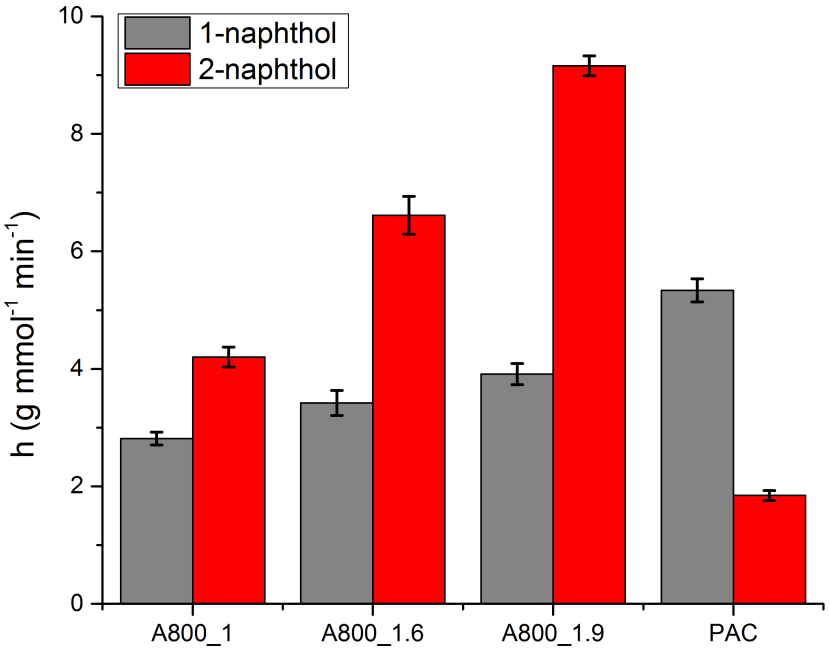

Figure 4.5: Initial pseudo-second order adsorption rates of 1-naphthol and 2-naphthol on algibons with different textural properties and PAC

2-naphthol differ.

4.3.4 Influence of textural properties on adsorption equilibria

Adsorption isotherms of naphthols on A800_1, A800_1.6, A800_1.9 and PAC were investigated in a batch adsorption experiment to identify the maximum adsorption capacity. The adsorbents were incubated in a range of different naphthol concentrations for an appropriate time, identified in the kinetics study, to ensure adsorption equilibrium. The experimental data were fitted with Langmuir and Freundlich isotherm models, described in Section 3.3.4. The Langmuir model demonstrated the best data fit with a correlation coeffiecient of 0.999–1.000 for 1-naphthol and 0.996–0.999 for 2-naphthol. The isotherms fitted with the Langmuir model are shown in Figure 4.6, and Langmuir isotherm parameters are tabulated in Table 4.1. The Freundlich model did not describe the experimental data as well (0.972–0.987 R^2) (Appendix B, isotherms in Figure B.2, model parameters in Table B.1).

The order of maximum adsorption capacity of the adsorbents for 1-naphthol, according to Langmuir model, is:

$$PAC < A800\_1 < A800\_1.6 < A800\_1.9 \tag{4.3}$$

The order of maximum adsorption capacity for 2-naphthol is:

$$A800\_1 < A800\_1.6 < PAC < A800\_1.9 \tag{4.4}$$

The isotherm data confirmed the findings of the kinetics experiment — the algibon with the greatest surface area and pore volume, A800_1.9, has the greatest adsorption capacities for both naphthols. This trend is different to phenol adsorption, where the greatest adsorption capacity was demonstrated by PAC, the material with the greatest surface area. The overall adsorption capacities for both naphthols (4.77–8.83 mmol g^{-1}) are higher than for phenols (0.5–2.6 mmol g^{-1}, Chapter 3), which could be a result of a greater π-π interaction between bicyclic aromatic system and the aromatic-rich surface.

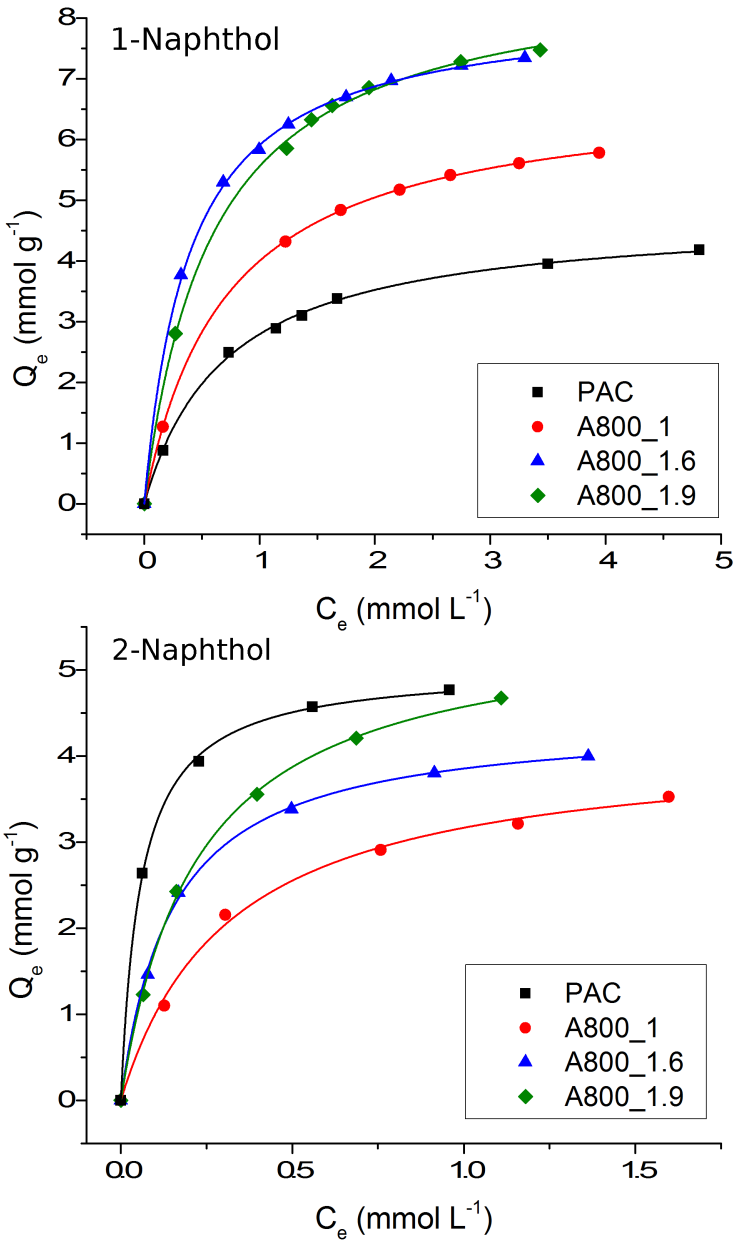

Figure 4.6: 1-Naphthol and 2-naphthol adsoprtion isotherms on algibons and PAC fitted with Langmuir model

Table 4.1: Langmuir adsorption parameters (maximum adsorption capacity Q_{max}, equilibrium constant K, and correlation coefficient R^2) for 1-naphthol and 2-naphthol adsorptions on algibons and PAC

1-Naphthol			
Material	Q_{max} [mmol g^{-1}]	K [L $mmol^{-1}$]	R^2
A800_1	6.61 ± 0.03	1.41 ± 0.02	1.000
A800_1.6	8.22 ± 0.05	2.56 ± 0.08	1.000
A800_1.9	8.83 ± 0.16	1.70 ±0.13	0.999
PAC	4.77 ± 0.06	1.42 ± 0.07	0.999
2-Naphthol			
Material	Q_{max} [mmol g^{-1}]	K [L $mmol^{-1}$]	R^2
A800_1	4.38 ± 0.51	4.71 ± 1.59	0.996
A800_1.6	4.47 ± 0.24	6.20 ± 1.44	0.999
A800_1.9	5.59 ± 0.24	4.33 ± 0.62	0.999
PAC	5.11 ± 0.26	14.88 ± 3.64	0.999

4.3.5 Adsorption capacities vs. textural properties

The relationship between adsorption capacities and textural properties of adsorbents are shown in Figure 4.7. For 1-naphthol, a linear correlation between the maximum adsorption capacity and the mesopore volume is observed (Figure 4.7.A). Adsorption capacity also correlates with the BET surface area of the algibons.

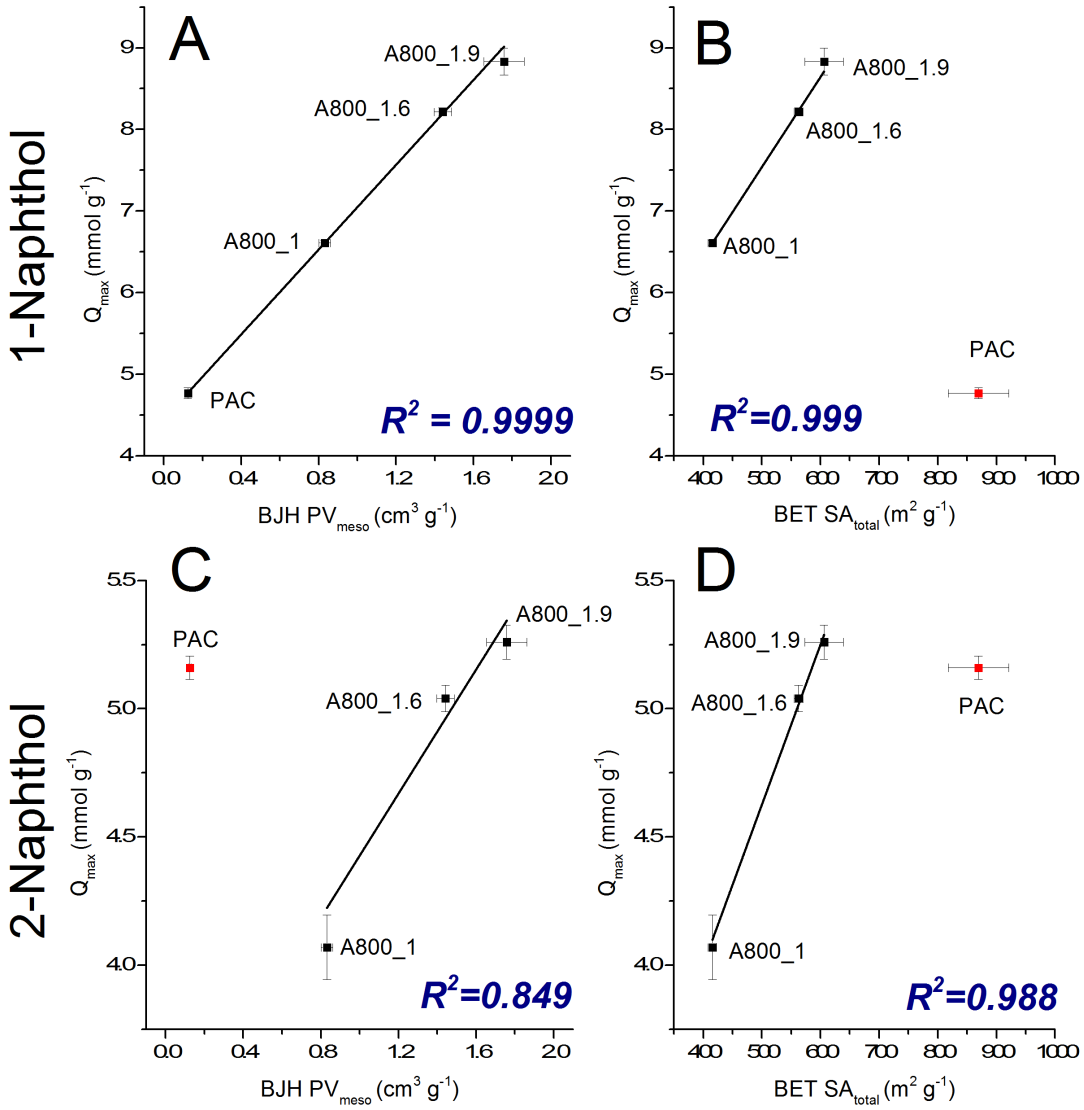

Figure 4.7: Relationship between textural properties of adsorbents (surface area SA_{BET} and mesopore volume PV_{meso}) and maximum adsorption capacity Q_t for naphthols (error bars represent experimental errors of SA_{BET}, PV_{meso}, and Q_{max})

The maximum adsorption capacity of 2-naphthol correlates well with the surface area of algibons (Figure 4.7.D), and to a lesser extent with the mesopore volume of

algibons (Figure 4.7.C). The maximum adsorption capacity of PAC for 2-naphthol does not display the same correlation as the algibons.

Overall, the data demonstrates that 1-naphthol adsorption is proportional to the mesopore volume of algibons and PAC, and adsorption of 2-naphthol is proportional to the surface area of algibons.

4.3.6 Surface coverage by naphthols

The surface area covered by naphthols, assuming face-to-face interactions between the surface and the molecules, was determined using molecular dimensions calculated with the HyperChem software (Figure 4.1). The results are tabulated in Table 4.2. The apparent coverage of the surface exceeds the BET surface area of the materials by 1.5–3.5 times. The data suggests that, in order to accommodate all adsorbed naphthols, either multilayer or edge-to-face adsorption must take place. Similar findings were reported by Zhao et al., who found that the maximum surface coverage of graphene nanosheets by 1-naphthol exceeds the surface area of the adsorbent.[76]

Table 4.2: The surface of adsorbents covered with 1-naphthol and 2-naphthol

	1-Naphthol		2-Naphthol	
	[m^2 g^{-1}]	[% of BET SA]	[m^2 g^{-1}]	[% of BET SA]
A800_1	1624	391	1052	253
A800_1.6	2019	359	1075	191
A800_1.9	2170	358	1342	221
PAC	1171	135	1228	141

4.3.7 Adsorption thermodynamics

The temperature dependence of the Langmuir equilibrium constant K was studied to understand the unusual adsorption trends. Adsorption of naphthols was performed at 30–60 °C, and the isotherms are shown in Figure B.3 and Figure B.4, Appendix B. The Langmuir equilibrium constants were plotted on a van't Hoff plot, shown in Figure 4.8, according to the thermodynamic relationship expressed in Equation 4.5. The Gibbs free

energy ΔG_{ads} was calculated with Equation 4.6. The enthalpy ΔH_{ads}, entropy ΔS_{ads}, and Gibbs free energy are tabulated in Table 4.3.

$$lnK = \frac{\Delta S_{ads}}{R} - \frac{\Delta H_{ads}}{RT} \tag{4.5}$$

Equation 4.5: Thermodynamic relationship between equilibrium constant K, adsorption entropy change ΔS_{ads}, adsorption enthalpy change ΔH_{ads} and temperature

$$\Delta G_{ads} = \Delta H_{ads} - T\Delta S_{ads} \tag{4.6}$$

Equation 4.6: Adsorption Gibbs free energy change

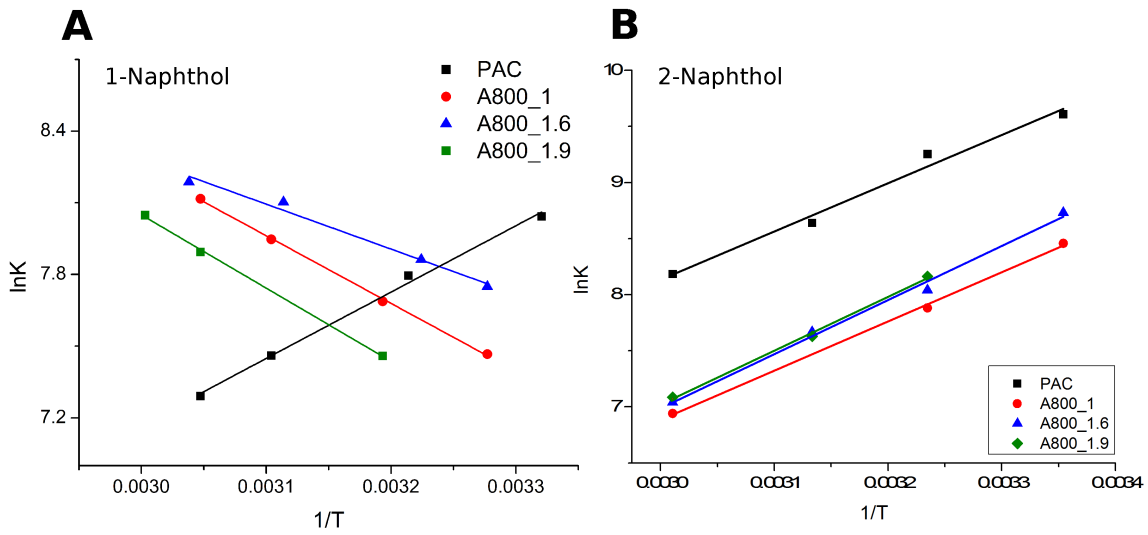

Figure 4.8: van't Hoff plot of thermodynamic dependence of Langmuir adsorption constant and temperature of naphthols adsorptions on algibons and PAC

The negative values of ΔG_{ads} indicate that the adsorption of naphthols is a spontaneous process. The positive values of ΔH_{ads} for adsorption of 1-naphthol on algibons indicate an endothermic process. The adsorption of 2-naphthol is an exothermic process, indicated by the negative ΔH_{ads}. PAC displays exothermic adsorption of both naphthols. The magnitude of enthalpy change (15–40 kJ mol^{-1}) is within the range of energy of formation/breaking of physical bonds.[96]

The ΔH_{ads} data suggest that two different mechanisms of adsorption of naphthols on algibons take place. In classic exothermic adsorption, observed in adsorption of 2-naphthol on algibons and PAC, the process has a net energy release from the system. In adsorption of 1-naphthol on algibons, the process requires energy, which could be explained by the energy input needed to desolvate the surface of the adsorbent and

adsorbate molecules for adsorption to take place. Interestingly, endothermic adsorption of 1-naphthol was previously reported on multiwalled carbon nanotubes and graphene nanosheets with ΔH_{ads} of 20.8 and 17 kJ mol^{-1}, respectively.[76,93]

The ΔS_{ads} of 1-naphthol adsorption is positive (115–143 J mol^{-1} K^{-1}), indicating an unusual increase in disorder of the system brought about by adsorption. This finding could be rationalized as follows. The surface of algibon and the 1-naphthol molecule are hydrated through hydrogen bonding, van der Waals interactions, or Yoshida hydrogen bonding (hydroxyl to π electrons).[97] This bound water possesses fewer degrees of freedom than free water. When 1-naphthol is adsorbed on the surface through face-to-face π-π interaction, some of the water is released, leading to the increase in entropy that outweighs the entropy decrease due to 1-naphthol immobilization.[76,96] This desolvation requires energy, leading to the endothermic adsorption. Face-to-face adsorption of 1-naphthol is likely to occur in multilayer fashion, leading to a higher adsorption capacity, which could explain the magnitude of the entropy increase. An entropy increase of similar magnitude for 1-naphthol adsorption on multiwalled carbon nanotubes and graphene nanosheets was reported previously, with ΔS_{ads} of 127 and 105 kJ mol^{-1}K^{-1}, respectively.[76,93]

The ΔS_{ads} of 2-naphthol adsorption is negative, indicating a decrease in disorder in the system. Extending the rationalization given for the positive entropy in case of 1-naphthol, it could be suggested that 2-naphthol adsorption is edge-to-face, with hydroxyl groups interacting with the aromatic electrons e.g. through Yoshida hydrogen bonding, leading to fewer water molecules displaced from the surface and a net negative entropy change.[97] Adsorption thermodynamics of 2-naphthol on carbonaceous materials has not been reported to date, to the author's knowledge, thus these results cannot be compared to other types of porous carbonaceous materials.

Table 4.3: Thermodynamic parameters of 1-naphthol and 2-naphthol adsorption

1-Naphthol			
	ΔG_{ads}	ΔH_{ads}	ΔS_{ads}
	[kJ mol^{-1}]	[kJ mol^{-1}]	[J mol^{-1}K^{-1}]
A800_1	negative	23.5 $\pm$ 0.4	139.2 $\pm$ 1.4
A800_1.6	negative	15.6 $\pm$ 1.3	115.8 $\pm$ 4.3
A800_1.9	negative	25.4 $\pm$ 0.7	143.3 $\pm$ 2.3
PAC	negative	-23.0 $\pm$ 1.0	-9.65 $\pm$ 3.4
2-Naphthol			
	ΔG_{ads}	ΔH_{ads}	ΔS_{ads}
	[kJ mol^{-1}]	[kJ mol^{-1}]	[J mol^{-1}K^{-1}]
A800_1	negative	-36.5 $\pm$ 1.3	-52.3$\pm$ 4.2
A800_1.6	negative	-40.1 $\pm$ 2.2	-62.3 $\pm$ 7.0
A800_1.9	negative	-40.1 $\pm$ 2.2	-61.4 $\pm$ 7.0
PAC	negative	-35.8 $\pm$ 3.2	-39.7 $\pm$ 10.2

4.3.8 Desorption of naphthols

Column desorption of naphthols was performed with ethanol in a flow system. Three cycles of adsorption/desorption were performed with 100% adsorption rate in each cycle. Desorption rates for each compound are shown in Figure 4.9.

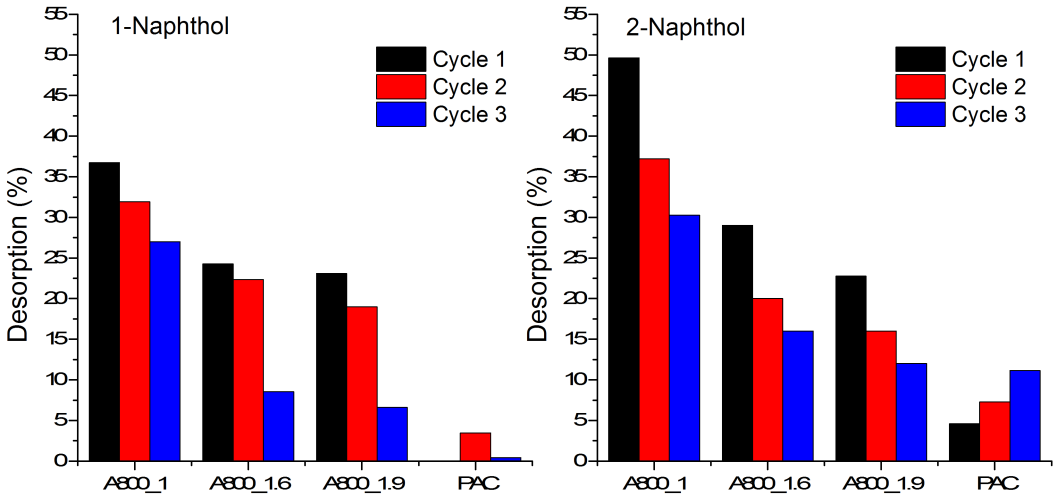

Figure 4.9: Desoprtion rates of 1-naphthol and 2-naphthol from algibons and PAC over three adsorption/desorption cycles

The quantity of naphthol desorbed from algibons is 5–7 times greater than desorption from PAC. This finding is attributed to the mesoporous nature of algibons. In mesopores, the strength of the adsorbate adhesion is lower than in micropores, and the ability of the eluting solvent to diffuse in and out of the larger pore is greater. The greatest desorption was achieved with A800_1, the lowest pore volume algibon. The same observation was reported for phenols desorption in Section 3.3.6. 2-Naphthol appears to desorb better than 1-naphthol, indicating that either the interaction of 2-naphthol with the surface is weaker than that of 1-naphthol, or 2-naphthol is more accessible by the solvent. Interestingly, desorption of naphthols from algibons decreases after each cycle. The reason for this trend is unclear.

4.3.9 Summary of naphthols adsorption

Based on the experimental data (adsorption kinetics, isotherms, thermodynamics and desorption) a mechanism of adsorption is proposed, reflecting an unusual behaviour of naphthols on the algibon surface. Adsorption of 1-naphthol takes place as multilayer

face-to-face π-π stacking on the surface. The mechanism of 2-naphthol adsorption, on the other hand, is likely to occur via edge-to-face interaction, possibly through interaction of hydroxyl groups with aromatic electrons that act as π donors in the hydrogen bonds.[97] In Figure 4.10 the summary of these findings is presented in support of the proposed adsorption mechanisms.

In PAC, adsorption of 1-naphthol and 2-naphthol are likely to follow similar mechanisms proposed for algibon. The multilayer adsorption of 1-naphthol on PAC is restricted by the smaller pore volume available for 1-naphthol stacking, leading to the lower adsorption capacity. The effect of the smaller pore geometry is even more pronounced with 2-naphthol adsorption, which relies on the available surface area in an adequately sized pore. As a result, it is likely that smaller pores in PAC are incompletely occupied by 2-naphthol.

The adsorption capacities for naphthols demonstrated by algibons are the greatest for carbonaceous materials reported in the literature to date (Table 4.4). Algibons outperform other novel advanced materials, such as graphene, mesoporous carbons and carbon nanotubes, which also require intensive manufacturing.

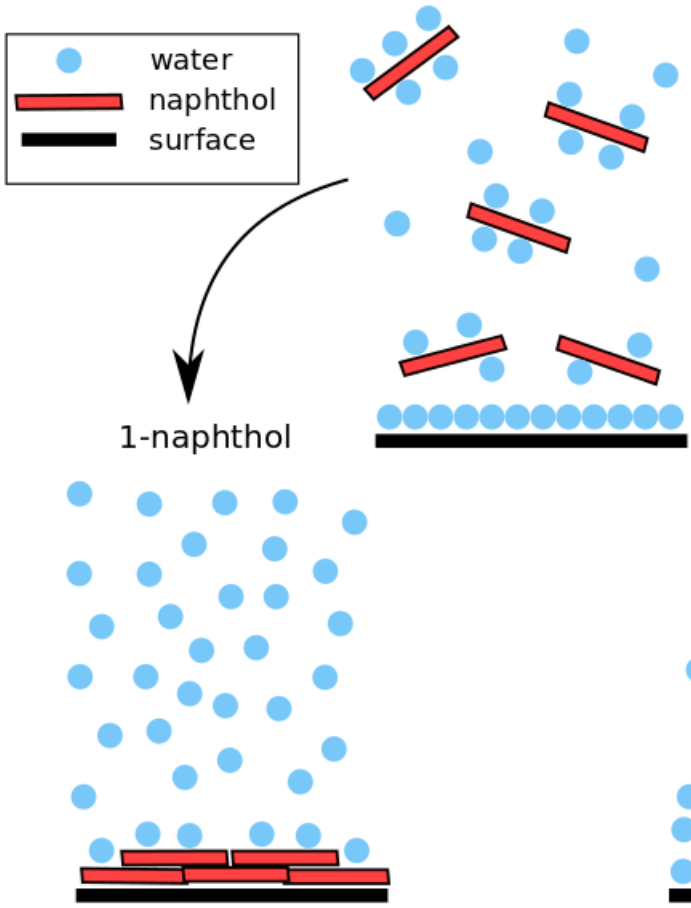

adsorption capacity exceeds BET surface area for single layer face-to-face adsorption by 390 %	adsorption capacity exceeds BET surface area for single layer face-to-face adsorption by 250 %
adsorption capacity is proportional to pore volume	adsorption capacity is proportional to surface area
adsorption is endothermic (energy needed to desolvate the surface and 1-naphthol)	adsorption is exothermic (energy is released on interaction of 2-naphthol with surface)
entropy change is positive	entropy change is negative
up to 37 % desorption achieved	up to 50 % desorption achieved

Figure 4.10: Summary of the supporting evidence for the proposed adsorption mechanism of 1-naphthol and 2-naphthol on algibon A800

Table 4.4: Comparison of adsorption capacities of a range of carbonaceous materials for 1-naphthol and 2-naphthol, and the textural properties of adsorbents (BET SA surface area and pore volume PV)

Material	BET SA_{total} (PV)	Capacity
1-Naphthol	[$m^2\ g^{-1}(cm^3g^{-1})$]	[mmol g^{-1}]
Starbons (present work)	606-416 (1.9-0.9)	6.8-8.9
Sulfonated graphene nanosheet[76]	520 (N/A)	2.3-6.4
Activated carbon (present work)	870 (0.5)	4.77
Oxidized mesoporous carbon[98]	985 (0.6)	2.99
Activated carbon[92]	1040 (0.43)	2.9
Orange peel biochar 700 °C[92]	201 (0.04)	0.31
Carbon nanotubes[93]	72 (0.41)	0.3
2-Naphthol	[$m^2\ g^{-1}(cm^3g^{-1})$]	[mmol g^{-1}]
Starbons (present work)	606-416 (1.9-0.9)	4.0-5.59
Activated carbon (present work)	870 (0.5)	5.11
Activated carbonvfrom sewage sludge[95]	321 (0.4)	0.8
Graphene[94]	239 (N/A)	0.6

4.4 Conclusion

The adsorption of 1-naphthol and 2-naphthol was systematically investigated on algibons prepared at different temperatures (500–800 °C) and on three algibons prepared at 800 °C possessing different textural properties. The aim was to evaluate the influence of the temperature-dependent surface chemistry and textural properties on adsorption parameters, and to compare these parameters with adsorption of naphthols on a conventional activated carbon. Adsorption kinetics, isotherms, thermodynamics and desorption were investigated. The following findings were made:

- algibon adsorption capacity for naphthols increases with preparation temperature, which is attributed to the increasing levels of aromatic conjugation, i.e. π electron density, and decreasing surface oxygen content;
- the adsorption kinetics of naphthols indicate a complex process, which could be attributed to the heterogeneity of the porous network;
- algibons have greater adsorption capacity for 1-naphthol compared to the PAC, and the maximum adsorption capacity is in a linear correlation with the mesopore volume;
- adsorption capacity of 2-naphthol is correlated with the BET surface area of algibons; however, PAC did not fully fit the trend, which was attributed to the geometry of 2-naphthol interactions with the PAC surface, restricted by narrow pores;
- the amount of naphthol desorbed from algibons is 5–7 times greater than from PAC, with 2-naphthol desorbing better than 1-naphthol;
- thermodynamically, adsorption of 1-naphthol on algibons is a spontaneous endothermic process driven by an entropy increase, which is unusual for an adsorption process, however, similar findings were reported previously for 1-naphthol adsorption on graphene and carbon nanotubes;[76,93]
- adsorption of 2-naphthol is spontaneous and exothermic, with a decrease in entropy of the system;

- it was concluded that adsorption of 1-naphthol is multilayer face-to-face stacking through π-π interactions, and 2-naphthol adsorption is edge-to-face, possibly through Yoshida hydrogen bonding;[97]
- the adsorption capacity for 1-naphthol and 2-naphthol demonstrated by algibons is the greatest reported to date for carbonaceous porous materials.

Overall, it was demonstrated that algibons are excellent materials for adsorption of 1-naphthol and 2-naphthol, outperforming advanced nanomaterials (graphene, nanotubes), which also require intensive manufacturing processes.[76,93] It is reasonable to assume that these conclusions would extend to the adsorption of other PAHs.

Investigation of naphthol and phenol adsorption demonstrates that the advantages of algibons over conventional activated carbons in adsorption applications become more pronounced with increasing molecular size of adsorbates. Even a small change in the molecular size from phenols to naphthols leads to a substantial difference in adsorption performance.

4.5 Future Work

It would be of interest to investigate adsorption of other PAHs (e.g. naphthalene) and larger molecules on algibons with different textural properties. In addition, application of algibons for gas scrubbing off PAHs, generated during fuel or waste burning, could be explored. The optimization of materials recovery through desorption could be attempted with different solvents, and the performance of recycled materials evaluated.

Interactions between naphthols and the surface require closer investigation, with e.g. Raman spectroscopy or X-ray powder diffraction, to verify the proposed adsorption mechanism.

Chapter 5

Freeze drying from aqueous *t*-butanol — a novel route to mesoporous polysaccharide aerogels

Part of the work presented in this chapter appears in Borisova et al., A Sustainable Freeze-Drying Route to Porous Polysaccharides with Tailored Hierarchical Meso- and Macroporosity, *Macromol. Rapid Commun.*, 36 (8), 774–779.[99]

5.1 Introduction

Pectin is one of the most abundant gelling polysaccharides, found in a wide range of land plants.[100] Pectin can be processed into a low density mesoporous aerogel with a procedure previously reported by White et al.[27] The preparation of pectin aerogel follows the same method as the expansion of alginic acid and starch.[25] An aqueous solution of a polysaccharide is thickened, i.e. gelled, through thermal treatment and allowed to retrograde at 4 °C to enable the polysaccharide network to restructure.[25] The water is then removed by a lower surface tension solvent, e.g. ethanol or acetone, and the resulting alcogel is dried with $scCO_2$ to preserve the porous structure.

This method has a number of drawback from the economic and environmental stand points. The procedure is time- and labour-intensive, requires large quantities of solvent and generates large quantities of waste. Moreover, in the scope of the present work, up-scaling of the procedure beyond the experimental scale (1 g of polysaccharide) to the preparation scale (>10 g polysaccharide) yielded unacceptably low quality pectin aerogels. The solvent exchange and $scCO_2$ drying were particularly problematic on the larger scale, due to the superior thickening potential of pectin compared to starch and alginic acid, demonstrated in Figure 5.1.

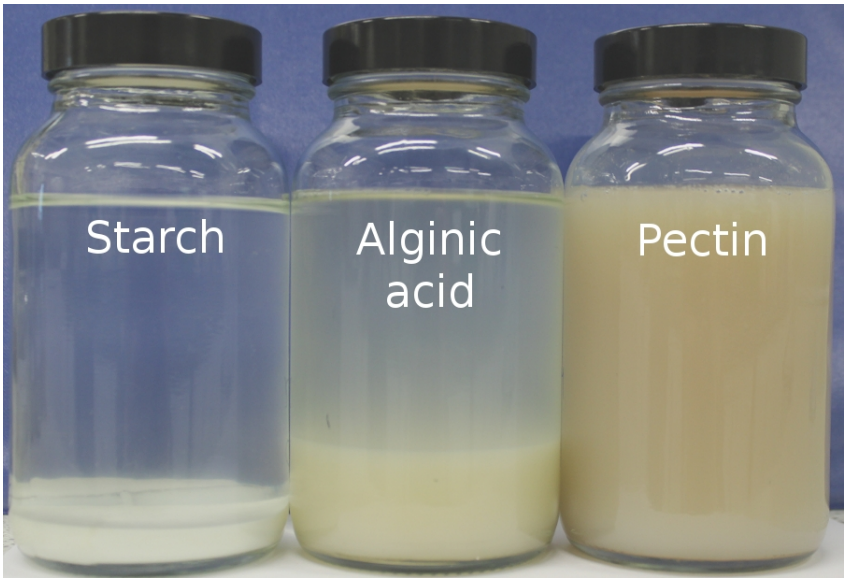

Figure 5.1: Gelation of polysaccharides: 10 wt% aqueous solutions of starch, alginic acid and pectin

The solvent exchange and drying of a polysaccharide alcogel is believed to be a cru-

cial step in preserving the porosity, developed during retrogradation. The alternatives to $scCO_2$ drying are air drying, vacuum drying, and freeze-drying.[101] Air and vacuum drying yield low surface area materials due to the capillary forces and incomplete drying.[101,102] On the other hand, the freeze drying of an aqueous polysaccharide solution is known to generate low density macroporous aerogels with low surface area and no mesoporosity.[30,103–105] No account of successful preparation of mesoporous aerogels from gelling polysaccharides using freeze drying was found prior to this work.

Freeze drying is a widely used and accessible technique developed for preservation of food and biological samples. The underlying principle is the sublimation of solid solvent under low pressures and temperatures, corresponding to the segment of the water phase diagram below the triple point (0.01 °C, 4.6 Torr/0.006 atm) (Figure 5.2).

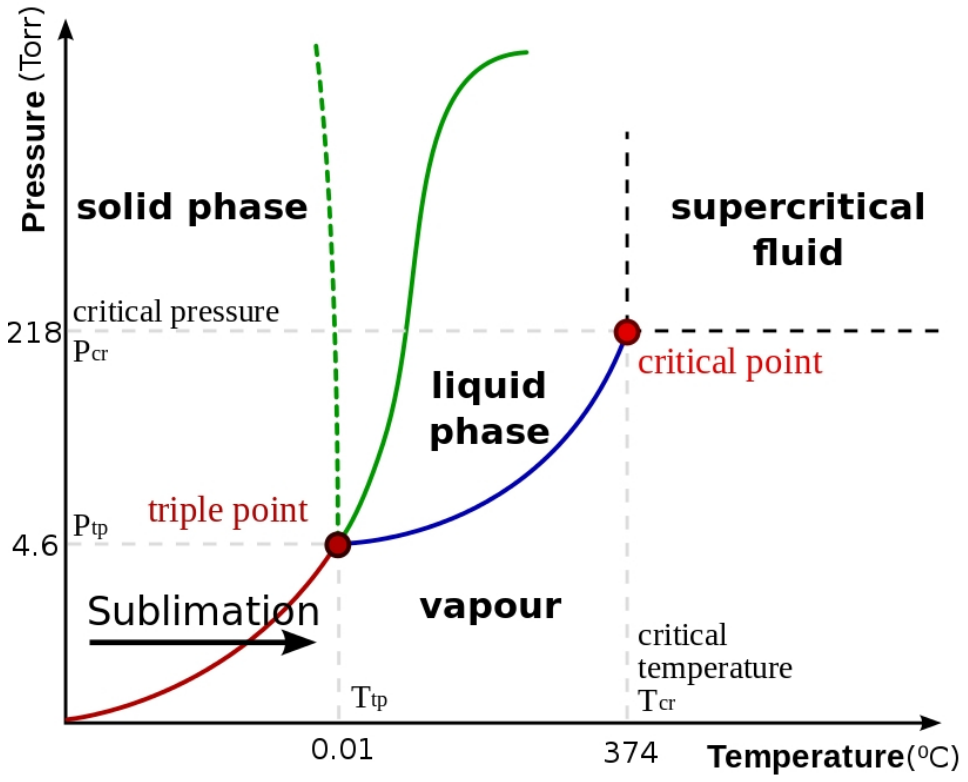

Figure 5.2: Phase diagram of water (*Wikimedia Commons*)

In the field of ceramics (e.g. alumina, hydroxyapatite, zirconia), synthetic polymers (resorcinol-formaldehyde polymers, polystyrene), and non-gelling polysaccharides (e.g. nanofibrillated cellulose), freeze drying from tertiary butanol (TBA) has been reported to generate mesoporous materials.[106–113] The mesoporosity is derived from TBA crystals acting as porogens, which are then removed during freeze drying, leaving the porous

structure intact.

Recently, Guizard et al. have demonstrated that different distributions of macropore sizes in zirconia and polyvinyl alcohol polymer can be achieved by varying the TBA/water concentration.[114] This tailoring was attributed to the different crystal habits, i.e. shapes and sizes of the crystals, in solutions with different TBA concentrations.[115,116]

The existing data demonstrate the potential of freeze drying to generate porous materials with different porous networks. The aim of the present work, therefore, was to investigate the feasibility of freeze drying of self-templating gelling polysaccharides as a route to mesoporous aerogels.

5.2 Aims

The aim of the present chapter was to generate mesoporous pectin aerogels from TBA/water solutions by freeze drying, and to investigate the parameters affecting the textural properties of the resulting aerogels. The work included:

- the investigation of the TBA/water phase diagram across the entire concentration range;
- demonstration of the effectiveness of the freeze drying route to generate mesoporous aerogels;
- porosimetry analysis of the aerogels;
- determination of the relationship between TBA concentration and the textural properties of aerogels;
- application of the developed method to alginic acid and starch gels to assess its versatility.

5.3 Results and discussion

5.3.1 TBA/water phase diagram

An understanding of the crystallization process of aqueous TBA was required for the present work. However, the few phase diagrams available in the literature were found to conflict in their account of the positions of the eutectic points and the number of solid phases.[114,115] In order to address the observed discrepancies, differential scanning

calorimetry (DSC) analysis of TBA/water solutions was performed to identify the number of solid phases and their melting points.

The DSC curves of a range of TBA solutions, presented in Figure 5.3, demonstrate the peculiar nature of the TBA/water interactions at different TBA concentrations. At low TBA concentrations of up to 25 wt%, two DSC transitions are observed: the E_1 eutectic point (-10 °C) and water (0 to -10 °C). The composition at E_1 is ≈25 wt% TBA, which is in agreement with the previously reported data.[115,117,118] The solid phase at E_1 is composed of fine crystals of water and TBA hydrate.[115] With TBA concentrations over 25 wt%, the hydrate peak separates from the eutectic, and at 70 wt% of TBA the solution is entirely composed of the physical compound α, which was previously identified as TBA dihydrate.[116] However, based on the molecular ratio, its unit structure is likely to consist of 4 TBA and 7 water molecules. At TBA concentrations above 70 wt%, the E_2 eutectic point is observed with a melting point at -4.6 °C, which is composed of ≈93 wt% TBA solution. Its solid phase consists of fine crystals of compound α and pure TBA.

Based on the DSC data, the TBA/water solid-liquid phase diagram was constructed (Figure 5.4). The structure of the diagram is in general agreement with those previously reported.[115,118] The diagram reflects the melting points and compositions of eutectic points E_1, E_2, and the compound α. This complex concentration-dependent solidification behaviour of TBA/water was previously demonstrated to alter the crystal habit of the solution.[115]

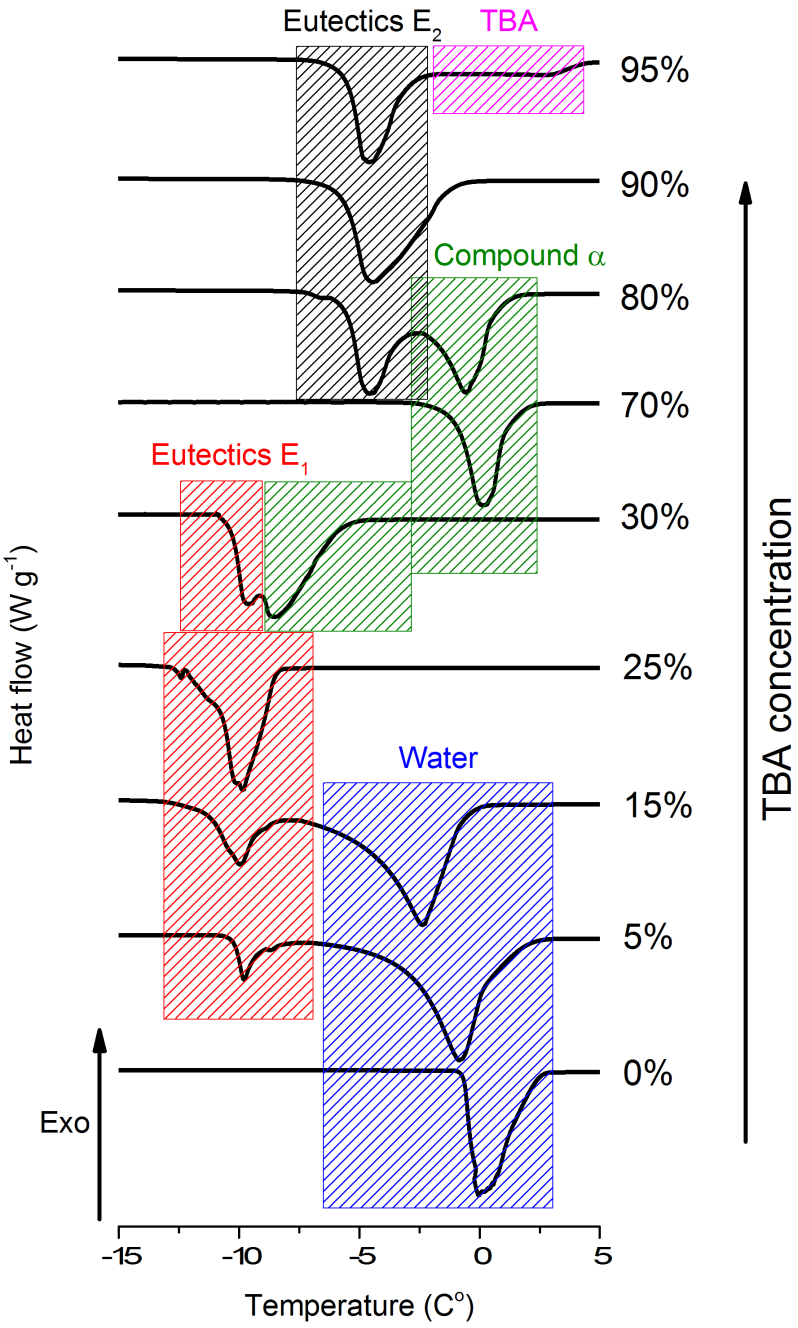

Figure 5.3: DSC heating traces of TBA/water solutions with different TBA concentration demonstrating the origins of the signals

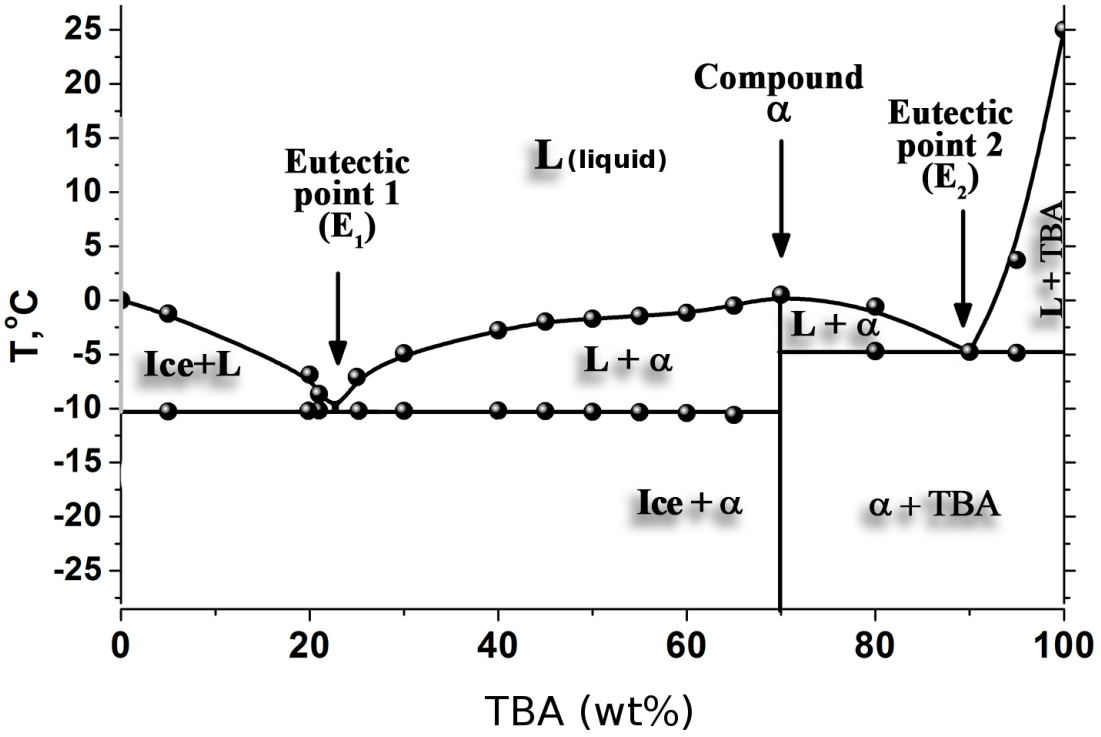

Figure 5.4: Experimentally determined TBA/water solid-liquid phase diagram at atmospheric pressure

5.3.2 Pectin characterisation

The DE of galacturonic acid in pectin was determined with the IR spectroscopy method reported by Manrique and Lajolo, described in the Experimental Chapter 8.[119] The DE of the pectin was 60±0.45% (n=3), which classifies it as a high methoxy pectin. The degree of esterification dictates the gelation mechanism of pectin: hydrophobic interactions dominate in high methoxy pectin, whereas in low methoxy pectin electrostatic and ionic bonding dominate.[37,120,121]

The elemental composition of pectin is shown in Table 5.1. The ash content, determined with TG analysis, is 3.5±0.4 %. The presence of inorganics could be attributed to the natural formation of salts of galacturonic acid in plant cells, particularly with Ca^{2+}, which are extracted along with pectin.[122] Also, the observed high levels of Na^{+} could be a contamination from the neutralization step in the conventional process of acid extraction of pectin from citrus peel.

Table 5.1: Elemental composition of pectin determined with CHN and ICP analyses

O (%)	C (%)	H (%)	Na (%)	K (%)	Ca (%)	N (%)	Fe (%)	Al (%)
56.67	35.25	4.54	2.10	0.69	0.36	0.25	0.02	0.01

5.3.3 Pectin aerogels freeze dried from TBA/water solutions

A 10 wt% pectin solution was prepared by blending deionized water and pectin with a domestic hand-held blender to a homogeneous consistency. The resulting gel was left to retrograde for 48 hours at 4 °C. The gel was distributed into separate vials, where the contents of each vial was adjusted with an appropriate quantity of TBA to yield TBA/water concentrations in the 0 to ≈100 wt% range. The resulting mixtures were frozen and freeze dried for at least 24 h in an SP Scientific Sentry 2.0 freeze drier. The obtained aerogels were subjected to N_2 porosimetry analysis to investigate the relationship between TBA concentration and their textural properties.

In Figure 5.5, the pore volumes and surface areas of the obtained aerogels are plotted against the respective TBA concentrations. The plots demonstrate that TBA concentration has a significant impact on the porosity of the aerogels. At 0 wt% TBA concentration, the aerogel has no detectable mesoporosity. As the TBA concentration

increases, the pore volume increases rapidly, achieving a maximum of 2.3±0.3 $cm^3\ g^{-1}$ at 30 wt% TBA. With a further increase in the TBA concentration, mesopore volume drops to 0.8 $cm^3\ g^{-1}$ at 55 wt%. It then reaches a second maximum of 1.8±0.3 $cm^3\ g^{-1}$ at about 80 wt%.

The BET surface area generally follows a similar pattern to the pore volume, i.e. the greater the pore volume, the higher the surface area. The average pore diameters, determined by N_2 porosimetry, are in a narrow mesopore range of 20-31 nm, and do not correlate strongly with the solvent composition. The microporosity of all aerogels is below 0.025 $cm^3\ g^{-1}$. The mesoporous nature of the resulting aerogels is further evident in the N_2 adsorption/desorption isotherms (Figure 5.6), which are of type IV, according to BDDT classification.

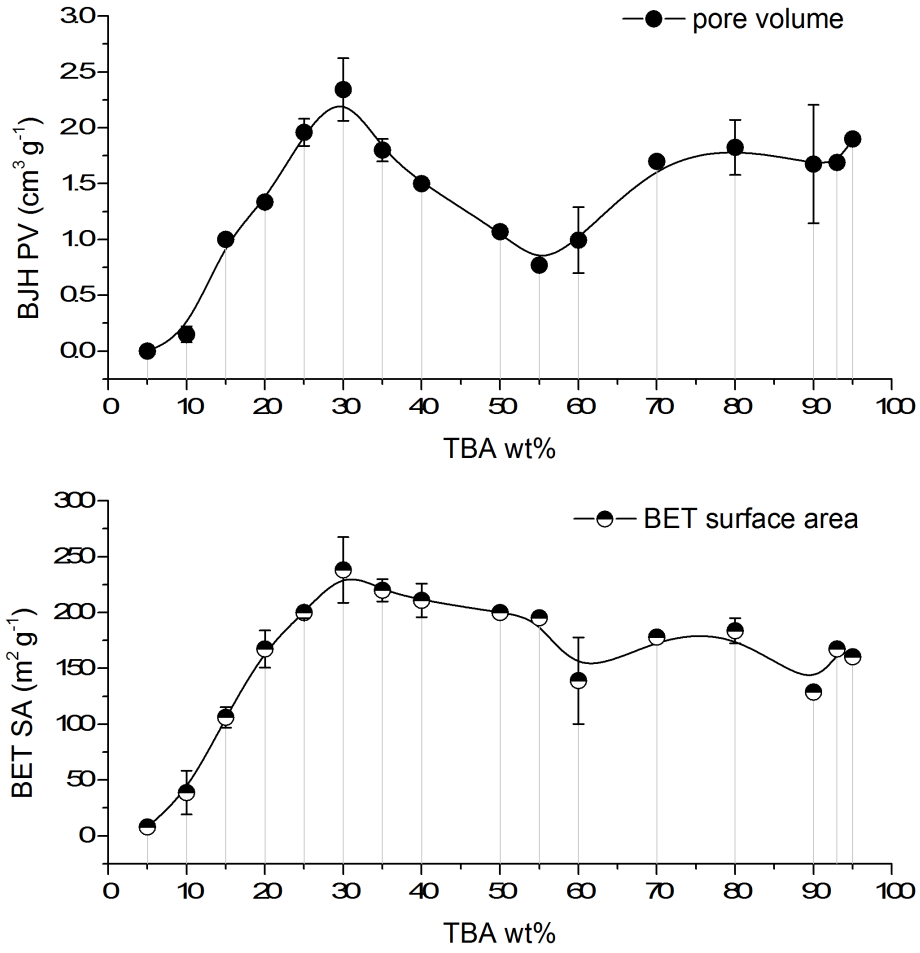

Figure 5.5: BJH pore volumes and BET surface areas of pectin aerogels plotted against TBA concentration of their respective solutions

These data demonstrate that the freeze drying route performs well at preserving

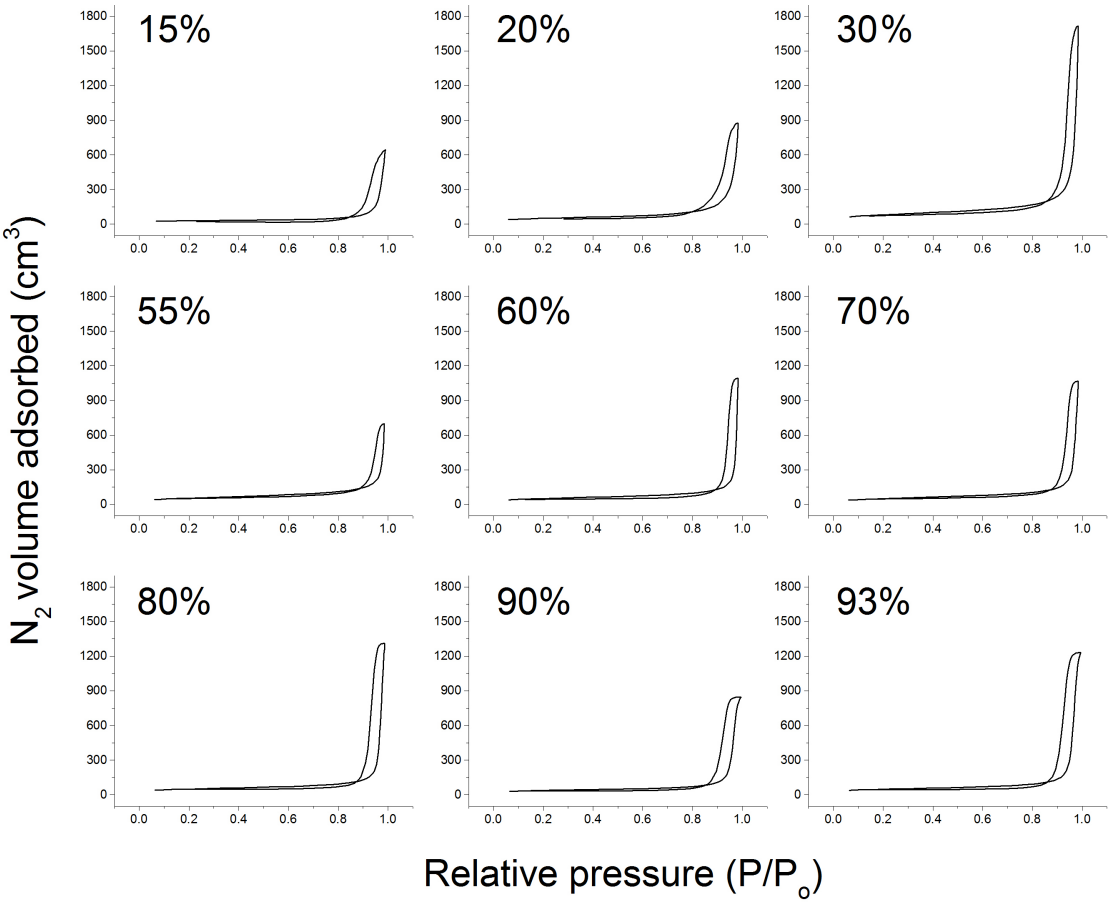

Figure 5.6: N_2 adsorption/desorption isotherms of the pectin aerogels freeze dried from solutions with different TBA concentrations

the mesoporosity of pectin gels. Moreover, the method outperforms the conventional process, which was reported to yield materials with a pore volume of 0.39 $cm^3\ g^{-1}$ and surface area of 200 $m^2\ g^{-1}$.[27] The variation in the pore volume with TBA concentration shows a remarkable similarity to the TBA/water phase diagram. The maxima in pore volume correspond to near-eutectic compositions of pure TBA/water solutions, and the pore volume decreases as the TBA concentration moves away from the eutectic points. This finding demonstrates that eutectic concentrations of TBA/water are favourable for mesoporosity preservation.

However, there is a noticeable shift in the first pore volume maximum from the true eutectic compositions. This maximum is at 30 wt% TBA, as opposed to 25 wt% TBA for a pure solution. This shift is rationalized by the complexity of the ternary water-TBA-pectin system. In this system, some of the TBA will associate with pectin through intermolecular interactions (van der Waals forces, hydrogen bonding, hydrophobic interactions) and thus will be removed from the interstitial space. The pectin sample in this study has a high degree of esterification, and it has been previously demonstrated to associate with TBA by hydrophobic interactions through methyl esters.[37,123] As a result of these interactions, the E_1 eutectic point of the water-TBA-pectin system shifts to a higher TBA concentration than in the bulk solution.

This interaction between the solvent and the pectin was indirectly confirmed by the DSC data. In Figure 5.7, the DSC signal of the pectin alcogel with 30 wt% TBA concentration and the DSC signal of the pure 30 wt% TBA solution are shown. The pure solvent shows two transitions: melting of eutectic E_1 and TBA hydrate, whereas the alcogel has a single peak arising from the melting of E_1, confirming that all interstitial solvent is of the eutectic composition. This finding provides the evidence for the link between eutectic solvent composition and mesoporosity. It was, however, not possible to obtain an informative DSC trace of the gel with 80 wt% TBA, due to precipitation of pectin. The DSC traces for pectin gels with different TBA levels are shown in Figure C.1 in Appendix C.

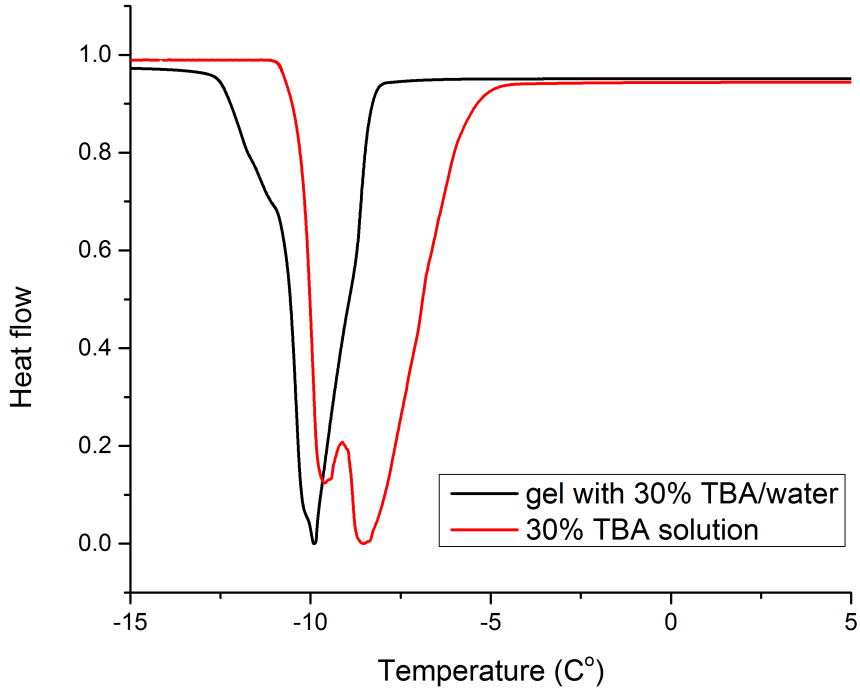

Figure 5.7: DSC heating traces of 30 wt% TBA solution with and without pectin demonstrating a shift to eutectic composition with the presence of pectin (data normalised to 0-1 range)

5.3.4 Mechanism of porosity formation in aerogel

There is a clear link between eutectic TBA/water concentrations and mesoporosity of pectin aerogels, as demonstrated by the porosimetry and DSC data above. Eutectic TBA/water solutions preserve mesoporosity. Based on the experimental data and existing knowledge from the field of ice-templation, the mechanism of pore development during freeze drying of pectin gel is proposed, and shown schematically in Figure 5.8.[114,124]

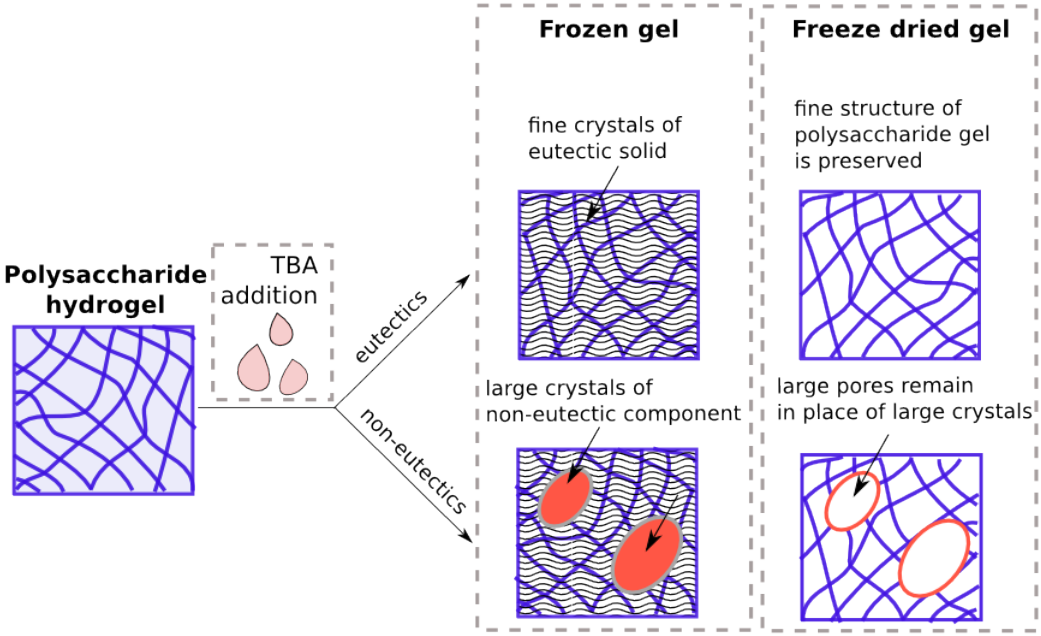

Figure 5.8: Schematic illustration of the process of porosity formation in pectin aerogels freeze dried from eutectic and non-eutectic TBA/water solutions

It is known that eutectic solutions of TBA/water form very fine crystals below their melting point.[115] However, away from the eutectic concentrations, larger crystals of the non-eutectic components form, destroying the fine structure of the gel. Upon sublimation, the solvent crystals are removed, leaving behind pores with the same geometry as the crystals. Freeze drying of aqueous pectin gels yields low density macroporous aerogels, due to the relatively large size dendritic water crystals.[115]

The scanning electron microscopy (SEM) images of aerogels, shown in Figure 5.9, support this proposed mechanism, and demonstrate the effect of the non-eutectic crystals. The large size of the water crystals, which results in high macroporosity, is evident in the sample with 0 wt% TBA. The size of macropores decreases with addition of TBA.

The aerogel derived from the eutectic TBA solution (30 wt%) shows no visible macropores, demonstrating the tendency of the eutectic composition to solidify into fine crystals. Above 30 wt% TBA, pectin precipitates from the solution (Figure 5.10), rendering the factors influencing porosity formation at higher TBA concentrations less obvious. However, the artefacts of solid solvent are seen in the SEM images of aerogels from 50 % and 90 % TBA solutions, in the form of larger pores.

The macroporosity demonstrated with SEM undergoes a dramatic change with TBA concentration — the size of pores changes considerably. However, the mesoporosity remains in a narrow range, from 20-31 nm, which further supports the conclusion that mesopores originate from the "gentle" freezing of the eutectic solution in the native pores of the pectin network, as opposed to templation by the solvent crystals.

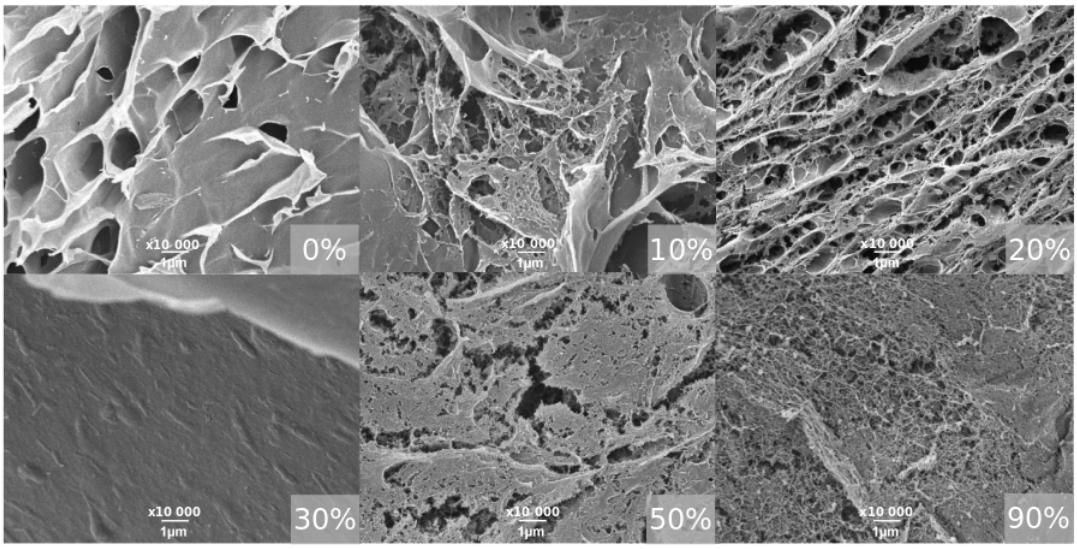

Figure 5.9: SEM images of pectin aerogels freeze dried from 0%, 10%, 20%, 30%, 50% and 90% TBA solutions (x10 000, bar is 1 μm)

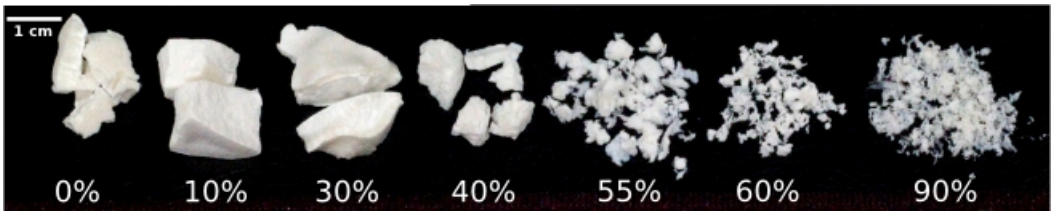

Figure 5.10: Pectin aerogels freeze dried from different TBA concentrations

5.3.5 Direct gelation in TBA/water solutions

The simplicity of the freeze drying route allowed for further optimization of the procedure, to reduce the time and the solvent volume required, and to improve scalability. The feasibility of direct gelation of pectin in a TBA/water solution, avoiding the solvent addition step, was investigated. A series of pectin gels were prepared in TBA/water solutions ranging from 0 to 100 wt% TBA. The gels were retrograded for 48 h, freeze dried and subjected to N_2 porosimetry.

Firstly, it was established that preparation of pectin gel was not possible above 30 wt% TBA due to pectin precipitation; the resulting freeze dried pectins had low mesoporosity, declining with the amount of TBA. Therefore, only gelation in solutions of up to 30 wt% TBA concentration is reported.

Secondly, it was demonstrated that pectin gels well in TBA solutions of up to 30 wt%, as demonstrated by the gel inversion test shown in Figure 5.11.A. The viscometric analysis of the gels, shown in Figure 5.11.B, demonstrates pseudo-plastic behaviour. It also shows that gel strength increases with TBA concentration up to 25 wt%; above this concentration the hydrophobicity of the solution becomes prohibitive for gelation.

The increase in gel viscosity with TBA addition is attributed to its high degree of esterification. Oakenfull and Scott have demonstrated a similar effect, when studying the role of hydrophobic interactions in gelation of high methoxy pectin.[37] They concluded that low quantities of TBA facilitate hydrophobic interactions between the methyl groups of galacturonic acid ester. Solvated TBA molecules reduce the repulsion between water and hydrophobic high-methoxy pectin. However, above 25 wt% TBA, the hydrophobicity of the solution increases, preventing non-esterified galacturonic acid from being solvated with water.

The textural properties of aerogels are tabulated in Table 5.2. These data show that the maximum pore volume is achieved at 25 wt% TBA, which corresponds to the most viscous gel in the series. In Figure 5.12, the total BJH pore volumes of aerogels directly gelled in TBA are compared to those prepared by the TBA addition method. The maximum pore volume generated is greater in the direct gelation method (3.1 $cm^3\ g^{-1}$) compared to the TBA addition method (2.3 $cm^3\ g^{-1}$). Microporosity was negligible.

The DSC analysis of the pectin gelled in 25 wt% TBA, shown in Figure 5.13 along with the DSC of the neat 25 % TBA solution, demonstrates that the sample has a high proportion of the eutectic solution, which leads to good preservation of the mesoporos-

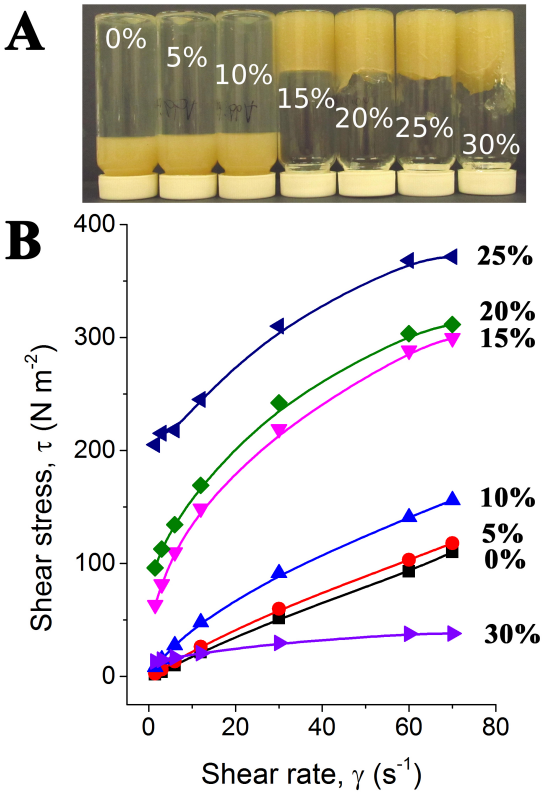

Figure 5.11: Pectin gels obtained with direct gelation in TBA/water solutions (number indicates TBA percentage): A. inversion test B. viscometric analysis

Table 5.2: Textural properties of pectin aerogels obtained with direct gelation in TBA solution

TBA %	BET SA_{total} [$m^2\ g^{-1}$]	BJH PV_{total} [$cm^3\ g^{-1}$]	PD [nm]
5	2	0	0
10	58	0.2	30
15	115	1.3	34
20	159	2.1	33.7
25	232	3.1	31.2
30	177	2.2	44.7

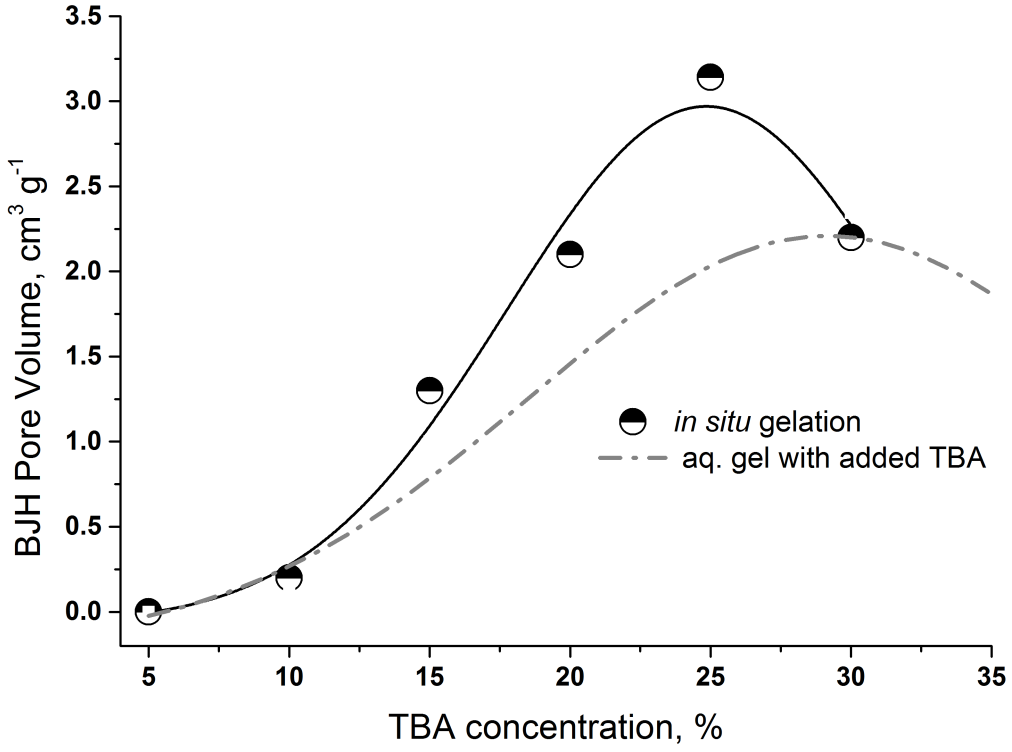

Figure 5.12: Total BJH pore volumes of pectin aerogels obtained with direct gelation in TBA solutions

ity during freeze drying. Overall, the direct gelation of pectin in 25 wt% TBA solution avoids the extra step of TBA addition, and yields the aerogel with the highest mesoporosity obtained in this study.

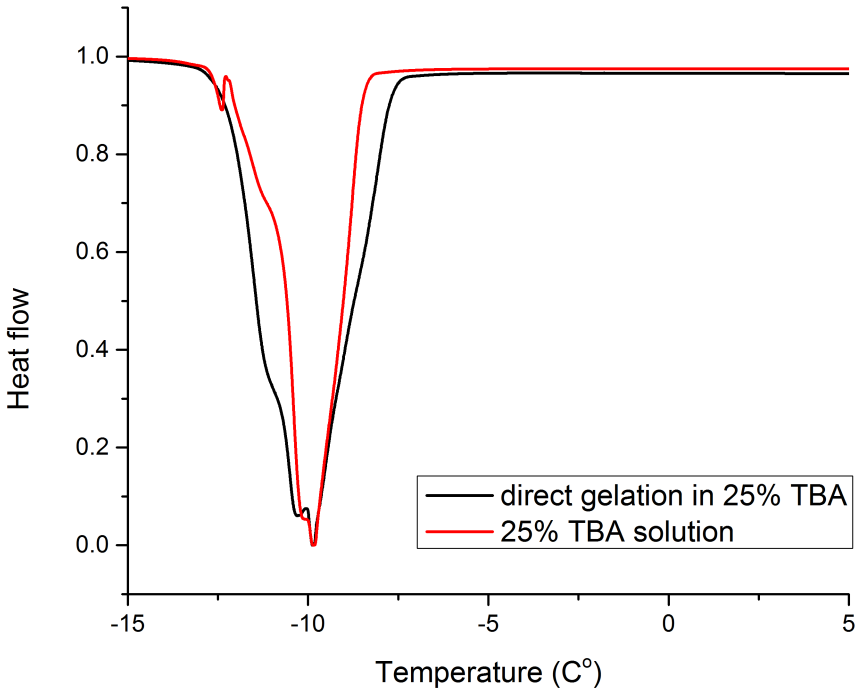

Figure 5.13: DSC heating traces of pectin gel with 25 % TBA concentration and neat 25 % TBA solution (data normalised to 0-1 range)

5.3.6 Freeze drying of alginic acid and starch aerogels

The applicability of the freeze drying route to other gelling polysaccharides was investigated. TBA was added to aqueous solutions of starch and alginic acid to yield a range of TBA concentrations. These solutions were retrograded at 4 °C for at least 24 h, frozen and freeze dried. Direct gelation in TBA solutions was also performed. In Figure 5.14, the pore volumes of alginic acid and starch aerogels are presented. Microporosity in all samples was negligible. The surface areas were 67–179 $m^2\ g^{-1}$ and 34–90 $m^2\ g^{-1}$ for starch, with TBA addition and direct gelation methods respectively, and 129–227 $m^2\ g^{-1}$ and 90–135 $m^2\ g^{-1}$ for alginic acid, with TBA addition and direct gelation methods respectively.

The pore volume data of alginic acid and starch aerogels show similar profiles to those reported above for pectin aerogels — the highest mesoporosity was achieved around the eutectic points, E_1 and E_2. Both the direct gelation and TBA addition methods produced mesoporous materials. However, TBA addition was more effective with alginic acid and direct gelation was more effective with starch.

Overall, the freeze drying method was found suitable for fabrication of mesoporous starch and alginic acid aerogels; however, more investigation is required to compare the DSC and viscosity profiles of the starch and alginic acid gels to the results from the study of pectin gels above.

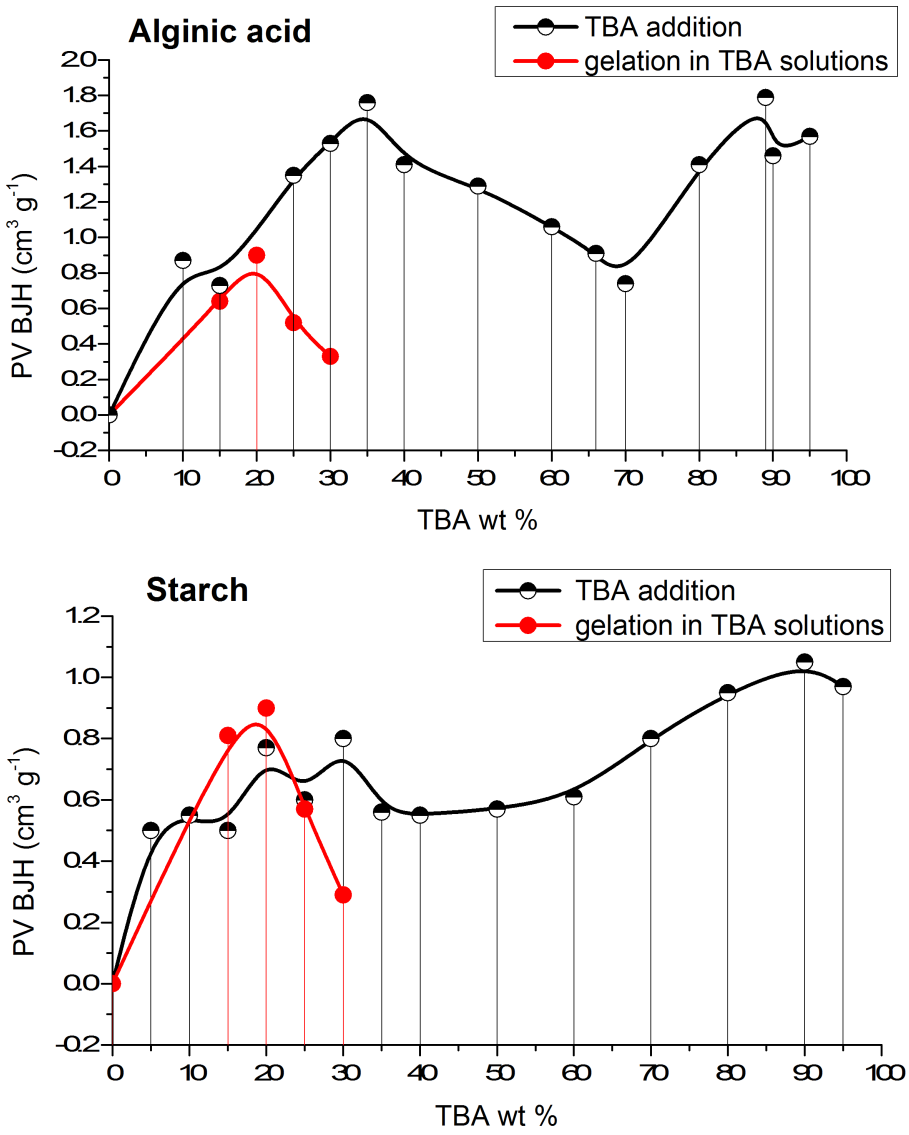

Figure 5.14: BJH pore volumes of alginic acid and starch aerogels obtained with TBA addition and direct gelation in TBA solutions and starch aerogels obtained with TBA addition and direct gelation in TBA solutions

5.4 Conclusion

In this chapter, a novel route to mesoporous polysaccharide aerogels was reported based on the freeze drying of polysaccharide alcogels containing TBA. The route was demonstrated to yield highly mesoporous pectin aerogels (up to 2.3±0.3 $cm^3\ g^{-1}$ and 240 $m^2\ g^{-1}$), and reduce solvent usage by 90 % compared to the conventional solvent exchange method.[25]

A strong link between mesopore volume and TBA/water eutectics was revealed, which is the first report of this kind. The conclusion was made that fine eutectic crystals freeze in the native pores of a polysaccharide gel network, preserving the porosity during the drying process, whereas non-eutectic crystals grow larger in size, leading to macropores. The conclusion was supported with:

- porosimetry data showing a relationship between the TBA/water phase diagram and change in mesoporosity;
- DSC analysis, demonstrating the presence of eutectic TBA/water solution in alcogels,
- SEM analysis, demonstrating the presence of larger macropores away from eutectic concentrations.

In addition, the freeze drying route to mesoporous aerogels was found to be applicable to other gelling polysaccharides — alginic acid and starch. The obtained aerogels were comparable in mesopore volume and surface area to aerogels obtained by the conventional method.[26,27,34]

The direct gelation of polysaccharides in eutectic and near-eutectic TBA solutions (20–30 wt% TBA) was found to further simplifying the procedure, reducing the time and resources required to fabricate the materials. Directly gelation of pectin and starch in TBA solutions showed improved mesoporosity compared to the TBA addition method. Alginic acid aerogels obtained with direct gelation in TBA solutions yielded lower, but acceptable, mesoporosity. Moreover, direct gelation could enable solvent reuse, as demonstrated in Figure 5.15, subject to process optimization.

In general, freeze drying is a widely accessible and available technology. TBA is considered a relatively good solvent from environmental, health and safety and disposal stand points, according to the GlaxoSmithKline and Pfizer solvent selection guides.[125,126]

These factors, in addition to resource and time efficiency, render the process economically and technologically viable.

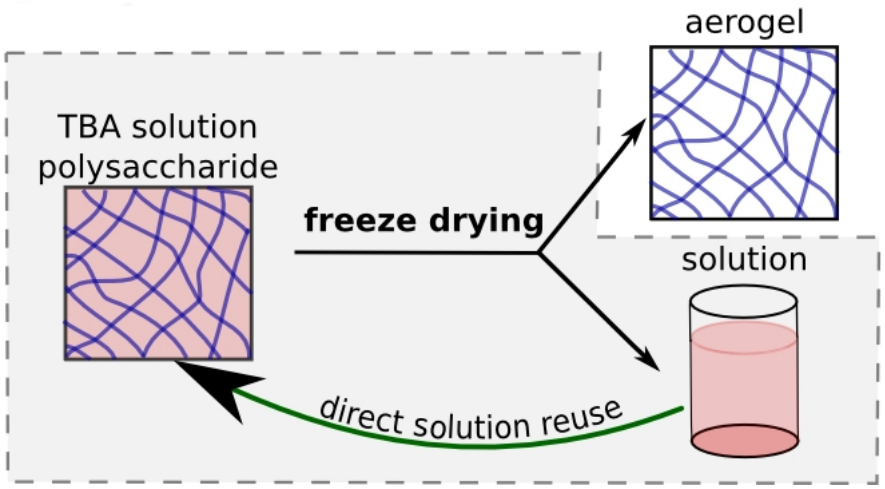

Figure 5.15: Potential closed-loop freeze drying fabrication of mesoporous polysaccharides

5.5 Future work

The work described in the present chapter is in the early stages of development, and the full potential of freeze drying to produce mesoporous materials is yet to be explored. The following research questions should be addressed in the future:

- investigation of the relationship between the degree of esterification of pectin, viscosity of pectin solutions and mesoporosity of the resulting aerogels;
- investigation of the macroporosity, to better understand the structure of aerogels as a function of TBA concentration;
- investigation into additives to control crystal growth of solvents for porosity tailoring;
- optimization of the procedure for closed loop solvent reuse;
- carbonization of aerogels to produce Starbons.

Chapter 6

Pectin aerogel pyrolysis: product characterisation and application

6.1 Introduction

The class of carbonaceous mesoporous materials known as pecbons, generated through controlled pyrolysis of pectin aerogels, is the third member of the Starbon family, along with starch and alginic acid-derived materials. The preparation and characterisation of pecbons were first reported by White et al.[27] In their work, pectin aerogel was prepared by the well established route of aqueous expansion followed by solvent exchange and $scCO_2$ drying.[101,103]

In the present work, expanded pectin (pectin aerogel) was obtained by a novel freeze drying route, discussed in Chapter 5. The simplicity and efficiency of this route renders it attractive for larger scale Starbon production. However, freeze dried polysaccharide aerogels differ to those prepared by conventional $scCO_2$ drying in porous structure and presence of TBA. It is, therefore, important to address these differences and their impact on the properties of the carbonised materials.

Moreover, it is also important to understand the process of pyrolysis in pectin aerogels and its impact on the chemical and textural properties of pecbons. A number of reports of pectin carbonisation are available in the literature. For instance, Sharma et al. have previously reported pyrolysis of pectin, and associated chemical and structural change, in the context of biochar production.[127] Fisher et al. investigated pyrolysis behaviour of pectin at temperatures above 400 °C.[47]

Applications of pecbons have not been previously explored. Adsorption of the dyes methylene blue (MB) and acid blue 92 (AB) on starch and alginic acid Starbons have previously been reported, hence, these adsorbates were deemed to be a suitable starting point in the exploration of pecbon's adsorption performance. This approach also allows for direct comparison of adsorption performance across all three Starbon types.

6.2 Aims

The aims of the present chapter were as follows:

- to study the pectin aerogel pyrolysis process with TG-IR to identify decomposition events and pyrolysis gas composition;
- to analyse the chemical structure and the surface chemistry of pecbons obtained at temperatures from 25–800 °C, using FT-IR, Raman, and pH drift;

- to characterise the textural properties of pecbons with N_2 adsorption/desorption porosimetry, SEM and transmission electron microscopy (TEM);
- to apply pecbons prepared at 300, 400 and 800 °C (Pec300, Pec400, Pec800) in adsorption of MB and AB;
- to propose an adsorption mechanism of MB and AB on pecbon by analysing the adsorption kinetics, adsorption isotherms and desorption;
- to compare MB and AB adsorption data on all three types of Starbon materials (starch-, alginic acid- and pectin-derived).

6.3 Results and Discussion

6.3.1 Thermogravimetric analysis

The pyrolysis of pectin aerogels changes their physical and chemical properties, as is evident in the change in the materials' appearance (Figure 6.1). **TG!** (**TG!**) was used to study the thermal degradation of pectin aerogel (Pec0) and original, non-expanded pectin. In Figure 6.2, the TG profiles of both materials are shown.

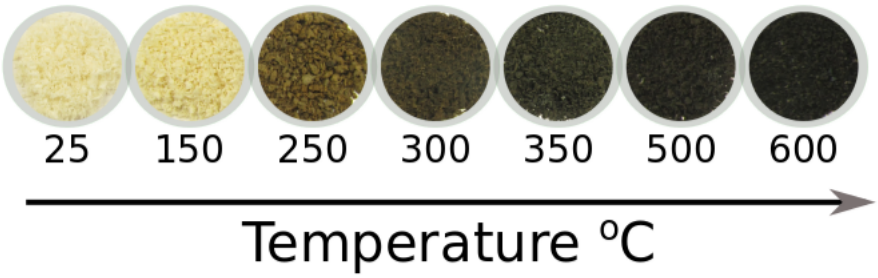

Figure 6.1: Image showing change in the appearance of pectin aerogel with temperature

The TG profile of Pec0 shows two mass loss maxima (Figure 6.2). The first loss of 10.4±2.8 % (n=2), at 80–120 °C, is attributed to physisorbed water and TBA, as confirmed by the IR analysis of the evolved gases (Figure 6.3). The second mass loss of 46.5±0.9 %, at 235±1 °C, coincides with the evolution of a complex gas mixture, containing water, alcohols, carbonyl compounds and CO_2 (Figure 6.3), indicating thermal decomposition. The mass loss plateaus around 600 °C, and the yield of pecbon at 800 °C (Pec800) is 23.5±1.5 %.

A difference was observed in the position of the degradation peak between Pec0 (235±1 °C) and the original pectin (227±0.75 °C) (Figure 6.1). This suggests that pectin undergoes structural changes during the gelation and freeze drying processes. Einhorn-Stoll and Kunzek have previously demonstrated that stronger interactions within the polymer network due to gelation delay the onset of degradation.[128] White et al. have previously reported a similar shift in the degradation temperature between non-expanded pectin and pectin aerogel prepared by the conventional scCO_2 method.[27]

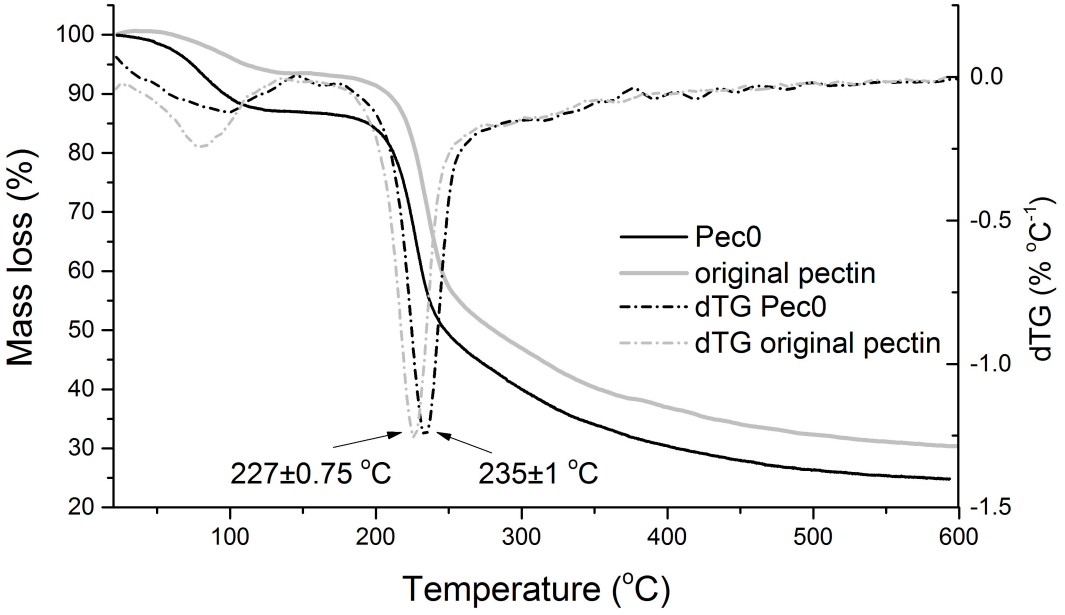

Figure 6.2: TG profiles of Pec0 and original pectin in inert atmosphere (10 °C min^{-1}, N_2) and the first derivative of TG signals

6.3.2 IR analysis of pyrolysis gas

The TG pyrolysis gases were analysed by in-line IR spectroscopy in order to investigate the mechanism of pectin pyrolysis. The IR spectra of the gas produced at different temperatures are shown in Figure 6.3. The spectrum from 100 °C shows the presence of water (broad 3980–3500 cm^{-1}, 1990-1300 cm^{-1}) and TBA (2979, 1211, 1140, 916 cm^{-1}) in the pyrolysis gas (reference IR spectra are shown in Appendix D, Figure D.1 and D.2, respectively). This corresponds to the first mass loss identified with TG at 80–120 °C. TBA was not detected in the original non-expanded pectin, and, therefore, its presence in the aerogel is due to its association with galacturonic acid methyl esters during aerogel preparation.[37]

Between 190–360 °C, the identified components of the pyrolysis gas are CO_2 (2362, 665 cm^{-1}), water, methanol (1036, 2982 cm^{-1}), CO (2177, 2100 cm^{-1}) and carbonyl-containing compounds (1796, 1716 cm^{-1}). The standard IR spectra for these compounds are given in Appendix D.7. Based on their peak positions, the carbonyl signals may arise from acetic acid (1795 cm^{-1}) at 130–200 °C and furfural (1716 cm^{-1}) at 250–360 °C.

Above 400 °C, the composition of the pyrolysis gas changes. The observed components are CO_2, CO and methane (3016, 1303 cm^{-1}). This change in the evolved gas and

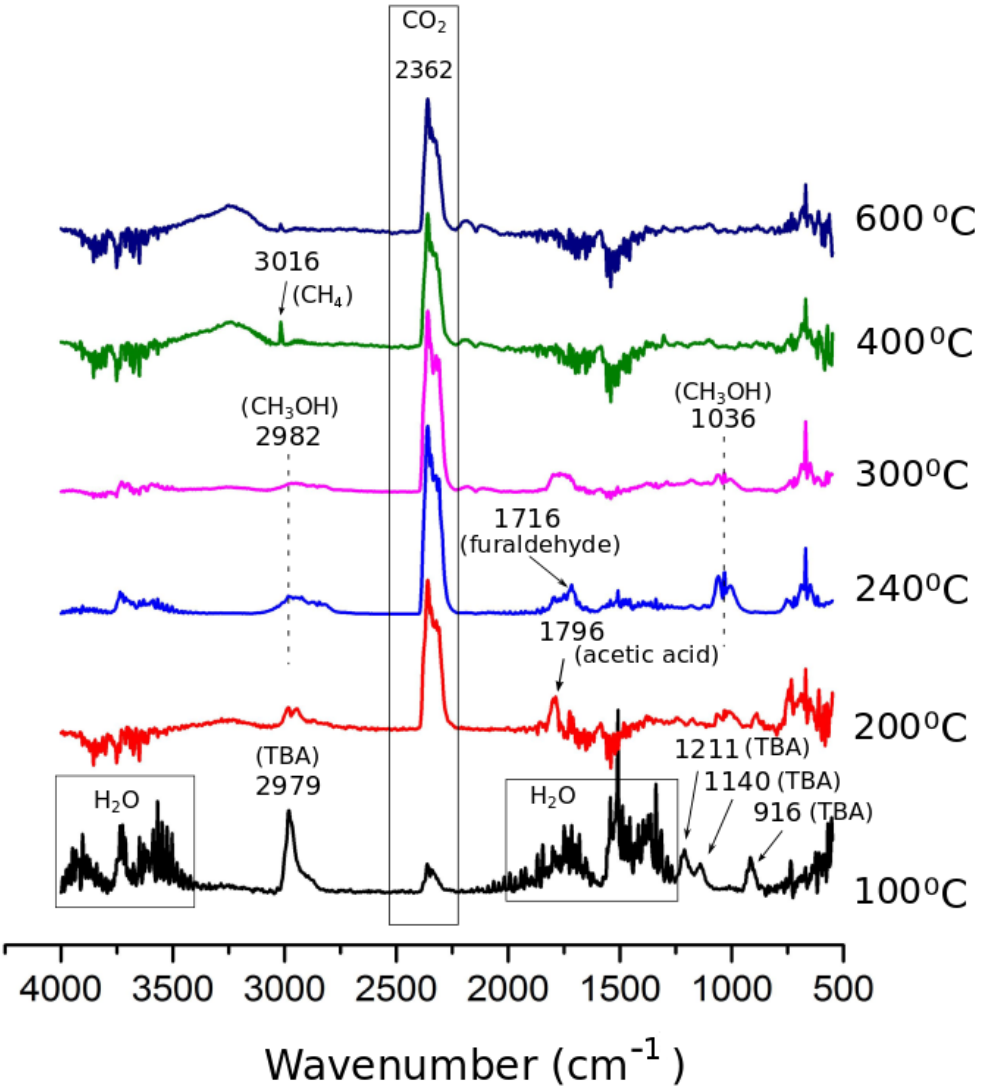

Figure 6.3: **A.** IR spectra of evolving gases of pectin aerogel pyrolysis over 50–800 °C temperature range. **B.** IR spectra of segments

the negligible mass loss indicate that the pyrolysis mechanism is different at these temperatures. The oxygen-poor composition of the gas and the formation of CO indicate that the oxygen content of the aerogel has declined considerably. Fisher et al. have previously observed a similar change in the degradation pathway, which has been referred to as secondary pyrolysis.[47]

6.3.3 FT-IR of pecbons

The solid product from thermal decomposition of pectin aerogels at different temperatures have been systematically analysed, in addition to the pyrolysis gas. The thermally-induced changes in the surface chemistry were investigated by FT-IR at 50 °C intervals. The obtained IR spectra were processed into a 2D map, shown in Figure 6.4, demonstrating the evolution of the surface chemistry with temperature. Above 600 °C, the material becomes electrically conductive and reflects the electromagnetic radiation.[51] As a result, the IR spectra become uninformative, and are not shown.

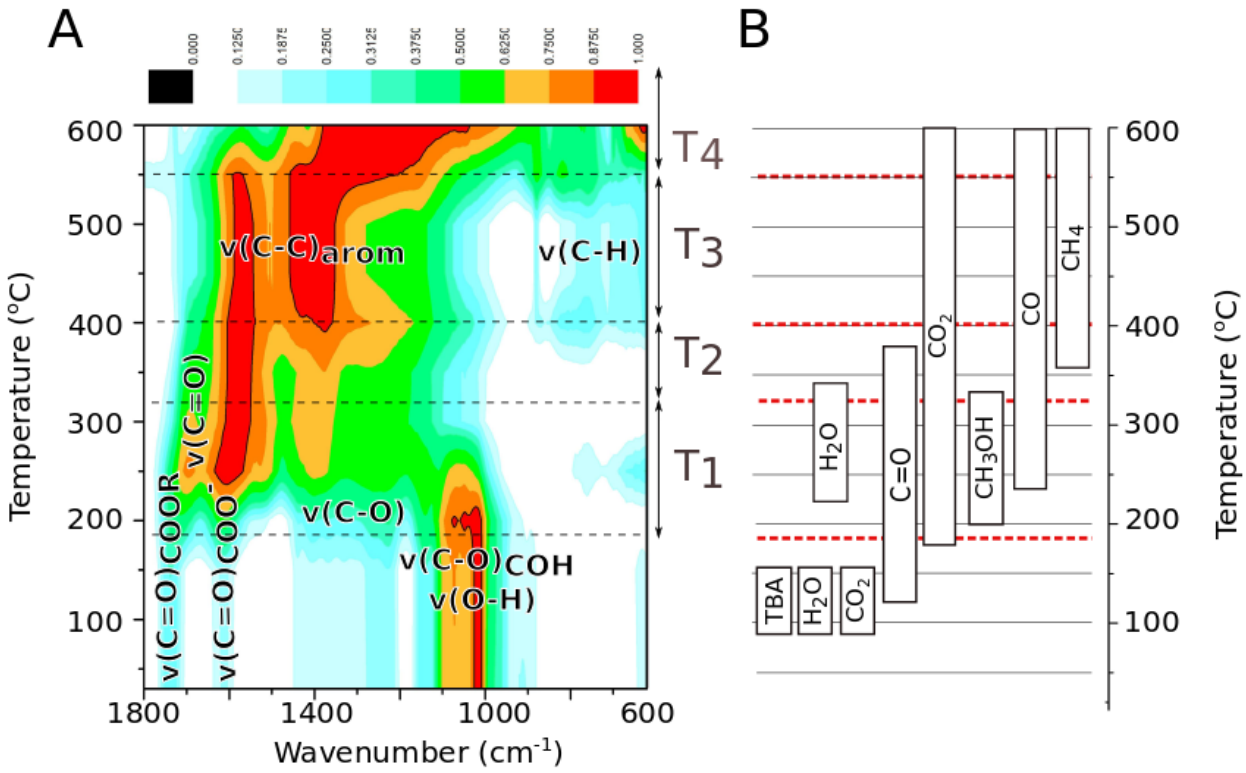

Figure 6.4: **A.** 2D FT-IR spectra of pecbon surface change with temperature. **B.** Corresponding volatile compounds detected with TG-IR

The temperature interval of 50–600 °C was broken down into smaller intervals de-

noted as T_1 (190–320 °C), T_2 (320–400 °C), T_3 (400–550 °C), and T_4 (> 550 °C). These intervals correspond to the major chemical changes in the structure. The FT-IR data was complemented by the composition of the pyrolysis gas (Figure 6.4.B).

T_1, 190–320 °C

Characteristic pectin backbone vibrations (1200–900 cm^{-1}) and carbonyl groups of galacturonic acid (-COOH, -$COOCH_3$ at 1740 cm^{-1}, -COO^- at 1610 cm^{-1}) disappear at ≈235 °C. This degradation correlates with the water release, and is a result of decomposition of monosaccharide fragments.[45] This is a common thermal degradation mechanism in polysaccharides.[45] The bands at 1690 cm^{-1} and 1300-1000 cm^{-1} arise from conjugated carbonyls and C-O functionalities respectively, which are produced by extensive dehydration and decarboxylation of the pectin structure. The presence of furfural, detected with TG-IR, is attributed to the decomposition of galacturonic acid.[45]

The decrease in the intensity of the 1740 cm^{-1} band, arising from galacturonic acid methyl ester, is accompanied by the release of methanol. This decomposition is complete by 330 °C.

T_2 320–400 °C

In this temperature region, the band due to conjugated carbonyl functionalities at 1690 cm^{-1} is rapidly decreasing in intensity, due to ongoing decarboxylation, which is substantiated by the CO_2 release seen in the TG-IR data. Concurrently, water, methanol and furfural concentrations in the gas diminish, and are not observed above 400 °C. The rate of mass loss significantly decreases, and the chemical structure undergoes internal rearrangements leading to the onset of aromatic conjugation, as evident from the formation of $\nu(C\text{-}C)_{arom}$ bands at 1570 and 1400 cm^{-1}.

T_3 400–550 °C

The onset of methane release coincides with the development of extended aromaticity, accompanied by negligible mass loss. The release of methane marks the onset of secondary pyrolysis.[47]

T_4 >550 °C

Above 600 °C, the material becomes electrically conductive and reflects the electromagnetic radiation.[51] As a result, the IR spectra become uninformative.

6.3.4 Raman spectroscopy

The long-range aromatic conjugation in higher temperature pecbons was investigated with Raman spectroscopy. In Figure 6.5.A, Raman spectra of Pec800 and char pyrolysed from original pectin at 800 °C are shown. The band assignments and origins used here were introduced in more detail in the previous discussion of alginic acid-derived Starbons (Chapter 2, Section 2.3.3).

The Raman spectra of Pec800 and pectin char feature characteristic D (disorder) and G (graphitic) bands, which are the hallmark of graphitic materials with short-range polycrystallinity.[52] In the second order Raman spectra of carbon materials (over 2500 cm^{-1}), the poorly defined band at 2844 cm^{-1} is also characteristic of poorly ordered graphitic material.[52] The D and G bands were fitted with four Gaussian peaks (Figure 6.5.B) to identify their peak parameters. Integrated peak intensities, and the calculated degree of disorder in the graphitic structure, are shown in Table 6.1.

Table 6.1: D and G band parameters identified with Gaussian peak fitting and the degree of disorder (DD) of Pec800 and non-porous pectin-derived char

	D band		G band		
	Area (I)	**Width**	**Area (I)**	**Width**	**DD (%)**
	[a.u.]	[a.u.]	[a.u.]	[a.u.]	ID/(ID+IG)
char	403106 ± 12701	149 ± 3	93064 ± 5580	59 ± 1	81.0
Pec800	447526 ± 10878	123 ± 1	145555 ± 4795	55 ± 1	75.5

According to the Raman data, the degree of disorder is greater in pectin char (81.2 %) than in Pec800 (75.5 %). This finding could be rationalised by assuming that the gelation process results in a more ordered structure within the polymer strands, and, when carbonised, these ordered segments remain in proximity, leading to a more ordered turbostratic arrangement in pecbon.

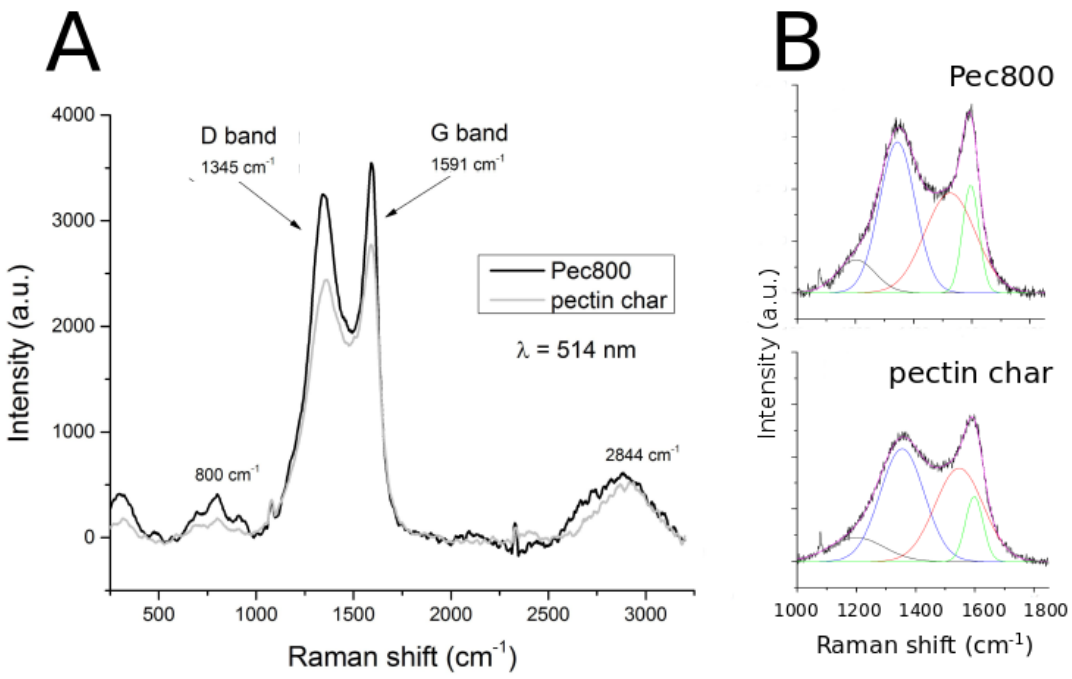

Figure 6.5: **A.** Raman spectra of Pec800 and char derived from non-porous pectin at 800 °C (λ=514 nm) **B.** Raman spectra of Pec800 and char derived from non-porous pectin fitted with four Gaussian peaks

Rouzaud et al. have previously demonstrated with carbon films that an increase in the number of stacked layers leads to an increase in the resolution of the D and G bands.[129] The same effect could be responsible for the difference in the Raman spectra between pecbon and char. Alginic acid-derived Starbons have also demonstrated a similar trend in degree of disorder, as discussed in Section 2.3.3. It appears that carbonized polysaccharide aerogels are more ordered than their non-porous counterparts. This is an interesting finding; however, it requires more investigation with analytical techniques complementary to Raman, such as XRD or XPS.

Van Krevelen diagram of pecbons

The change in the elemental composition (C, H, O) of pecbons with temperature is another important aspect of the pyrolysis process. A van Krevelen diagram, introduced in Section 2.3.2 (Chapter 2) is a common tool used to classify carbonaceous materials according to their CHO composition. The van Krevelen diagram of pecbons is shown in Figure 6.6. The arrows indicate the general direction of the O:C and H:C shifts arising due to dehydration, decarboxylation, and demethylation.

At the onset of heating, the elemental composition of pectin aerogel changes due to dehydration. At 250 °C, a shift towards the decarboxylation direction is observed, due to the onset of thermal degradation of the polysaccharide. Between 250 and 400 °C, the degradation mechanism includes a combination of dehydration and decarboxylation. From 600 °C, the thermal degradation occurs in the demethylation direction. All of these processes, visualized with the van Krevelen diagram, are in agreement with the TG-IR and FT-IR data reported above.

The elemental compositions of pecbons at different temperatures are comparable to the general van Krevelen classes of biomass, chars and coals. For instance, expanded pectin is similar to wheat.[130] In Pec150–Pec200, the hydrogen and carbon indices are comparable to peat.[131] At 250-350 °C, the pecbons' elemental composition is close to coal. Finally, Pec600 and Pec800 are similar to stone coal and anthracene, respectively.[49,132] A number of other literature reports on pyrolysis of biomass also suggest a relationship between CHO and pyrolysis temperature.[50]

During pyrolysis, a wide range of biomass undergoes a change from its native oxygen-rich structure to graphitic biochar.[50] The thermal transitions reported in the present study for pecbon were previously observed in starch and alginic acid aerogels.[38] Keiluweit et al. attempted to generalize the thermal transformations in wood

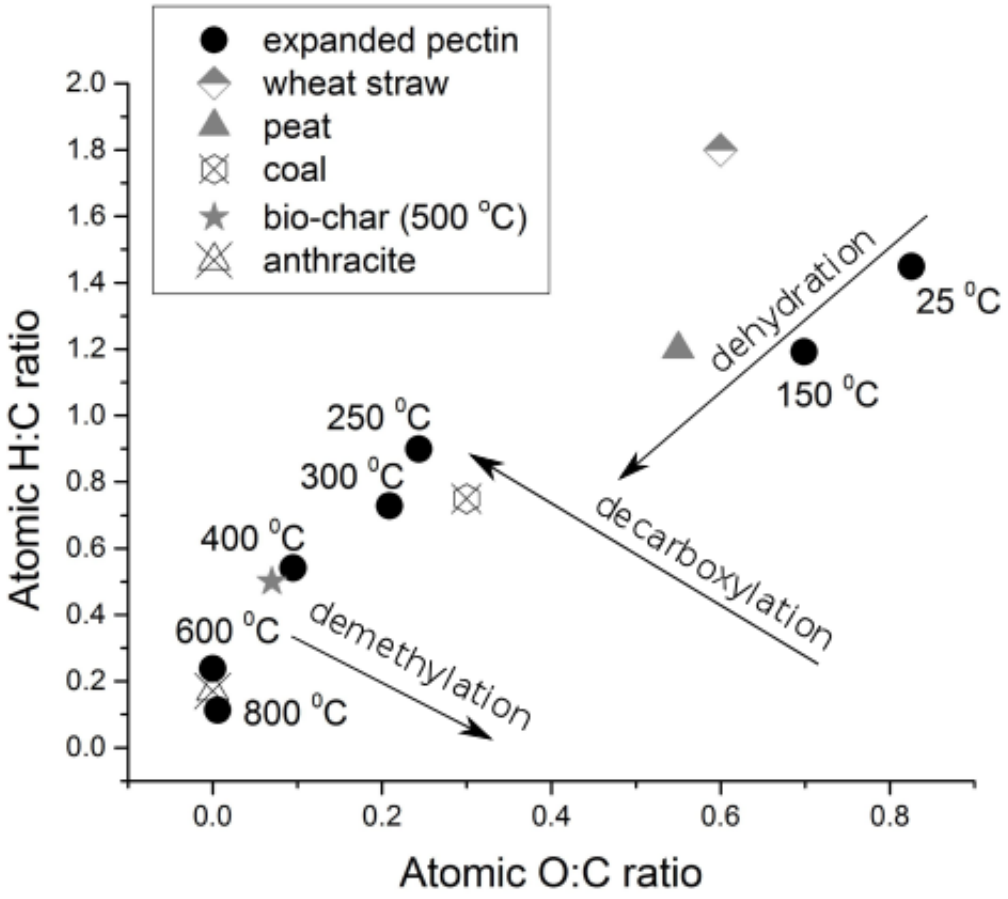

Figure 6.6: Van Krevelen diagram of pecbons and a number of other carbon-based materials (values references are shown in text)

and grass-derived biochars, and identified transitions analogous to the T_1–T_2 transitions in Figure 6.4.A.[133] They referred to the structures as transition char, amorphous char, composite char, and turbostratic char.

A number of other independent reports have found a similarity of the thermal degradation pathways in biomass regardless of its origin. The similar positions on the van Krevelen diagram observed for biochars derived from different biomass at the same temperatures indicate a link between temperature and decomposition mechanisms.[50] Overall, all of these facts point to a common underlying thermal degradation process in all biomass.

6.3.5 Textural properties of pecbons

Carbonisation of pectin aerogel was carried out at different rates to find the optimal conditions for mesoporosity preservation. The textural properties (surface area, pore volume and pore diameter) of the resulting pecbons are tabulated in Table 6.2. The optimum heating rate in the present work was 0.5 °C min^{-1}, preserving over 98 % of the original pore volume.

Rapid heating rates were found to lead to loss of mesoporosity and an increase in microporosity, due to structural shrinking or collapse. This is also evident from the decreasing average pore diameter. At fast heating rates, thermal degradation is rapid and structural stability is lost due to bonds breaking, e.g. depolymerisation of the polysaccharide backbone, and the structure does not have time to rearrange to form new bonds. Melting of pectin around the decomposition temperature has previously been reported.[127] Moreover, the extent of melting, accompanied by formation of bubbles, increases with heating rate, and even cellulose, which does not melt under normal conditions, was shown to melt when heated at a rate of >100 °C sec^{-1}.[47]

Table 6.2: Influence of carbonisation rate on the textural properties of Pec300 determined with N_2 porosimetry

Rate [°C min^{-1}]	SA_{BET} [m^2 g^{-1}]	PV_{total} [cm^3 g^{-1}]	PV_{micro} [cm^3 g^{-1}]	PD [nm]
0	148	1.23	0.02	25
0.5	160	1.21	0.03	24
1	140	0.98	0.04	23
2	96	0.67	0.03	21
3	61	0.44	0.27	19

Textural properties (surface area, pore volume and average pore diameter) of pecbons, prepared at 25–800 °C, are tabulated in Table 6.3. The BET surface area values range from 227.0 to 118.8 m^2 g^{-1}, and the pore volume undergoes a decline from 1.2 cm^3 g^{-1} to 0.5 cm^3 g^{-1}. A comparable decline in the pore volume was previously reported by

White et al.[27]

Table 6.3: Change in textural properties with carbonization temperature

Material	T	SA_{BET}	PV_{total}	PV_{meso}	PV_{micro}	PD
	[°C]	[$m^2\ g^{-1}$]	[$cm^3\ g^{-1}$]	[$cm^3\ g^{-1}$]	[$cm^3\ g^{-1}$]	[nm]
Pec0	25	148.2	1.23	1.22	0.02	25.0
Pec150	150	152.0	1.24	1.22	0.02	24.7
Pec200	200	118.8	1.03	1.01	0.02	24.6
Pec250	250	157.1	1.30	1.28	0.03	26.2
Pec300	300	160.1	1.21	1.19	0.03	23.6
Pec350	350	143.9	0.80	0.77	0.03	18.3
Pec450	450	154.9	0.80	0.77	0.03	18.1
Pec500	500	227.0	1.12	1.07	0.05	21.3
Pec650	650	138.5	0.56	0.53	0.03	15.7
Pec800	800	173.6	0.49	0.44	0.05	14.1

The mesoporous nature of pecbons was confirmed using N_2 adsorption/desorption isotherms, shown in Figure 6.7.A, and it is maintained across the entire temperature range. The isotherms are type IV in the BDDT classification, which is characteristic of mesoporous materials, with H1 type hysteresis loops. The decline in pore volume with temperature is attributed to a progressive decline in average pore size (Figure 6.7.B) from 25 to 14 nm. There is a negligible increase in microporosity with temperature from 0.02 $cm^3\ g^{-1}$ in Pec0 to 0.05 $cm^3\ g^{-1}$ in Pec800.

6.3.6 SEM and TEM

The texture of pecbon aerogels was investigated using SEM and TEM (Figure 6.8). The SEM images demonstrate surface roughness, and disappearance of observable macroporosity inherent to the original aerogel, shown in Figure 5.9. In the TEM images of

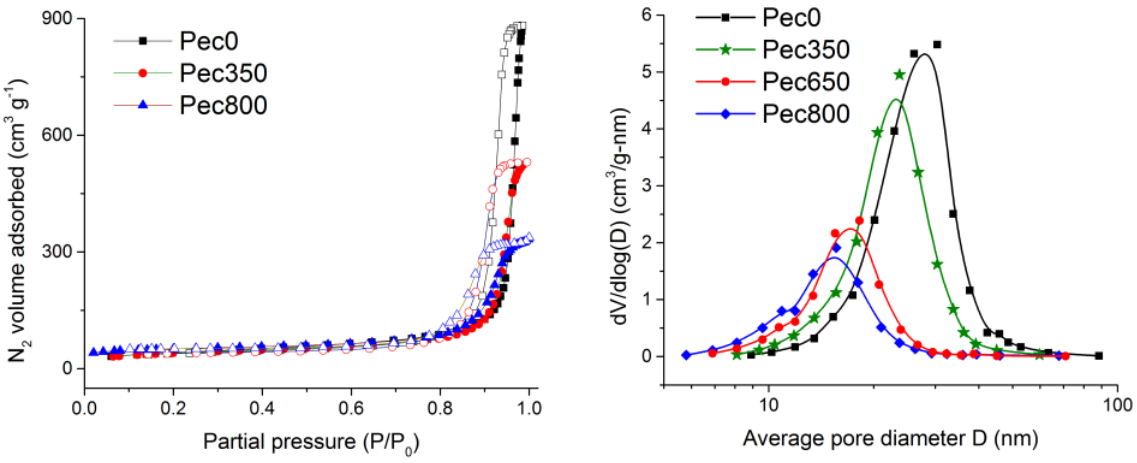

Figure 6.7: **A.** N_2 adsorption (filled symbols)/desorption (empty symbols) isotherms of Pec0, Pec350 and Pec800 (only three materials are shown for image clarity). **B.** BJH desorption pore volume distributions in Pec 0, Pec350, Pec650 and Pec800

Pec300, Pec400 and Pec800, the fibrous structure of the materials is seen, and the shrinking of the fibres with temperature is also evident. White et al. have previously demonstrated similar structural features in expanded pectin-derived Starbons.[27]

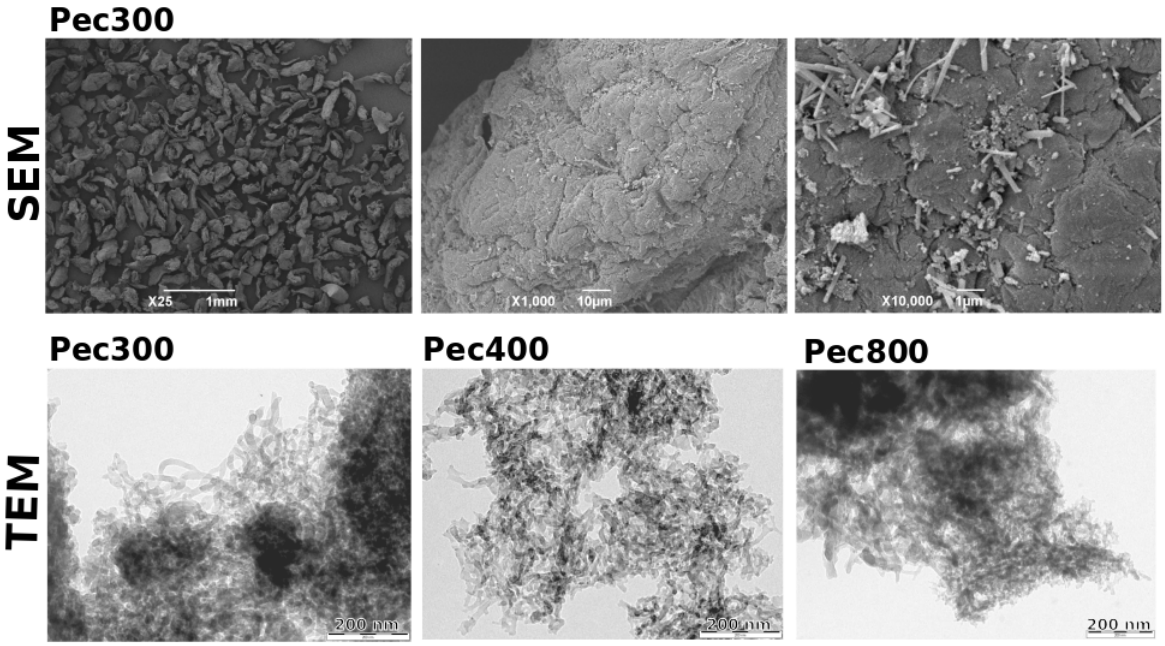

Figure 6.8: SEM images of Pec300 at x25, x1,000 and x10,000 magnification. TEM images of Pec300, Pec400 and Pec800 (bar is 200 nm)

6.3.7 Surface charge and pH_{pzc}

Pec300, Pec400 and Pec800 pecbons were subjected to pH drift analysis to identify the pH at which the overall surface charge is zero, pH_{pzc}. The underlying principle of the pH drift method is discussed in Section 2.3.5. In Figure 6.9, the pH drift curves and pH_{pzc} values for each material are shown.

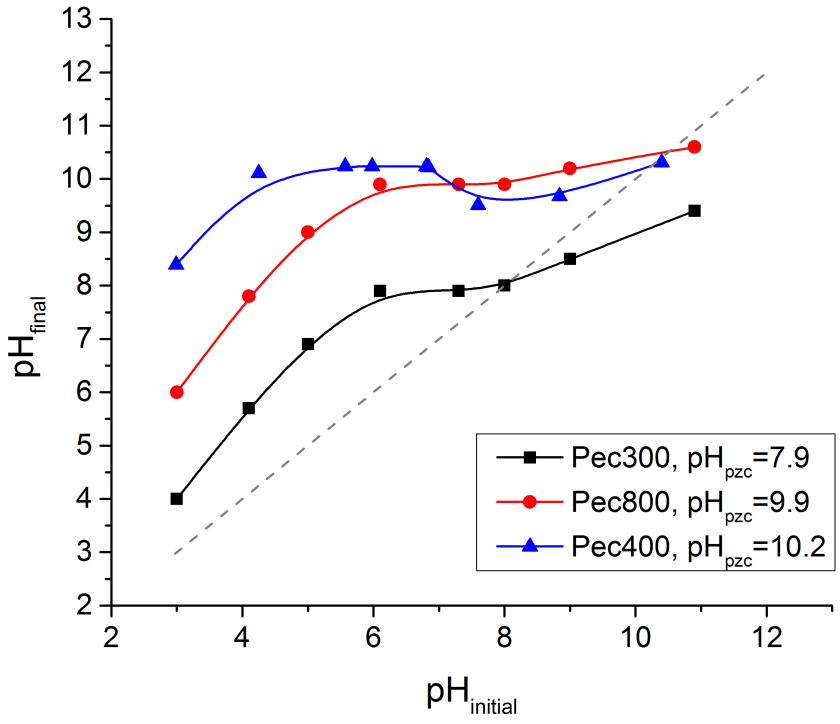

Figure 6.9: Point of zero charge (pH_{pzc}) determination of Pec300, Pec400, and Pec800 determined with pH drift method

The order of basicity is Pec300<Pec400<Pec800, which follows the same trend as alginic acid-derived Starbons (Section 2.3.5): the greater the pyrolysis temperature, the higher the pH_{pzc}. However, pecbons show higher basicity compared to other Starbons. For example, S300 has pH_{pzc} of 4.3 and A300 pH_{pzc} is 5.4, whereas Pec300 showed a pH_{pzc} of 9.9. This could be a result of the higher ash content present in pectin. Surface charge is an important parameter in the chemical and physical events taking place on the surface.

6.3.8 Adsorptions of methylene blue and acid blue 92 on pecbons

Three pecbons, Pec300, Pec400 and Pec800 were applied to the adsorption of dyes. The structures of the dyes, methylene blue (MB) and acid blue 92 (AB), are shown in Figure 6.10. The selection of pecbons covers a broad range of available surface functionalities, as demonstrated with FT-IR. Therefore, the adsorption data should provide an insight into the role of surface chemistry in the adsorption of these dyes on pecbon. The textural properties of the adsorbents are shown in Table 6.4.

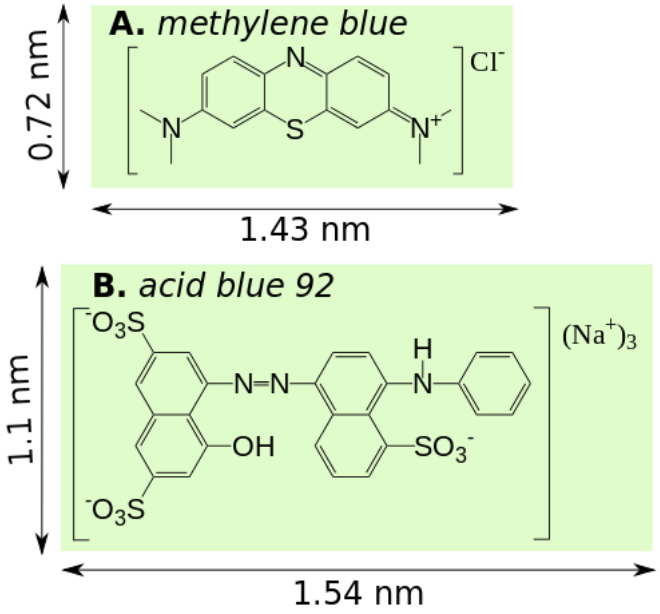

Figure 6.10: Chemical structures of **A.** methylene blue (MB) and **B.** acid blue 92 (AB). Dimentions shown were calculated with HyperChem software

Adsorption equilibrium was achieved after 35 h for adsorption of MB, and 25 h for adsorption of AB (Figure 6.11). Adsorption isotherms were fitted with the Langmuir model, described in Section 3.3.4 (Figure 6.12), and the isotherm parameters are tabulated in Table 6.5. Desorption of the dyes was investigated on a solid-phase extraction manifold with ethanol as an eluting solvent. The percentage desorption is shown in Table 6.6, where 100 % represents the total amount of material adsorbed under experimental conditions.

The order of adsorption capacity (q_{max}, determined using the Langmuir model) for MB is Pec300$\gg$Pec400>Pec800, and it does not correlate with the BET surface area, nor the pore volume of the adsorbents. Therefore, the trend in adsorption capacity was linked to the chemical nature of MB and the surface functionalities of the pecbon. MB

Table 6.4: Textural properties of pecbons Pec300, Pec400, and Pec800 used in MB and AB adsorption

Material	SA_{BET}	PV_{total}	PV_{meso}	PV_{micro}	PD
	[$m^2\ g^{-1}$]	[$cm^3\ g^{-1}$]	[$cm^3\ g^{-1}$]	[$cm^3\ g^{-1}$]	[nm]
Pec300	160.1	1.21	1.19	0.03	23.6
Pec400	262.6	1.49	1.42	0.07	26.9
Pec800	173.6	0.49	0.44	0.05	14.1

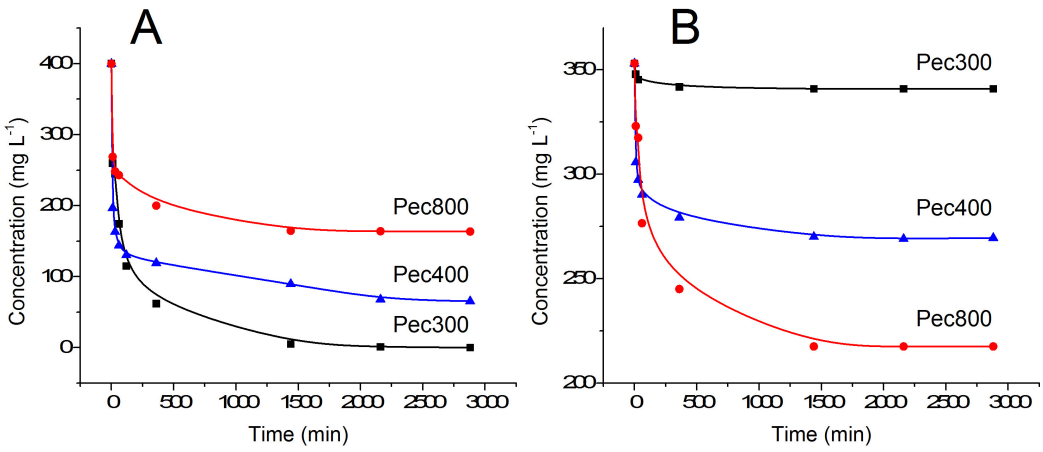

Figure 6.11: **A.** Adsorption progress over time of **(A)** MB and **(B)** AB

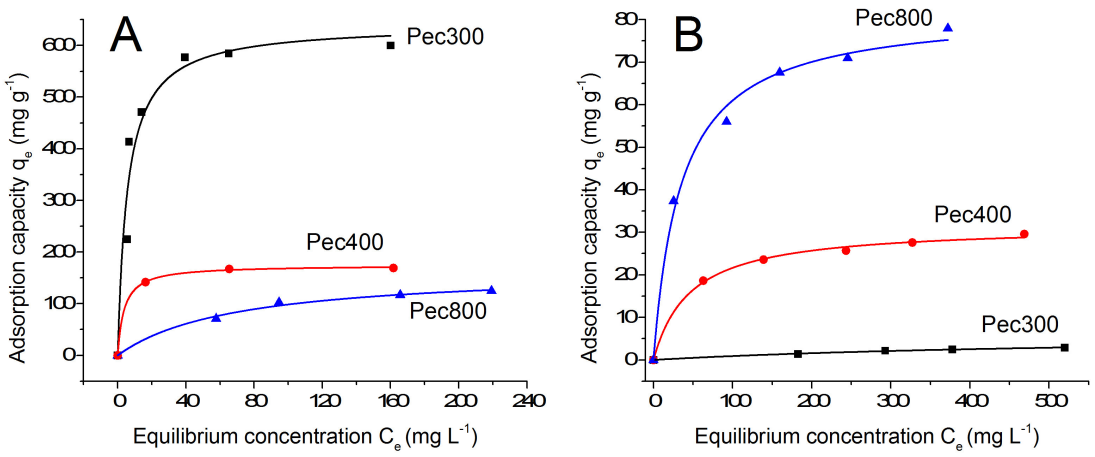

Figure 6.12: Adsorption isotherms of **(A)** MB and **(B)** AB on pecbons fitted with non-linear Langmuir model

Table 6.5: Langmiur isotherm parameters for adsorption of MB and AB on Pec300, Pec400, and Pec800 and theoretical surface area (SA_{MB} and SA_{AB}) occupied by adsorbed dyes

Methylene blue	q_{max} [mg g^{-1}]	K [mg L^{-1}]	R	SA_{MB} [m^2 g^{-1}]
P300	641.0 ± 41.2	0.174 ± 0.049	0.944	1243.1 ± 79.9
P400	174.6 ± 1.8	0.270 ± 0.027	0.999	338.7 ± 3.4
P800	166.4 ± 12.2	0.015 ± 0.003	0.992	322.7 ± 23.7
Acid Blue 92	q_{max} [mg g^{-1}]	K [mg L^{-1}]	R	SA_{AB} [m^2 g^{-1}]
Pec300	6.2 ± 1.0	0.002 ± 0.000	0.977	9.1 ± 1.5
Pec400	31.6 ± 0.7	0.022 ± 0.002	0.997	46.4 ± 1.1
Pec800	82.3 ± 2.8	0.029 ± 0.005	0.991	120.7 ± 4.1

Table 6.6: Percentage desorption of MB and AB with ethanol from Pec300, Pec400, and Pec800

	Pec300 (%)	Pec400 (%)	Pec800 (%)
MB	0	79	85
AB	0	0	14

is a cationic dye, and it interacts readily with electron-rich moieties, e.g. carboxylate, carbonyl, and hydroxyl groups. According to the FT-IR (Figure 6.4.B) and elemental composition (Figure 6.6) of the pecbons, Pec300 has more carbonyl functionalities and twice the atomic O/C ratio of Pec400. Pec800 has negligible oxygen content. The important role of these functionalities is evident in the dramatic drop in adsorption capacity between Pec300 and Pec400, 641.0$\pm$41.2 and 174.6$\pm$1.8 mg g^{-1}, respectively.

In the desorption study, Pec300 fully retained MB, whereas high desorption rates of MB from Pec400 (79 %) and Pec800 (85 %) were achieved. These results indicate strong, irreversible adsorption of MB on Pec300, and weaker, reversible adsorption on Pec400 and Pec800.

Interestingly, the surface coverage of MB on pecbons exceeds the N_2 BET surface area by 7.8 times for Pec300, 1.3 times for Pec400 and 1.9 times for Pec800 (Table 6.5). Two separate adsorption mechanisms are proposed to explain this observation. In aqueous solution, MB forms a face-to-face dimer.[134] In Pec800, the aromatic MB dimer adsorbs via $\pi - \pi$ interactions with the surface, due to the graphitic character of the material, as demonstrated by Raman spectroscopy. However, in Pec300, oxygen-containing functional groups act as adsorption sites for edge-to-face adsorption of the MB dimer, thus accommodating a higher number of MB molecules. The proposed adsorption mechanisms of MB on Pec300 and Pec800 are schematically shown in Figure 6.13.

The chemical nature of Pec400 is in transition between Pec300 and Pec800. The surface functionality of Pec400 has significantly less oxygen-containing groups and thermally induced aromatic conjugation is underdeveloped, leading to lower adsorption capacity per unit of surface compared to Pec300 and Pec800.

The adsorption capacity for AB is in the reverse order to MB, Pec800>Pec400> Pec300. AB is an anionic molecule, and it is repelled by the negatively charged surface of Pec300, resulting in an adsorption capacity of only 6.2$\pm$0.1 mg g^{-1}. The adsorp-

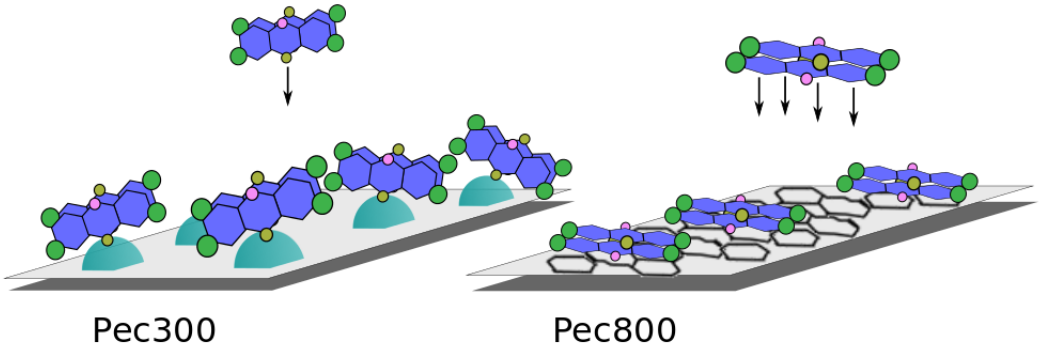

Figure 6.13: Possible adsorption mechanisms of MB on Pec300 and Pec800

tion capacity increases with increasing aromatic character of the materials, with Pec400 adsorbing 31.6±0.7 mg g^{-1} and Pec800 adsorbing 82.3±2.8 mg g^{-1}.

Some desorption of AB was achieved from Pec800 (14 %), indicating weaker interaction, whereas Pec300 and Pec400 have retained all the adsorbed AB. In Pec800, AB is likely to be adsorbed through $\pi - \pi$ interactions. Incomplete surface coverage (73 % of BET surface area) could be a result of surface curvature due to 5-membered rings in the graphitic structure of Pec800, as reported by Marriott et al., and the relatively large size of the planar AB molecule.[59]

It is evident that the adsorption mechanism of AB is also different across pecbons, and experimental data suggests similarities to the mechanism proposed for MB (Figure 6.13). In Pec300, the moieties with low electron densities, i.e. α,β-unsaturated groups, could act as adsorption sites. In Pec400, the number of α,β-unsaturated moieties increases, leading to greater adsorption capacity. In Pec800, the adsorption mechanism changes to weaker $\pi - \pi$ interactions, enabling some desorption.

Overall, the adsorption investigation demonstrated that the surface chemistry plays a crucial role in the capacity and strength of the adsorption of MB and AB on pecbons. Textural properties, i.e. BET surface area and pore volume, do not correlate with adsorption parameters. More importantly, the data demonstrate the power of thermal treatment to tailor pecbon properties for various applications.

Moreover, the different relative strengths of adsorption on Pec300 and Pec800 allows for the selection of the most appropriate materials for different applications, e.g. solid-phase extraction (SPE) with recovery or adsorption for complete removal. The selectivity of Pec300 for MB over AB could extend to other similar molecules for applications in

separation.

Finally, Pec300 demonstrated a very high adsorption capacity for MB, and, to the author's knowledge, it is one of the greatest MB adsorption capacities reported for carbonaceous materials. Some of the recent reports are tabulated in Table 6.7.

Table 6.7: Comparison of a number of previously reported adsorption capacities of carbonaceous materials for MB

Material	q_{max} [mg g^{-1}]	Reference
Pectin-derived Starbon Pec400	174	Present work
Alginic acid-derived Starbon A300	186	Parker *et al.*[44]
Porous carbon derived from waste banana peel	385	Liu *et al.*[135]
Pectin-derived Starbon Pec300	641	Present work
Porous carbon derived from waste plastic	769	Gong *et al.*[136]

6.4 MB and AB adsorptions on three classes of Starbons

It is evident, from the literature and the present study, that all polysaccharide-derived Starbons undergo similar thermal transitions resulting in similar surface chemistry.[38] It follows that, in applications where surface chemistry plays a key role, Starbons produced at the same temperature would have similar performance. Adsorption of MB and AB on starch and alginic acid Starbons was previously investigated by Parker et al, reporting different adsorption performances between the materials.[44] Their data were complemented with pecbon adsorption data to identify the sources of the observed differences.

In Table 6.8, textural properties of adsorbents, point of zero charge pH_{pzc}, ash content, adsorption capacity for MB and AB, and adsorption capacity per m^2 of adsorbents are shown. The latter value is a normalized adsorption capacity per unit of BET surface, introduced to eliminate the differences due to surface area.

Table 6.8: Textural properties and adsorption capacities of Pec300, Pec400, Pec800, S300, S800, A300 and A800 for MB and AB (MB q_{max} and AB q_{max} are Langmuir adsorption capacities for MB and AB, q_{max}/SA_{MB} and q_{max}/SA_{AB} are a measure of how many mg of MB and AB are adsorbed per m^2 of adsorbent)

	SA_{BET}	PV_{meso}	PV_{micro}	PD	MB q_{max}	AB q_{max}	q_{max}/SA_{MB}	q_{max}/SA_{AB}	pH_{pzc}	Ash content
	$[m^2\ g^{-1}]$	$[cm^3\ g^{-1}]$	$[cm^3\ g^{-1}]$	[nm]	$[mg\ g^{-1}]$	$[mg\ g^{-1}]$	$[mg\ m^2]$	$[mg\ m^2]$	pH	%
Pec300	198	0.55	0.01	9.6	641.0	6.2	3.2	0.0	7.9	11.9
A300[44]	280	1.52	0.11	19.3	186.0	82.0	0.7	0.3	5.4	2.1
S300[44]	332	0.99	0.17	17.4	82.0	27.0	0.2	0.1	4.2	0.1
Pec400	263	1.49	0.07	26.9	174.6	31.6	0.7	0.1	10.2	14.2
Pec800	174	0.49	0.05	14.1	166.4	82.3	1.0	0.5	9.9	12.9
A800[44]	265	1.12	0.04	19.3	97.0	108.0	0.4	0.4	8.9	3.1
S800[44]	535	0.97	0.22	11.8	52.0	39.0	0.1	0.1	7.5	0.0

The general trend in adsorption capacity for MB and AB is the same across all materials, and the adsorption order for MB is 300>800, and AB 800>300. The cationic MB is more attracted to the oxygen-rich surface of 300 °C Starbons, whereas anionic AB is repelled by it. In 800 °C Starbons, π–π interaction with the graphitic surface is the main interaction mechanism.

However, Starbons prepared at the same temperature but from different precursors show significantly different adsorption capacities, and no strong correlation between textural properties and adsorption performance is evident, i.e. higher surface area materials do not show greater adsorption capacity (Table 6.8). This suggests the presence of another variable not investigated to date.

There is a correlation between a combination of parameters: adsorption capacity, preparation temperature, and pH_{pzc} (Figure 6.14). The 300 °C and 800 °C Starbons were grouped separately, due to the significant differences in their surface chemistries.

The pH_{pzc} is an indicator of the relative basicity or acidity of a material: the greater the value, the more basic the material. There is a direct correlation between pH_{pzc} and ash content within the 300 °C and 800 °C groups.

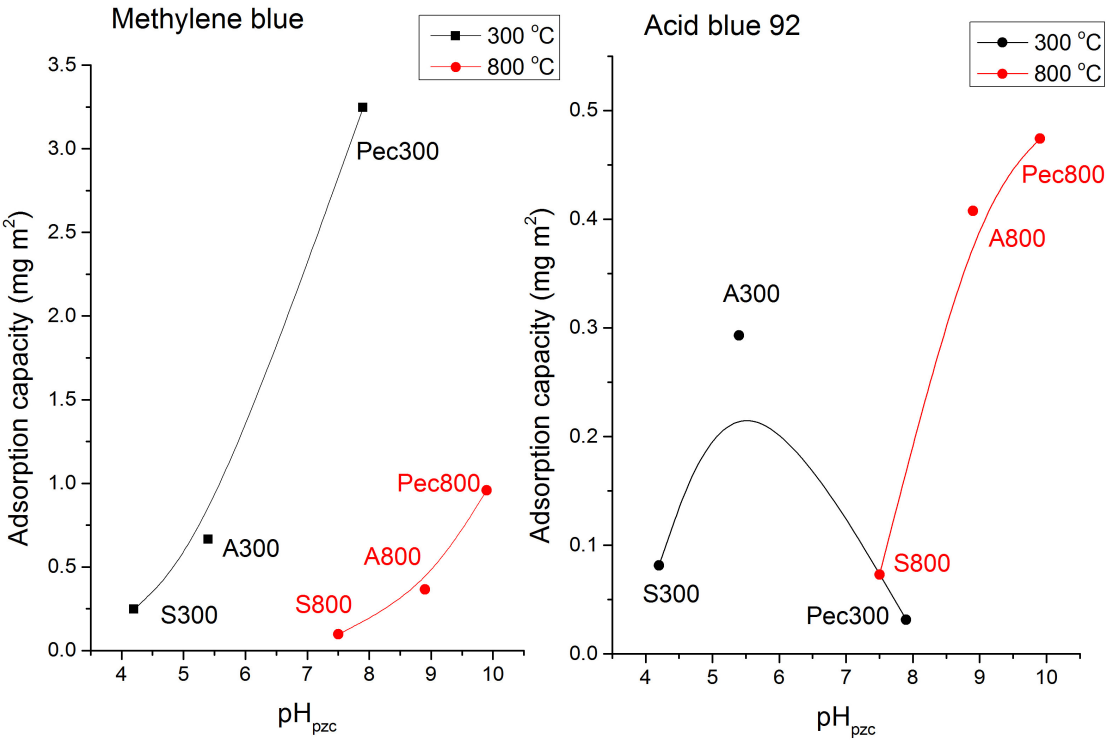

Figure 6.14: Relationship between pH_{pzc} and adsorption capacity of MB and AB per unit of surface area of various Starbons

It is expected that MB would adsorb more on a basic surface, as demonstrated in Figure 6.14. However, the reverse behaviour is expected for AB, which is not supported by experimental data. It is likely that ash, in combination with the surface functionality, affects the adsorption performance through ion-exchange mechanisms.[50] It is important to note, that ash alone does not influence adsorption capacity: there is no uniform trend between ash content and adsorption capacity. However, it could be concluded that ash content plays an important, but not exclusive role in surface phenomena in Starbons.

If ash content does indeed have such a dramatic impact on adsorption performance, then it requires attention as a variable in Starbon applications. Moreover, it would be an additional powerful tool in tailoring of material properties, along with temperature. Ahmad et al. have also concluded that ash content in biochars is an important parameter affecting ion exchange potential in adsorption applications.[50]

6.5 Conclusion

In this chapter, the carbonisation behaviour of freeze dried pectin aerogels was studied in detail. The goal was to compare the freeze drying route with the conventional $scCO_2$ drying route, in terms of their ability to yield aerogels suitable for preparation of Starbons. A number of conclusions were made:

- freeze drying does not have a significant impact on the thermal stability and carbonization behaviour of pecbons, despite the presence of TBA and greater degree of macroporosity in the structure;

- a correlation was established between the chemical properties of the pecbons Pec0-Pec800, their elemental composition, and the temperatures of thermal transitions. This correlation is similar to the analogous correlations discussed for alginic acid-derived aerogels in Chapter 2;

- the temperature-dependent surface functionality of pecbons is comparable to starch and alginic acid-derived Starbons;

- the carbon structure of pecbon Pec800 is more ordered than that of pectin-derived char carbonized at the same temperature, as demonstrated with Raman spectroscopy;

- the freeze dried aerogels were successfully carbonized to 800 °C yielding mesoporous pecbons, demonstrating the viability of the freeze drying route.

Adsorption of MB and AB on Pec300, Pec400 and Pec800 was investigated, which is another significant contribution towards understanding the potential of Starbons in adsorption applications. A number of interesting findings and observations were made:

- the trends in MB and AB adsorption on pecbons are comparable to starch and alginic acid-derived Starbons: cationic MB shows greater adsorption on oxygen-rich 300 °C materials, and anionic AB shows greater adsorption on graphitic 800 °C materials.

- different adsorption mechanisms were proposed to explain the experimental data, i.e. adsorption, desorption, surface coverage of the materials. This difference in adsorption mechanism could be utilized in pecbon applications, e.g. SPE, chromatography, and separations;

- Pec300 has the greatest adsorption capacity for MB in the Starbon family;

Overall, pecbon was demonstrated to have good adsorption performance, rendering the material a valuable addition to the Starbon family. The experimental data highlighted the magnitude of the influence that physical and chemical variables have on adsorption and desorption performance, e.g. surface chemistry and elemental composition. It is important to consider these variables in any application design.

6.6 Future work

It would be interesting to investigate whether the degree of esterification (DE) has a significant impact on the carbonisation behaviour of pectin aerogels and, as a result, on pecbon surface properties. DE can vary from 0 % to almost 100 %, depending on the pectin extraction and processing method used. For pecbon quality control, it is important to assess the effect of this variable.

More experimental investigation is needed to understand the influence of ash content on the surface chemistry and adsorption performance of pecbons. Materials with different ash contents should be prepared and tested in further MB adsorption experiments.

Chapter 7

Conclusions and Future Work

In the present study, the advances in characterisation, preparation and application of Starbons — mesoporous carbonaceous polysaccharide-derived materials — were presented and discussed. The aim of the project was to improve our understanding of the textural and chemical properties of these materials, and their roles in adsorption applications of different classes of organic environmental pollutants. Consideration was given to green aspects of the preparation and application of these materials, since the context of the work was the use of Starbons in environmental remediation of waste water and recovery of waste chemicals for potential reuse. A number of findings were made, which are of significant importance to the future research and applications of Starbons.

In **Chapter 2**, the thermal evolution of the chemical properties of expanded alginic acid was systematically investigated. The obtained data provides a comprehensive information on the properties of algibon at any given preparation temperature. The major thermal decomposition events identified are degradation at 211 °C, sp^2 conjugation at 300 °C, and aromatization at 500 °C. The structure of the carbonized materials transitions from peat-like (300 °C) to anthracite-like (800 °C). The low-temperature algibons A300 and A400 have oxygen-rich surface, and are unstable to leaching of water-soluble humic acid-like decomposition products. The A500 algibon, is oxygen-poor, stable to leaching, and shows the onset of aromaticity formation. In algibons prepared at >500 °C the increase in the size of the graphitic "grains" is evident from the Raman data. The A800 algibon is turbostratic with a high degree of disorder due to low density, high ash content, and structural defects, e.g. non-hexagonal aromatic rings. However, the turbostratic structure of A800 is more ordered than alginic acid-derived char prepared at the same temperature, which is attributed to the inherent structural ordering of the polysaccharide brought about by the gelation process. And finally, the batch-to-batch variation of the textural properties (surface area, pore volumes) in algibons was highlighted as a potential impact on the algibon production and application.

A number of research questions were posed by the work. For instance, the data on the thermal decomposition events could be complemented with the data of activations energy of the carbonization at different temperatures. The difference in crystallinity between expanded and non-expanded carbonaceous materials could be further investigated with XRD. The measurement of the surface charge of algibons in aqueous environment requires further investigation and correction for organic and inorganic leaching.

In **Chapter 3**, adsorption of phenols (resorcinol, m-aminophenol and 5-amino-o-

cresol) on algibons prepared at different temperatures (500–800 °C) and algibons A800 with different textural properties were discussed. Three key factors affecting adsorption were probed: the chemical nature of adsorbing surface, the physical nature of porous network, and the chemical structure of adsorbate molecules.

It was established that adsorption capacity for phenols increases with algibon preparation temperature, which was attributed to the decrease in the surface oxygen and the increase in the aromaticity required for π-π interaction between phenols and adsorbing surface. In A800, the adsorption capacity increases with the increase in the BET surface area of the materials. The adsorption capacity, adsorption rate, and density of the surface coverage decrease with increasing substitution of phenol ring (resorcinol>m-aminophenol>5-amino-o-cresol). As a rationalization, it was suggested that either bulky functional groups physically inhibit π-π interactions between phenols and the surface, or they polarize the molecule affecting electron distribution of the aromatic ring. The non-destructive desorption of phenols from algibons can be achieved with ethanol elution, yielding 73–95 % recovery. The recovery values achieved with solvent elution were greater than previously reported recovery for pH desorption.

Although the apparent adsorption capacity values of algibons were lower than capacities of the conventional activated carbon PAC, when normalise to the surface area, comparable adsorption per unit of surface unit is achieved. Moreover, efficient desorption of phenols from algibons provides a considerable advantage over activated carbon. The PAC adsorbs more and faster; however, if desorption and recovery of chemicals is a priority, then algibon offers an advantage of greater solvent diffusion and, therefore, greater desorption rates. This is of particular arelevance for solid-phase extractions, separation and chromatography.

Based on the finding in the present work, general advice for the future experimental work on adsorption/desorption with Starbons would be an inclusion of materials with different textural properties and surface chemistries to identify the correlations, which would aid understanding of the adsorption process and its optimization. The role of surface oxygen and aromaticity in phenol adsorption could further be evaluated by preparing higher temperature algibons (>800 °C) and oxidation of the oxygen-free algibons.

In **Chapter 4**, adsorption of 1-naphthol and 2-naphthol was systematically investigated on algibons prepared at different temperatures (500–800 °C) and on three algibons prepared at 800 °C possessing different textural properties. The aim was to evaluate the

influence of the textural properties and temperature-dependent surface chemistry on adsorption parameters, and to compare these parameters with adsorption of naphthols on PAC.

It was established that algibon adsorption capacity for naphthols increases with preparation temperature, which was attributed to the increasing levels of aromatic conjugation, i.e. π electron density, and decreasing surface oxygen content. The study adsorption kinetics of naphthols indicated a complex process, compared to the adsorption of phenols, which was attributed to the heterogeneity of the porous network. The A800 algibons showed greater adsorption capacity for 1-naphthol compared to the PAC, and the maximum adsorption capacity was in a linear correlation with the mesopore volume of all investigated materials. The adsorption capacity of 2-naphthol was in a linear correlation with the BET surface area of algibons. The amount of naphthols desorbed from algibons was 5–7 times greater than from PAC, with 2-naphthol desorbing better than 1-naphthol. The adsorption of 1-naphthol on algibons was found to be a spontaneous endothermic process driven by an entropy increase, which is unusual for an adsorption process; however, similar findings were reported previously for 1-naphthol adsorption on graphene and carbon nanotubes.[76,93] The adsorption of 2-naphthol was found to be a spontaneous and exothermic process, with a decrease in entropy of the system. Based on the data, it was concluded that adsorption of 1-naphthol is multilayer face-to-face stacking through π-π interactions, and 2-naphthol adsorption is edge-to-face, possibly through Yoshida hydrogen bonding.[97] Finally, the adsorption capacity for 1-naphthol and 2-naphthol demonstrated by algibons is the greatest reported to date for carbonaceous porous materials. It is reasonable to assume that these conclusions would extend to the adsorption of other PAHs.

Investigation of naphthol and phenol adsorption demonstrates that the advantages of algibons over conventional activated carbons in adsorption applications become more pronounced with increasing molecular size of adsorbates. Even a small change in the molecular size from phenols to naphthols leads to a substantial difference in adsorption performance. However, interactions between naphthols and the surface require closer investigation, with e.g. Raman spectroscopy or X-ray powder diffraction, to verify the proposed adsorption mechanism.

It would be of interest to investigate adsorption of other PAHs (e.g. naphthalene) and larger molecules on algibons with different textural properties. In addition, application of algibons for gas scrubbing off PAHs, generated during fuel or waste burning,

could be explored. The optimization of materials recovery through desorption could be attempted with different solvents, and the performance of recycled materials evaluated.

In **Chapter 5**, a novel route to mesoporous polysaccharide aerogels was reported based on the freeze drying of polysaccharide alcogels containing TBA. The route was demonstrated to yield highly mesoporous pectin aerogels (up to 2.3±0.3 $cm^3\ g^{-1}$ and 240 $m^2\ g^{-1}$), and reduce solvent usage by 90 % compared to the conventional solvent exchange method.[25]

A strong link between mesopore volume and TBA/water eutectics was revealed, which is the first report of this kind. The conclusion was made that fine eutectic crystals freeze in the native pores of a polysaccharide gel network, preserving the porosity during the drying process, whereas non-eutectic crystals grow larger in size, leading to macropores. The porosimetry data showed a relationship between the TBA/water phase diagram and the change in mesoporosity. The DSC analysis demonstrated the presence of eutectic TBA/water solution in alcogels, which yielded the greatest mesopore volume. Analysis of the aerogels with SEM revealed fine non-macroporous structure of eutectic aerogels and the presence of larger macropores away from eutectic concentrations.

In addition, the freeze drying route to mesoporous aerogels was found to be applicable to other gelling polysaccharides — alginic acid and starch. The obtained aerogels were comparable in mesopore volume and surface area to aerogels obtained by the conventional method.[26,27,34] The direct gelation of polysaccharides in eutectic and near-eutectic TBA solutions (20–30 wt% TBA) was found to further simplifying the procedure, reducing the time and resources required to fabricate the materials.

However; this work is in the early stages of development, and the full potential of freeze drying to produce mesoporous materials is yet to be explored. The relationship between the degree of esterification of pectin, viscosity of pectin solutions and mesoporosity of the resulting aerogels should be investigated. The macroporosity of the aerogels should also be systematically investigated, to better understand the structure of aerogels as a function of TBA concentration.

In **Chapter 6**, the carbonisation behaviour of freeze dried pectin aerogels was investigated. The goal was to compare the freeze drying route with the conventional $scCO_2$ drying route, in terms of their ability to yield aerogels suitable for preparation of Starbons. The obtained pecbons were high surface area mesoporous materials, and, therefore, the freeze drying route was deemed suitable for Starbon preparation. A similar correlation was established between the chemical properties of the pecbons Pec0-

Pec800, their elemental composition, and the temperatures of thermal transitions to the one reported in Chapter 2 for alginic acid-derived aerogels. The temperature-dependent surface chemistry of pecbons were found comparable to starch and alginic acid-derived Starbons. The carbon structure of pecbon Pec800 was found more ordered than that of pectin-derived char carbonized at the same temperature, as was demonstrated with Raman spectroscopy.

Adsorption of MB and AB on pecbon, investigated in this study, is the first reported application of pectin-derived Starbons. Pec300 demonstrated the greatest adsorption capacity for MB of all Starbons. Overall, pecbons were demonstrated to have good adsorption performance, rendering the material a valuable addition to the Starbon family. The comparison of MB and AB adsorption performance by starch-, alginic acid-, and pectin-derived Starbons with their textural and chemical properties revealed the magnitude of the influence that physical and chemical variables have on adsorption performance, e.g. surface chemistry and ash content. It is important to consider these variables in any application design.

It would be interesting to investigate whether the degree of esterification (DE) has a significant impact on the carbonisation behaviour of pectin aerogels and, as a result, on pecbon surface properties. More experimental investigation is needed to understand the influence of ash content on the surface chemistry and adsorption performance of pecbons.

Overall, the present work has demonstrated the capability of Starbons to yield a wide range of carbonaceous materials with different surface chemistries and porous structures, which lead to diverse performance in adsorption applications. This diversity in the performance will translate to versatility for selective adsorption and recovery of a wide range of environmental pollutants and valuable chemicals from post-consumer wastes, which will be highly valuable in the context of a closed-loop green economy.

Chapter 8

Experimental

8.1 Chapter 2: Alginic acid-derived Starbons

8.1.1 Materials and chemicals

Alginic acid derived from brown algae (*Macrocystis pyrifera*, CAS-9005-32-7) was purchased from Sigma-Aldrich (UK). Analytical grade ethanol and acetone were supplied by VWR Chemicals (UK). FT-IR grade potassium bromide was purchased from Sigma-Aldrich. Sodium chloride (99.8 % purity) and 0.1 M HCl and 0.1 M NaOH solutions for pH drift experiment were supplied by Fisher (UK).

8.1.2 Preparation of expanded alginic acid

The procedure for expanded alginic acid preparation, previously reported by White et al, was linearly scaled up.[34] For gelatinisation, alginic acid (300 g) was placed in a pressure cooker with 4 L of deionized water (1:13 ratio). The resulting mixture was stirred in the pressure cooker for 2 h at 120°C (393 K), allowed to cool to the room temperature and transferred into a glass beaker for 48 h retrogradation at 4 °C (277 K). Six solvent exchange steps were performed: three with ethanol and three with acetone. In each solvent exchange, 2 L of solvent were stirred with alginic acid solution for 2 h. Centrifugation was used to separate the solvent and alginic acid between the solvent exchanges. After the last solvent exchange, alginic acid was separated with vacuum filtration in a sintered funnel to maximise acetone removal. The solids were air dried prior to $scCO_2$ drying in 500 mL Thar SFE500 extractor at 120 bar, 40°C (313 K), and flow rate of 40 g min^{-1} for 2 h. The dried expanded alginic acid, also referred to as aerogel, was stored in sealed plastic bags.

8.1.3 Thermogravimetric analysis (TGA)

The TG analysis of expanded and non-expanded alginic acid was performed on Netzsch STA 409 instrument to study thermal decomposition profiles. The samples (50 mg) were carbonised under nitrogen in a ceramic cup at different heating rates (0.5, 5, 10 °C min^{-1}). The data were processed in Origin Pro 9 software.

8.1.4 Carbonisation of expanded alginic acid to A300-A800

The small scale carbonisation of expanded alginic acid (prepared according to method in Section 8.1.2) to algibons A300-A800 was carried out on Netzsch STA 409 instrument un-

der nitrogen flow (100 mL g^{-1}). The samples (250–300 mg) were heated at 0.5 °C min^{-1} to 400 °C, and at 2 °C min^{-1} to 800 °C, depending on the desired end temperature, to preserve porous structure.

The larger scale preparation of algibon was carried out in a furnace under vacuum. Expanded alginic acid (20-30 g) was carbonised to 300 °C and 800 °C at 0.5 °C min^{-1} to 400 °C, and at 2 °C min^{-1} from 400 to 800 °C, and allowed to cool down. Algibons were stored in sealed glass jars.

8.1.5 Elemental analysis

The elemental analysis was carried out on a CHN analyzer in duplicates by Dr Graeme McAllister (University of York). The ash content (inorganic content) was determined with Netzsch STA 409 instrument. A sample of expanded alginic acid (100 mg) was heated to 600 °C at 10 °C min^{-1} in air and held at 600 °C for 2 h for mass stabilisation. The remaining mass of the sample was assumed to be ash content. The oxygen content was assumed to be the mass difference between the total mass, CHN and ash contents.

8.1.6 IR-DRIFT spectroscopy

A range of algibon samples prepared at 50 °C interval to 800 °C (according to the method in Section 8.1.4) were subjected to IR-DRIFT analysis on Bruker Equinox 55. The sample preparation consisted of thoroughly grinding 495 mg of KBr and 5 mg of a sample in a mortar. The data acquisition were performed with OPUS 5.5 software. The data were processed into 2D IR map with Origin Pro 9 software.

8.1.7 Raman spectroscopy

Renishaw InVia Raman microscope with 514 nm laser, equipped with edge filter for anti-stokes scattering removal and charged-couple device detector was used to analyse the carbonised samples, prepared according to the method described in Section 8.1.4. The analysis was performed by Maria Isabel Munoz Ochando at the Instituto de Ciencia y Tecnologia de Polimeros (Madrid, Spain).

8.1.8 pH Drift

Solutions with a range of pH (3–12) were prepared in sodium chloride solution (0.01 M), degassed by boiling. For pH adjustment, 0.1 M HCl and 0.1 M NaOH solutions were

used, and the pH adjustment procedure was performed under nitrogen. The pH was measured with Jenway 3505 pH meter at room temperature of 23-25 °C.

For sample preparation, 30 mg of A300–A800 and 10 mL of each pH solution were incubated for 48 hours at ambient conditions and with constant stirring. The samples were allowed to settle and the pH was measured with Jenway 3505 pH meter. The obtained data were plotted on a graph of $pH_{initial}$ vs. pH_{final}, where the plateau or intercept of the experimental curve with no change curve ($pH_{initial}$ = pH_{final}) is the pH_{pzc}.

8.1.9 Analysis of organic leaching from algibons

The leachate was extracted from 3 g of A300 with deionised water at ambient temperature by stirring it for 1 h. The filtrate was collected and freeze dried on SP Scientific Sentry 2.0 freeze drier for 24 h. The obtained solid was subjected to IR analysis on Vertex 70 ATR-IR spectrometer instrument by Bruker.

8.1.10 N_2 adsorption/desorption porosimetry

Nitrogen porosimetry at 77 K was used to measure surface area, pore volume and pore size distributions on TriStar porosimeter by Micromeritics. Degassing of the samples was carried out on Flow Prep 060 thermal nitrogen degasser by Micromeritics. Degas of carbonised samples was carried out at 180 °C for 3 hours under continuous nitrogen flow; degas of expanded alginic acid was carried out at 90 °C for 3 hours under continuous nitrogen flow to remove water while preserving the structure.

The standard analysis conditions were 0.02–0.995 partial pressure interval and 7 sec equilibration between each data point. The BET model was used for the surface area identification, BJH model was used for pore volume calculation and the pore diameter distribution, assuming cylindrical pore shape.

8.2 Chapter 3: Adsorption of phenols on algibons

8.2.1 Materials and chemicals

Phenols (99% purity 5-amino-*o*-cresol, 100% purity resorcinol, 99.5% purity *m*-aminophenol) were supplied by Procter & Gamble (Darmstadt, Germany). Analytical grade ethanol was purchased from VWR Chemicals (UK). Commercial activated carbon (PAC) (par-

ticle size $\leq$40 μm) was acquired from Fluka Chemika (UK) and used as received. The preparation of algibons is described in Section 8.1.4.

8.2.2 Adsorbents characterisation

The elemental composition of adsorbents was determined as described in Section 8.1.5. The textural properties were analysed with N_2 adsorption/desorption porosimetry as described in Section 8.1.10

8.2.3 UV quantification of phenols

The quantitative analysis of phenols was performed on Jasco V-550 UV-Vis spectrophotometer at the appropriate wavelengths (5-amino-*o*-cresol 286 nm, resorcinol 275 nm, *m*-aminophenol 282 nm). A series of concentrations were prepared in deionised water and analysed in 1 mm quartz cuvettes. The calibration lines were constructed using Quantification tool of the Jasco software and are presented in the Figure 8.1, along with the analytical range, the path length and the correlation coefficient. All concentrations were corrected for purity, stated by the suppliers. In adsorptions analysis, the aqueous mixtures of phenols and algibons were centrifuged, and the clear algibon-free supernatant analysed.

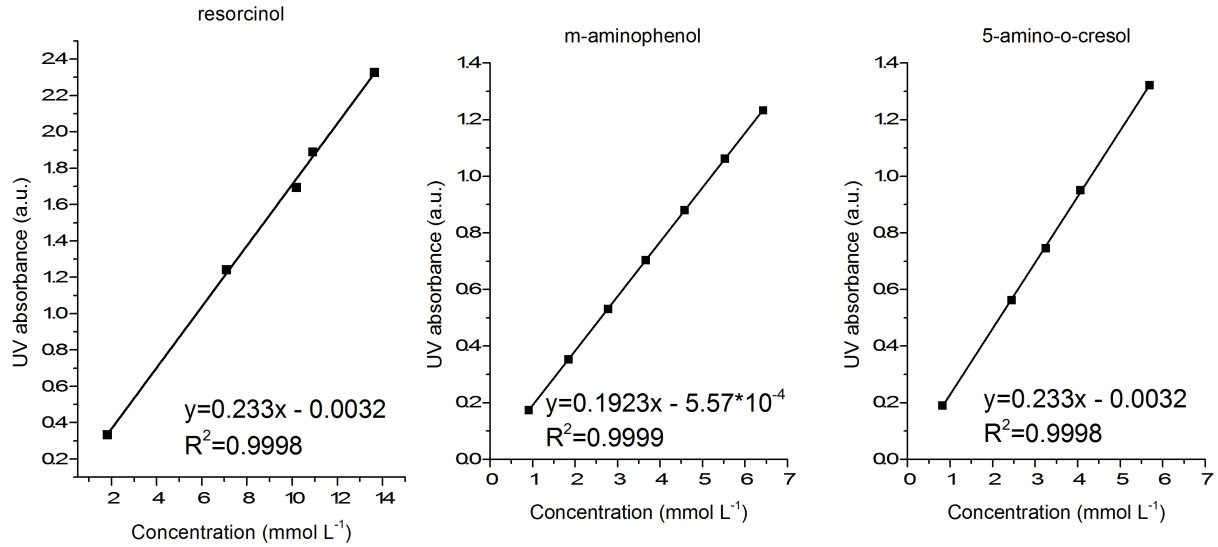

Figure 8.1: Phenols calibration lines for UV quantification

8.2.4 Adsorption screening of phenols on A500–A800 algibons

For batch adsorption, 10 mL of 200 mg L^{-1} solution of phenols was mixed with 20 mg of each adsorbent, in duplicates, and stirred until adsorption equilibrium was achieved. The adsorption mixtures were centrifuged and analysed with the UV quantification method, as described in Section 8.2.3.

8.2.5 Kinetics of phenols adsorption

For each phenol, 100 g of each adsorbent (PAC, A800_1, A800_1.6, A800_1.9) was mixed with 100 mL of 500 mg L^{-1} phenol solution, sealed and stirred at 200 rpm. A small sample (≈0.5 mL) was withdrawn from each mixture at different time intervals, centrifuged and analysed with the UV method, described in Section 8.2.3. The adsorption capacity at each time point was calculated according to Equation 3.1 and plotted against time.

8.2.6 Phenols adsorption isotherms

For each phenol, 10 ml of phenol solution with concentrations in the range of 100–700 mg L^{-1} were mixed with 10 mg of adsorbent and stirred constantly at 200 rpm until concentration equilibrium was reached. Each mixture was centrifuged and analysed with the UV method described in Section 8.2.3. The equilibrium adsorption capacities (Equation 3.1) were calculated and plotted against equilibrium concentrations. The experimental data was modelled with Langmuir and Freundlich isotherms in Origin Pro 9 software, using custom user equation tool.

8.2.7 Phenols desorption

Three cycles of adsorption/desorption of phenols was performed on an SPE manifold. Columns with 100 mg of each adsorbent were prepared and subjected to the following procedure:

1. The columns were preconditioned with 10 mL of ethanol followed by 10 mL of water.

2. For adsorption, 20 mL of 100 mg L^{-1} of phenol solution was slowly filtered through the columns with each adsorbent maintaining similar flow rate. The columns were allowed to dry for 30 min.

3. For desorption, the columns were flushed through with 10 mL of ethanol, followed by 10 mL of water.

4. The ethanol elution was dried under nitrogen, the samples were reconstituted in 5 mL of deionized water and subjected to UV analysis as described in Section 8.2.3.

5. The cycle was repeated 3 times with the same column.

8.3 Chapter 4: Adsorption of naphthols on algibons

8.3.1 Materials and chemicals

1-Naphthol (99 % purity) was supplied by Procter & Gamble (Darmstadt, Germany). 2-Naphthol was purchased from Sigma-Aldrich (UK). Analytical grade ethanol was purchased from VWR Chemicals (UK). Commercial activated carbon (PAC) (particle size $\leq$40 μm) was acquired from Fluka Chemika and used as received. Preparation of algibons is described in Section 8.1.4.

8.3.2 UV quantification of naphthols

The quantitative analysis of naphthols was performed on Jasco V-550 UV-Vis spectrophotometer at the appropriate wavelengths (1-naphthol 292 nm, 2-naphthol 273 nm). A series of concentrations were prepared in deionised water and analysed in 1 mm quartz cuvettes. The calibration lines were constructed using Quantification tool of the Jasco software and are presented in the Figure 8.2, along with the analytical range, the path length and the correlation coefficient. All concentrations were corrected for purity, stated by the suppliers. In adsorption experiments, the aqueous mixtures of naphthols and algibons were centrifuged, and the clear algibon-free supernatant analysed.

8.3.3 Adsorption screening of naphthols on A500–A800 algibons

For batch adsorption, 10 mL of 200 mg L^{-1} solution of naphthols was mixed with 20 mg of each adsorbent, in duplicates, and stirred until adsorption equilibrium was achieved. The adsorption mixtures were centrifuged and analysed with the UV quantification method described in Section 8.3.2.

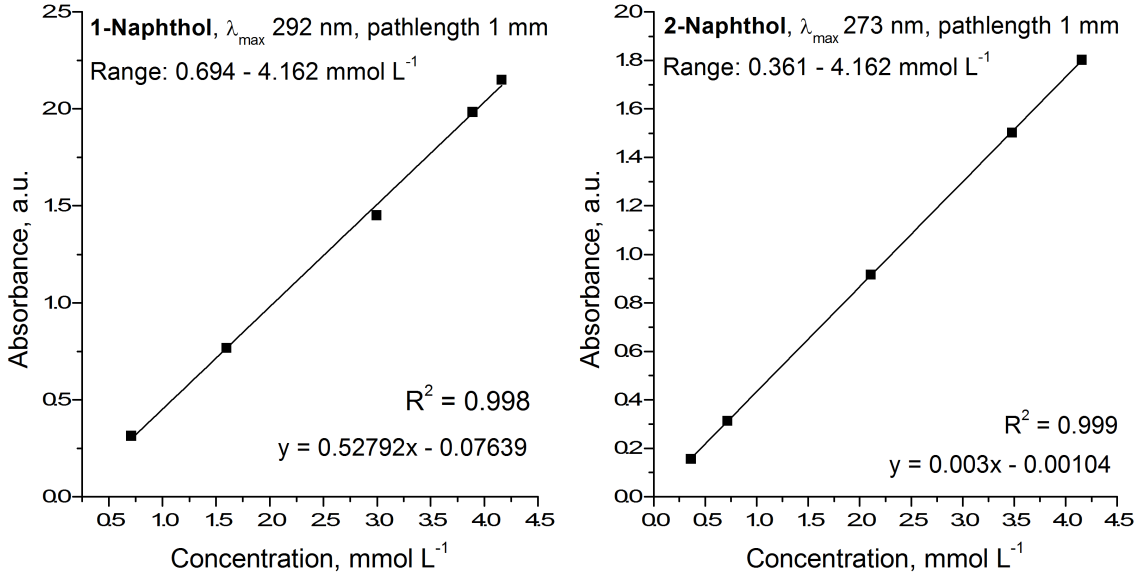

Figure 8.2: Naphthols calibration lines for UV quantification

8.3.4 Kinetics of naphthols adsorption

For each naphthol, each adsorbent (100 mg) was mixed with 100 mL of 500 mg L^{-1} naphthol solution, sealed and stirred at 200 rpm. A small sample (≈0.5 mL) was withdrawn from each mixture at different time intervals, centrifuged and analysed with the UV method. The adsorption capacity (Equation 3.1) at each time point was calculated and plotted against time.

8.3.5 Naphthols adsorption isotherms

For each naphthol, 10 ml of phenol solution with concentrations in the range of 100–700 mg L^{-1} were mixed with 10 mg of adsorbent and stirred constantly at 200 rpm until concentration equilibrium was reached. Each mixture was centrifuged and analysed with the UV method, described in Section 8.3.2. The equilibrium adsorption capacities (Equation 3.1) were calculated and plotted against equilibrium concentrations. The isotherms were fitted to Langmuir and Freundlich isotherms in Origin Pro 9 software.

8.3.6 Naphthols desorption

Refer to phenols desorption experiment in Section 8.2.7.

8.4 Chapter 5: Freeze drying route to mesoporous polysaccharide aerogels

8.4.1 Materials and chemicals

Citrus peel pectin (≥75 % galacturonic acid) was purchased from Sigma-Aldrich (UK). Analytical grade TBA (≥99 % purity) was purchased from Fluka Analytical (UK). Alginic acid derived from brown algae was purchased from Sigma-Aldrich (UK). Hylon VII corn starch was sourced from National Starch & Chemical Ltd (UK). Pectins with different degrees of esterification were supplied by Herbstreith & Fox KG (Germany) and CPKelco (Denmark). Analytical grade potassium hydroxide was purchased from Sigma-Aldrich (UK).

8.4.2 Differential scanning calorimetry of TBA/water solutions

A range of TBA/water solutions (5-95 wt%) was prepared by weight. Each solution was weighed out (7-10 mg) in an aluminium Tzero pan by TA, hermetically sealed with Tzero hermetic lid and analyzed with TA Instruments DSC Q2000. The following thermal programme was used: cooling at 5 °C min^{-1} to -50 °C and heating at 1 °C min^{-1} to 30 °C in two cycles. The data were evaluated with TA Universal Analysis software. The melting points identified from the DSC traces were used to construct the TBA/water phase diagram.

8.4.3 Degree of esterification

Degree of esterification of pectin was detmined with IR spectroscopy according to the method reported by Manrique and Lajolo.[119] Standard pectin samples, obtained from various manufacturers, with known degree of esterification were neutralized with potassium hydroxide solution to pH 7 in order to deprotonate all carboxylic groups to resolve methylated and deprotonated IR signals. Neutralized pectin solutions were freeze dried to remove all moisture and analysed with Vertex 70 ATR-IR spectrometer by Bruker. Spectra resolution was 2 cm^{-1}, sample and background number of scans were 32 with 4000-600 cm^{-1} acquisition range.

Background removal was performed on the OPUS software and peak integration tool was used to integrate 1740 cm^{-1} (methylated COOR) and 1605 cm^{-1} (acidic COOR)

peaks; relative peak intensity was calculated with Equation 8.1. Figure 8.3 shows correlation between degree of esterification and relative intensity of IR peaks.

$$Intensity = \frac{A_{1740}}{(A_{1740} + A_{1605})}) \tag{8.1}$$

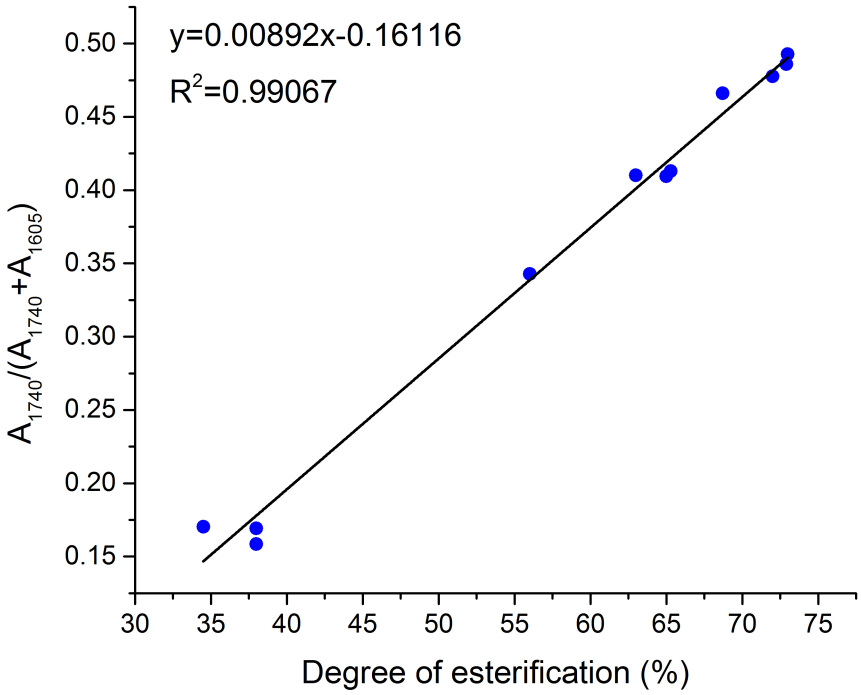

Figure 8.3: Linear correlation between degree of esterification and relative intensity of IR signal arising from esterified galacturonic acid

8.4.4 Elemental composition of pectin

The elemental analysis of pectin was carried out on a CHN analyzer by Dr Graeme McAllister (University of York). Inorganic content was identified by burning pectin sample at 600 °C for 2 h. The resulting ash was acid digested and subjected to Inductively Coupled Plasma (ICP) analysis coupled with MS detector; analysis performed by Dr Helen Parker (University of York). Oxygen content was assumed to be the mass difference between total mass and CNH and ash contents.

8.4.5 Preparation of aerogels from TBA/water solutions

As received pectin was homogenized in water (or TBA solutions) to make 5 wt% solution. Pectin solution was left at 4 °C for 24 h for retrogradation. Starch was rapidly gelled in water (or TBA solutions) (10 wt%) for 10 min at 140 °C and 200 watts in CEM SP Discover microwave and left at 4 °C for 48 h for retrogradation. Alginic acid (5 wt%) in water (or TBA solution) was gelled at 90 °C for 2.5 h, cooled and left at 4 °C for 24 h for retrogradation. In study of TBA addition, the gels were distributed into separate vials, the content of each vial was adjusted with appropriate quantity of TBA to yield TBA/water concentration in 0 to ≈100 wt% range. The resulting mixtures were frozen and freeze dried for at least 24 h in SP Scientific Sentry 2.0 freeze drier. The obtained aerogels were subjected to N_2 porosimetry analysis with the same conditions described in Section 8.1.10.

8.4.6 Viscometric analysis

Brookfield R/S-CPS+ rheometer equipped with RP3-50 plate spindle coupled with the Rheo3000 software was used for viscometric analysis of the gels with different TBA concentrations. Shear rate controlled mode was chosen with the shear rate set in the range of 1.5–70 s^{-1}. During analysis, the samples were maintained at 25 °C. The experimentally obtained shear stress was plotted against shear rate.

8.4.7 N_2 porosimetry

Refer to Section 8.1.10.

8.4.8 Differential scanning calorimetry of pectin gels

Same procedure as described in Section 8.4.2 was used to obtain DSC transitions of pectin gels with different TBA concentrations.

8.4.9 SEM analysis

The appearance of pectin aerogels was investigated and the micrographs were recorded with JEOL JSM-6490LV scanning electron microscope. The samples, mounted on an aluminium plate, were coated with Au-Pd prior to analysis. The acceleration voltage beam energy was 5 kV. The analysis was performed by Meg Stark (Biology Department, University of York).

8.5 Chapter 6: Pectin aerogel pyrolysis: product characterisation and application

8.5.1 Materials and chemicals

Methylene blue (100 % purity) and acid blue 92 (98 % purity) were purchased from Sigma-Aldrich (UK). Expanded pectin aerogel was prepared according to the method developed in Chapter 5, and the detailed preparation procedure is described in Section 8.4.5.

8.5.2 Thermogravimetric analysis (TGA)

Refer to thermogravimetric analysis of expanded alginic acid in Section 8.1.3.

8.5.3 TG-IR analysis

Thermogravimetric analysis coupled with IR analysis of the evolving gas was carried out on Netzsch STA 409 and Bruker Equinox 55 IR spectrometer, connected by 0.5 m heated tube. Each sample (50 mg) was carbonised in inert atmosphere with nitrogen as a carrier gas (100 mL min^{-1}) at 10 °C min^{-1}. The data were recorded and analysed with Opus software.

8.5.4 FT-IR analysis of carbonised pectin

The IR analysis of pecbons carbonised to different temperatures was performed with Vertex 70 ATR-IR spectrometer by Bruker, in 600–4000 cm^{-1} range with 2 cm^{-1} resolution and 32 sample and background scans. The pecbon samples were prepared in Netzsch STA 409 in inert atmosphere at 1 °C min^{-1} heating rate and analysed without any further processing.

8.5.5 Raman spectroscopy

Refer to algibon Raman spectroscopy in Section 8.1.7.

8.5.6 N_2 porosimetry

Refer to N_2 adsorption/desorption in Section 8.1.10.

8.5.7 SEM and TEM analysis

The appearance of pecbons was investigated and the micrographs were recorded with JEOL JSM-6490LV scanning electron microscope. The samples, mounted on an aluminium plate, were coated with Au-Pd prior to analysis. The acceleration voltage beam energy was 5 kV. TEM analysis was carried out with Tecnai 12 BioTwin instrument at 120 kV. Both analyses were performed by Meg Stark (Biology Department, University of York).

8.5.8 pH Drift

Refer to pH drift experiment in Section 8.1.8.

8.5.9 UV quantification of MB and AB

The quantitative analysis of MB and AB was performed on Jasco V-550 UV-Vis spectrophotometer at the appropriate wavelengths (MB 608 nm, AB 563 nm). A series of concentrations were prepared in deionised water and analysed in 1 mm quartz cuvettes. The calibration lines were constructed using Quantification tool of the Jasco software and are presented in the Figure 8.4. All concentrations were corrected for purity, stated by the suppliers. In adsorptions analysis, the aqueous mixtures of the dyes and pecbons were centrifuged, and clear, pecbon-free supernatant was analysed.

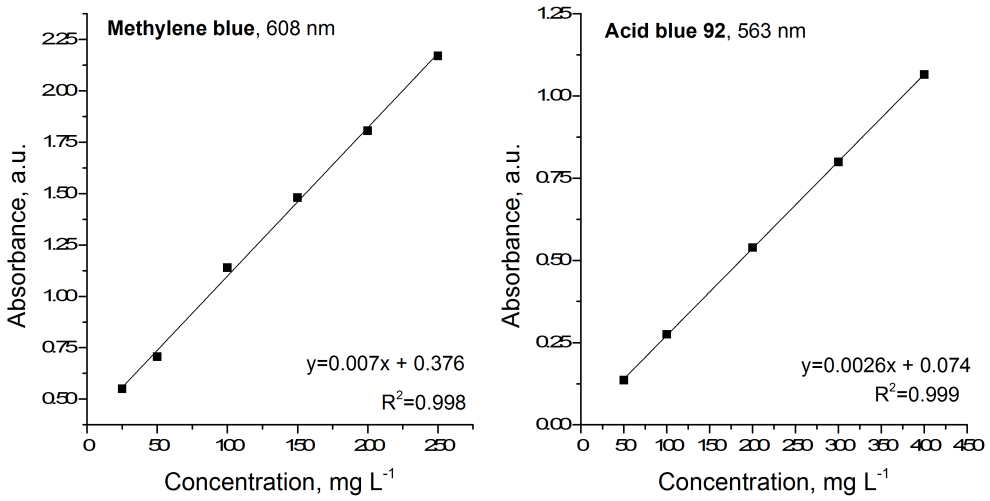

Figure 8.4: MB and AB concentrations calibration lines for UV-Vis quantification

8.5.10 MB and AB adsorption rates

Batch adsorption experiment was carried out with 10 mL of 400 mg L^{-1} solutions of each dye and 20 mg of either Pec300, Pec400 or Pec800. An adsorbate solution was mixed with an adsorbent and left stirring at 200 rpm. Small amount of sample (approximately 0.5 mL) was withdrawn at different time intervals, centrifuged for 5 min at 3000 rpm, and subjected to UV analysis, as described in Section 8.5.9. The measurements were taken until the adsorption equilibrium was reached.

8.5.11 MB and AB adsorption isotherms

For batch adsorption experiment, 10 mg of each adsorbent was mixed with a series of MB and AB solutions (100–500 mg L^{-1}) and left stirring at 200 rpm until adsorption equilibrium was reached. Due to high adsorption capacity of Pec300 for MB, 5 mg of the adsorbent was mixed with 15 mL of MB solutions in 100–500 mg L^{-1}. After adsorption equilibrium was reached, each adsorption mixture was centrifuged at 3000 rpm for 5 min and subjected to UV analysis, as described Section 8.5.9.

Appendix A

Appendix: Chapter 3

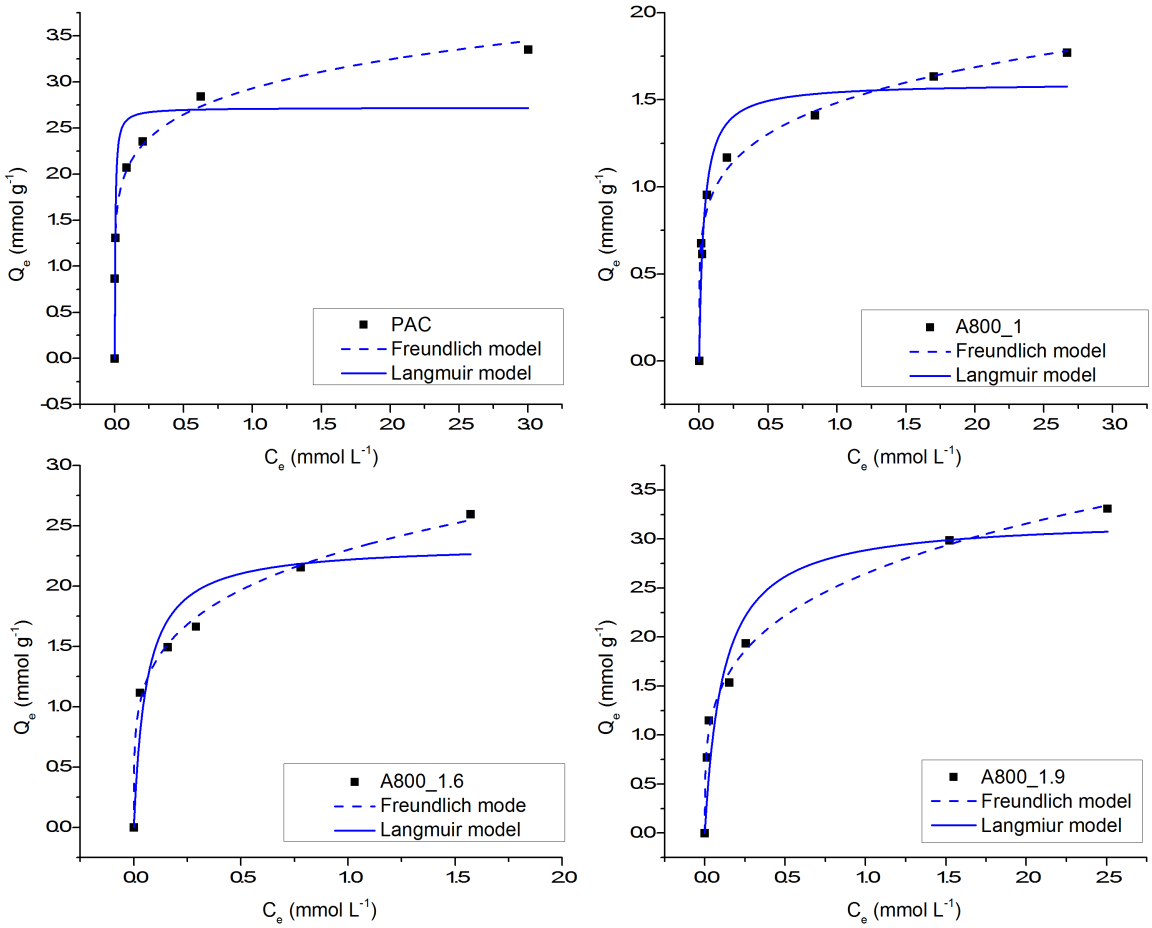

Figure A.1: Resorcinol adsorption isotherms fitted with Langmuir and Freundlich models

Table A.1: Resorcinol adsorption: Langmuir and Freundlich model parameters

Langmuir model			
Material	Q*max*	K	R^2
	mmol g^{-1}	L $mmol^{-1}$	
A800_1	1.60 ± 0.09	1.47 ± 0.39	0.938
A800_1.6	2.35 ± 0.24	17.24 ± 9.42	0.890
A800_1.9	3.21 ± 0.34	8.76 ± 3.99	0.889
PAC	2.72 ± 0.26	10.99 ± 7.93	0.829
Freundlich model			
	K	n	R^2
A800_1	0.85 ± 0.03	5.38 ± 0.37	0.987
A800_1.6	1.29 ± 0.06	10.14 ± 1.75	0.983
A800_1.9	1.24 ± 0.05	3.93 ± 0.19	0.994
PAC	1.89 ± 0.04	6.80 ± 0.30	0.996

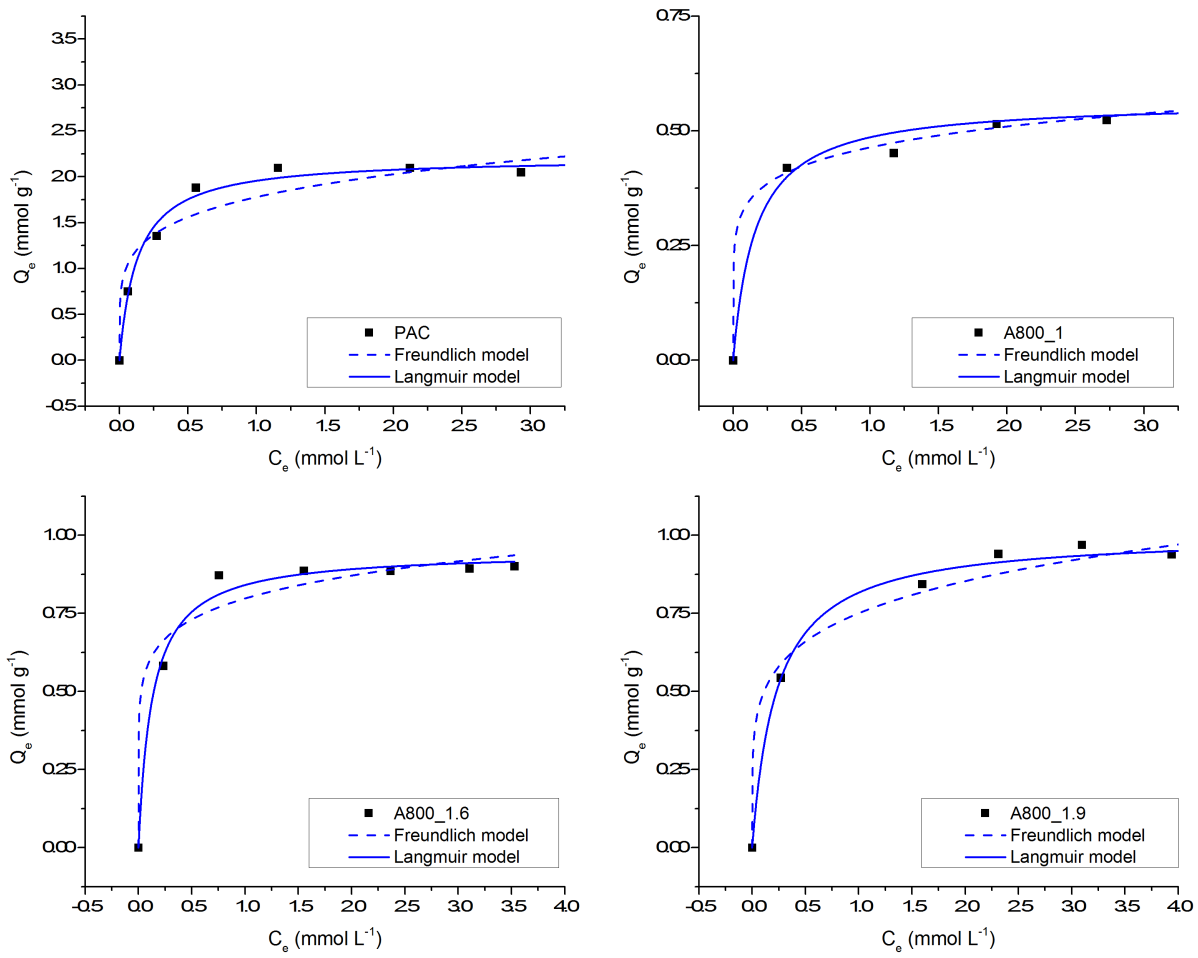

Figure A.2: 5-Amino-*o*-cresol adsorption isotherms fitted with Langmuir and Freundlich models

Table A.2: 5-amino-*o*-cresol adsorption: Langmuir and Freundlich model parameters

Langmuir model			
Material	$Qmax$	K	R^2
	mmol g^{-1}	L $mmol^{-1}$	
A800_1	0.57 ± 0.02	6.15 ± 1.77	0.982
A800_1.6	0.95 ± 0.02	7.78 ± 1.37	0.991
A800_1.9	1.00 ± 0.02	4.34 ± 0.55	0.994
PAC	2.21 ± 0.06	7.67 ± 1.17	0.987
Freundlich model			
	K	n	R^2
A800_1	0.46 ±0.01	7.42 ± 0.99	0.993
A800_1.6	0.80 ± 0.03	7.89 ± 2.33	0.963
A800_1.9	0.75 ± 0.03	5.40 ± 0.96	0.979
PAC	1.78 ± 0.09	5.30 ± 1.22	0.921

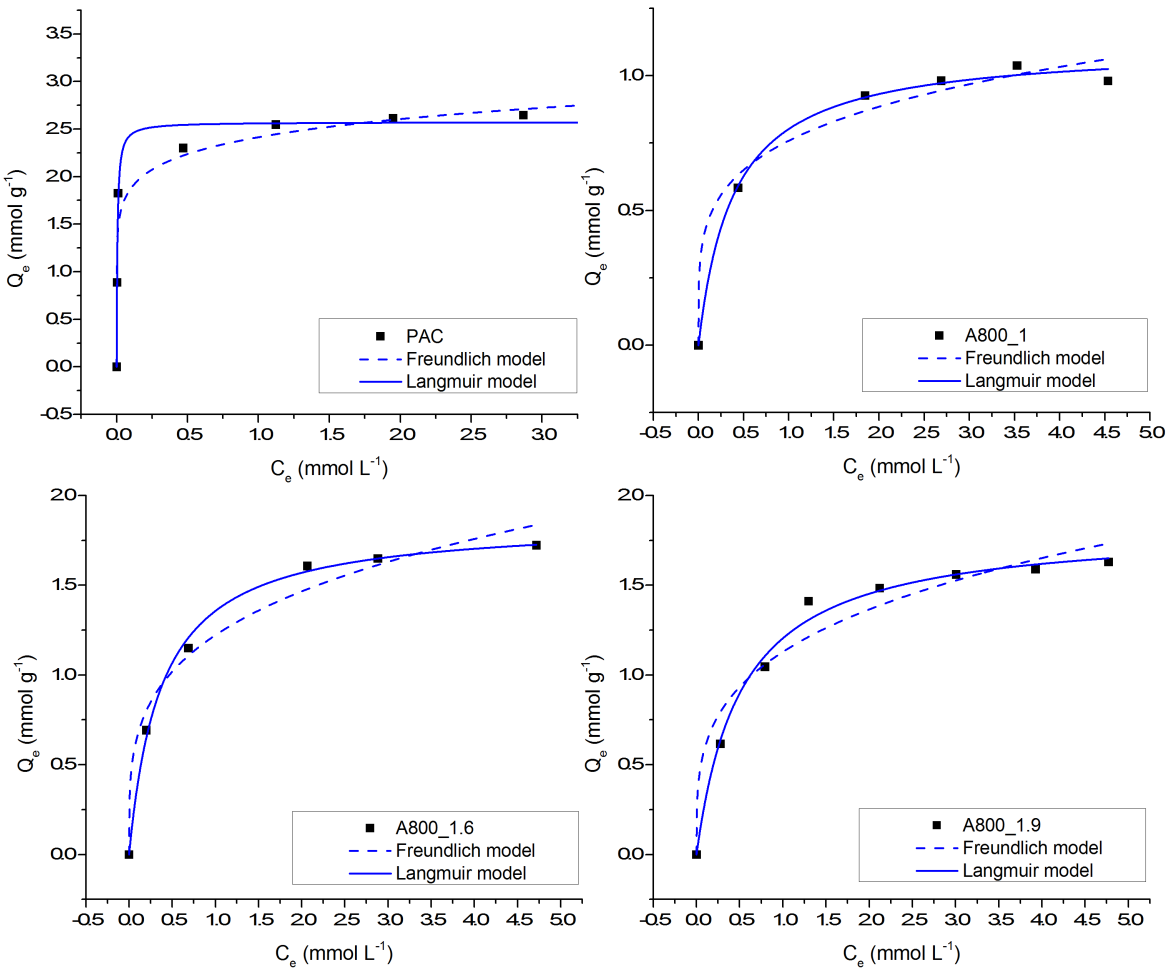

Figure A.3: *m*-Aminophenol adsorption isotherms fitted with Langmuir and Freundlich models

Table A.3: *m*-Aminophenol adsorption: Langmuir and Freundlich model parameters

Langmuir model			
Material	Q*max*	K	R^2
	mmol g^{-1}	L $mmol^{-1}$	
A800_1.6	1.86 ± 0.04	2.69 ± 0.25	0.997
A800_1.9	1.83 ± 0.05	1.93 ± 0.23	0.992
PAC	2.57 ± 0.06	184.46 ± 30.27	0.983
Freundlich model			
	K	n	R^2
A800_1	0.76 ± 0.04	4.50 ± 0.92	0.978
A800_1.6	1.22 ± 0.06	3.81 ± 0.56	0.976
A800_1.9	1.13 ± 0.06	3.65 ± 0.63	0.953
PAC	2.42 ± 0.09	9.13 ± 1.75	0.945

Appendix B

Appendix: Chapter 4

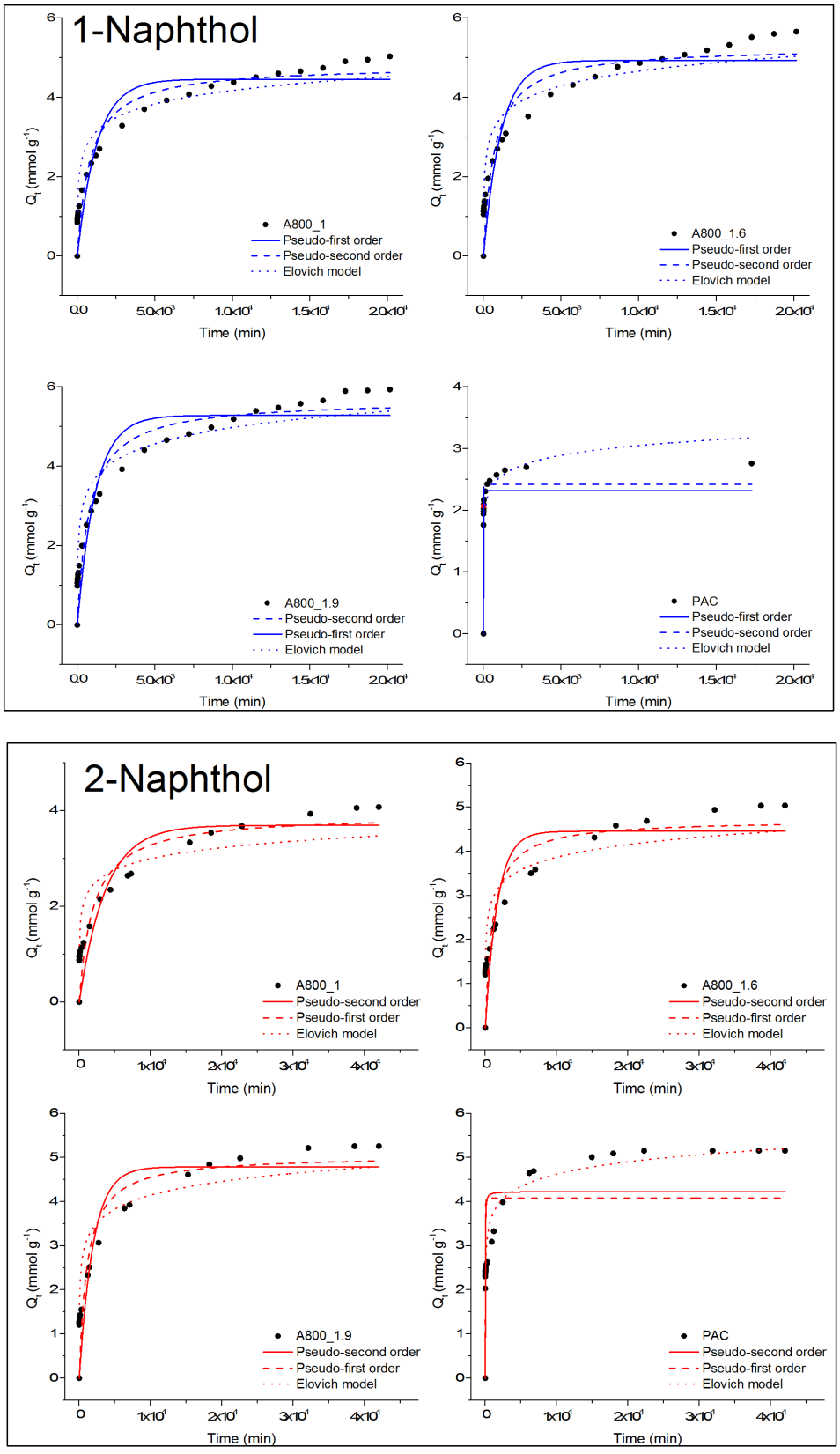

Figure B.1: Fitted pseudo-first, pseudo-second and Elovich kinetic models to 1-naphthol and 2-naphthol experimental data

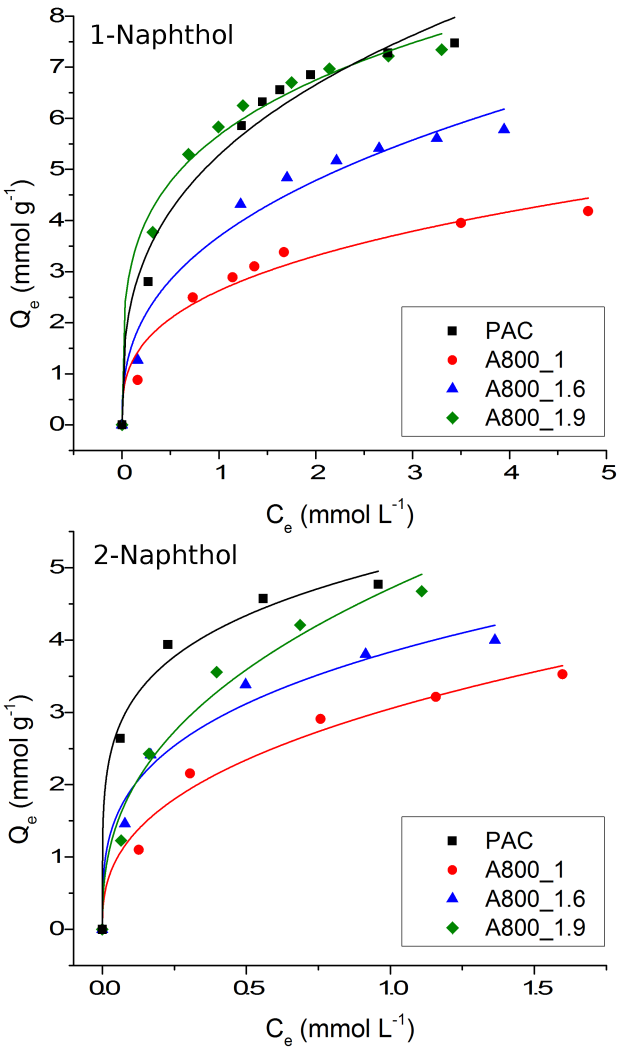

Figure B.2: 1-naphthol and 2-naphthol adsoprtion isotherm data fitted with Freundlich model

Table B.1: 1-Naphthol and 2-naphthol adsorption isotherms fitted with Freundlich model

1-Napthol			
Material	K	n	R^2
A800_1	3.6 ± 0.2	2.6 ± 0.3	0.971
A800_1.6	5.6 ± 0.1	3.9 ± 0.3	0.987
A800_1.9	5.2 ± 0.1	2.9 ± 0.3	0.976
PAC	2.6 ± 0.1	2.9 ± 0.4	0.960
1-Napthol			
Material	K	n	R^2
A800_1	3.0 ± 0.1	2.6 ± 0.3	0.977
A800_1.6	3.8 ± 0.1	3.3 ± 0.4	0.973
A800_1.9	4.7 ± 0.2	2.5 ± 0.3	0.976
PAC	4.9 ± 0.2	4.9 ± 0.7	0.987

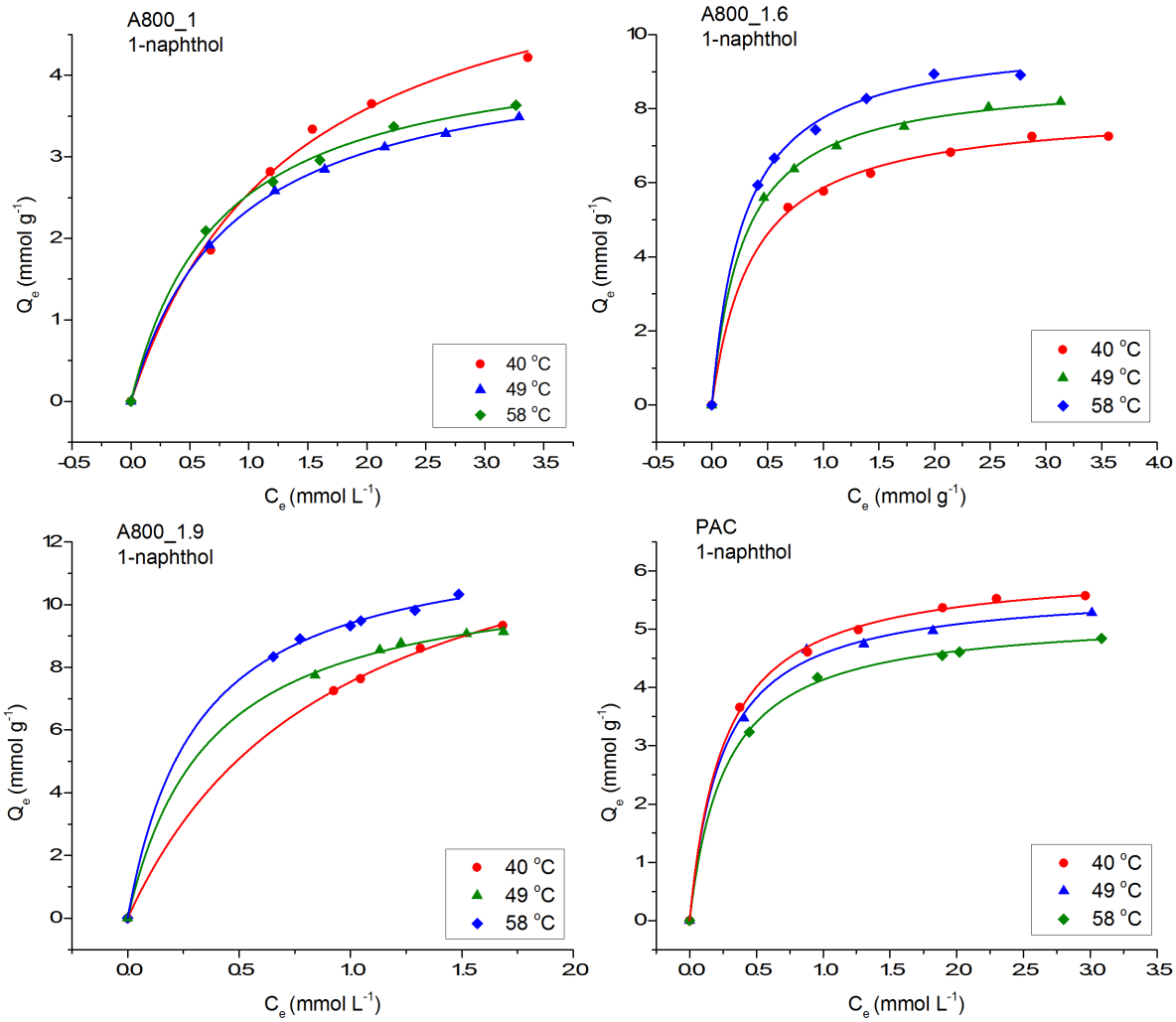

Figure B.3: 1-Naphthol adsorption isotherms at different temperatures

Table B.2: Langmuir adsorption parameters for 1-naphthol adsorption at 37–60 °C

	Temperature	K	Q_{max}	R^2
	Kelvin	L mol^{-1}	mmol g^{-1}	
A800_1	313	1046 ± 447	6.00 ± 0.21	0.995
	322	1249 ± 309	4.36 ± 0.12	0.999
	328	1210 ± 610	4.45 ± 0.21	0.997
A800_1.6	310	2700 ± 268	8.03 ± 0.13	0.999
	321	3508 ± 223	8.97 ± 0.09	1.000
	329	3527 ± 448	9.91 ± 0.19	0.998
A800_1.9	313	1070 ± 709	12.86 ± 0.00	0.976
	329	2440 ± 242	8.07 ± 0.11	0.999
	333	3050 ± 342	12.41 ± 0.31	0.997
PAC	311	2431 ± 198	5.01 ± 0.19	0.994
	322	1738 ± 666	4.44 ± 0.39	0.962
	328	1466 ± 616	4.23 ± 0.25	0.983

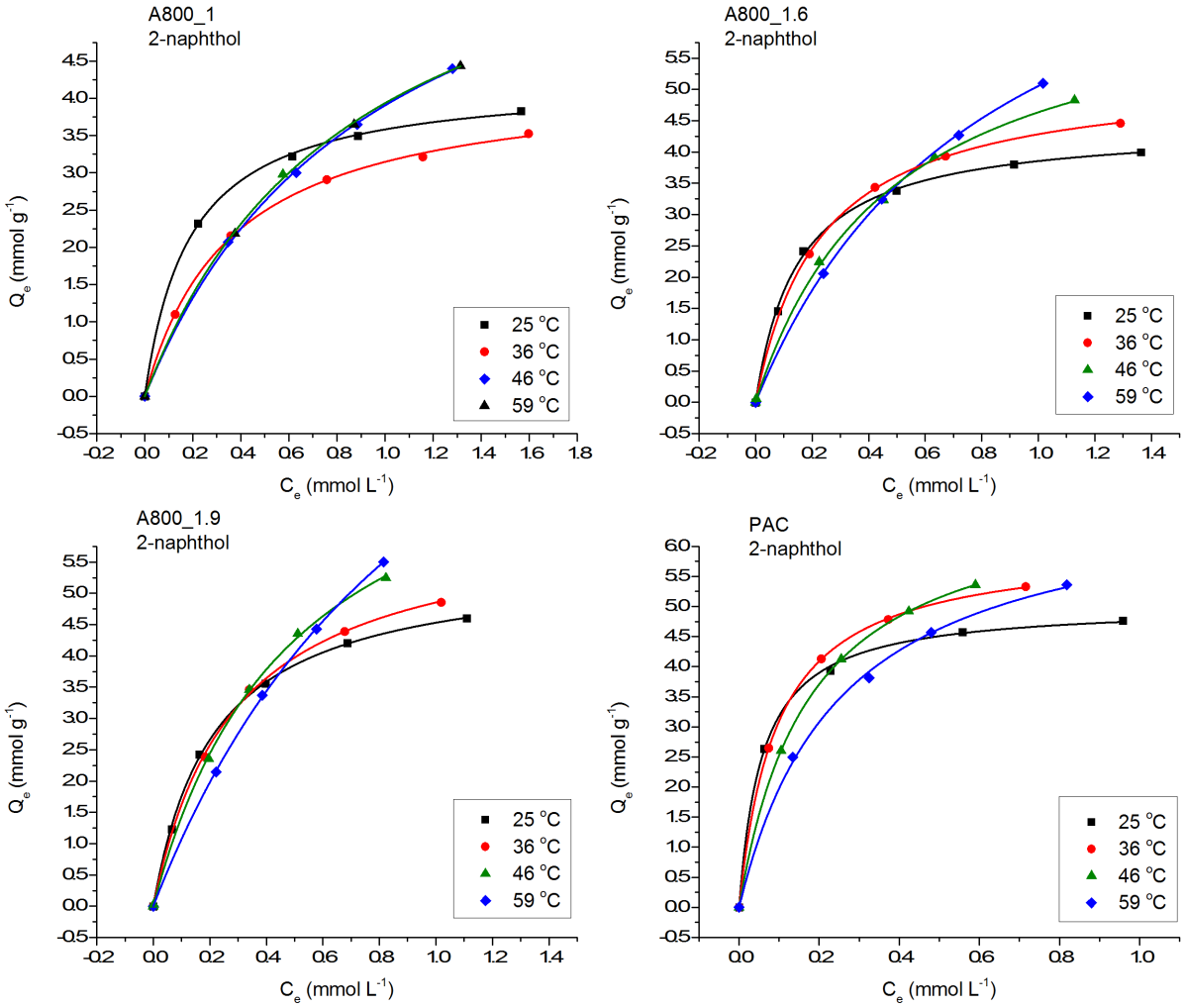

Figure B.4: 2-Naphthol adsorption isotherms at different temperatures

Table B.3: Langmuir adsorption parameters for 2-naphthol adsorption at 40, 49 and 59 °C

	Temperature	Q_{max}	K	R^2
	°C	mmol g^{-1}	L mol^{-1}	
A800_1	40	4.4 ± 0.4	2649.7 ± 1032.7	0.975
	49	8.0 ± 0.7	1078.8 ± 222.1	0.996
	59	7.5 ± 0.8	1034.0 ± 163.9	0.993
A800_1.6	40	6.1 ± 0.7	3108.0 ± 807.7	0.992
	49	6.8 ± 0.9	2140.8 ± 675.7	0.979
	59	8.5 ± 1.2	1141.8 ± 883.8	0.913
A800_1.9	40	6.2 ± 0.2	3513.5 ± 228.9	0.999
	49	8.5 ± 0.6	2056.6 ± 321.9	0.995
	59	9.1 ± 1.9	885.6 ± 701.0	0.940
PAC	40	6.0 ± 0.4	10438.7 ± 2818.5	0.980
	49	7.0 ± 1.1	5647.0 ± 2640.1	0.954
	59	7.1 ± 0.6	3582.1 ± 825.5	0.988

Appendix C

Appendix: Chapter 5

DSC traces of pectin gels

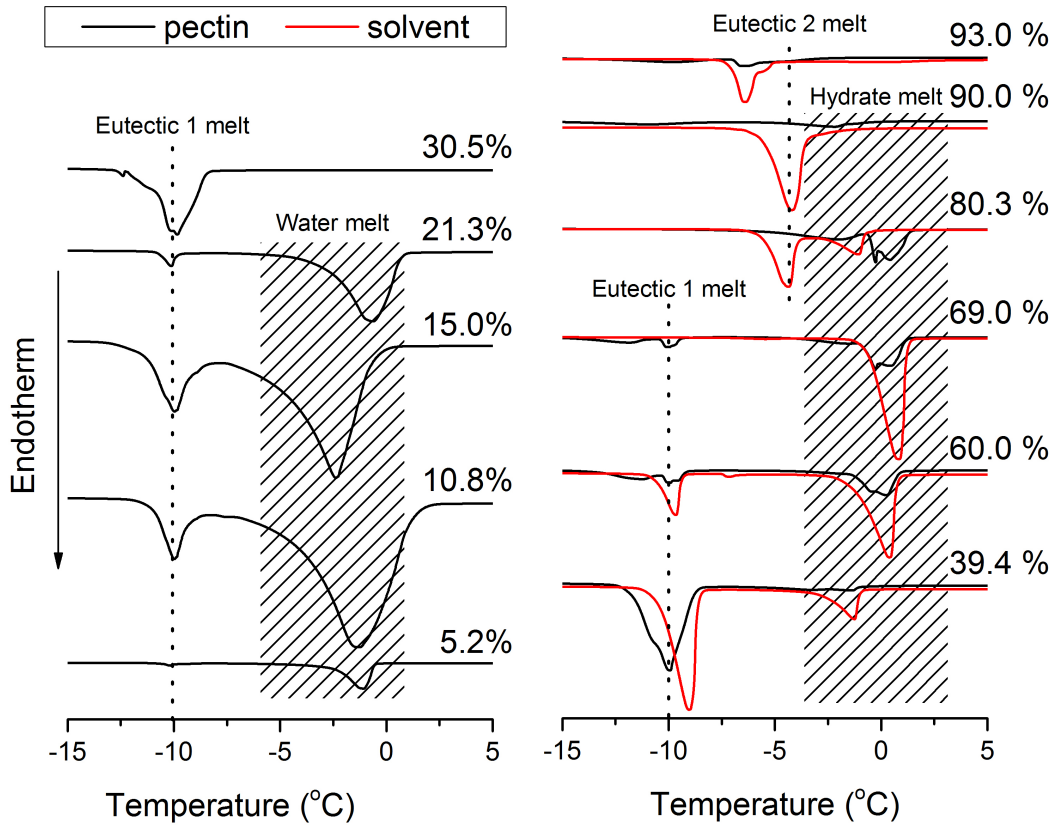

Figure C.1: DSC traces of pectin gels with different concentration of aquaeous TBA and pure TBA/water solutions

Appendix D

Appendix: Chapter 6

Standard gas-phase IR spectra of volatile products of thermal decomposition of polysaccharides

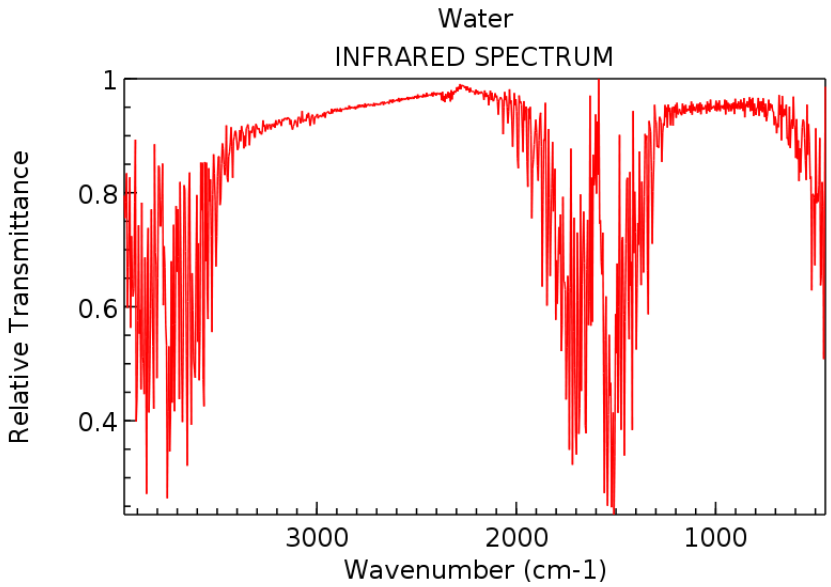

Figure D.1: Standard IR spectrum of water (source: NIST)

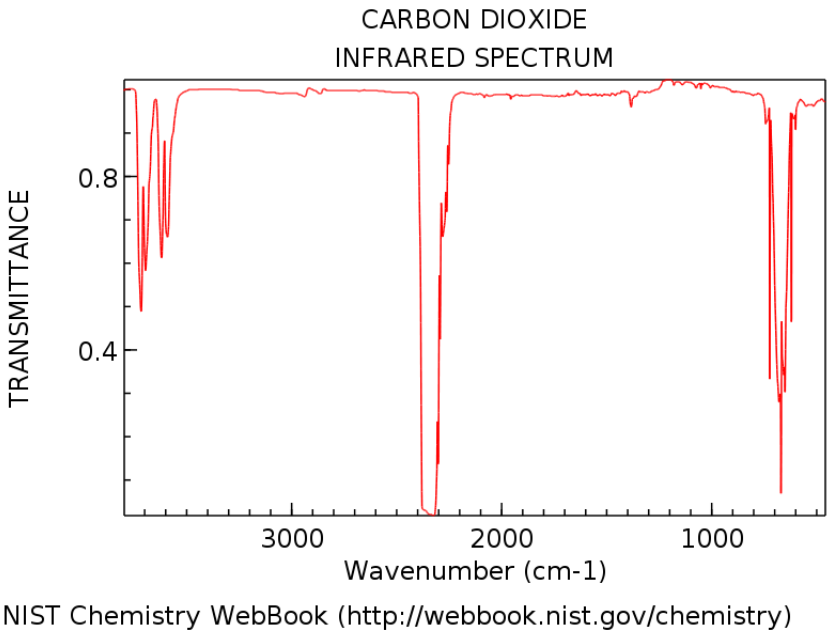

Figure D.2: Standard IR spectrum of carbon dioxide (source: NIST)

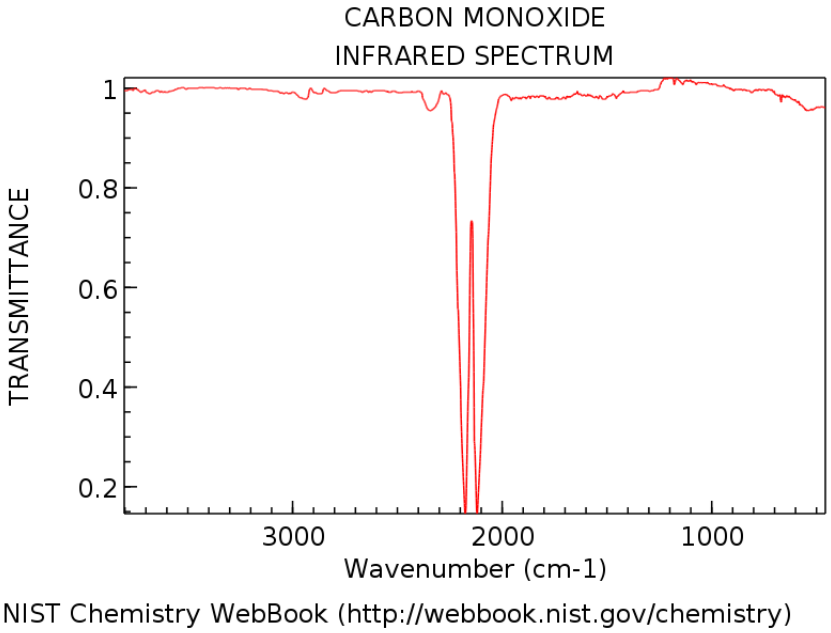

Figure D.3: Standard IR spectrum of carbon monoxide (source: NIST)

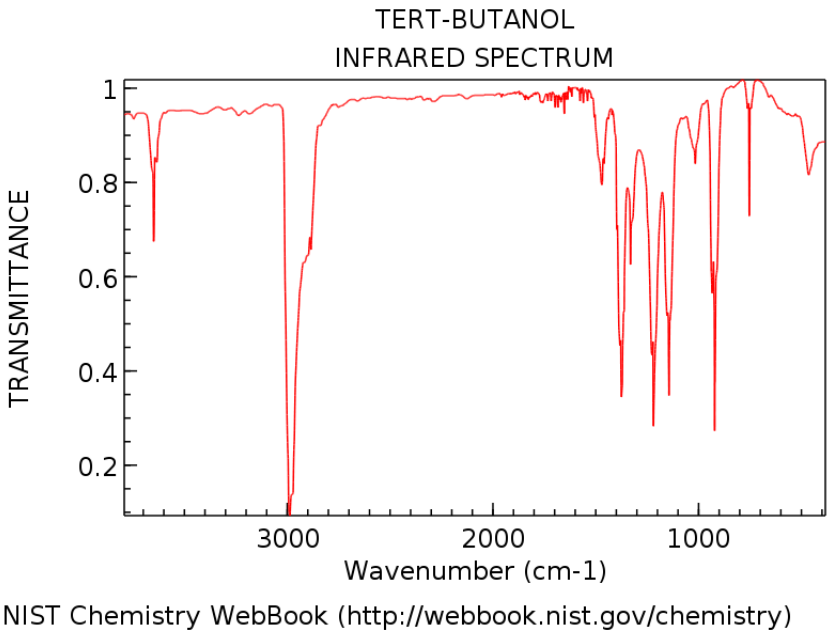

Figure D.4: Standard IR spectrum of t-butanol (source: NIST)

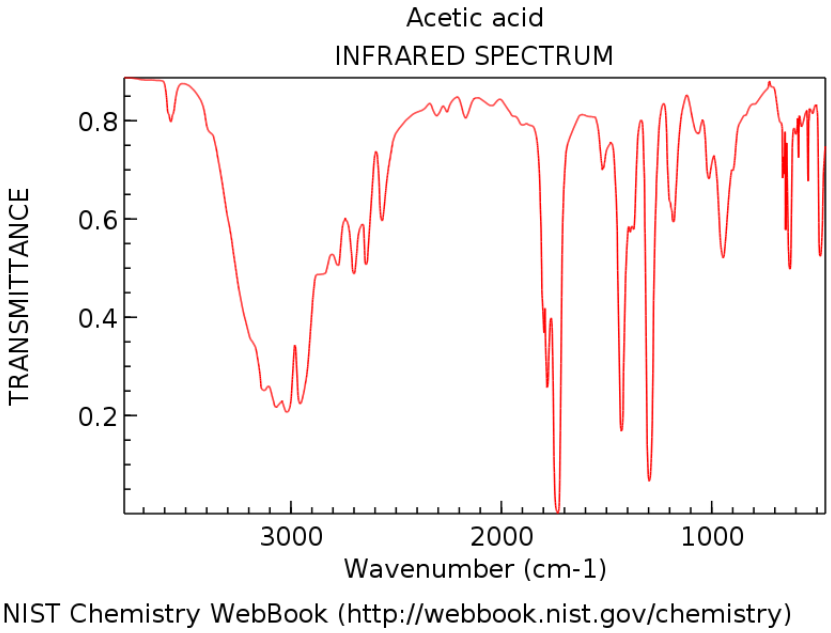

Figure D.5: Standard IR spectrum of acetic acid (source: NIST)

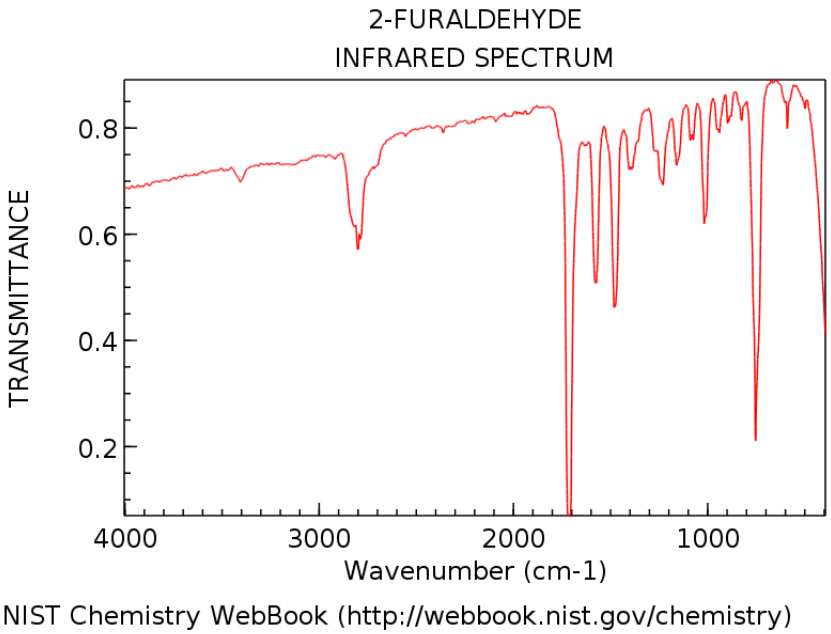

Figure D.6: Standard IR spectrum of furaldehyde (source: NIST)

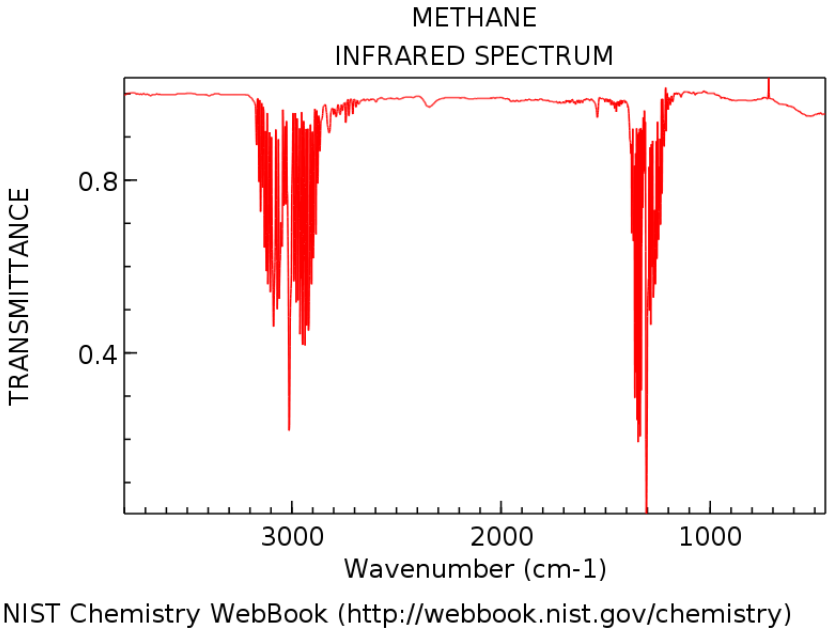

Figure D.7: Standard IR spectrum of methane (source: NIST)

List of Abbreviations

scCO$_2$ supercritical carbon dioxide

TBA tertiary butanol

DSC differential scanning calorimetry

SEM scanning electron microscopy

BJH Barrett-Joyner-Halenda model

BET Brunauer-Emmett-Teller

BDDT Brunauer-Deming-Deming-Teller

LCA Life Cycle Assessment

GWP global warming potential

DE degree of esterification

TGA thermogravimetric analysis

FTIR Fourier transform infra-red

PAC powdered activated carbon

FWHM full width at half maximum

PAHs polycyclic aromatic hydrocarbons

MB methylene blue

AB acid blue 92

TEM transmission electron microscopy

SPE solid-phase extraction

List of References

[1] P. G. Jessop, F. Ahmadpour, M. A. Buczynski, T. J. Burns, N. B. Green II, R. Korwin, D. Long, S. K. Massad, J. B. Manley, N. Omidbakhsh, R. Pearl, S. Pereira, R. A. Predale, P. G. Sliva, H. VanderBilt, S. Weller and M. H. Wolf, *Green Chem.*, 2015, **17**, 2664–2678.

[2] T. V. T. Phan, C. Gallardo and J. Mane, *Green Chem.*, 2015, **17**, 2846–2852.

[3] Euromonitor, *Latest Hair Care Market Study by Euromonitor's Highlights Opportunities for Ingredient Players*, 2011, specialchem4cosmetics.com/services/news.aspx?id=7155&q=Euromonitor%20and%20hair%20care, Last Accessed 20-Oct-2015.

[4] Euromonitor, *Ingredients in Hair Care*, 2010, http://blog.euromonitor.com/2011/08/ingredients-in-hair-care.html, Last Accessed 20-Oct-2015.

[5] V. Sherrow, *Encyclopedia of Hair: A Cultural History*, Greenwood Press, 2006.

[6] A. Meyer and K. Fischer, *Environ. Sci. Eur.*, 2015, **27**, 11.

[7] B. Hefford, *Soap, parfumery and cosmetic*, 2006, **79 (11)**, 49–56.

[8] S. C. Rastogi, H. Sosted, J. D. Johansen, T. Menne and R. Bossi, *Contact Dermatitis*, 2006, **55**, 95–100.

[9] Cosmetics Europe, *Good Sustainability Practice (GSP) for the Cosmetics Industry*, https://www.cosmeticseurope.eu/downloads/4814.html, Last Accessed 20-Oct-2015.

[10] *Life Cycle Assessment of Shampoo by Henkel AG & Co. KGAA*, 2008, http://www.pcf-projekt.de/files/1236586214/pcf_henkel_shampoo.pdf, Last Accessed 20-Oct-2015.

[11] C. U. Ajuzie and B. A. Osaghae, *Afr. J. Biotechnol.*, 2011, **10(11)**, 2066–2069.

[12] O. John, H. Ndom and E. Akortha, *Nigerian Journal of Microbiology*, 2009, **23(1)**, 1956–1964.

[13] D. L. Russell, in *Practical Wastewater Treatment*, John Wiley & Sons, Hoboken, New Jersey, USA, 2006, ch. 15. Carbon Adsorption, pp. 231–236.

[14] A. Dabrowski, P. Podkoscielny, Z. Hubicki and M. Barczak, *Chemosphere*, 2005, **58**, 1049–1070.

[15] V. Chiola, J. E. Ritsko and C. D. Vanderpool, *Process for producing low-bulk density silica*, 1971, US 3556725.

[16] M. Yue, Y. Chun, Y. Cao, X. Dong and J. Zhu, *Adv. Funct. Mater.*, 2006, **16**, 1717–1722.

[17] Z. Li, J. C. Barnes, A. Bosoy, J. F. Stoddart and J. I. Zink, *Chem. Soc. Rev.*, 2012, **41**, 2590–2605.

[18] C.-Y. Chen, H.-X. Li and M. E. Davis, *Microporous Mater.*, 1993, **2**, 17 – 26.

[19] D. Zhao, J. Feng, Q. Huo, N. Melosh, G. H. Fredrickson, B. F. Chmelka and G. D. Stucky, *Science*, 1998, **279**, 548–552.

[20] A. Popat, J. Liu, Q. Hu, M. Kennedy, B. Peters, G. Q. M. Lu and S. Z. Qiao, *Nanoscale*, 2012, **4**, 970–975.

[21] J. M. D. Aguado, J. M. Arsuaga, A. Arencibia, M. Lindo and V. Gascon, *J. Hazard. Mater.*, 2009, **163**, 213 – 221.

[22] C. Liang, Z. Li and S. Dai, *Angew. Chem., Int. Ed.*, 2008, **47**, 3696–3717.

[23] H. Chang, S. H. Joo and C. Pak, *J. Mater. Chem.*, 2007, **17**, 3078–3088.

[24] H. Wang, C. Zhang, Z. Chen, H. K. Liu and Z. Guo, *Carbon*, 2015, **81**, 782 – 787.

[25] V. Budarin, J. H. Clark, J. J. E. Hardy, R. Luque, K. Milkowski, S. J. Tavener and A. J. Wilson, *Angew. Chem.*, 2006, **118**, 3866–3870.

[26] R. White, V. Budarin and J. Clark, *ChemSusChem*, 2008, **1**, 408–411.

[27] R. White, V. Budarin and J. Clark, *Chem. Eur. J.*, 2010, **16**, 1326–1335.

[28] H. Fredriksson, J. Silverio, R. Andersson, A.-C. Eliasson and P. Aman, *Carbohydr. Polym.*, 1998, **35**, 119–134.

[29] M. J. Miles, V. J. Morris, P. D. Orford and S. G. Ring, *Carbohydr. Res.*, 1985, **135**, 271–281.

[30] K. S. Mikkonen, K. Parikka, A. Ghafar and M. Tenkanen, *Trends Food Sci. Technol.*, 2013, **34**, 124–136.

[31] International Starch Institute, `http://starch.dk`, Last Accessed 20-Oct-2015.

[32] H. Bixler and H. Porse, *J. Appl. Phycol.*, 2011, 321–335.

[33] K. Draget, G. S. Braek and O. Smidsrod, *Carbohydr. Polym.*, 1994, **25**, 31–38.

[34] R. J. White, C. Antonio, V. L. Budarin, E. Bergstrom, J. Thomas-Oates and J. H. Clark, *Adv. Funct. Mater.*, 2010, **20**, 1834–1841.

[35] *The Chemistry and Technology of Pectin*, ed. R. H. Walter, Academic Press Inc., 1991.

[36] B. J. Savary, A. T. Hotchkiss and M. L. Fishman, *Advances in Pectin and Pectinase Research*, Kluwer Academic Publishers, 2003.

[37] D. Oakenfull and A. Scott, *J. Food Sci.*, 1984, **49**, 1093–1098.

[38] P. S. Shuttleworth, V. Budarin, R. J. White, V. M. Gun'ko, R. Luque and J. H. Clark, *Chem. Eur. J.*, 2013, **19**, 9351–9357.

[39] V. L. Budarin, J. H. Clark, R. Luque and D. J. Macquarrie, *Chem. Commun.*, 2007, 634–636.

[40] R. Luque, V. Budarin, J. H. Clark and D. J. Macquarrie, *Green Chem.*, 2009, **11**, 459–461.

[41] R. Luque, V. Budarin, J. H. Clark, P. Shuttleworth and R. J. White, *Catal. Commun.*, 2011, **12**, 1471–1476.

[42] R. Luque and J. H. Clark, *Catal. Commun.*, 2010, **11**, 928–931.

[43] H. L. Parker, V. L. Budarin, J. H. Clark and A. J. Hunt, *ACS Sustainable Chem. Eng.*, 2013, **1(10)**, 1311–1318.

[44] H. L. Parker, A. J. Hunt, V. L. Budarin, P. S. Shuttleworth, K. L. Miller and J. H. Clark, *RSC Adv.*, 2012, **2**, 8992–8997.

[45] S. C. Moldoveanu, *Techniques and Instrumentation in Analytical Chemistry: Analytical Pyrolysis of Natural Organic Polymers*, Elsevier, 1998.

[46] P. T. Williams and S. Besler, *Renewable Energy*, 1996, **7**, 233–250.

[47] T. Fisher, M. Hajaligol, B. Waymack and D. Kellogg, *J. Anal. Appl. Pyrolysis*, 2002, **62**, 331–349.

[48] D. W. Van Krevelen, *Fuel*, 1950, **29**, 269–228.

[49] G. Trif-Tordai and I. Ionel, in *Alternative Fuel*, ed. M. Manzanera, Intech, 2011, ch. 12, Waste Biomass as Alternative Bio-Fuel - Co-Firing versus Direct Combustion, pp. 285–306.

[50] M. Ahmad, A. U. Rajapaksha, J. E. Lim, M. Zhang, N. Bolan, D. Mohan, M. Vithanage, S. S. Lee and Y. S. Ok, *Chemosphere*, 2014, **99**, 19–33.

[51] V. Budarin, J. Clark, R. Luque, D. Macquarrie, K. Milkowski and R. White, *Carbonaceous materials*, 2008, EU Pat. 20,070,726,967.

[52] A. Cuesta, P. Dhamelincourt, J. Laureyns, A. Martinez-Alonso and J. Tascon, *Carbon*, 1994, **32**, 1523–1532.

[53] A. C. Ferrari and J. Robertson, *Phys. Rev. B*, 2001, **64**, 075414.

[54] F. Tuinstra and J. L. Koenig, *J. Chem. Phys.*, 1970, **53**, 1126–1130.

[55] A. C. Ferrari, *Solid State Commun.*, 2007, **143**, 47–57.

[56] D. Leal, B. Matsuhiro, M. Rossi and F. Caruso, *Carbohydr. Res.*, 2008, **343**, 308–316.

[57] M. de Veij, P. Vandenabeele, T. De Beer, J. P. Remon and L. Moens, *J. Raman Spectrosc.*, 2009, **40**, 297–307.

[58] J. S. Macedo, L. Otubo, O. P. Ferreira, I. de Fatima Gimenez, I. O. Mazali and L. S. Barreto, *Microporous Mesoporous Mater.*, 2008, **107**, 276–285.

[59] A. Marriott, A. Hunt, E. Bergstrom, K. Wilson, V. Budarin, J. Thomas-Oates, J. Clark and R. Brydson, *Carbon*, 2014, **67**, 514–524.

[60] N. Shimodaira and A. Masui, *J. Appl. Phys.*, 2002, **92**, 902–909.

[61] M. Sevilla and A. Fuertes, *Chem. - Eur. J.*, 2009, **15**, 4195–4203.

[62] L. Hawelek, N. Woznica, A. Brodka, V. Fierro, A. Celzard, A. Bulou and A. Burian, *J. Phys.: Condens. Matter*, 2012, **24**, 495303.

[63] X. Li, J. Hayashi and C. Li, *Fuel*, 2006, **85**, 1700–1707.

[64] A. Primo, P. Atienzar, E. Sanchez, J. M. Delgado and H. Garcia, *Chem. Commun.*, 2012, **48**, 9254–9256.

[65] M. Takayama, T. Johjima, T. Yamanaka, H. Wariishi and H. Tanaka, *Spectrochim. Acta, Part A*, 1997, **53**, 1621–1628.

[66] D. M. Keown, J.-I. Hayashi and C.-Z. Li, *Fuel*, 2008, **87**, 1127–1132.

[67] Y. S. Al-Degs, M. I. El-Barghouthi, A. H. El-Sheikh and G. M. Walker, *Dyes and Pigments*, 2008, **77**, 16–23.

[68] H. T. Gomes, S. M. Miranda, M. J. Sampaio, A. M. Silva and J. L. Faria, *Catal. Today*, 2010, **151**, 153–158.

[69] J. Rivera-Utrilla, I. Bautista-Toledo, M. Ferro-Garcia and C. Moreno-Castilla, *J. Chem. Technol. Biotechnol.*, 2001, **76**, 1209–1215.

[70] M. Lopez-Ramon, F. Stoeckli, C. Moreno-Castilla and F. Carrasco-Marin, *Carbon*, 1999, **37**, 1215–1221.

[71] A. Rodrigues, A. Brito, P. Janknecht, M. F. Proenca and R. Nogueira, *J. Environ. Monit.*, 2009, **11**, 377–382.

[72] S. Jayaganesh and V. Senthurpandian, *Asian J. Earth Sci.*, 2010, **3**, 130–135.

[73] *Adsorption by Carbons*, ed. E. J. Bottani and J. M. Tascon, Elsevier Science, 2005.

[74] Y. Ho and G. Mckay, *Process Saf. Environ. Prot.*, 1998, **76**, 183–191.

[75] Y.-S. Ho, *J. Hazard. Mater.*, 2006, **136**, 681–689.

[76] G. Zhao, J. Li and X. Wang, *Chem. Eng. J.*, 2011, **173**, 185–190.

[77] N. Kannan and M. M. Sundaram, *Dyes Pigm.*, 2001, **51**, 25–40.

[78] Y. Ho and G. McKay, *Process Biochem.*, 1999, **34**, 451–465.

[79] D. D. Do., *Adsorption analysis : equilibria and kinetics*, Imperial College Press, 1998, vol. 2.

[80] B. K. Singh and N. S. Rawat, *J. Chem. Technol. Biotechnol.*, 1994, **61**, 57–65.

[81] K. Akhrib, F. Kaouah, T. Berrama and Z. Bendjama, *Desalination and Water Treatment*, 2013, **51**, 6049–6057.

[82] A. Kumar, S. Kumar and S. Kumar, *Carbon*, 2003, **41**, 3015–3025.

[83] H. Teng and C.-T. Hsieh, *J. Chem. Technol. Biotechnol.*, 1999, **74**, 123–130.

[84] B. L. Dunicz, *J. Chem. Educ.*, 1961, **38**, 357.

[85] J. Li, R. Lu, B. Dou, C. Ma, Q. Hu, Y. Liang, F. Wu, S. Qiao and Z. Hao, *Environ. Sci. Technol.*, 2012, **46**, 12648–12654.

[86] T. Sutlknot and K. J. Himmelstein, *Ind. Eng. Chem. Fundam.*, 1983, **22**, 420–425.

[87] S. Suresh, V. C. Srivastava and I. M. Mishra, *J. Chem. Eng. Data*, 2011, **56**, 811–818.

[88] F. Mohamed, W. Khater and M. Mostafa, *Chem. Eng. J.*, 2006, **116**, 47–52.

[89] *EPA documentation on PAHs*, `epa.gov/bpspill/pahs.html`, Last Accessed 20-Oct-2015.

[90] I. C. Nisbet and P. K. LaGoy, *Regul. Toxicol. Pharmacol.*, 1992, **16**, 290–300.

[91] K. Yang, L. Zhu and B. Xing, *Environ. Sci. Technol.*, 2006, **40**, 1855–1861.

[92] B. Chen and Z. Chen, *Chemosphere*, 2009, **76**, 127–133.

[93] G. Sheng, D. Shao, X. Ren, X. Wang, J. Li, Y. Chen and X. Wang, *J. Hazard. Mater.*, 2010, **178**, 505–516.

[94] Z. Pei, L. Li, L. Sun, S. Zhang, X. quan Shan, S. Yang and B. Wen, *Carbon*, 2013, **51**, 156–163.

[95] L. Gu, Y. Wang, N. Zhu, D. Zhang, S. Huang, H. Yuan, Z. Lou and M. Wang, *Bioresour. Technol.*, 2013, **146**, 779–784.

[96] M. Alkan, O. Demirbas, S. Celikcapa and M. Dogan, *J. Hazard. Mater.*, 2004, **116**, 135–145.

[97] Z. Yoshida and E. Osawa, *J. Am. Chem. Soc.*, 1966, **88**, 4019–4026.

[98] M. Anbia and S. E. Moradi, *Chem. Eng. J.*, 2009, **148**, 452–458.

[99] A. Borisova, M. De Bruyn, V. L. Budarin, P. S. Shuttleworth, J. R. Dodson, M. L. Segatto and J. H. Clark, *Macromol. Rapid Commun.*, 2015, **36**, 774–779.

[100] D. S. Domozych, I. Sorensen, Z. A. Popper, J. Ochs, A. Andreas, J. U. Fangel, A. Pielach, C. Sacks, H. Brechka, P. Ruisi-Besares, W. G. Willats and J. K. Rose, *Plant Physiol.*, 2014, **165**, 105–118.

[101] R. Valentin, K. Molvinger, C. Viton, A. Domard and F. Quignard, *Biomacromolecules*, 2005, **6**, 2785–2792.

[102] C. Garcia-Gonzalez, J. Uy, M. Alnaief and I. Smirnova, *Carbohydr. Polym.*, 2012, **88**, 1378–1386.

[103] F. Quignard, R. Valentin and F. Di Renzo, *New J. Chem.*, 2008, **32**, 1300–1310.

[104] P. Sriamornsak, S. Sungthongjeen and S. Puttipipatkhachorn, *Carbohydr. Polym.*, 2007, **67**, 436–445.

[105] S. Arora, J. Ali, A. Ahuja, R. Khar and S. Baboota, *AAPS PharmSciTech*, 2005, **6**, 372–390.

[106] L. Qian and H. Zhang, *J. Chem. Technol. Biotechnol.*, 2011, **86**, 172–184.

[107] H. Tamon, H. Ishizaka, T. Yamamoto and T. Suzuki, *Carbon*, 2000, **38**, 1099–1105.

[108] H. Tamon, H. Ishizaka, T. Yamamoto and T. Suzuki, *Carbon*, 1999, **37**, 2049–2055.

[109] S. R. Mukai, H. Nishihara and H. Tamon, *Microporous Mesoporous Mater.*, 2003, **63**, 43–51.

[110] A. Celzard, V. Fierro, A. S. G. Amaral-Labat, F. Braghiroli, J. Parmentier, A. Pizzi, L. Grishechko and B. Kuznetsov, *Bol. Grupo Espanol Carbon*, 2012, **26**, 2–7.

[111] H. Sehaqui, Q. Zhou and L. A. Berglund, *Compos. Sci. Technol.*, 2011, **71**, 1593–1599.

[112] J. Cai, S. Kimura, M. Wada, S. Kuga and L. Zhang, *ChemSusChem*, 2008, **1**, 149–154.

[113] H. Jin, Y. Nishiyama, M. Wada and S. Kuga, *Colloids Surf., A*, 2004, **240**, 63–67.

[114] C. Guizard, J. Leloup and S. Deville, *J. Am. Ceram. Soc.*, 2014, **97**, 2020–2023.

[115] K. Kasraian and P. DeLuca, *Pharm. Res.*, 1995, **12**, 484–490.

[116] K. Kasraian and P. DeLuca, *Pharm. Res.*, 1995, **12**, 491–495.

[117] S. Wittaya-Areekul and S. L. Nail, *J. Pharm. Sci.*, 1998, **87**, 491–495.

[118] J. B. Ott, J. R. Goates and B. A. Waite, *J. Chem. Thermodynamics*, 1979, **11**, 739–746.

[119] G. D. Manrique and F. M. Lajolo, *Postharvest Biol. Technol.*, 2002, **25**, 99–107.

[120] D. A. Rees and E. J. Welsh, *Angew. Chem., Int. Ed. Engl.*, 1977, **16**, 214–224.

[121] M. Rinaudo, *Macromol. Biosci.*, 2006, **6**, 590–610.

[122] D. Mohnen, *Curr. Opin. Plant Biol.*, 2008, **11**, 266–277.

[123] I. Plashchina, M. Semenova, Y. Slovokhotov, Y. Struchkov, E. Braudo, V. Tolstoguzov and G. Ignatov, *Carbohydr. Polym.*, 1986, **6**, 1–13.

[124] R. Chen, C.-A. Wang, Y. Huang, L. Ma and W. Lin, *J. Am. Ceram. Soc.*, 2007, **90**, 3478–3484.

[125] R. K. Henderson, C. Jimenez-Gonzalez, D. J. C. Constable, S. R. Alston, G. G. A. Inglis, G. Fisher, J. Sherwood, S. P. Binks and A. D. Curzons, *Green Chem.*, 2011, **13**, 854–862.

[126] K. Alfonsi, J. Colberg, P. J. Dunn, T. Fevig, S. Jennings, T. A. Johnson, H. P. Kleine, C. Knight, M. A. Nagy, D. A. Perry and M. Stefaniak, *Green Chem.*, 2008, **10**, 31–36.

[127] R. Sharma, J. Wooten, V. Baliga and M. Hajaligol, *Fuel*, 2001, **80**, 1825–1836.

[128] U. Einhorn-Stoll and H. Kunzek, *Food Hydrocolloids*, 2009, **23**, 40–52.

[129] J. Rouzaud, A. Oberlin and C. Beny-Bassez, *Thin Solid Films*, 1983, **105**, 75–96.

[130] N. Mahinpey, P. Murugan, T. Mani and R. Raina, *Energy Fuels*, 2009, **23 (5)**, 2736–2742.

[131] A. Ross, J. Jones, M. Kubacki and T. Bridgeman, *Bioresour. Technol.*, 2008, **14**, 6494–6504.

[132] S. Schimmelpfennig and B. Glaser, *J. Environ. Qual.*, 2011, **41**, 1001–1013.

[133] M. Keiluweit, P. S. Nico, M. G. Johnson and M. Kleber, *Environ. Sci. Technol.*, 2010, **44**, 1247–1253.

[134] M. D. Milosevic, M. M. Logar, A. V. Poharc-Logar and N. L. Jaksic, *Int. J. Spectrosc.*, 2013, **3**, 923–939.

[135] R.-L. Liu, Y. Liu, X.-Y. Zhoua, Z.-Q. Zhanga, J. Zhang and F.-Q. Dang, *Bioresour. Technol.*, 2014, **154**, 138–147.

[136] J. Gong, J. Liu, X. Chen, Z. Jiang, X. Wen, E. Mijowska and T. Tang, *J. Mater. Chem. A*, 2015, **3**, 341–351.